SAPIENZA
UNIVERSITÀ DI ROMA

Doctoral School "Vito Volterra"in
Astronomical, Chemical, Earth, Mathematical
and Physical Sciences

Ph.D. in Earth Sciences
Cycle XXXIII

High pressure experiments on kinetic and rheological properties of primitive alkaline magmas: constraints on deep magmatic processes at the Campi Flegrei Volcanic District

Ph.D. Canditate
Barbara Bonechi

Supervisor
Prof. Mario Gaeta

2021

BB

SAPIENZA
UNIVERSITÀ DI ROMA

Doctoral School "Vito Volterra" in Astronomical, Chemical, Earth,

Mathematical and Physical Sciences

Ph.D. in Earth Sciences

XXXIII cycle

High pressure experiments on kinetic and rheological properties of primitive alkaline magmas: constraints on deep magmatic processes at the Campi Flegrei Volcanic District

SSD GEO/08

Ph.D. Candidate:
Barbara Bonechi

Supervisor: **Prof. Mario Gaeta**

Co-Supervisors: **Dr. Cristina Perinelli, Prof. Vincenzo Stagno**

2021

Revised by:

Prof. Matteo Masotta

Department of Earth Sciences,

University of Pisa,

Via S. Maria 53 - 56126 Pisa Italy

Dr. Fabio Arzilli

School of Earth and Environmental Sciences,

University of Manchester,

Oxford Road, Manchester, M139PL, UK

High pressure experiments on kinetic and rheological properties of primitive alkaline magmas: constraints on deep magmatic processes at the Campi Flegrei Volcanic District

Ph.D. thesis. Sapienza University of Rome

Author's email: barbara.bonechi@uniroma1.it

"There's No Denying It. It's a great feeling when others believe in you. But today, I want to encourage you to believe in yourself, no matter what! Always believe in yourself, wholeheartedly. No matter what people may say or think, if You believe in your capabilities to do something, Do It. Allow your passion to motivate you every step of your journey. Allow your passion to give you strength when doubt tries to set in. Stay true to yourself and do it how You see it! And remember: It's okay to be different! Be uniquely You"

- Stephanie Lahart-

Table of contents

Summary

Defining the timescales of magma storage and ascent beneath active volcanoes is a fundamental tool in volcanological investigation of the last decade to constrain pre-eruptive magmatic processes and magma chamber dynamics, since it is able to provide the basis for volcanic hazard assessment. This Ph.D. project focuses on the investigation of the deep portion of the Campi Flegrei Volcanic District plumbing system (crustal-mantle boundary; ~25 km of depth), in correspondence of which the presence of a possible crystallization zone has been hypothesized on the basis of melt inclusion studies, seismic data interpretations, gravimetric and petrological modelling and experimental data. The Campi Flegrei Volcanic District, which includes the Campi Flegrei and the islands of Ischia and Procida, represents one of the most active volcanic areas in the Mediterranean region and one of the most dangerous volcanic complexes on Earth owing to the intense urbanization of the area. Many petrological, geochemical and geophysical surveys were carried out in the Campania Active Volcanic Area that have helped to define the main architecture and the development of the sub-volcanic system. Nevertheless, the dynamic processes that operate during the earliest, deepest differentiation steps of primitive magmas that fed all Campi Flegrei eruptions are yet poorly constrained. The knowledge of the dynamics and residence and ascent timescales of magma at deep levels, indeed, may be the key to understand the triggering mechanisms of volcanic eruptions, and are essential for understanding the rates at which magmas are supplied to volcanic complexes. In this thesis, the investigation of the kinetic and rheological properties of a K-basaltic magma at Moho depth, together with the

partitioning of trace elements between crystal and melts, has allowed to fill some gaps relative to the knowledge of the deep portion of the Campi Flegrei Volcanic District plumbing system, providing magma residence time and ascent timescales, and models for deep magmatic differentiation processes.

Introduction

State of research in the field

The Campi Flegrei Volcanic District (CFVD, southern Italy; Fig. 1), includes the Campi Flegrei and Ischia and Procida islands and it represents one of the most active volcanic areas in the Mediterranean region. This volcanic area is located near the south-western margin of the Campania Plain, within a graben linked to the extension occurred along the south-western margin of the Apennine Mountains during the opening of the Tyrrhenian Sea basin in the Pliocene-Quaternary (Acocella et al., 1999).

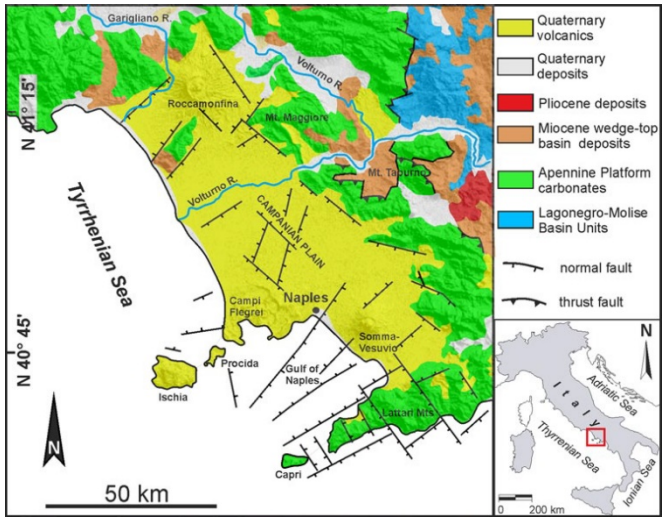

Figure 1. *Geological sketch map of the Campanian Plain. After Vitale and Isaia (2014) (modified from Vitale and Ciarcia 2013; Orsi et al. 1996).*

Its volcanic products, mostly pyroclastic rocks, show a well-documented compositional variation spanning from rare K-basalt and shoshonite through latite to predominant trachyte and slightly peralkaline phonolite, identifying a potassic, mildly alkaline series (Fig. 2; e.g., Armienti et al., 1983; Civetta et al., 1997; D'Antonio et al., 1999a, 1999b; de Vita et al., 1999; Melluso et al., 2012; Orsi et al., 1995; Pappalardo et al., 1999). The origin of the CFVD magmatism has been identified in a K-rich mantle, whose enrichment, according to the most accredited hypothesis is due to fluids/melts released by the subducting Ionian oceanic lithosphere, which was part of the wider Tethys Ocean (Avanzinelli et al., 2009; D'Antonio et al., 1999a, 1996; Mazzeo et al., 2014; Peccerillo, 2017; Schiano et al., 2004; Tonarini et al., 2004). The 2 Ma old, calc-alkaline volcanic products found in Parete and Castelvolturno bore-holes (north-west of Campi Flegrei; Beccaluva et al., 1991 and references therein) may represent a distinct cycle of volcanic activity associated to a source different from the one that originated the recent potassic magmas of the Campania Province. The change from calc-alkaline to variable K-alkaline rock series, also observed in other volcanic districts of the circum-Tyrrhenian region (Beccaluva et al., 2013; Conticelli et al., 2009), provides evidence of the increasingly marked metasomatic modification of the upper mantle following the recycling of crustal components via subduction. To date many petrological and geochemical studies (Peccerillo, 2017 and references therein) have been addressed to reconstruct the differentiation processes at the origin of the CFVD igneous rock types (from silica-saturated to slightly silica-undersaturated, potassic compositions). Nevertheless, to unravel the differentiation processes affecting the CFVD magmas is not a trivial task.

Indeed, most of the erupted magmas are characterized by evolved compositions with their trace-element distributions and isotopic characteristics masked by shallow processes like fractional crystallization and mingling/mixing (e.g., Armienti et al., 1983; Civetta et al., 1997; D'Antonio et al., 1999b; de Vita et al., 1999; Melluso et al., 2012; Orsi et al., 1995; Pappalardo et al., 1999; Peccerillo, 2017). The least-evolved volcanic rocks of the whole CFVD are K-basaltic scoria clasts occurring in the hydromagmatic tuff of the Solchiaro eruption (Procida Island, ~22 ka ago; Morabito et al., 2014; Fig. 2), like the APR16 sample (D'Antonio et al., 1999a; De Astis et al., 2004; Mazzeo et al., 2014; Perinelli et al., 2019), used as starting material in the experiments of this thesis. The isotopic composition of the APR16 is characterized by low $^{87}Sr/^{86}Sr$ ratio (0.70506) and high $^{143}Nd/^{144}Nd$ (0.51273) representing, therefore, the least radiogenic composition of the whole area reported in literature to date (Mazzeo et al., 2014). The similarity in geochemical and isotopic features among Procida, Ischia and Campi Flegrei and between the CFVD and Somma-Vesuvio products highlights a strong relationship within the Campania Province magmas and allows to consider the K-basaltic scoria clasts from Procida as the parental magmas of the recent (<50 ka) volcanic products of the Campania Province (Civetta et al., 2004; Fedi et al., 2018; Mazzeo et al., 2014; Pappalardo and Mastrolorenzo, 2012).

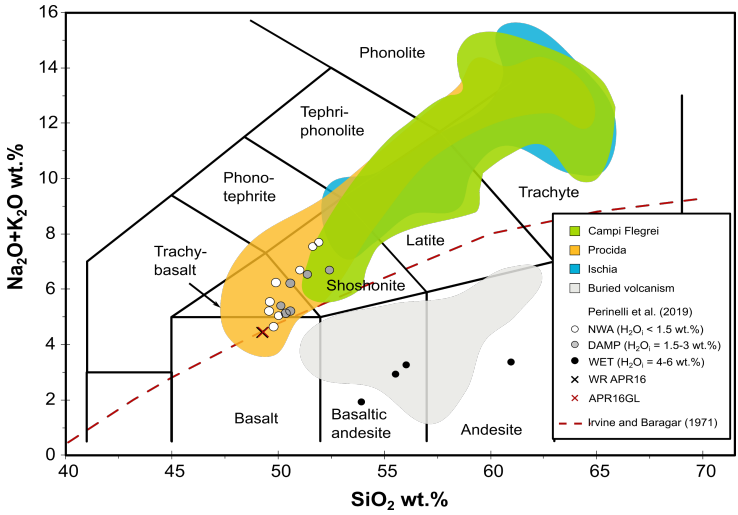

Figure 2. *TAS classification diagram (Le Maitre et al., 2002) for Campi Flegrei volcanic rocks. Literature data of Procida Island (ochre coloured field), of Campi Flegrei Volcanic District (green coloured field) and of Ischia Island (light blue coloured field) are from GEOROC database (http://georoc.mpch-mainz.gwdg.de/georoc/Start.asp). The grey coloured field represents the high-K calc-alkaline rocks from the Parete and Castelvolturno bore-holes (north-west of Campi Flegrei). Symbols indicate the anhydrous (white), damp (grey) and hydrous (black) experimental runs of Perinelli et al. (2019). Black and red crosses indicate the APR16 and APR16GL starting materials of Perinelli et al. (2019). Alkaline/subalkaline limit (red dotted line) is after Irvine and Baragar (1971).*

It has been known for long time that the timescale of magma formation, storage and ascent beneath active volcanoes is the key to constrain pre-eruptive magmatic processes and magma chamber dynamics, which provide the basis for volcanic hazard assessment (e.g., Blake and Ivey, 1986; Druitt et al., 2012; Martin et al., 2008; Morgan et al., 2006; Petrone et al., 2016; Saunders et al., 2012; Sparks et al., 1997). Estimates of these timescales and knowledge of magmatic processes can be obtained by several methods (Costa et al., 2020, and reference therein), among which the

investigation of kinetics of crystal nucleation and growth, dissolution kinetics, rheological properties and partitioning of trace elements between crystals and melts.

The kinetics of crystal nucleation and growth are fundamental for the interpretation of rock textures in terms of thermal history of a magma during its ascent to the surface and to constrain timescales of magmatic processes. Indeed, deep-level ascent rates may be the key to understand the triggering mechanisms of volcanic eruptions and are essential for understanding the rates at which magmas are supplied to volcanic complexes (Armienti et al., 2013; Perinelli et al., 2018). In this regard, the experimental approach is used to reproduce natural processes on a small scale as reliably as possible. The performance of experiments together with a series of assumptions targeted at constraining the countless variables present in nature, provides fundamental data for developing petrological models aimed at interpreting and predicting what happens in nature. In particular, as regards the kinetic properties, there are two main experimental procedures generally used: "static" and "dynamic" experiments. As reported by Hammer (2008), "static" experiments are composed of an initial equilibration period followed by rapid decompression or rapid cooling, executed in a single step or ramp that is short compared to the duration of the subsequent dwell period. Conversely, "dynamic" experiments include continuous changes in temperature and/or pressure, such as multi-step decompression, constant-rate cooling, and various combinations of dwell and ramp segments. Furthermore, on the basis of the experimental *T*-*t* path, the experiments are also distinguished into isothermal and sub-cooling experiments. As reported in detail by

Masotta et al. (2020) in isothermal experiments, temperature is linearly increased to the target resting temperature (T_{rest}) and the early clinopyroxene nucleation at T comprised between the glass transition temperature (T_g) and the T_{rest} determines the formation of many small-size crystals. On the other hand, in undercooling experiments, the T_{rest} is approached after a short annealing time at temperature above the liquidus and clinopyroxene growth at $T > T_{rest}$ determines the formation of fewer, but larger (>100 mm) and compositionally-zoned crystals. While undercooling experiments reproduce more effectively the natural conditions of clinopyroxene growth during cooling and/or degassing of magmas, isothermal ones are more useful to reproduce crystal growth in steady condition like in a magma reservoir. For this reason, since this thesis is focused on the investigation of magmatic processes occurring in a deep magmatic reservoir, static isothermal experiments have been chosen as experimental procedure.

In this thesis clinopyroxene and amphibole growth rates were investigated in detail, since they are the predominant phases under the studied conditions (see next section §*Choice of the experimental conditions* for details). Clinopyroxene, indeed, is a common phenocryst in basaltic systems and, due to its wide crystallization range, it may contain the most complete record of evolutionary history of a magma. Amphibole, instead, is a typical phase of mafic to felsic hydrous magmas (Arculus and Wills, 1980; Cawthorn et al., 1973; Davidson et al., 2007) through which it was possible to qualitatively and quantitatively infer magmatic crystallization pressure and temperature as well as magma storage, mixing and ascent processes (e.g., Rutherford and Devine, 2008; Turner et al., 2013; Zhang et al., 2017).

However, to date, experimental studies of clinopyroxene crystallization kinetics in primitive alkaline compositions are few and limited to low pressure conditions (≤ 0.5 GPa; e.g., Arzilli and Carroll, 2013; Orlando et al., 2008; Pontesilli et al., 2019), as well as the investigations on the kinetics of amphibole crystallization, that are all addressed to investigate calc-alkaline rocks affinity (i.e., Shea and Hammer, 2013; Simakin et al., 2009; Zhang et al., 2019). In Chapter 1 of this thesis, the cooling rate and the deep-level ascent rates of K-basaltic magmas were evaluated by combining the clinopyroxene growth rate determined by high-pressure crystallization experiments with data from crystal size distribution analyses and thermobarometry of clinopyroxenes occurring in the most primitive scoria clasts of the CFVD. The aim, indeed, was to investigate the CFVD magmas transport at Moho-lower crust depth and provide an estimate of magma recharge of the deep reservoirs.

Knowledge of dissolution kinetics of minerals is important to provide constraints on crystal residence times and magma chamber dynamics. Dissolution is a fundamental process in igneous petrology and it often occurs, for instance, during xenolith and/or xenocryst digestion by magma assimilation and transport processes (e.g., Edwards and Russell, 1998). Among the studies available in the literature regarding the dissolution of minerals in silicate melts, those focusing on clinopyroxene dissolution are few and sparse (Chen and Zhang, 2009; Kuo and Kirkpatrick, 1985; Kutolin and Agafonov, 1978; Scarfe et al., 1980; Van Orman and Grove, 2000; Zhang et al., 1989) and only those by Scarfe et al. (1980) and Brearley and Scarfe (1986) report data on clinopyroxene dissolution in alkali basaltic compositions. The clinopyroxene dissolution rates calculated in Chapter 1

of this thesis were employed to determine the dissolution times of phenocrysts from the Campi Flegrei caldera, since the omission of the effect of the dissolution of the crystals, could lead to an underestimation of the residence times.

Evidence that the re-activation of volcanic areas is supported by an input of deeply formed magmatic batches, implies that the eruptive style at surface is influenced by the physical and chemical conditions of magmas at depths of the upper mantle. In the case of Campi Flegrei, several studies have pointed out the geochemical and seismic signature for the presence of mantle-derived magmas, the rheological properties of which remained unexplored so far. Experimental studies have provided the pressure dependence of viscosity first by performing quench experiments in multi anvil and piston cylinder (Kushiro et al., 1976) although limited to viscosities > 1 Pa·s. More recent experimental studies performed at high pressure and temperature representative of mantle regions by means of in situ radiographic techniques combined with high-pressure apparatus have allowed to explore a wider range of silicate melt compositions like basaltic (Sakamaki et al., 2013), trachy-andesitic (Suzuki et al., 2005), albitic (Suzuki et al., 2002) and dacitic (Tinker et al., 2004) melts. To date, experimental studies on the rheological properties of magmas of interest for the Campi Flegrei Volcanic District (CFVD; Italy) investigate only differentiated compositions from latites to trachytes at low (< 0.5 GPa) and atmospheric pressure (Caricchi et al., 2008; Giordano et al., 2009, 2004; Misiti et al., 2011, 2006; Romano et al., 2003). Viscosity data measured in Chapter 2 of this thesis were used to model *i*) the mobility and migration rate of APR16 K-basaltic melt at upper mantle conditions corresponding to a scenario of new

batches of magma that form in the mantle source and move upward creating the conditions of re-filling of the chamber at crustal depths; and ii) the flow regime and magma ascent rate from deep to shallow reservoirs, and up to the surface.

Finally, a central factor in the evolution of an igneous body is the partitioning of elements between the melt and the crystallizing minerals. The study of the factors influencing the partitioning coefficients is of paramount importance since the latter are frequently used in petrological and geochemical studies to better understand magmatic processes, like fractional or equilibrium crystallization, assimilation, and partial melting (e.g., Mollo et al., 2016). Trace elements partitioning results to be controlled by several parameters like temperature and pressure (e.g., Blundy and Wood, 2003; Mollo et al., 2018; Sun and Liang, 2012), mineral composition (e.g., Blundy and Wood, 1991, 1994; Onuma et al., 1968; Mollo et al., 2016), melt composition (e.g., Bennett et al., 2004; Gallahan and Nielsen, 1992; Mysen and Virgo, 1980), redox conditions (Aigner-Torres et al., 2007; Cartier et al., 2014), and kinetic effects (e.g., Arzilli et al., 2018; Lofgren et al., 2006; Mollo et al., 2011, 2013). Among these latter only few are relative to clinopyroxene (Lofgren et al., 2006; Mollo et al., 2013; Shimizu, 1981). In Chapter 3 of this thesis, trace element partition coefficients between clinopyroxene and K-basaltic melts were investigated aiming to *i*) provide clinopyroxene-melt partition coefficient experimental data for primitive compositions in the CFVD area; *ii*) understand the role of the crystallization kinetics on trace elements partitioning behaviour relevant for deep magmatic reservoirs, and *iii*) model deep differentiation of primitive parental K-basaltic magmas of the CFVD.

Choice of the experimental conditions

Pressure. The main pressure investigated in this thesis (0.8 GPa) is representative of the crustal-mantle boundary in the Phlegraean area (~25 km of depth; Di Stefano et al., 2011; Fig. 3). At that depth, the presence of a possible crystallization zone was hypothesized on the basis of the results of melt inclusion studies (Moretti et al., 2013; Mormone et al., 2011), seismic data interpretations (Chiarabba et al., 2008; Di Stefano et al., 1999; Piochi et al., 2005), gravimetric and petrological modelling (Fedi et al., 2018) and experimental data (Perinelli et al., 2019). Moreover, in Chapter 2 pressures between 0.7 and 7 GPa are considered to investigate the mobility of the APR16 K-basaltic melt from the mantle region to the deep reservoir.

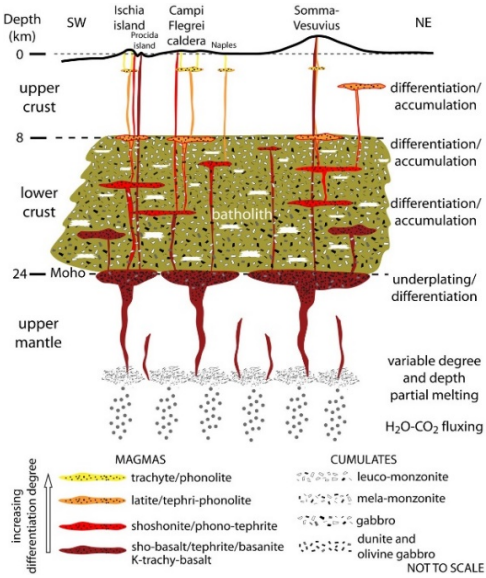

***Figure 3**. Volcanological and petrological interpretative sketch of the low-density source of the Campania Volcanic Area. From Fedi et al. (2018).*

Temperature and water content. Temperature and water amount of the experimental runs of Chapters 1.1-1.3 of this thesis (T = 1030-1250 °C and H_2O_i = 0-4 wt.%) have been chosen to have clinopyroxene as the only crystallized phase when possible (anhydrous conditions), otherwise as liquid phase in the presence of other mineral phases (hydrous conditions), based on the T-H_2O_f content projections of Perinelli et al. (2019), where phase relations of the APR16 and APR16GL compositions (i.e., the natural and glassy starting materials used in the experiments) are shown (Fig. 4).

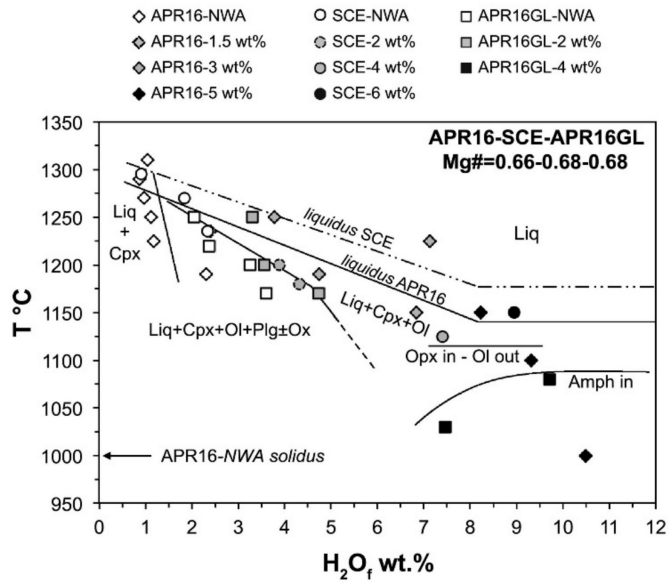

Figure 4. *T vs.H_2O_f in melt phase diagram showing experimental saturation curves (dashed when estimated), phase assemblages and stability fields for APR16, APR16GL and SCE compositions. The diagram combines the results from NWA, damp and wet experiments of Perinelli et al. (2019). NWA solidus temperature of APR16 composition is from Bonechi et al. (2017). Liq: liquid; Cpx: clinopyroxene; Ol: olivine; Plg: plagioclase; Opx: orthopyroxene; Amph: amphibole. Error bars are smaller than symbol size. After Perinelli et al. (2019).*

As shown in the *T*-H_2O_f diagram of Perinelli et al. (2019), indeed, the liquidus temperature is at about 1300 °C in the NWA (no water added) runs and below 1150 °C for H_2O_f contents higher than 8 wt.%. In the NWA runs, clinopyroxene is the liquidus phase (1270-1295 °C) followed by olivine and oxide (Cr-spinel) at 1250 °C and by plagioclase at 1190-1235 °C. In the damp runs, i.e., 1.5-3 wt.% H_2O_i, olivine begins to crystallize reaching a degree of crystallization (≤15 w.t%) lower than that at NWA conditions (≥20 wt.%). In the wet runs, i.e., 4-6 wt.% H_2O_i, olivine joints clinopyroxene at 1150 °C and it is replaced by orthopyroxene coexisting with oxide at 1100 °C. By lowering the temperature (*T* = 1080 °C), amphibole becomes stable and the resulting mineral assemblage for temperatures down to 1000 °C is composed by Cpx + Amph + Ox + Opx. Notably, in the hydrous runs at 1030 and 1080 °C the predominant crystallization of Amph compared to that of Cpx allowed to estimate its growth rate (Chapter 1.3).

Differently, temperatures of the experimental runs of Chapters 1.4 and 2 are superliquidus temperatures (1300-1350 °C and 1300-2000 °C, respectively). As regards Chapter 1.4 (i.e., dissolution kinetics), they were necessary to avoid the occurrence of the crystallization process which would disturb the diffusion and dissolution processes (Chen and Zhang., 2009); as regards Chapter 2 (i.e., rheological properties), instead, they were necessary to perform falling-sphere viscosity measurement via ultrafast imaging (Kono et al., 2014).

Aim of the Ph.D. project

The goal of this Ph.D. project is to give a contribution to the scientific debate about pre-eruptive magmatic processes and magma chamber dynamics occurring in the deep portion of the Campi Flegrei Volcanic District plumbing system, providing estimates of timescales of magma storage and ascent through the experimental investigation of the kinetic and physical properties of a primitive alkaline basalt at deep levels.

Structure of the Ph.D. thesis

This Ph.D. thesis is divided in 4 chapters:

Chapter 1 includes three papers and a manuscript about crystallization and dissolution kinetics:

- **Chapter 1.1** is a paper published in *Bulletin of Volcanology* about clinopyroxene growth rates in a primitive alkaline basalt at 0.8 GPa. The candidate is the first author and the main responsible for experimental work, analytical work, data analysis and interpretation, picture production, and for the writing of the manuscript draft.
- **Chapter 1.2** is a paper published in *Minerals* about the influence of pre-existing nuclei on the clinopyroxene crystallization in primitive alkaline magmas. The candidate is the sole author and the responsible for experimental work, analytical work, data analysis and interpretation, picture production, and for the writing of the manuscript draft.
- **Chapter 1.3** is a paper published in *Lithos* about amphibole growth rates in a primitive alkaline basalt at 0.8 GPa. The candidate is the first author and the main responsible for experimental work, analytical work, data

analysis and interpretation, picture production, and for the writing of the manuscript draft.

– **Chapter 1.4** is a manuscript (under review in *Chemical Geology*) about clinopyroxene dissolution in an alkaline basaltic melt at high pressure. The candidate is the first author and the main responsible for sample preparation, analytical work, data analysis and interpretation, picture production, and for the writing of the manuscript draft.

Chapter 2 is a manuscript (to be submitted) about the rheological properties of a primitive K-basalt at high pressure and high temperature conditions. The candidate is the first author and the main responsible for experimental work, analytical work, data analysis and interpretation, picture production, and for the writing of the manuscript draft.

Chapter 3 is a manuscript (under review in *Geochimica et Cosmochimica Acta*) about the trace element partition coefficients between clinopyroxene and a primitive K-basaltic melt. The candidate is the first author and the main responsible for experimental work, analytical work, data analysis and interpretation, picture production, and for the writing of the manuscript draft.

Chapter 4 contains the final discussion and conclusions.

Electronic appendixes A-F include the tables and the supplementary materials of Chapters 1-3.

Chapter 1.1

Clinopyroxene growth rates at high pressure: constraints on magma recharge of the deep reservoir of the Campi Flegrei Volcanic District (south Italy)

Barbara Bonechi[1], Cristina Perinelli[1], Mario Gaeta[1]

[1]Dipartimento di Scienze della Terra, Sapienza Università di Roma, P. le Aldo Moro 5, 00185 Rome, Italy

Published in *Bulletin of Volcanology*, 2020, vol. 82(1), 5

Abstract

Clinopyroxene growth rates were experimentally determined in a K-basaltic rock from Campi Flegrei Volcanic District (south Italy). The primary objective was to provide constraints on the clinopyroxene crystallization kinetics at high pressure: we carried out a series of experiments at 0.8 GPa, 1030–1250 °C, $1 \leq H_2O \leq 4$ wt.%, with durations of 0.25, 3, 6 and 9 h. Overall, growth rate reaches a maximum value in the shortest experiments (~$3 \cdot 10^{-7}$ cm·s^{-1}), decreasing to ~$1 \cdot 10^{-8}$ cm·s^{-1} in the longest duration runs. Temperature and water content do not seem to significantly affect the growth rate. Moreover, partition coefficients based on the crystal-liquid exchange show that mineral chemistry progressively approaches equilibrium with increasing run duration. Furthermore, to estimate the magma recharge of the deep reservoirs, we combined the determined growth rates with data from thermobarometry and from crystal size distribution analyses of clinopyroxenes in the most primitive scoria clasts of the Campi Flegrei Volcanic District (CFVD). We obtained a minimum residence time of ~5 months for the larger clinopyroxene population, and an ascent velocity of ~$0.5 \cdot 10^{-4}$ m·s^{-1} for the CFVD K-basaltic magma. The smaller clinopyroxene phenocrysts and microlite populations, however, suggest that the late stage of Procida magma crystallization took place in disequilibrium conditions.

Keywords: Crystal growth rate, Alkaline basalt, Clinopyroxene, Crystal size distribution, Chamber residence time, Campi Flegrei

Introduction

The kinetics of crystal nucleation and growth are fundamental for the interpretation of rock textures in terms of thermal history of a magma during its ascent to the surface and to constrain timescales of magmatic processes. Crystallization kinetics has been investigated in lunar and terrestrial basalts (Dowty et al. 1974; Lofgren 1974, 1983; Grove and Walker 1977; Grove and Raudsepp 1978; Walker et al. 1978; Lesher et al. 1999) and in silicic hydrous systems (Lofgren 1980; Kirkpatrick et al. 1981; Hammer and Rutherford 2002; Hammer 2006; Zieg and Lofgren 2006; Pupier et al. 2008). However, there are relatively few investigations of alkaline compositions (e.g., Conte et al. 2006; Agostini et al. 2013; Arzilli et al. 2015). Clinopyroxene (Cpx) is a common phenocryst in basaltic systems and, due to its wide crystallization range, it may contain the most complete record of evolutionary history of a magma. To date, experimental studies of Cpx crystallization kinetics (e.g., crystal growth rate) in primitive alkaline compositions are few and limited to low pressure conditions (≤ 0.5 GPa; e.g., Orlando et al. 2008; Arzilli and Carroll 2013; Pontesilli et al. 2019). To constrain clinopyroxene crystallization kinetics at high pressure, we experimentally investigated the growth rate of clinopyroxene in an alkaline basalt (APR16 sample; Bonechi et al. 2017) representative of the least-evolved rocks of the whole Campi Flegrei Volcanic District (CFVD). Both anhydrous and hydrous experiments were conducted at a pressure of ~0.8 GPa that is representative of the crustal-mantle boundary (~25 km of depth; Di Stefano et al. 2011) in the Phlegraean area, and the location of a possible crystallization zone, hypothesized on the basis of melt inclusion studies (Mormone et al. 2011; Moretti et al. 2013), seismic data (Di Stefano et al. 1999;

Piochi et al. 2005a, 2005b; Chiarabba et al. 2008) and gravimetric and petrological modelling (Fedi et al. 2018). Moreover, Perinelli et al. (2019) demonstrated that early magmatic storage and crystallization at high pressure (i.e., at the local crust base) contributed to the differentiation of primitive magmas of the Campania Province. For these reasons, the experimental data on high-pressure clinopyroxene growth kinetic will be useful for constraining timescales of magmatic processes in this area. In particular, the estimation of the magma ascent rate in the CFVD is of paramount significance in terms of volcanic hazard. Indeed, deep-level ascent rates may be the key to understand the triggering mechanisms of volcanic eruptions and are essential for understanding the rates at which magmas are supplied to volcanic complexes (Armienti et al. 2013; Perinelli et al. 2018). Thus, to investigate the CFVD magmas transport at Moho-lower crust depth and provide an estimate of magma recharge of the deep reservoirs, we assessed the cooling rate and the deep-level ascent rates of K-basaltic magmas by combining the clinopyroxene growth rate determined by high-pressure crystallization experiments with data from crystal size distribution analyses and thermobarometry of clinopyroxenes occurring in the most primitive scoria clasts of the CFVD.

Experimental and analytical techniques

Starting material

The starting material used in this work is an anhydrous glass (APR16GL; Table 1) prepared by melting the APR16 natural powder in a gas-mixing furnace at 1400 °C and atmospheric pressure for 15 min to reduce all Fe^{3+} to Fe^{2+} using a CO/CO_2 gas mixture at the Bayerisches Geoinstitut (Bayreuth, Germany). The starting material did not contain crystalline phases, as analysed by both microprobe and image analyses. The APR16 sample (Table 1) is a primitive alkaline basalt found as scoria clast in the deposits of the Solchiaro hydromagmatic centre located in Procida island (Campi Flegrei, Italy). It is characterized by 12 vol.% of forsteritic olivine and diopsidic clinopyroxene phenocrysts in a groundmass of olivine, clinopyroxene, plagioclase, Ti-magnetite, alkali feldspar and glass (D'Antonio et al. 1999; De Astis et al. 2004).

Experimental technique

Experiments were performed, at the isobaric pressure of 0.8 GPa, as function of temperature, water content and time by using the ½ inch end loaded piston cylinder apparatus at the HP-HT Laboratory of the Earth Sciences Department (Sapienza University, Rome, Italy). The assembly consists of an outer CaF_2 cell, graphite furnace and MgO crushable spacers. Firstly, the APR16GL glass was crushed and ground in an agate mortar under acetone to a grain size ≤ 10 μm. Then this glassy powder (40–50 mg) was dried at 110 °C for at least 2 h to remove the moisture before being loaded and pressed into $Au_{75}Pd_{25}$ capsules, along with distilled water for hydrous experiments, and then welded. For each experiment, the capsule was placed

in the MgO crushable spacers and surrounded by powder of alumina (for no water added experiments) or pyrophyllite (for water added ones). Temperature was measured using a type D W_3Re_{97}-$W_{25}Re_{75}$ thermocouple and maintained with an uncertainty of ±5 °C. The experimental assembly was first pressurized to the target pressure by a piston-out procedure (Johannes et al. 1971; Presnall et al. 1978) that applies an overpressure of ~10% of the run pressure and then gradually increases the temperature to the working temperature, while correcting for pressure drops due to stress relaxation within the assembly during heating. The heating rate was imposed at 150 °C/min. The sample was maintained at the pressure and temperature for a given duration (nominal duration), and then quenched by turning off the power. The temperature dropped to below 500 °C within <5 s (average cooling rate of 150 °C/s). All the runs were self-buffered; we estimated fO_2 through the equation of Kress and Carmichael (1991) using the liquid Fe^{3+}/Fe_{tot} mole ratios from K_D Fe-Mg ol/liq calculated following Toplis (2005). This procedure yielded fO_2 values of ΔNNO +0.12 to +2, in agreement with those estimated for similar furnace assemblages (Conte et al. 2009; Weaver et al. 2013). We performed a total of 24 experiments, whose experimental conditions are reported in Table 2. The experiments were divided into three series based on the amount of water added to the starting material. All series were run at a constant pressure and at four different dwell times (0.25, 3, 6 and 9 h). Experiments of Series 1 (i.e., APR16-C1) were run at anhydrous conditions (no water added to the starting material, NWA) and at temperatures of 1200 °C (subseries APR16-C1A) and 1250 °C (subseries APR16-C1B). Experiments of Series 2 (i.e., APR16-C2) were run at hydrous conditions (2 wt.% H_2O added to the starting material), and at

temperatures of 1170 °C (subseries APR16-C2A) and 1220 °C (subseries APR16-C2B). Experiments of Series 3 (i.e., APR16-C3) were run at hydrous conditions (4 wt.% H_2O added to the starting material), and at temperatures of 1080 °C (subseries APR16-C3A) and 1030 °C (subseries APR16-C3B). Initial water contents and experimental temperatures were chosen on the basis of the melt inclusion studies (Moretti et al. 2013) and phase data were taken from high-pressure anhydrous/hydrous experiments on Procida alkaline basalt magmas as reported in Perinelli et al. (2019). Finally, because undercooling ($\Delta T = T_{liquidus} - T_{experiment}$) is one of the critical parameters that influences the kinetics of magma crystallization, we determined the effective undercooling (ΔT_{eff}) for each sample. This is defined as the difference between the equilibrium clinopyroxene liquidus temperature (T_{CpxL}) and the experimental temperature (Hammer and Rutherford 2002). The T_{CpxL} values used to calculate ΔT_{eff} for each experiment were taken from Procida K-basalt experimental data (Perinelli et al. 2019) and from calculations using MELTS software (Ghiorso and Sack 1995; Asimow and Ghiorso 1998). Resulting T_{CpxL} and ΔT_{eff} are listed in Table 2.

Table 2 Experimental run conditions, calculated water contents, phases assemblage and proportions in run products

Run #	T (°C)	$TCpx_L$ (°C)	ΔT_{eff} (°C)	Time (h)	H_2O_i(wt%)	Phases	H_2O_f(wt%)	Σr^2	% ΔFe^3
Series 1									
Subseries C1A									
APR16-C1Aa	1250	1295	45	0.25	NWA	Gl(97) + Cpx(3)	1.61	1.75	-7
APR16-C1Ab	1250	1295	45	3	NWA	Gl(75) + Cpx(25)	0.90	0.62	-12
APR16-C1Ac	1250	1295	45	6	NWA	Gl(83) + Cpx(15) + Ol(2)	2.03	0.83	-20
APR16-C1Ad	1250	1295	45	9	NWA	Gl(90) + Cpx(10)	1.95	0.65	-19
Subseries C1B									
APR16-C1Ba	1200	1295	95	0.25	NWA	Gl(50) + Cpx(41) + Ol(6) + Plg(3)	2.21	0.11	-30
APR16-C1Bb	1200	1295	95	3	NWA	Gl(54) + Cpx(33) + Ol(6) + Plg(7)	2.92	0.38	-40
APR16-C1Bc	1200	1295	95	6	NWA	Gl(57) + Cpx(45) + Plg(2) + Ox(5)	2.72	0.64	-7
APR16-C1Bd	1200	1295	95	9	NWA	Gl(45) + Cpx(37) + Ol(3) + Plg (12) + Ox(3)	2.02	0.84	-4
Series 2									
Subseries C2A									
APR16-C2Aa	1220	1270	50	0.25	2	Gl(91) + Cpx(4) + Ol(1) + Ox(4)	1.92	0.02	-25
APR16-C2Ab	1220	1270	50	3	1.9	Gl(68) + Cpx(23) + Ol(4) + Plg(1) + Ox*	1.56	0.66	-17
APR16-C2Ac	1220	1270	50	6	2.1	Gl(65) + Cpx(27) + Ol(5) + Plg(3)	2.47	0.93	-25
APR16-C2Ad	1220	1270	50	9	1.9	Gl(80) + Cpx(17) + Ol(3) + Ox*	1.30	0.25	-26
Subseries C2B									
APR16-C2Ba	1170	1270	100	0.25	2	Gl(65) + Cpx(29) + Ol(1) + Plg(5)	1.61	3.56	-19
APR16-C2Bb	1170	1270	100	3	2	Gl(63) + Cpx(30) + Ol(6) + Plg(1)	1.39	0.77	-27
APR16-C2Bc	1170	1270	100	6	2	Gl(58) + Cpx(33) + Ol(5) + Plg(1)	3.77	0.73	-27
APR16-C2Bd	1170	1270	100	9	1.8	Gl(57) + Cpx(34) + Ol(2) + Plg(3) + Ox(4)	2.02	0.56	-4

Table 2 Continued

Run #	T (°C)	$TCpx_L$ (°C)	ΔT_{eff} (°C)	Time (h)	H_2O_i (wt%)	Phases	H_2O_f (wt%)	Σr^2	% $\Delta Fe^{\S}$
Series 3									
Subseries C3A									
APR16-C3Aa$^{\lozenge}$	1080	1218	138	0.25	4	Gl† + Amph + Cpx +Plg + Ox*			
APR16-C3Ab$^{\lozenge}$	1080	1218	138	3	4	Gl† + Amph + Cpx +Plg + Ox*			
APR16-C3Ac	1080	1224	144	6	3.8	Gl(60) + Cpx(37) + Ol(3)	6.5	0.62	-10
APR16-C3Ad	1080	1233	153	9	3.3	Gl(55) + Amph(24) + Cpx(20) + Ox(1)	10.2	0.41	-1
Subseries C3B									
APR16-C3Ba$^{\lozenge}$	1030	1224	194	0.25	3.8	Gl† + Amph + Cpx + Plg + Ox			
APR16-C3Bb$^{\lozenge}$	1030	1225	195	3	3.7	Gl† + Amph + Cpx + Plg + Ox			
APR16-C3Bc$^{\lozenge}$	1030	1232	202	6	3.4	Gl† + Amph + Cpx + Opx + Ox			
APR16-C3Bd	1030	1216	186	9	4.2	Gl(40) + Amph(35) + Cpx(24) + Ox(1)	8.3	0.18	-1

Notes: NWR natural water rock; Gl glass; Cpx clinopyroxene; Ol Olivine; Plg plagioclase; Amph amphibole; Ox oxide. $TCpx_L$ is the equilibrium clinopyroxene liquidus temperature (°C) determined on the basis of phase relations experimental data from Perinelli et al. (2019) and on the calculations by using MELTS software (Ghiorso and Sack 1995; Asimow and Ghiorso 1998). ΔT_{eff} is the difference between the clinopyroxene liquidus temperature and the nominal temperature of the runs. H_2O_i % of water added to the charge. H_2O_f as determined by the *by-difference* calculation method (respect to the total of EMP analyses). Σr^2 values from mass balance calculation. § Percent of relative Fe loss from starting material based on difference between the starting material and calculated bulk composition of experiment obtained from mass-balance calculations. †Phases too small for analysis; *crystals present in trace; $^{\lozenge}$ in these runs it was no possible to do mass balance calculation.

Analytical techniques

The recovered samples were mounted in epoxy resin, ground flat and polished. Textural aspects of the recovered samples were analysed by Scanning Electron Microscopy (SEM) using a FEI Quanta-400 equipped for microanalysis with an EDAX Genesis system at the Earth Sciences Department (Sapienza University, Rome, Italy). A minimum of eight backscattered electron (BSE) images were acquired for each experimental sample in order to accurately measure the nucleation of clinopyroxene and other crystallized mineral phases (e.g., Clarke et al. 2007; Couch 2003; Hammer et al. 2000). Phase compositions were analysed at the CNR-Istituto di Geologia Ambientale e Geoingegneria (Rome), with a Cameca SX50 electron microprobe equipped with five wavelength dispersive spectrometers (WDS). Quantitative compositional analyses were performed using 15 kV accelerating voltage and 15 nA beam current. As standards we employed metals for Mn and Cr, jadeite for Na, wollastonite for Si and Ca, orthoclase for K, corundum for Al, magnetite for Fe, rutile for Ti and periclase for Mg. Counting times were 20 s for elements and 10 s for backgrounds. Light elements were counted first to prevent loss by volatilization. The PAP correction method (Pouchou and Pichoir 1991) was used. Minerals were analysed using a beam diameter of 1 μm while for glasses a defocused electron beam of 10 to 15 μm was used. From chemical analyses, the water contents of experimental glasses were estimated according to the by-difference method (Devine et al. 1995). We are aware that this method may result in significant errors in the estimates of H_2O contents in the melts, particularly for H_2O-poor glasses (uncertainty of ~0.5 wt.% for H_2O melt ≤ 1 wt.%; Devine et al. 1995). However, the obtained H_2O

values are close to those determined by micro-Raman spectroscopy measurements on residual melts of equilibrium experiments performed on the same composition, at the same *P*, *T* and initial hydrous conditions (see Perinelli et al. 2019, for details). Therefore, the H_2O calculated using the by-difference method, with EPM analyses, can be considered to be reliable estimates of water contents of experimental melts. Finally, phase proportions were calculated using bulk and experimental phase compositions and the least squares regression routine implemented in EXCEL®. Image analysis conducted with ImageJ software was used to estimate the fraction of total solids in each experiment. Estimates of crystal fraction obtained by the latter approach did not produce good results for all samples due to the difficulty in clearly distinguishing the minor phases from glass by applying the thresholding process to backscattered images. However, due to the strong dominance of clinopyroxene in almost all experiments, it is reasonable to assume that the clinopyroxene crystal fraction (Cpx-ϕ) is representative of the crystallinity of each experiment. Figure S1 in Online Resource 1 displays the comparison of Cpx-ϕ values obtained by the two methods.

Growth rate calculation

In the SEM images, crystal dimensions were measured using the measure tool in the ImageJ® software. The maximum growth rate (G_L) values were calculated using a common method reported in literature (Burkhard 2002; Hammer and Rutherford 2002; Couch et al. 2003; Baker 2008; Iezzi et al. 2011):

$$G_L = \frac{(L \cdot W)^{0.5}}{t \cdot 2} \quad (1)$$

where L and W are the mean length and width, respectively, of the ten largest crystals for each BSE image (Fig. 1) and t is the duration of the experiments (s). As also shown in the literature, the main growth event often occurs at the beginning of the experiment, since diffusion- or interface-controlled growth normally display lower incremental growth rates as the system approaches equilibrium (e.g., Arzilli et al. 2015; Couch et al. 2003; Orlando et al. 2008). Consequently, long-lasting experiments could show an apparent decrease in G_L as time increases.

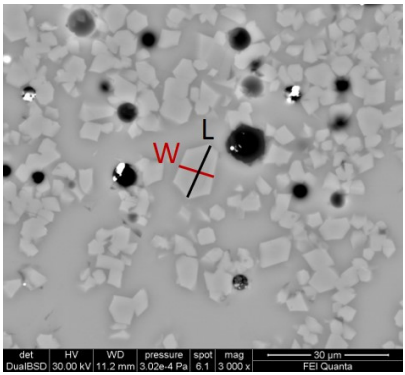

Fig. 1 *Backscattered SEM image of a typical experimental result. L and W are the dimensions (i.e., length and width, respectively) that were measured to calculate the growth rate.*

Crystal size distribution analysis

For textural analyses, we used ImageJ® software (Abramoff et al. 2004; Schneider et al. 2012) on BSE images from which binary images of each mineral were constructed following the procedure described by Philpotts and Ague (2009). Manual reconstruction of edges of overlapping crystals was necessary before conversion into binary images. Subsequently, the data were transferred to the CSDcorrections® software (v.1.6 2018; Higgins 2000, 2002) to perform the 2D to 3D conversion and the calculation of CSD plots for each mineral type. Following Higgins (1994), a clinopyroxene aspect ratio of 1:2:2 and a roundness factor of 0.1 were used, and crystals were assumed to have a uniform shape. Indeed, most of the clinopyroxene crystals have an aspect ratio (A, long/short dimension) ranging from one to four with equant habit, while only few crystals have higher aspect ratios (A ~8) with elongate habits, as shown in Fig. 2 and Fig. S2 in Online Resource 1. The APR16-C1A runs reported in Fig. 2 suggest that crystals tend to start anisotropic (e.g., APR16-C1Aa, APR16-C1Ab) and then become more equant with time (e.g., APR16-C1Ad); this is visible in all the runs (Fig. S2 in Online Resource 1). The CSD theory (Randolph and Larson 1971; Cashman and Marsh 1988; Marsh 1988) assumes that a steady crystal population grows with a growth rate G (cm·s^{-1}) producing a number of crystals $n(L)$ with length L per unit volume. The total number of crystals is:

$$N(L) = \int_0^L n(L)dL \quad (2)$$

With a characteristic crystal residence time S, the growth rate is:

$$G = L/S \quad (3)$$

and the steady variation of population per size interval dL is:

$$\frac{dn(L)}{dL} = -n/G \quad (4)$$

where n is the number density of crystals. The integration of Eq. (4) provides:

$$n = n_0 exp(-L/GS) \quad (5)$$

that taking the natural logarithm, the relation is:

$$\ln(n) = \ln(n_0) - L/GS \quad (6)$$

where n_0 is the number of nuclei at the time of consideration, which is represented here by the time at isothermal conditions. On a plot ln(n) versus L the continuous crystallization ideally provides a linear relation with a slope of $-1/GS$, from which G may be evaluated if S is known, or vice versa. In the same plot, the intercept provides the nucleation density, $\ln(n_0)$. The nucleation rate J can now be derived from:

$$J = n_0 G \quad (7)$$

When the natural logarithm of the population density of crystals varies linearly with the crystal length, CSDs can provide insight into time scales of magmatic processes (e.g., Mangan 1990; Piochi et al. 2005b; Brugger and Hammer 2010a).

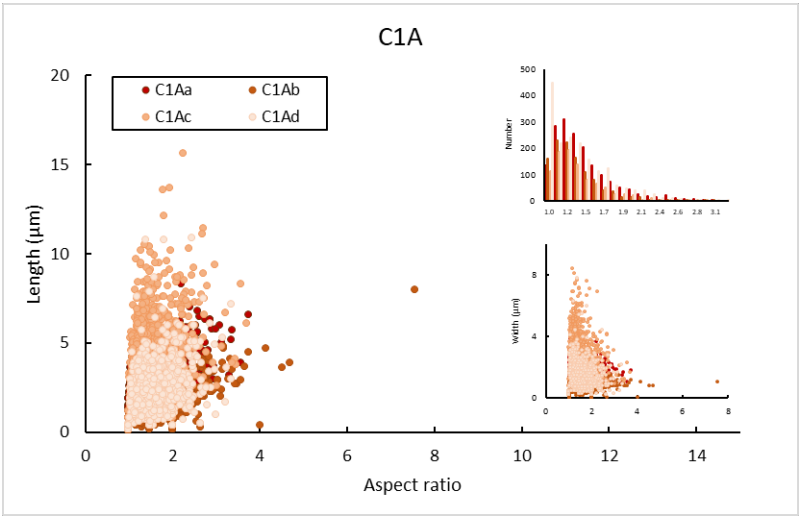

Fig. 2 *Length vs. aspect ratio for APR16-C1A runs. We also give the width vs aspect ratio plot (lower inset) and aspect ratio histogram (upper inset).*

Experimental results

BSE images allowed us to identify differences in texture, crystal dimensions and phase abundances as well as to calculate the growth rates of the crystallized phases in each of the experimental Series and determine the Crystal Size Distribution (CSD) formed during the experiments.

Phase relations and crystallinity

The experimental products consist of glass and microlites of clinopyroxene (Cpx) ± olivine (Ol) ± plagioclase (Plg) ± oxide (Ox) ± amphibole (Amph). Small bubbles dispersed within the residual glasses or grouped along the capsule walls are frequently observed in the experiments at H_2O-undersaturated conditions, that for the Procida K-basalt magmas occur

when water content in the melt is < 8 wt.% (Perinelli et al. 2019). These bubbles were probably trapped within the glassy powder during the experimental charge preparation, and served as nucleation sites, as testified by the crystal clusters around them. Phase relations obtained from the three experimental Series are shown in the diagram T vs water content in the residual glasses (H_2O_f; Fig. 3). The mineral assemblage as well as the phase abundances obtained in the long experiments (6 and 9 h) generally matches those obtained from equilibrium experiments reported by Perinelli et al. (2019) (see Table S1 in Online Resource 2). For our study, mass balance calculations indicate variable crystallization degrees within each subseries of experiments showing, as a general rule, crystallinity increasing with time (Table 2). Exceptions are the APR16-C1A (NWA, 1250 °C runs) and APR16-C2A (H_2O_i = 2 wt.%, 1220 °C runs) subseries, in which the initial increase of crystal fraction is followed by a significant decline in mineral abundance (i.e., runs at 9 h of dwell time; Table 2). In contrast, crystallization data determined from backscattered image analyses indicate higher degrees of crystallization than those determined by mass balance calculations and a similar crystallinity between runs of 3, 6 and 9 h for both the APR16-C1A and APR16-C2A subseries (Fig. S1 in Online Resource 1). Image analysis also shows a good correspondence between the mass balance versus image analyses for Cpx-ϕ values of the APR16-C1B (NWA, 1200 °C runs) and APR16-C2B (H_2O_i = 2 wt.%, 1170 °C runs) subseries (Fig. S1 in Online Resource 1). This is probably related to the high undercooling (ΔT_{eff} ~100 °C) for both the APR16-C1B and APR16-C2B experimental subseries, which drives the melt towards a crystallization degree approaching that of equilibrium conditions (Lesher et al. 1999; Conte et al. 2006; Hammer 2008).

Concerning the APR16-C1A and APR16-C2A subseries experiments, several lines of evidence suggest that heterogeneous nucleation is the general rule in all experiments (i.e., preferential nucleation of clinopyroxenes along the capsule surfaces or around small bubbles, Fig. S3 in Online Resource 1). In heterogeneous nucleation, the nuclei growing on pre-existing surfaces in the liquid require less energy to reach the critical size than that required for homogeneous nucleation (Cashman 1993), where the appearance of new crystals is promoted. Thus, for the APR16-C1A and APR16-C2A experimental subseries, the variation in crystallization degree and phase relations can be explained by heterogeneous nucleation that promoted crystallization of a specific mineral phase at the expense of the others or influenced the crystal-melt distribution along the wall of sample holder producing chemical inhomogeneities of residual glass that were not completely equilibrated.

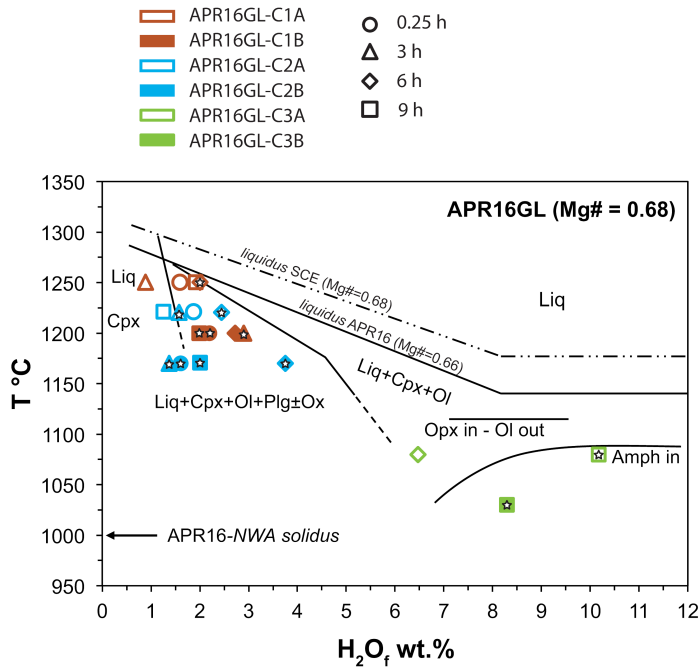

Fig. 3 *Phase relation data from this experimental study plotted in the diagram of temperature vs. water content in the melt phase (H_2O_f). The diagram reports experimental saturation curves (dashed when estimated), phase assemblages and stability fields at 0.8 GPa, for K-basaltic scoria clasts of the Solchiaro deposit and APR16GL (modified after Perinelli et al. 2019). Black stars are the experiments in which the crystallized mineral assemblage matches that obtained in the equilibrium experiments of Perinelli et al. (2019). Phase abbreviations are Liq: liquid; Cpx: clinopyroxene; Ol: olivine; Ox: oxide; Plg: plagioclase; Opx: orthopyroxene and Amph: amphibole.*

Textural features of the experimental runs

Experimental textures of the three Series show limited variations mainly linked to the increase of crystal abundance in the charge. In general, relatively large pools of residual glass (≥50 × 50 μm in size; Fig. S3-S4 in Online Resource 1) are confined to the boundary of sample holder and crystal aggregation is observed (Fig. S4-S5 in Online Resource 1).

Series 1 In the runs of the subseries APR16-C1A (1250 °C, NWA; Fig. S3a in Online Resource 1), the dominant phase is Cpx while olivine (Ol) crystallizes only in the APR16-C1Ac run at 6 h (Table 2). The habit and sizes of Cpx vary with time: subhedral grains with sizes of 5 μm occur in the shortest run (APR16-C1Aa; 0.25 h), while those that are euhedral in shape and up to 15 μm in size appear in the run with longest duration (APR16-C1Ad; 9 h). Olivine is euhedral with well-faceted faces and sizes of ~10 μm (Fig. 4). The runs of the subseries APR16-C1B (1200 °C, NWA; Fig. S3b in Online Resource 1) show a higher degree of crystallization than those of the APR16-C1A subseries and the mineral assemblage consists of Cpx + Ol + Plg + Ox. In the run with shortest duration (APR16-C1Ba; 0.25 h), Cpx is present as subhedral crystals, sometimes forming aggregates. With increasing duration, Cpx develops euhedral habits with sizes up to 20 μm. Similarly, Plg forms large tabular crystals (up to ~100 μm in length and ~30 μm in width) in the run with longest duration (APR16-C1Bd; 9 h). Olivine and Ox (present only in the runs at 6 and 9 h) have euhedral habits with sizes of ~25 and 15 μm, respectively. Some Ox crystals are characterized by a Cr-rich core.

Series 2 The mineral phases crystallized in subseries APR16-C2A (1220 °C, 2 wt.% H_2O_i; Fig. S4a in Online Resource 1) are the same as those that

crystallized in subseries APR16-C1B. Clinopyroxene and Ol are ubiquitous in these runs, whereas Plg is present only in the runs at 3 and 6 h and Ox is absent in the run at 6 h. Clinopyroxene shows a subhedral habit in the run with shortest duration and is euhedral in the other runs, with sizes between ~10 and 20 μm. Olivine crystals are well-faceted with sizes of ~15 μm; occasionally they contain embayments. Plg is euhedral with sizes up to ~40 μm. The runs of the subseries APR16-C2B (1170 °C, 2 wt.% H_2O_i) show a higher degree of crystallization (Fig. S4b in Online Resource 1) and the mineral assemblage is Cpx + Ol + Plg ± Ox (Table 2). Clinopyroxene, Ol and Plg crystallize in all the runs, while Ox occurs only in the longest run (APR16-C2Bd; 9 h). Textural features are very similar to subseries APR16-C1B.

Series 3 In the runs of subseries APR16-C3A (1080 °C, 4 wt.% H_2O_i; Fig. S5a in Online Resource 1) and APR16-C3B (1030 °C, 4 wt.% H_2O_i; Fig. S5b in Online Resource 1), the main phase is Amph, which is ubiquitous. The runs with the shortest durations (APR16-C3Aa, APR16-C3Ba and APR16-C3Ab, APR16-C3Bb; 0.25 and 3 h, respectively) are characterized by an extensive distribution of tiny crystals, most of them smaller than 10 μm in size, frequently occurring in crystalline aggregates (Fig. S5 in Online Resource 1). Small plugs of glass occasionally occur at the edge of these aggregates, but they are too small to be accurately analysed. The runs with the longest duration (APR16-C3Ad and APR16-C3Bd, 9 h) are characterized by the crystallization of Amph, Cpx and Ox. Clinopyroxene crystals are euhedral, up to ~5 μm in size, and sometimes constitute the core of Amph crystals (Fig. 5). Amphibole and Ox show euhedral habits with sizes up to ~ 60 and 40 μm, respectively.

An interesting feature concerns Ol crystal, which has a morphology that can be described as polyhedral, according to the classification of Faure et al. (2003). Polyhedral Ol crystals contain embayments or cavities, formed during multiple growth steps (Faure and Schiano 2005); these polyhedral habits were found in several experimental runs (e.g., APR16-C2Bb, APR16-C2Bc, APR16-C2Bd). In particular, it was possible to recognize (i) melt inclusions isolated inside their host crystals, with sizes between 1 and 3 μm, and shapes that can be spherical, sub-spherical or ovoid, up to irregular but still curvilinear (Fig. 6a); and (ii) open melt inclusions (embayments) extending to the crystal rim through a narrow or wide neck (Fig. 6b). This type of texture is sometimes interpreted as resulting from processes unrelated to the growth of the host crystal (e.g., chemical resorption due to crystal-melt disequilibria or thermal erosion at the crystal-liquid interface associated with transport in the magma conduit; Helz and Wright 1992; Thornber 2001; Pan and Batiza 2002). However, in our experiments, as found by Faure and Schiano (2005), this embayed texture was formed during olivine crystal growth under near-equilibrium conditions.

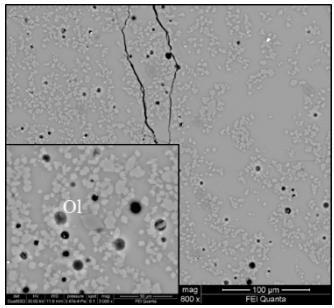

Fig. 4 *Backscattered SEM image of an olivine crystal showing a euhedral habit with well-faceted faces from run APR16-C1Ac of Series 1.*

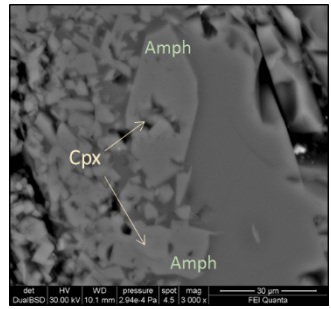

Fig. 5 *Backscattered SEM images of Cpx crystals constituting the core of Amph from run APR16-C3Ad of Series 3.*

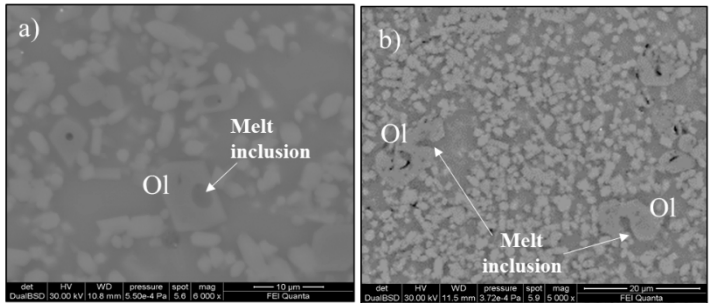

Fig. 6 *Backscattered SEM images of polyhedral Ol crystals containing embayments formed in run APR16-C2Bc of Series 2. a Closed melt inclusion isolated inside their host crystals. b Open melt inclusions extending to the crystal rim through a narrow or wide neck.*

Clinopyroxene composition and approach to equilibrium

Chemical compositions of clinopyroxene and glass are given in Table S2 in Online Resource 2. Clinopyroxene crystals are augitic (Wo_{42}-En_{41}-Fs_{18}) and diopsidic (Wo_{47}-En_{43}-Fs_{10}) in composition according to the classification scheme of Morimoto et al. (1998). Overall, the Mg# of Cpx (calculated as the molar MgO/(MgO+FeO_{tot}) ratio) varies between 0.76 and 0.88, while the Mg# of glass lies between 0.52 and 0.77. The Fe–Mg distribution coefficients between clinopyroxene and melt ($K_D(Fe\text{-}Mg)^{Cpx\text{-}liq} = Fe_{Cpx} \times Mg_{liq}/Mg_{Cpx} \times Fe_{liq}$, calculated assuming all Fe as Fe^{2+} in both phases) varies between 0.39±0.05 and 0.30±0.05 for APR16-C1A runs, 1.00±0.10 and 0.29±0.01 for APR16-C1B runs, 0.43±0.06 and 0.31±0.06 for APR16-C2A runs, and 0.57±0.06 and 0.34±0.04 for APR16-C2B runs. As shown in Fig. 7, all the shortest experiments, and in particular those of the subseries APR16-C1B and APR16-C2B, show significant deviation from the equilibrium range ($K_D(Fe\text{-}Mg)^{Cpx\text{-}liq}$ = 0.28±0.08 according to Putirka (2008)), while runs of 3 h or more increasingly reach equilibrium conditions.

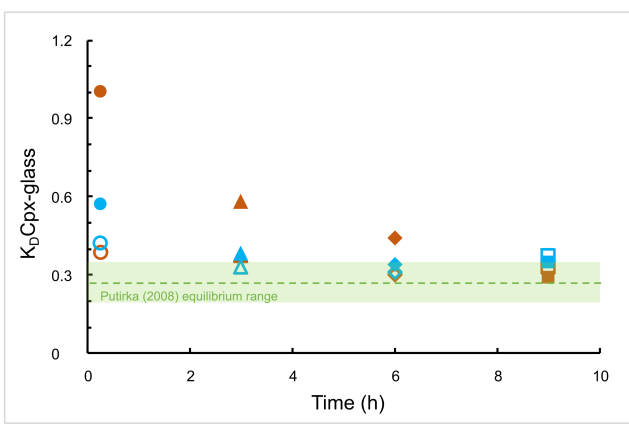

Fig. 7 *Relation between $K_D(Fe\text{-}Mg)^{Cpx\text{-}liq}$ and time. The duration of each run is indicated with different symbols: circles for 0.25 h runs, triangles for 3 h runs, diamonds for 6 h runs and squares for 9 h runs. Series are indicated with different colours: red for APR16-C1, light blue for APR16-C2. Within each series, subseries are indicated with full (runs at lower temperature) and empty (runs at higher temperature) symbols. The green field represents the equilibrium range according to Putirka (2008), while the dotted line represents the average K_D value for Cpx (0.28±0.08; Putirka 2008).*

Crystal growth rates

Maximum growth rates determined for clinopyroxene are reported in Table 3, and Fig. 8 shows the relationships between (a) crystal size (L) and experimental duration, and (b) crystal growth rate (G_L) and experiment duration. In Series 1, we observed an increase in crystal size with increasing experiment duration. Moreover, Cpx in APR16-C1A runs at 1250 °C are smaller than in APR16-C1B runs at 1200 °C. As regards crystal growth rates, the obtained values decrease by about an order of magnitude with increasing duration of the experiments, decreasing from 10^{-7} to 10^{-8} cm·s^{-1} as duration increases from 0.25 to 9 h.

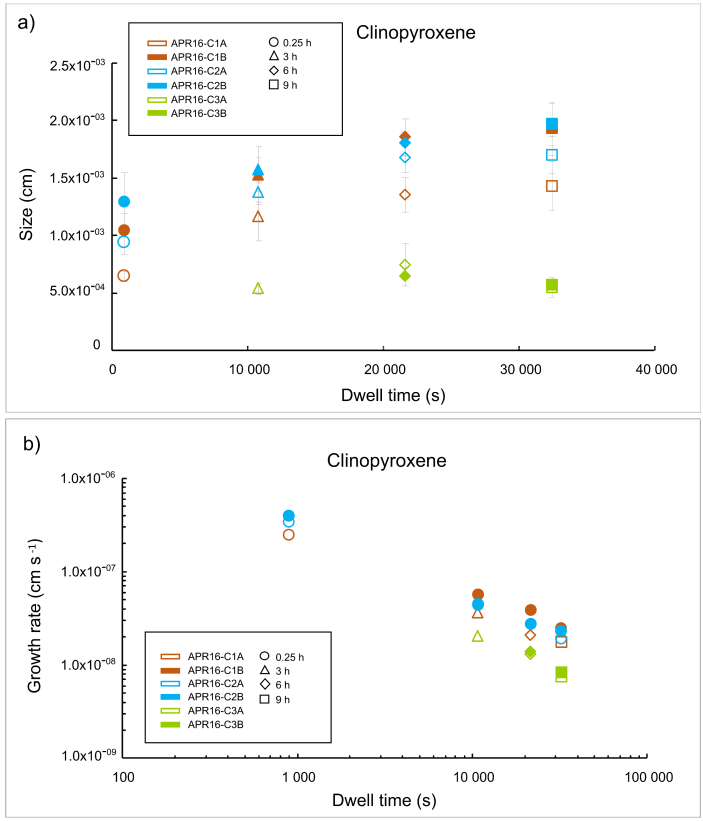

Fig. 8 *Relation between a Cpx size (L) and experimental duration, and b Cpx growth rate (G_L) and experimental duration (t). The duration of the runs is indicated with different symbols: circle for 0.25 h runs, triangle for 3 h runs, diamond for 6 h runs and square for 9 h runs. Series are indicated with different colours: red for APR16-C1, light blue for APR16-C2 and green for APR16-C3. Within each series, each subseries is indicated with full (runs at lower temperature) and empty (runs at higher temperature) symbols. In Fig. 8b, the error bars are not shown since they are inside the symbols.*

Within each series, G_L calculated from experiments at higher temperatures are slightly lower than those obtained from experiments at lower temperatures (Fig. 8b). Growth rates calculated for other phases are in Table

4. As seen for clinopyroxene, the calculated growth rates of all other phases decrease with increasing time. For both Ol (Fig. 9a) and Plg (Fig. 9b), G_L decreases from about 10^{-6} to 10^{-8} cm·s^{-1} (Table 4) as time increases from 0.25 to 9 h. For Amph and Ox, we were able to calculate the growth rates only for the runs with duration ≥ 3 h, and these had values of ~10^{-8} cm·s^{-1} (Table 4).

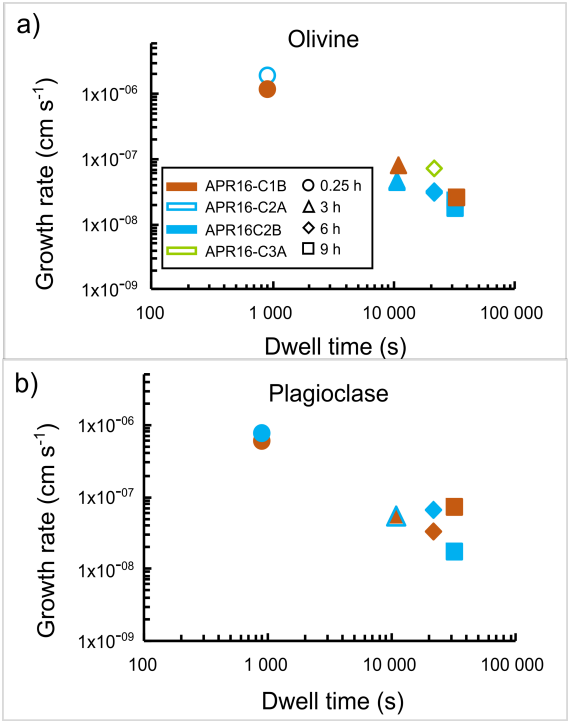

Fig. 9 *Relation between the growth rate (G_L) and the experiment duration (t) for olivine (a) and plagioclase (b). Symbols are as in Fig. 8. Error bars in Fig. 9b are not shown since they are inside the symbols.*

Crystal size distribution analysis

The CSDs calculated for the APR16GL runs of Series 1 and 2 are shown in Fig. 10a-d. For the runs of Series 3, it was not possible to perform CSD analysis due to the small size of the Cpx (which was below the detection limit). CSD theory predicts that steady-state conditions of continuous nucleation and growth will produce a linear CSD plot with a negative slope, while deviations from linearity suggest the involvement of other processes (Cashman and Marsh 1988; Marsh 1988, 1998; Lentz and Mcsween 2000). For instance, a turnover at the smallest grain sizes may be due to (*i*) a complete cessation of nucleation with continued growth that favours the growth of the smallest grains in the next largest bin sizes, but with no replacements produced by nucleation (Lentz and Mcsween 2000); (*ii*) annealing that causes absorption of small grains with balancing growth of larger ones (Lentz and Mcsween 2000); and/or (*iii*) a limitation to the imaging technique (Marsh 1988). Another possible deviation from linearity is an increase of the largest grain sizes that implies an excess of large grains compared with smaller sizes; this may be due to accumulation or addition of large phenocrysts (Marsh 1988). All runs suitable for CSD analysis show similar curves. In the longest runs (6–9 h), in particular, CSDs yield two best-fit lines with different slopes: a gentler slope for coarser crystals and a steeper slope for the smallest crystals (< 8 μm in size). Moreover, a reduction in both slope and intercept leads to a counter-clockwise rotation of the CSD with time (Fig. 10a-d), which indicates an absence of new nucleation (Ni et al. 2014). Small crystals may also partly or completely dissolve due to their higher surface energies, which causes their population density to fall below the log-linear CSD curve (Ni et al. 2014). Moreover, by using the growth

rates calculated in this work for the APR16 runs, we estimated nucleation rates J ($J = n_0 G_L$) of 10^5 and 10^3 $mm^{-3} \cdot s^{-1}$ in the run with the shortest (0.25 h) and the longest (9 h) durations, respectively (Table S3 in Online Resource 2).

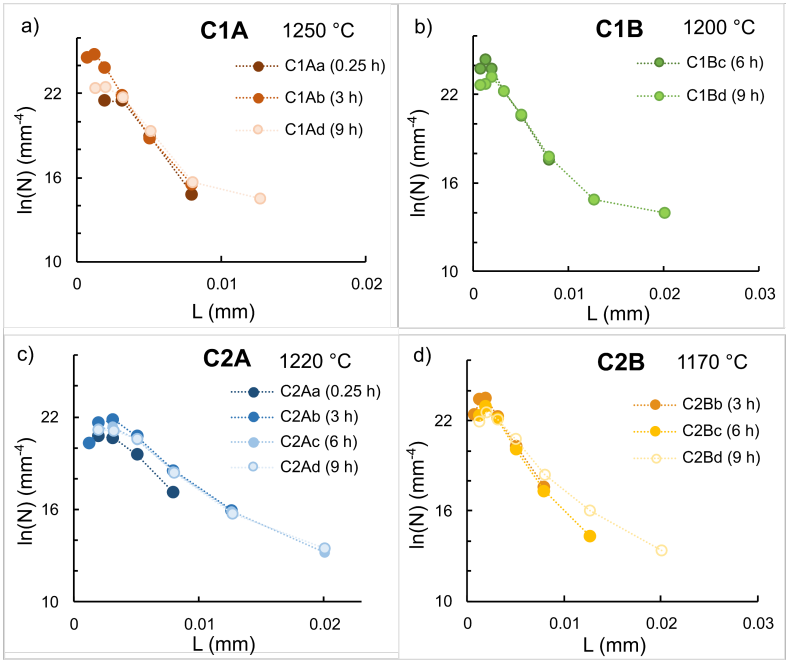

Fig. 10 *CSD relation between the natural logarithm of the population density of crystals (ln(L)) and the crystal length (L) for the APR16-C1A (a), APR16-C1B (b), APR16-C2A (c) and APR16-C2B (d) subseries.*

Discussion

Chemical and crystal fraction equilibrium of experimental clinopyroxene

Putirka (1999) and Putirka et al. (2003) have demonstrated that Fe–Mg exchange between clinopyroxene and the melt ($K_D(Fe\text{-}Mg)^{Cpx\text{-}liq}$ = $Fe_{Cpx} \times Mg_{liq}/Mg_{Cpx} \times Fe_{liq}$) can be extremely useful for the assessment of equilibrium conditions. The $K_D(Fe\text{-}Mg)^{Cpx\text{-}liq}$ calculated for our experimental runs show that chemical equilibrium was reached at between 3 and 6 h. In order to observe if the crystal fraction equilibrium is achieved in the same amount of time as the chemical equilibrium, we plotted clinopyroxene fraction against experimental dwell time (Fig. 11). In Fig. 11a, we observed a rapid increase in Cpx-ϕ, and increase that occurs in the first 15 min, after which Cpx-ϕ remains approximately constant. In the APR16-C1A and APR16-C2A experiments, however, Cpx-ϕ increases for up to 3 h before approaching a constant value, suggesting an approach to crystal fraction equilibrium conditions (Fig. 11a). This trend is similar to those obtained in previous studies (Melnik and Sparks 2005; Polacci et al. 2018), in which the crystal content initially increases rapidly, and then increases less slowly, but linearly, until it reaches equilibrium. Moreover, evolution towards equilibrium is also testified by the decrease in the crystallization rate with time (Fig. 11b). Thus, our experiments show that for Procida K-basalt magmas, independently of ΔT_{eff} and for $H_2O_i \leq 2$ wt.%, the approach to clinopyroxene equilibrium (both chemical and crystal fraction) occurs after 3 h of dwell time.

Growth rate dependence on time

As observed in previous studies (e.g., Hammer and Rutherford 2002; Couch 2003; Arzilli and Carroll 2013; Arzilli et al. 2015), time plays a key role in the crystallization processes of silicate melts. The effective Cpx growth rate calculated in this work varies by an order of magnitude between the runs with the shortest and those with the longest durations (Fig. 8b). In particular, starting from a dwell time of ≥ 3 h, the runs begin to achieve conditions close to the textural equilibrium, at which point kinetic processes (i.e., growth and nucleation) begin to slow down. In detail, as shown in Fig. 11a, Cpx crystallization is negligible after 15 min for the two samples with ΔT_{eff} ~100 °C but continues for up to 3 h for the two samples with ΔT_{eff} ~50 °C. Concerning the sizes of Cpx, instead, for all considered undercoolings, they show a general increase increasing the dwell time only up to 6 h runs (Fig. 8a), remaining approximately constant for longer experimental times. All that suggests that the G_L values determined for long-lasting (> 6 h) experiments are apparent and that, at this point, we are approaching conditions near to the textural equilibrium (Fig. 11; Arzilli et al. 2015). The influence of time on crystal growth rate thus appears to be strictly related to the equilibration time of the growing phases, as observed by previous studies (e.g., Couch 2003; Couch et al. 2003; Orlando et al. 2008; Arzilli et al. 2015). These authors, indeed, noted that the growth of some mineral phases, such as plagioclase and clinopyroxene, require different times to reach the equilibrium conditions. For instance, time has no resolvable influence on plagioclase at experimental durations longer than 1–2 h, a time which appears to be sufficient for the Plg-melt system to approach a near-equilibrium state (Couch 2003; Couch et al. 2003; Arzilli et al. 2015).

Clinopyroxene may also require longer times (of the order of 20 h; Orlando et al. 2008).

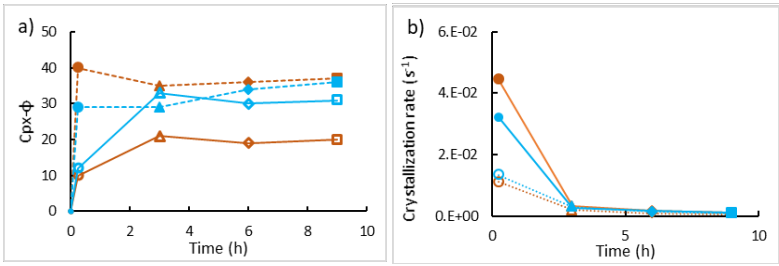

Fig. 11 *Relation between a crystal fraction (Cpx-Φ) and time, and b crystallization rate and time. Symbols are as in Fig. 7.*

Differences of clinopyroxene growth rate

There are several studies of clinopyroxene growth (e.g., Baker 2008; Burkhard 2002, 2005; Orlando et al. 2008), although they are completely absent for high-pressure conditions (> 0.5 GPa). There is, though a difference between the pressure values of our study and those available in literature (e.g., Baker 2008; Burkhard 2002, 2005; Orlando et al. 2008; Oze and Winter 2005; Pontesilli et al. 2019; Shea and Hammer 2013; Simakin et al. 2003; Table S3 in Online Resource 2). However, the Cpx growth rates (10^{-5} -10^{-9} cm·s^{-1}) appear to be comparable since they show similar trends in the growth rate vs dwell time diagram (Fig. 12). In particular, our data combined with literature data outline three parallel trends. The first is an upper trend which includes single-step cooling and decompression experiments on a basaltic-andesite (dwell times of 12-48 h at 995-1025 °C and 65-150 MPa) as reported by Shea and Hammer (2013). It also includes the dynamic isothermal time-series experiments on a trachybasaltic composition (dwell times of 0.5-24 h

at 1100 °C and 400 MPa) reported by Pontesilli et al. (2019) and is characterized by high growth rates. The second is a low endmember trend that includes the CSD analyses performed by Burkhard (2002) on re-heated Hawaiian basalts (crystal residence times of ~0.01-7 h) and by Oze and Winter (2005) on natural basalts (crystal residence times of ~0.04-9 h). It also includes the static experiments of Burkhard (2005) on re-heated anhydrous basaltic glasses (dwell times of 22-576 h at 930-990 °C and 1 atm) and is characterized by low growth rate values. The third is a middle trend which includes our static experiments on the APR16 alkaline basalt and the experiments (dwell times of 3-40 h at 1170 °C and 1 atm) on a K-trachybasalt from Mt. Etna by Orlando et al. (2008). It is characterized by growth rate values between the two endmembers. All of the above experiments were performed at different temperature conditions and H_2O contents (Table S4 in Online Resource 2), which are two key factors controlling the viscosity of magmas (e.g., Pinkerton and Stevenson 1992; Dingwell et al. 1993; Giordano et al. 2004). Notably, variations in melt viscosity deeply affect the kinetics of the crystallization process and then the value of G_L (Orlando et al. 2008; Vona and Romano 2013). Therefore, differences in melt viscosity appear to be the main factor in explaining the differences between the three trends observed in Fig. 12. For example, the runs of Shea and Hammer (2013) that fall in the upper trend (Fig. 12) were performed under saturation conditions. Hence, the high amount of water, reducing the viscosity and increasing element diffusivity in the melt, explains high growth rate values in respect to the runs that are undersaturated. Regarding the runs of the middle and the lower trends (Fig. 12), instead, the different growth rate values can be explained by taking into account the effect of chemical composition and

temperature on the viscosity. The runs of the lower trend, indeed, were performed using a tholeiitic basalt as starting material. This is characterized by higher SiO_2 and lower Σ_{alkali} contents than the APR16-basalt of this study and the Mt. Etna trachybasalt of Orlando et al. (2008), making the tholeiitic melts of the lower trend more viscous than the alkaline ones of the middle trend (see below and Fig. S6 of Online Resource 1). This, consequently, determines the low growth rate values observed for such tholeiitic basaltic composition (~10^{-9} cm·s^{-1}), with respect to the G_L values (~10^{-8} cm·s^{-1}) obtained for the alkaline basalts of the middle trend (Fig. 12). Furthermore, the runs of the lower trend were carried out at lower temperatures (~900 °C) with respect to those of the middle trend (~1100-1250 °C). The high temperature, as well as the water content, will affect the crystal growth rate due to its depolymerizing effect, reducing viscosity and increasing element diffusivity in the melt (Ni et al. 2015). To verify this hypothesis, we calculated the viscosity of all compositions reported in Fig. 12 at atmospheric pressure using the EXCEL® spreadsheet of Giordano et al. (2008). As seen in Fig. S6 in Online Resource 1, at the temperatures considered here (900-1200 °C), the samples have viscosity values that confirm our inference, since they match the distribution observed for the growth rates in the diagram of Fig. 12. However, the growth rates calculated by Pontesilli et al. (2019) for a trachybasaltic composition (10^{-6}–10^{-8} cm·s^{-1}) show values higher than those of the middle trend defined here in Fig. 12. We expect them to fall in this trend since they have a composition very close to the K-trachybasalt of Orlando et al. (2008) which is that plotted here. For this case viscosity cannot explain the different growth rate values between these two trachybasalts since they show the same viscosity variation trend

with temperature (Fig. S6 in Online Resource 1). Instead, we suggest that the difference in G_L is a function of the undercooling and the cooling rate (e.g., Lesher et al. 1999; Conte et al. 2006; Arzilli et al. 2015). The experiments performed by Pontesilli et al. (2019), indeed, are characterized by a cooling rate of 80 °C/min and higher degrees of undercooling (80-120 °C) with respect to the static low undercooling (ΔT = 20 °C) experiments of Orlando et al. (2008).

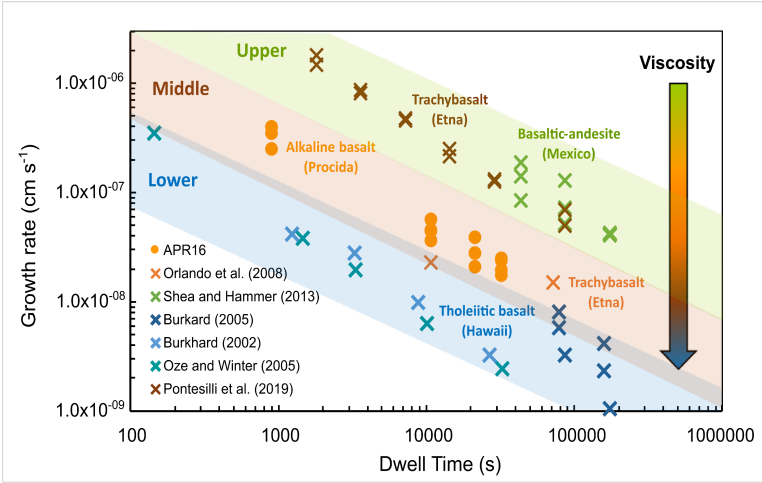

Fig. 12 *Relation between crystal growth rate (G_L) and experimental duration (t) for this and previous studies on clinopyroxenes. Literature experimental data are from Burkhard (2002, 2005), Orlando et al. (2008), Oze and Winter (2005), Pontesilli et al. (2019) and Shea and Hammer (2013). The coloured fields represent: the upper trend in green, the middle trend in dark orange and the lower trend in light blue. Coloured fields correspond to different viscosity values (see Fig. S6 in Online Resource 1) that tend to increase from the upper to the lower trend, as shown by the coloured arrow on the right. The runs of Pontesilli et al. (2019), which should fall in the middle trend based on viscosity, fall instead in the upper one due to the higher undercooling and cooling rate.*

Considering, also, the influence of water content on crystal growth rate, due to its depolymerizing effect that reduces viscosity and increases element diffusivity in the melt (Hess and Dingwell 1996; Ni et al. 2015), in our experiments the calculated growth rates at different water contents remain in the same (order of magnitude) field (Fig. 13). In particular, we note that growth rates of runs with H_2O_f (i.e., water dissolved in the melt) between 2 and 4 wt.% are slightly higher than those with H_2O_f < 2 wt.%, and similar to those observed by Pontesilli et al. (2019). The very minor influence of water on crystal growth rate, and consequently on viscosity of our results, and those of Pontesilli et al. (2019), is probably due to the composition used in the experiments; being alkaline in both cases. Alkaline magmas are more depolymerized than calc-alkaline compositions, due to the presence of alkalis that act as "modifier networks" (Hess et al. 1995). This difference has been noted in the literature, where the model accounting for non-Arrhenian variation of viscosity in calc-alkaline magmas has been proved to not apply to alkaline magmas (Giordano et al. 2006). Moreover, growth rates calculated in runs with high-water contents in the melt (> 5 wt.%) are lower than those obtained for runs with lower water contents (1-3 wt.%). As observed by Bonechi et al. (2019), this is probably due to the dominance on crystallization of the hydrous phase, amphibole, which grows at the expense of Cpx that, indeed, never exceeds a size of ~10 μm in our experiments (Fig. 8a).

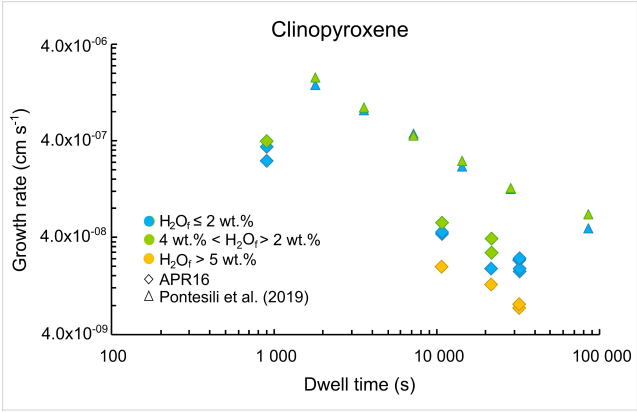

Fig. 13 *Relation between Cpx growth rate (G_L) and water content dissolved in the melt (H_2O_f). Diamonds represent APR16 runs while triangles are the results of Pontesilli et al. (2019). Colours indicate different amounts of water content dissolved in the melt: $H_2O_f \leq 2$ wt.% in light blue, 4 wt.% < $H_2O_f > 2$ wt.% in green, $H_2O_f > 5$ wt.% in yellow.*

Magma refilling of the deep reservoir of the Campi Flegrei Volcanic District

Measurements of CSD, when combined with experimental growth rate data, can provide useful information to better constrain the time of magma crystallization (Cashman and Marsh 1988; Marsh 1988; Piochi et al. 2005b; Armienti et al. 2007; Brugger and Hammer 2010b; Arzilli et al. 2016). To date, there is limited kinetic data (crystal growth rate) on alkaline products and most of them concern feldspar minerals (e.g., Orlando et al. 2008; Agostini et al. 2013; Arzilli et al. 2015). Here we focused on Cpx growth rate, since (*i*) as demonstrated by Perinelli et al. (2019), clinopyroxene is the liquidus phase of the APR16 composition at high pressure (0.8 GPa), and (*ii*) thermobarometric estimates obtained from natural less evolved samples of CFVD indicate an initial stage of clinopyroxene crystallization near the Moho (~25 km depth; Di Stefano et al. 2011). Moreover, Cpx growth rate

data combined with thermobarometric data provide an estimate of deep-level ascent rate for CFVD primitive magmas (Armienti et al. 2013). We assume that a deep episode of magmatic crystallization takes place at low undercooling, a condition that produces slow crystal growth rates. This condition has been verified, here, by CSD investigations for clinopyroxene growth of natural samples. Cpx-CSDs were measured for two K-basaltic scoria clasts (SCE and SOG samples) collected in the deposit of the Solchiaro tuff ring (of Procida island). Both SCE and SOG have chemical compositions very close to that of APR16 sample (Table 1, Table S5 in Online Resource 2, and Online Resource 3). Note that, parameters used for the CSD analysis of natural samples were the same as those used for the experimental runs applied here. CSD results for these two scoria clasts show an upward curvature (Fig. 14). This indicates the possible involvement of a number of processes, including changes in the magma cooling rate, crystal aggregation, magma mixing, or textural coarsening, during the crystallization history of these samples (Armienti et al. 1994; Higgins 1998, 2002; Higgins and Roberge 2003; Marsh 1998; Zieg and Marsh 2002). We recognize three populations of clinopyroxenes, each of which has an almost linear distribution (Fig. 14). The first population is of larger phenocrysts with size > 0.32 mm that can be interpreted as early formed phenocrysts. The second is of smaller phenocrysts with sizes between 0.04 and 0.32 mm. The third involves microlites with $L < 0.04$ mm. The portion of the CSD plot relative to the larger phenocrysts shows that, on the basis of their composition and thermobarometric data (see Online Resource 3), they formed during a crystallization stage at a deep (20-25 km) level. This is apparent from an almost horizontal slope and a low intercept, which

suggests that these crystals formed at low and almost constant undercooling and growth rates (Armienti et al. 1994). Using the growth rate value obtained here of $2.2 \cdot 10^{-8}$ cm·s^{-1} (i.e., the average of G_L values that on the basis of K_D(Fe-Mg)$^{Cpx\text{-}liq}$ fall in the field representing equilibrium conditions; Fig. S7 in Online Resource 1), it is possible to evaluate the minimum growth time. Using this value, a minimum residence time of the largest SCE and SOG clinopyroxenes can be obtained (Cashman and Marsh 1988; Armienti et al. 1994). This value is estimated as ~5 months for a Cpx growth of ~3 mm. Moreover, the ascent rate of primitive CFVD magmas can be assessed by combining data on Cpx growth rate with thermobarometric data of natural clinopyroxenes (Armienti et al. 2013).

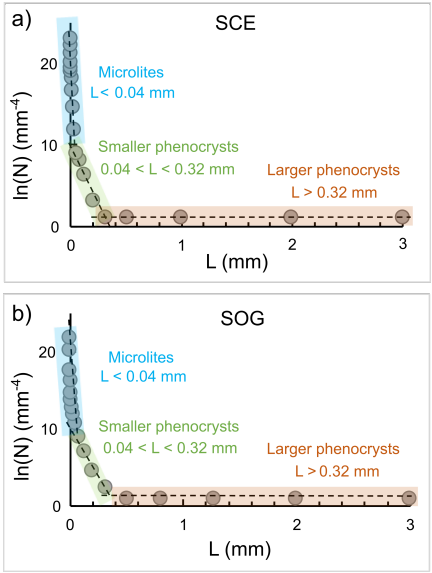

Fig. 14 *Relation between population density (ln(N)) and length (L) of clinopyroxenes for SCE (a) and SOG (b) natural samples. Coloured rectangles indicate three different Cpx populations: in orange larger phenocrysts (L > 0.32 mm); in green smaller phenocrysts (0.04 < L < 0.32 mm); in light blue microlites (L < 0.04 mm).*

The range of temperatures and pressures of crystallization estimated for the larger population of clinopyroxenes obtained here are 1141-1178 °C and 0.7-0.9 GPa (which converts to a 20-25 km depth assuming an average crustal density of 2.8 g·cm^{-3}). According to the approach of Armienti et al. (2013), for a ΔT of 37 °C (ΔT = 1178-1141 °C), a ΔL of ~0.3 cm (based on the magnitude of deep growth of clinopyroxene from CSD analyses; Fig. 14) and a growth rate of 2.2·10^{-8} cm·s^{-1}, as estimated by our experiments, the cooling rate during the ascent of CFVD K-basaltic magmas can be estimated to be 0.3·10^{-5} °C/s. This value, combined with the dP/dT from thermobarometry (see Online Resource 3), provides a deep-level ascent velocity of ~0.5·10^{-4} m·s^{-1}, which is comparable with the average magma transport rate of 3.6·10^{-4} m·s^{-1} estimated for Mt. Etna for depth > 6 km (Armienti et al. 2013). Nevertheless, the olivine/clinopyroxene ratio (~1) of the SCE and SOG scoriae indicates, according to the experimental phase relations at 0.2-0.8 GPa (Granati 2016), that the most primitive magmas of CFVD pond at relatively shallow levels before eruption. This is confirmed by barometric estimates based on the smaller phenocrysts, whose crystallization onset occurred at 0.3-0.5 GPa (8-14 km depth; see Online Resource 3). Consequently, the calculated residence time of the larger Cpx population (i.e. 5 months at least) multiplied by the magma volume erupted from the CFVD tuff ring (0.1-1 km^3; Mastrolorenzo et al. 2017) could represent the minimum recharge rate of the large magmatic reservoir, whose top has been located in the CFVD at a depth of about 8 km (e.g. Rapolla et al. 1989; Cecchetti et al. 2001; Auger et al. 2001; Zollo et al. 2008; Esposito et al. 2011; Pappalardo and Mastrolorenzo 2012; Fanara et al. 2015; Fedi et al. 2018).

Conclusions

Through this work, we have improved knowledge of crystallization kinetics of clinopyroxene in alkaline basaltic melts, providing new crystal growth rate data under high-pressure conditions. At the investigated conditions, clinopyroxene growth rate (G_L) is strongly affected by time, with values that vary from 10^{-7} to 10^{-8} cm·s^{-1} from the shortest (0.25 h) to the longer-lasting (6-9 h) experiments. By comparing our clinopyroxene growth rate data with those available in the literature, we observe that viscosity, and composition, undercooling and cooling rate are the factors that most affect crystal growth rate. This is a result of their control over element diffusivity in the melt. On the other hand, pressure appears to have no influence on crystal growth rate. The experimental Cpx growth rate combined with data from CSD and thermobarometry of CFVD clinopyroxenes suggests that recharge by primitive magmas in the deep CFVD reservoirs occurs with a relatively high ascent rate (~$0.5 \cdot 10^{-4}$ m·s^{-1}).

Acknowledgments

We warmly thank the executive editor A. Harris, the associate editor K.V. Cashman and the reviewer F. Arzilli for their constructive comments that significantly improved our paper. We thank Luca Ziberna (BGI Bayreuth) for preparing APR16GL sample, M. Albano (CNR-IGAG) for help in electronic backscattered images and M. Serracino (CNR-IGAG) for help in EMP analyses. This research has been conducted with the financial support of the HP-HT Laboratory of the Earth Sciences Department, Sapienza University of Rome.

Supplementary data

Supplementary data to this article can be found online at

https://doi.org/10.1007/s00445-019-1342-5

Chapter 1.2

Influence of Pre-Existing Nuclei on the Crystallization Kinetics of Primitive Alkaline Magmas: Insights on the Deep Feeding System of the Campi Flegrei Volcanic District

Barbara Bonechi

Dipartimento di Scienze della Terra, Sapienza Università di Roma, P. le Aldo Moro 5, 00185 Rome, Italy

Published in *Minerals*, 2020, vol. 10(3), 324

Abstract

Aiming to evaluate the influence of pre-existing nuclei on the clinopyroxene crystallization kinetics, time-series experiments were performed using both natural and vitrified starting materials. Experiments were carried out at pressure of 0.8 GPa, temperatures between 1220 and 1250 °C, and dwell times ranging from 0.16 to 12 h. Clinopyroxene growth rates of the runs performed using the natural starting material containing pre-existing nuclei (~2×10^{-7} to ~6×10^{-8} cm·s^{-1}) are higher than those of the runs performed using the vitrified one (~3×10^{-7} to ~2×10^{-8} cm·s−1). In both cases the growth rates decrease with increasing time. Conversely, clinopyroxene nucleation rates are lower in the experiments performed using the natural powder (10^2 and 10 mm^{-3} s^{-1}) compared to those performed with the glassy starting material (10^5 and 10^3 mm^{-3}·s^{-1}). The nucleation rates tend to decrease increasing dwell time in all the series up to ~3 h, after which it remains nearly constant. Finally, the combination of the obtained clinopyroxene growth rates with the crystal size analysis of natural clinopyroxenes, allowed to estimate the magma ascent rate and the recharge rate of the Campi Flegrei Volcanic District deep reservoir.

Keywords: pre-existing nuclei; heterogeneous nucleation; crystal growth rate; clinopyroxene; high pressure; Procida island

Introduction

Knowledge of crystallization kinetics in silicate melts is a fundamental tool in the Earth and material sciences due to the importance of crystallization processes in both natural and synthetic melts (Tiller, 1977; Davis and Ihinger, 2002). Crystallization consists of two main processes, nucleation and growth, that are both strongly influenced by composition, temperature, volatile components (Fenn, 1977; Swanson, 1977; Muncill and Lasaga, 1988; Davis et al., 1997) and thermal history (e.g., Lofgren, 1983; Kirkpatrick, 1977; Cashman and Marsh, 1988; Uda, 1994; Mishima et al., 1996). Concerning the nucleation kinetic, it includes two basic mechanisms: homogeneous nucleation during which spontaneous new crystals form in the liquid and heterogeneous nucleation during which, instead, new crystals form on pre-existing surfaces (Berkebile and Dowty, 1982). This latter has long been recognized as an important and more efficient means of nucleation of crystals and bubbles under magmatic conditions (e.g., Fenn, 1977; Lofgren, 1983; Philpotts and Ague, 2009; Hammer et al., 2010; Špillar and Dolejš, 2015). Due to this, it is critical for magma crystallization experiments the choice to use as starting material powder of raw or vitrified natural samples or synthetically reconstructed compositions. Glassy starting materials (synthetic composition prepared from oxide and carbonate reagents or vitrified natural samples) have the advantage of being completely homogeneous and able to achieve a state of total chemical equilibrium (Pichavant et al., 2007; Shea and Hammer, 2013); however, the preparation of these glasses requires multiple fusion cycles at high temperature that strongly affect the nucleation behavior of aluminosilicate melts (e.g., Walker et al., 1978; Davis and Ihinger, 2002; Pupier et al., 2008; Shea and Hammer,

2013). This is reflected in the experimental products that could be difficult to correlate to crystallization path of natural magmas. Furthermore, the nucleation behavior and, consequently, the textures observed in some experimental products performed using glassy starting material, result to be also influenced by the thermal path before crystallization (Hammer, 2008; Masotta et al., 2020). Indeed, as shown by Masotta et al. (2020), in isothermal experiments the crystallization starts before resting temperature (T_{rest}) is reached ($T < T_{rest}$). If the crystallized mineral (cpx in this case) remains within its stability field, the further heating up to the T_{rest} does not allow the dissolution of these early crystals (pre-existing nuclei) favoring a texture formed by many crystals with small sizes (~10 μm). During undercooling experiments, instead, the sample is initially heated at superliquidus conditions (generally ~15–30 min of pre-annealing time) before cooling it to the resting temperature. In this condition the crystallization starts at $T > T_{rest}$ favoring the formation of few crystals with big sizes (>100 μm). Conversely, natural crushed starting materials are more easily comparable to natural magmas in terms of crystallization kinetics (Pichavant et al., 2007; Hammer, 2008; Shea and Hammer, 2013); however, they are able to reach only a state of partial equilibrium since they are not completely homogenous due to the possible presence of phenocryst cores that may be in disequilibrium with the groundmass. Considering that both natural and vitrified starting materials have advantages and disadvantages, several authors (e.g., Lesher et al., 1999; Hammer and Rutherford, 2002; Shea et al., 2009; Shea and Hammer, 2013) preferred to use natural starting materials because, due to the virtual presence of nuclei also in aphyric lavas, they yield initial conditions more akin to those of natural magmas. As observed in the

literature (e.g., Lofgren, 1983; Mollo et al., 2012; Vetere et al., 2013, 2015; Špillar and Dolejš, 2015; Masotta et al., 2020), the occurrence of pre-existing nuclei strongly affects the crystallization kinetics (i.e., nucleation and growth). In the presence of pre-existing nuclei, indeed, the low interfacial energy between them and the nucleating phase concentrates the supply of chemical elements in the liquid near the new growing crystals, limiting in this way the formation of new nucleation sites and favoring, instead, the growth. Many of the works in the literature deal with the influence of pre-existing nuclei on the crystallization kinetics (e.g., Mollo et al., 2012; Vetere et al., 2013, 2015; Shea and Hammer, 2013; Arzilli et al., 2015), but they are mainly focused on feldspar crystals. Clinopyroxene is a common mineral in basaltic systems and, due to its wide crystallization range, it may fully record the evolutionary history of a magma. Therefore, in order to evaluate the influence of pre-existing nuclei on the clinopyroxene crystallization kinetics at high pressure, here are reported the results of an experimental investigation performed using both natural and vitrified starting material, which is an alkaline basalt (APR16 sample) (Bonechi et al., 2017; Perinelli et al., 2019; Bonechi et al., 2020a, 2020b) representative of the least-evolved rocks of the Campi Flegrei Volcanic District (CFVD). The experimental runs were grouped in two series carried out at the same pressure (0.8 GPa): (*i*) natural starting material series that includes the runs performed in this study at 1225 °C and at dwell times between 0.16 and 12 h; (*ii*) glassy starting material series that includes the runs performed by Bonechi et al. (2020b) at 1250 and 1220 °C and at dwell times between 0.25 and 9 h, using as starting material the vitrified APR16 powder. Among the experiments of Bonechi et al. (2020b), the APR16-C1A and APR16-C2A series were chosen to be

compared with that performed in this study due to their similar temperatures and effective undercoolings. Moreover, using the clinopyroxene experimental growth rates obtained from natural and synthetic starting materials and the crystal size distribution analysis of clinopyroxenes occurring in the most primitive scoria clasts of the CFVD, an estimate of the deep magma ascent rate and of the recharge rate of the CFVD deep reservoir was made.

Materials and Methods

Starting Material

The starting material used in this study is a natural rock powder with alkali basaltic composition (Bonechi et al., 2017; Perinelli et al., 2019; Bonechi et al., 2020a, 2020b) (Table 1). In particular, the natural sample is a primitive K-basalt (APR16 sample) found as scoria clast in the deposits of the Solchiaro eruption (~22 ka; Morabito et al., 2014) located in Procida island (Campi Flegrei, Italy). The sample consists of 12 vol. % of forsteritic olivine and diopsidic clinopyroxene phenocrysts dispersed in a groundmass made of olivine, clinopyroxene, plagioclase, Ti-magnetite, alkali feldspar and glass (D'Antonio et al., 1999a; De Astis et al., 2004). The powder, used as starting material in the runs of natural starting material series, was obtained by grinding the APR16 rock sample in an agate mortar under acetone. The glass, instead, was prepared by Bonechi et al. (2020b) by melting for 15 min the APR16 natural powder in a 1-atm gas-mixing furnace (Bayerisches Geoinstitut, Bayreuth, Germany) at 1400 °C and oxygen fugacity buffered at the Nickel-Nickel Oxide level using a CO/CO_2 gas mixture.

Experimental Procedure

Experiments were carried out at pressure of 0.8 GPa, as function of temperature and time by using the ½ inch end loaded piston cylinder apparatus at the HP-HT Laboratory of the Earth Sciences Department (Sapienza University, Rome, Italy). The assembly consists of an outer CaF_2 cell, graphite furnace and MgO crushable spacers. About 40–50 mg of powdered starting material was dried at 110 °C for at least 2 h to remove the moisture before being loaded and pressed into $Au_{75}Pd_{25}$ capsules and then welded. For each experiment, the capsule was put in the MgO crushable spacers and surrounded by powder of alumina. Temperature was measured using a type D W_3Re_{97}-$W_{25}Re_{75}$ thermocouple and maintained with an uncertainty of ±5 °C. The experimental assembly was first pressurized to the target pressure by a piston-out procedure (Johannes et al., 1971; Presnall et al., 1978) that applies an overpressure of ~10% of the run pressure and temperature was gradually increased to the resting temperature, while correcting for pressure drops due to stress relaxation within the assembly during heating. The heating rate was set at 150 °C/min. The sample was maintained at the pressure and temperature for a given duration (nominal duration), and then quenched by turning off the power. The temperature dropped to below 500 °C within < 5 s with an average cooling rate of 150 °C/s. All the runs were self-buffered; when possible fO_2 was estimated through the equation of Kress and Carmichael (1991) using the liquid Fe^{3+}/Fe_{tot} mole ratios from K_D Fe-Mg ol/liq calculated following Toplis (2005). This procedure yielded fO_2 values of ΔNNO +0.12 to +2, in agreement with those estimated for similar furnace assemblages (Conte et al., 2009; Weaver et al., 2013). A total of 12 experiments, whose experimental conditions are

reported in Table 2, were considered in this study. The experiments were grouped into two main series carried out at a constant pressure and at different dwell times: experiments of natural starting material series carried out in this study at temperatures of 1225 °C and dwell times of 0.16, 3, 6 and 12 h; experiments of glassy starting material series performed by Bonechi et al. (2020b) at temperatures of 1250 and 1220 °C, respectively, and dwell times of 0.25, 3, 6 and 9 h.

Table 2 Experimental run conditions, calculated water contents, phases assemblage and proportions in run products

Run #	T (°C)	$TCpx_L$ (°C)	ΔT_{eff} (°C)	Time (h)	H_2O_t (wt%)	Phases	H_2O_f (wt%)	Σr^2	% $\Delta Fe^{\S}$
APR16-N									
APR16-3B	1225	1280	55	0.16	NWA	Gl + $Cpx^{\#}$+ $Ol^{\#}$ + $Ox^{\#}$	1.77		
APR16-1C	1225	1280	55	3	NWA	Gl(94) + Cpx(6) + $Ol^{\#}$ + $Ox^{\#}$	0.96	0.38	-5
APR16-35	1225	1280	55	6	NWA	Gl(96) + Cpx(4) + $Ol^{\#}$	1.70	0.14	-22
APR16-2B	1225	1280	55	12	NWA	Gl(90) + Cpx(10) + $Ol^{\#}$	2.13	0.11	-35
APR16-C1A									
APR16-C1Aa	1250	1295	45	0.25	NWA	Gl(97) + Cpx(3)	1.61	1.75	-7
APR16-C1Ab	1250	1295	45	3	NWA	Gl(75) + Cpx(25)	0.90	0.62	-12
APR16-C1Ac	1250	1295	45	6	NWA	Gl(83) + Cpx(15) + Ol(2)	2.03	0.83	-20
APR16-C1Ad	1250	1295	45	9	NWA	Gl(90) + Cpx(10)	1.95	0.65	-19
APR16-C2A									
APR16-C2Aa	1220	1270	50	0.25	2	Gl(91) + Cpx(4) + Ol(1) + Ox(4)	1.92	0.02	-25
APR16-C2Ab	1220	1270	50	3	1.9	Gl(68) + Cpx(23) + Ol(4) + Plg(1) + Ox*	1.56	0.66	-17
APR16-C2Ac	1220	1270	50	6	2.1	Gl(65) + Cpx(27) + Ol(5) + Plg(3)	2.47	0.93	-25
APR16-C2Ad	1220	1270	50	9	1.9	Gl(80) + Cpx(17) + Ol(3) + Ox*	1.30	0.25	-26

Notes: NWR natural water rock; Gl glass; Cpx clinopyroxene; Ol Olivine; Plg plagioclase; Ox oxide. $TCpx_L$ is the equilibrium clinopyroxene liquidus temperature (°C) determined on the basis of phase relations experimental data from Perinelli et al. (2019) and on the calculations by using MELTS software (Ghiorso and Sack, 1995; Asimow and Ghiorso, 1998). ΔT_{eff} is the difference between the clinopyroxene liquidus temperature and the nominal temperature of the runs. H_2O_t % of water added to the charge. H_2O_f as determined by the *by-difference* calculation method (respect to the total of EMP analyses). Σr^2 values from mass balance calculation. § Percent of relative Fe loss from starting material based on difference between the starting material and calculated bulk composition of experiment obtained from mass-balance calculations. $^{+}$Phases too small for analysis; *crystals present in trace; $^{\Diamond}$ in these runs it was no possible to do mass balance calculation; $^{\#}$pre-existing crystals.

Analytical techniques

The recovered charges were mounted in epoxy resin, ground flat and polished. Textural features of the recovered samples were analyzed by Scanning Electron Microscopy (SEM) using a FEI Quanta-400 equipped for microanalysis with an EDAX Genesis system at the Earth Sciences Department (Sapienza University, Rome, Italy). At least eight back-scattered electron (BSE) images were acquired for each experimental run in order to accurately measure the number of clinopyroxene nuclei and other mineral phases (e.g., Hammer et al., 2000; Couch, 2003; Clarke et al., 2007). Phase compositions were analyzed at the CNR-Istituto di Geologia Ambientale e Geoingegneria (Rome, Italy), with a Cameca SX50 electron microprobe equipped with five wavelength dispersive spectrometers (WDS). Quantitative compositional analyses were performed using 15 kV accelerating voltage and 15 nA beam current. As standards we employed metals for Mn and Cr, jadeite for Na, wollastonite for Si and Ca, orthoclase for K, corundum for Al, magnetite for Fe, rutile for Ti and periclase for Mg. Counting times were 20 s for elements and 10 s for backgrounds. Light elements were counted first to prevent loss by volatilization. The PAP correction method was used. Mineral phases were analysed using a beam diameter of 1 μm while for glasses a defocused electron beam of 10 to 15 μm was used. The water contents of experimental glasses were estimated from chemical analyses according to the by difference method (Devine et al., 1995).

Growth and nucleation rate calculation

Crystal dimensions were measured in SEM images by using the measure

tool of the ImageJ® software (version 1.50i). The maximum growth rate (G_L) values were calculated using a common method reported in literature (e.g., Hammer and Rutherford, 2002; Couch et al., 2003; Iezzi et al., 2011) based on the dimensions of the largest crystals (i.e., major and minor axes of best fit ellipse):

$$G_L = (L \cdot W)^{0.5}/t^*2 \quad (1),$$

where L and W are the mean length and width, respectively, of the ten largest crystals for each BSE image and t is the duration of the experiments (s). As also observed in the literature, most of the growth often occurs at the beginning of the experiment, since diffusion- or interface controlled growth normally display lower incremental growth rates as the system approaches equilibrium (Couch et al., 2003; Orlando et al., 2008; Arzilli et al., 2015; Pontesilli et al., 2019; Bonechi et al., 2020a, 2020b; Masotta et al., 2020). Therefore, long lasting experiments could show an apparent decrease in G_L with increasing time. The nucleation rate of the Cpx crystallized in the runs of natural starting material series were calculated following the procedure reported in Bonechi et al. (2020b), through which the nucleation rate of Cpx crystallized in glassy starting material series has been calculated. Textural analyses were performed by using ImageJ® software (Abramoff et al., 2004; Schneider et al., 2012) on BSE images from which binary images of each mineral phase were constructed following the procedure of Philpotts and Ague (2009). Manual reconstruction of edges of overlapping crystals was necessary before conversion into binary images. Successively, the data were transferred to the CSDcorrections® software (version 1.6 2018) (Higgins, 2000, 2002) to perform the 2D to 3D conversion and the calculation of CSD plots for each mineral phase.

Results

Textural Features of the Experimental Runs

Natural Starting Material Series

In APR16-3B run (1225 °C, 0.16 h; Figure 1a, b) the mineral phases occurring in the charge are Ol, Cpx and Ox. Olivine size ranges from 10 to 30 μm and shows anhedral and subhedral habit. Clinopyroxene is present in small quantity and shows anhedral and subhedral habit with size up to 20 μm. Oxide is present in trace with size up to 20 μm and anhedral shape. The phase assemblage in APR16-1C run (1225 °C, 3 h; Figure 1c, d) is Cpx, Ol and Ox crystals and large amount of glass. Olivine size ranges from 10 to 30 μm and the habit is anhedral. Clinopyroxene (size up to 50 μm) are zoned and show euhedral habit. Oxide is very small in size (~5 μm) with subhedral to anhedral shape. In APR16-35 run (1225 °C, 6 h; Figure 1e) it was observed the occurrence of Cpx sometimes characterized by inclusion of rounded Ol. Homogeneous and zoned clinopyroxenes show euhedral habit reaching sizes up to 80 μm. Finally, the phase assemblage of APR16-2B run (1225 °C, 12 h; Figure 1f) is Cpx and glass. As seen in the APR16-35 run, rare small olivines (~10 μm in size) are present as resorbed mineral into Cpx grains. Clinopyroxene are both homogeneous and zoned and show euhedral and subhedral habits. The size of these crystals is up to 90 μm. By analysing the textural features of Ol and Cpx in the four experiments at 1225 °C (NWA) it was possible to note that olivine tends to be resorbed from APR16-3B (0.16 h) to APR16-2B (12 h) runs, decreasing in size from 40 μm to 5 μm, whereas Cpx increases in size from 20 μm up to 80 μm. Moreover, it is visible a change of the habit of both minerals increasing the duration of the experiments: at 0.16 h Ol and Cpx have both anhedral and/or subhedral

habit; after three hours Ol habit becomes anhedral while Cpx shows a noticeable core-rim zoning; after 6 h, instead, anhedral Ol is almost disappeared, while Cpx has euhedral habit pointing out to a crystal-melt equilibrium.

Glassy Starting Material Series

Textural features of these two series are described in detail in Bonechi et al. (2020b). Here a briefly description of the fundamental aspects is reported. In the runs of APR16-C1A (1250 °C) series the dominant phase is Cpx (Table 2), whose habit and sizes vary with time: subhedral with sizes of 5 μm in the shortest run (APR16-C1Aa; 0.25 h), and euhedral with sizes up to 15 μm in the longest run (APR16-C1Ad; 9 h). In the APR16-C1Ac run (6 h) Ol, characterized by euhedral habit and sizes of ~10 μm, occurs together with the Cpx. The mineral phases crystallized in APR16-C2A (1220 °C) series are Cpx + Ol + Plg + Ox (Table 2). In these runs Cpx and Ol are ubiquitous, while Plg occurs only in the runs at 3 and 6 h and Ox is absent in the run at 6 h. Clinopyroxene has subhedral habit in the run with the shortest duration and euhedral in the other runs, with sizes between ~10 and 20 μm. Olivine and Plg crystals are euhedral with sizes of ~15 and ~40 μm, respectively.

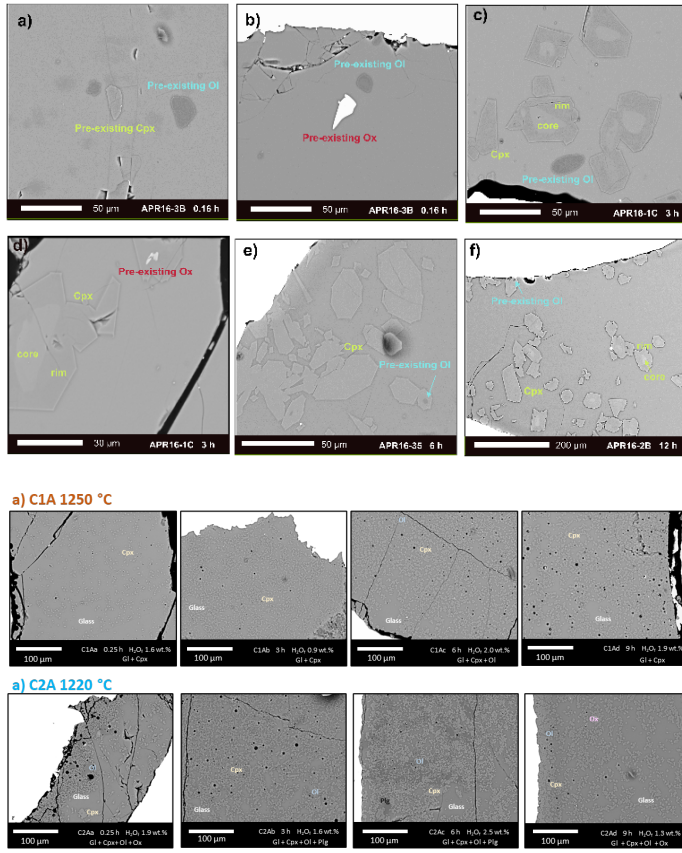

Figure 1. *Backscattered SEM image of natural starting material runs: (a,b) APR16-3B run (0.16 h) is characterized by the presence of pre-existing nuclei of Cpx, Ol and Ox with anhedral and subhedral habit; (c,d) APR16-1C run (3 h) is characterized by the presence of both zoned Cpx grown on the pre-exiting nuclei and new Cpx, pre-existing Ol and Ox; (e) APR16-35 run (6 h) shows euhedral Cpx with homogenous and zoned compositions, while Ol is present as resorbing crystal inside Cpx; (f) APR16-2B run (12 h) is characterized by zoned and homogenous Cpx and resorbed Ol included in Cpx crystals. For comparison are reported also SEM images of the glassy starting material runs (C1A 1250 °C and C2A 1220 °C). Modified from Bonechi et al. (2020b).*

Phases Composition

Chemical compositions of Cpx, glass and Ol of natural starting material and glassy starting material runs are reported in Tables S1 in the Supplementary Material. Chemical compositions of the other phases crystallized in glassy starting material runs are reported in Bonechi et al. (2020b).

Natural Starting Material Series

Clinopyroxene. Clinopyroxene crystals in natural starting material runs are classified as diopsides ($Wo_{41–49}En_{44–50}Fs_{4–9}$) according to the classification scheme of Morimoto et al. (1998). Some clinopyroxene crystals show core-rim compositional variations. For example, in APR16-1C and APR16-2B runs the Cpx core is characterized by higher CaO and lower Al_2O_3 and Na_2O content than those of the rim (Tables S1 in the Supplementary Material). As highlighted in the previous sections, textural evidences suggest mineral-melt disequilibrium in the short experiments (≤ 3 h runs) and also the chemistry in term of clinopyroxene-liquid Fe-Mg exchange coefficient, calculated by using the formula $(FeO/MgO)^{Cpx}/(FeO/MgO)^{liq}$, is quite in agreement with textural evidences. The ${}^{Cpx\text{-}liq}K_{DFe\text{-}Mg}$ value in the APR16-3B run (0.16 h) is 0.43, in APR16-1C run (3 h) is 0.28 ± 0.02 for the core and 0.33 ± 0.02 for the rim, in APR16-35 run (6 h) is 0.33 ± 0.06 for the core and 0.32 ± 0.02 for the rim, and in APR16-2B run (12 h) is 0.56 ± 0.21 and 0.47 ± 0.02 for the core and for the rim, respectively. According to Putirka (2008), the calculated K_D value for APR16-35 and APR16-1C indicate equilibrium between clinopyroxene and liquid, whereas only in the shortest (APR16-3B) and in the longest (APR16-2B) experiment the chemical Cpx-liquid equilibrium has been not achieved (Figure 2). Notably, the K_D calculated for

the APR16-2B run (12 h) could be due to the significant loss of Fe in the melt related to the long experimental dwell time.

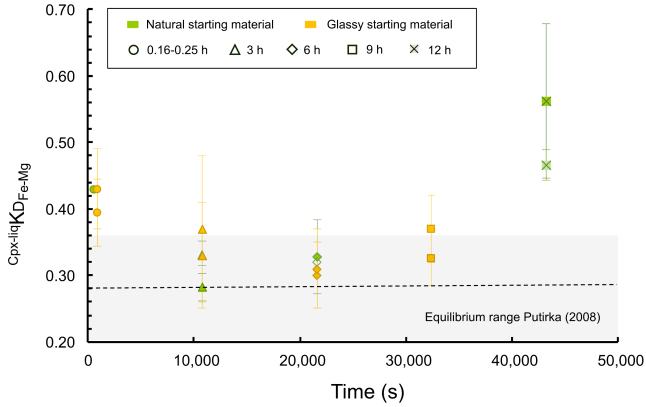

Figure 2. *Relation between K_D(Fe-Mg)Cpx-liq and time (s). The duration of each run is indicated with different symbols: circle for 0.16 and 0.25 h runs, triangle for 3 h runs, diamond for 6 h runs, square for 9 h runs and square with internal cross for 12 h run. Series are indicated with different colours: green for natural starting material, and yellow for glassy starting material. For natural starting material runs are used empty symbols for Cpx rims and full symbols for Cpx cores. The grey field represents the equilibrium range according to Putirka (2008), while the dotted line represents the average K_D value for Cpx (0.28 ± 0.08; Putirka, 2008).*

Olivine. Olivine crystals show a variation in their forsteritic content from ~91 (APR16-35; 6 h) to 87 (APR16-3B; 0.16 h) decreasing the experimental time. These values suggest a dissolution of Ol that becomes more restitic increasing the duration of the experiments. Moreover, the forsteritic content of Ol present in the APR16-3B run (Fo_{87}), that is the same value reported by D'Antonio et al. (1999a) for natural olivines in APR16 sample, confirms that they are remnant of the natural starting material rather than phases crystallized during the experiment.

Glassy Starting Material Series

Clinopyroxene. Clinopyroxene crystals are augitic ($Wo_{42}En_{41}Fs_{18}$) and diopsidic ($Wo_{47}En_{43}Fs_{10}$) in composition according to the classification scheme of Morimoto et al. (1998). Generally, the Mg# of Cpx (calculated as the molar MgO/(MgO + FeO_{tot}) ratio) varies between 0.76 and 0.88, whilst the Mg# of glass varies between 0.52 and 0.77. The Fe–Mg distribution coefficients between Cpx and melt ($K_D(Fe\text{-}Mg)^{Cpx\text{-}liq} = Fe_{Cpx} \times Mg_{liq}/Mg_{Cpx} \times Fe_{liq}$, calculated assuming all Fe as Fe^{2+} in both phases), varies between 0.39 ± 0.05 and 0.30 ± 0.05 for APR16-C1A runs, and between 0.43 ± 0.06 and 0.31 ± 0.06 for APR16-C2A runs. As illustrated in Figure 2, all the shortest runs deviate significantly from the equilibrium range ($K_D(Fe\text{-}Mg)^{Cpx\text{-}liq} = 0.28 \pm 0.08$ according to Putirka (2008)), whereas runs of 3 h or more progressively reach equilibrium conditions. As previously observed for the longest run of natural starting material series (APR16-2B; 12 h), the slightly deviation from the equilibrium range of the K_D calculated in the run at 9 h, could be due to the loss of Fe in the melt related to the long experimental dwell time.

Other phases. Oxide crystals are generally spinels (APR16-C1Ab, APR16-C2Aa and APR16-C2Ab) and hercynites (APR16-C2Ab). Olivine is present in the run APR16-C1Ac with a forsteritic content of Fo_{89} and in the runs APR16-C1Aa, APR16-C1Ab and APR16-C1Ac with compositions of $Fo_{86\text{-}90}$. Plagioclase grains occurring only in the runs APR16-C2Ab and APR16-C2Ac are bytownitic and labradoritic in composition.

Textural and chemical evidence of the occurrence of pre-existing nuclei

In the runs of natural starting material series, the use of a natural starting material containing pre-existing nuclei results in growth around pre-

existing crystals. Textural and chemical evidence suggest that the Cpx observed in the APR16-3B run (0.16 h, 1225 °C) are pre-existing Cpx, while in the other runs the pre-existing crystals constitute the cores of the zoned Cpx. As regards textural features, the scarce abundance of the Cpx crystals observed in APR16-3B run (Figure 1a) and their anhedral and subhedral habits with size of ~10–20 μm, suggest that they are not crystallized during the experiments but are relic of the phenocrysts present in the natural starting material. Indeed, in comparison, the Cpx crystallized in APR16-C1Aa run (0.25 h, 1250 °C) obtained using the glassy starting material, are more abundant and show subhedral and euhedral habit with maximum size of 10 μm. As regards chemical evidences, the Al^{IV} vs Al^{VI} and Na vs Al^{VI} diagrams (Figure 3), in which both natural starting material and glassy starting material series and some natural Cpx belonging to the same deposits of the APR16 sample (D'Antonio and Di Girolamo, 1994) are reported, allowed to identify the presence of pre-existing nuclei. In particular, the Al^{IV} vs Al^{VI} diagram represents a good indicator of pressure conditions at which clinopyroxene crystallizes, due to the preference of Al to occupy tetrahedral and octahedral sites at high *T* and *P*, respectively (Thompson, 1974; Herzberg, 1978). Moreover, it is important to stress that the Al concentration in Cpx can be influenced not only by pressure, but also by kinetic effects (e.g., Pontesilli et al., 2019). Similar function has the diagram in which Al^{VI} is plotted versus Na, suggested to be a pressure sensitive element (Putirka, 2008). As possible to see in these diagrams, the Cpx of the APR16-3B run and the cores of the zoned Cpx of the APR16-1C, APR16-35 and APR16-2B runs fall in the field corresponding to a pressure ≤ 0.5 GPa as well as the natural Cpx. Conversely, the rim of natural starting

material series and the Cpx of the glassy starting material series fall in the field corresponding to a pressure ≥ 0.7 GPa. Moreover, both Al^{IV} and Na content allowed to discriminate between pre-existing Cpx and Cpx crystallized during the experiments, as shown also in Figure 4. In particular, in the diagrams of Figure 4 (Al^{IV} vs Mg# and Na vs Mg#) these two kinds of Cpx are separated by a red dotted line, drawn in correspondence of the higher Al^{VI} and Na values (0.06 and 0.02 apfu, respectively) of natural Cpx (D'Antonio and Di Girolamo, 1994). The pre-existing nuclei, indeed, are located near the red dotted lines while the rims and the Cpx crystallized in the glassy starting material series are located far from the lines, showing higher Al^{VI} and Na values. The Cpx cores of APR16-35 (6 h) and APR16-2B (12 h) runs, however, are slightly different from the cores of APR16-3B and APR16-1C runs. This difference could be due to the loss of Fe occurred in their melt during the experiments but also to kinetic effects, as stated by Pontesilli et al. (2019). These authors, indeed, observed that in time-series experiments, but also in experiments performed at constant dwell time, compositional changes in Cpx crystals are function of dwell time, according to the cation exchange (Si + Mg) → (^{T}Al and Fe^{3+}).

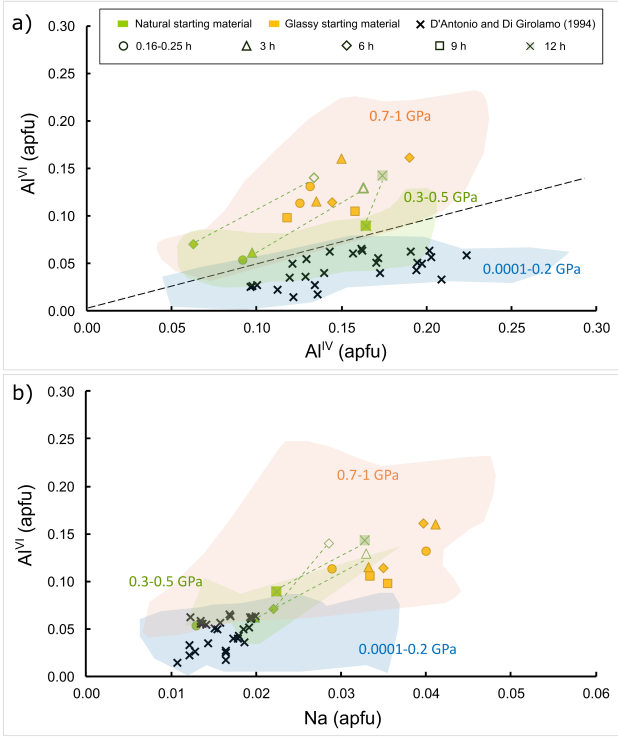

Figure 3. *Al^{IV} vs Al^{VI} (a) and Na vs Al^{VI} (b) diagrams. Literature data (black crosses) are from D'Antonio and Di Girolamo (1994). The new forming Cpx can be distinguished from the pre-existing nuclei: the former fall in the high-pressure field (P > 0.7 GPa), while the latter in the low pressure one (P ≤ 0.5 GPa). The black dotted line bounding the fields of high-low pressure Cpx is an arbitrary limit drawn on the basis of results of experiments on APR16 composition at 0.2, 0.4 (low-P field) and 0.8 GPa (high-P field) (Perinelli et al., 2019). The green dotted lines, instead, connect Cpx core and rim. Series are indicated with different colours: green for natural starting material, and yellow for glassy starting material. The duration of each run is indicated with different symbols: circle for 0.16 and 0.25 h runs, triangle for 3 h runs, diamond for 6 h runs, square for 9 h runs and square with internal cross for 12 h run. In natural starting material series empty symbols indicate Cpx rim, while full symbols indicate Cpx cores. Coloured field represents literature experimental data (Perinelli et al., 2019). Error bars are smaller than symbol size.*

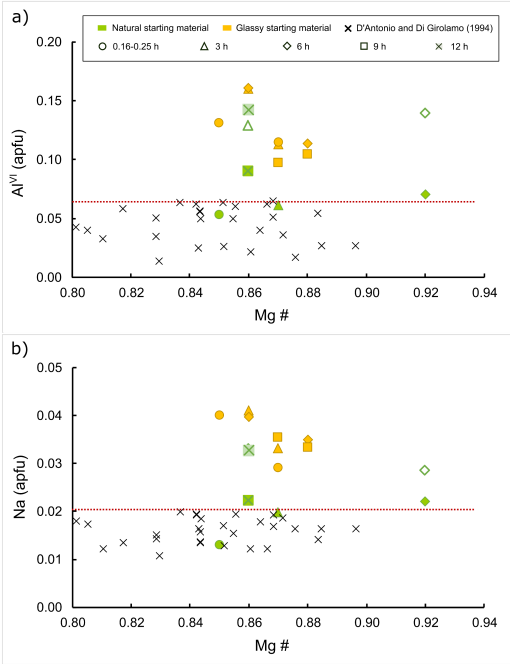

Figure 4. *Al^{VI} (apfu) vs Mg# (a) and Na (apfu) vs Mg# (b). Symbols are as in Figure 3. The red dotted line allows to discriminate between pre-existing nuclei and new forming crystals. This is an arbitrary limit drawn on the basis of the obtained results of this study and literature data from D'Antonio and Di Girolamo (1994).*

Clinopyroxene growth and nucleation rates

Maximum growth rates determined for clinopyroxene are reported in Table 3. Figure 5 illustrates the relation between a) crystal size (L) and experimental time, and b) crystal growth rate (G_L) and experiment time. In both series it was possible to observe an increase in crystal size with increasing time, while the growth rates decrease by about an order of magnitude with increasing duration of the experiments. In the runs of

natural starting material series, the G_L decreases from ~2×10^{-7} to ~6×10^{-8} cm·s^{-1} as duration increases from 3 to 12 h, while in the runs of glassy starting material series the G_L decreases from ~3×10^{-7} to ~2×10^{-8} cm·s^{-1} as duration increases from 0.25 to 9 h (Bonechi et al., 2020b). Moreover, it is possible to see that both the sizes and the G_L values of natural starting material runs are higher than those of glassy starting material ones. The growth rates obtained for the two series are comparable with those available in literature for basaltic and trachybasaltic compositions (Burkhard, 2002, 2005; Oze and Winter, 2005; Baker, 2008; Orlando et al., 2008; Pontesilli et al., 2019). In particular, the growth rates of the glassy starting material runs show values in agreement with those obtained in the static experiments of Burkhard (2005) on re-heated anhydrous basalt (dwell times of 22-576 h, T = 930-990 °C and P = 1 atm) and of Orlando et al. (2008) on anhydrous trachybasalt (dwell times of 3–40 h, T = 1170 °C, P = 1 atm and ΔT = 20 °C). The growth rates of the natural starting material run, instead, are an order of magnitude higher than these latter. Their values, indeed, are similar to those obtained in the dynamic experiments of Pontesilli et al. (2019) on a anhydrous and hydrous trachybasalt (dwell times of 0.5-24 h, T = 1100 °C, P = 400 MPa and ΔT = 80-120 °C), of Shea and Hammer (2013) on a hydrous basaltic-andesite (dwell times of 12-48 h, T = 995-1025 °C, P = 65-150 MPa and ΔT = 52-155 °C) and of Baker (2008) on a trachybasalt (dwell times of 3.5-14 h, T = 1150 °C, P = 1000 MPa and ΔT = 75 °C). Finally, growth rates of both natural and glassy starting material runs show higher values than those obtained by Burkhard (2002) on re-heated Hawaiian basalt (~0.01–7 h of crystal residence times) and by Oze and Winter (2005) on tholeiitic basalt (~0.04–9 h of crystal residence times). The nucleation rate (J) determined for

clinopyroxene are reported in Table 4. Calculated nucleation rates for natural starting material runs vary between 10^2 and 10 $mm^{-3}\,s^{-1}$ from 3 to 12 h, while for the glassy starting material runs vary between 10^5 and 10^3 $mm^{-3}{\cdot}s^{-1}$ from the shortest (0.25 h) to the longest (9 h) durations, respectively. Figures 6 and 7a show the nucleation rate vs time and the nucleation rate vs undercooling (ΔT) diagrams, respectively. In both diagrams it is possible to note that Cpx nucleation rates of natural starting material runs are lower than those of glassy starting material runs. In Figure 6, J tends to decrease increasing dwell time in all the series: in particular, the nucleation seems to decrease up to ~3 h, after which it remains quite constant. In Figure 7a, instead, the nucleation rate decreases increasing the ΔT.

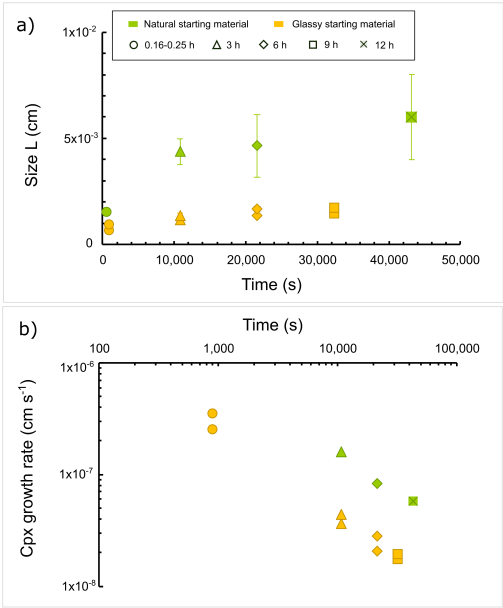

Figure 5. *Relation between (a) Cpx size (L) and experimental time, and (b) Cpx growth rate (G_L) and experimental time. Symbols are as in Figure 2. Error bars are not shown when they are inside the symbols.*

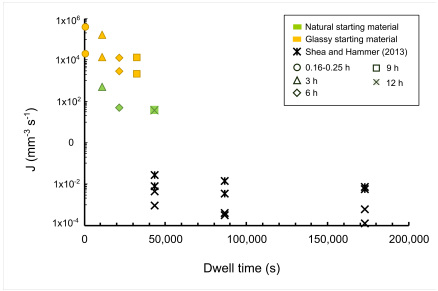

Figure 6. *Relation between the nucleation rate (J) and the experimental time. Symbols are as in Figure 2. Black asterisks indicate the single step cooling runs (ΔT_{eff} = 52-82 °C) of Shea and Hammer (2013).*

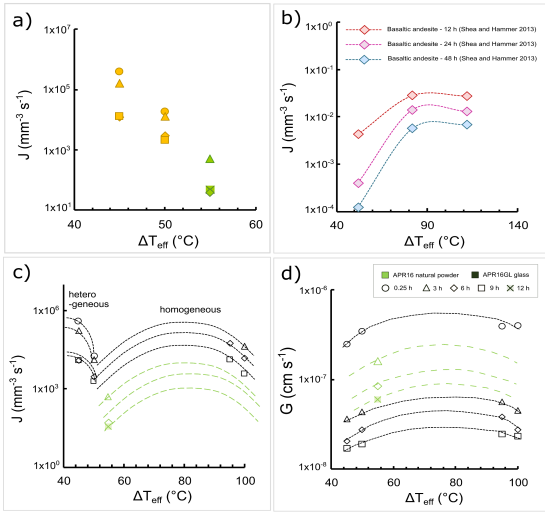

Figure 7. *Variation of (a–c) the nucleation rate (J) with the undercooling (ΔT_{eff}) and (d) the growth rate (G_L) with the undercooling (ΔT_{eff}). In Figure 7a are reported the runs of natural starting material series (in green), and glassy starting material series (in yellow); symbols are as in Figure 2. Figure 7b shows the single step cooling runs of Shea and Hammer (2013) for comparison; colours indicate different duration of the runs: in red the 12 h-runs, in purple the 24 h-runs and in blue the 48 h-runs. Figure 7c, d show the runs investigated in this study (ΔT_{eff} < 60 °C) and those of Bonechi et al. (2020b) (ΔT_{eff} > 60 °C); symbols are as in Figure 2. Dotted lines indicate the hypothetical variation of J with ΔT_{eff} (Figure 7c) and of G with ΔT_{eff} (Figure 7d). Green lines indicate runs obtained using natural starting material while black ones run obtained using vitrified starting material.*

Discussion

Influence of Pre-Existing Crystals on Nucleation and Growth Rate

Crystallization implies two successive processes: nucleation and crystal growth. While a rapid cooling suppresses the nucleation process favoring the formation of a glass, a moderate to slow cooling, instead, allows nucleation that can be either homogeneous or heterogeneous (Vetere et al., 2015). In the homogeneous nucleation case nuclei have the same probability to form spontaneously in any part of the melt, whereas in the second case nucleation occurs preferentially on pre-existing surfaces (e.g., Dowty, 1980; Lofgren, 1980; Kirkpatrick, 1981; Cashman, 1991; Hammer, 2008; Zhang, 2008; Mollo et al., 2012a, 2012b; Vetere et al., 2015). As stated by Špillar and Dolejš (2015), in presence of pre-existing nuclei the interfacial energy between the nucleating phase and the pre-existing nuclei is lower than that between the nucleating phase and the melt because of lesser number of broken bonds between two solid phases. The pre-existing nuclei, therefore, represent a site of energetically favourable nucleation, which is statistically preferred due to the structural similarity between the substrates (e.g., Lofgren, 1983; Mollo et al., 2012a; Vetere et al., 2013). As observed by Vetere et al. (2013, 2015), the structural similarities between the pre-existing nuclei and the nucleating phases concentrate the supply of chemical elements in the liquid surrounding the new growing crystals, limiting in this way the formation of new nucleation sites. Moreover, according to Masotta et al. (2020), element diffusivity in the melt also plays a fundamental role in determining either new nucleation or growth on pre-existing nuclei. This influence of the pre-existing crystals on the nucleation has been observed also in this study. Firstly, the Cpx crystallized in natural starting material

series are present as big crystals (up to ~80 μm) in smaller quantities than those crystallized in glassy starting material one, that are small in size (up to ~20 μm) and very abundant (Figures 1 and 3a and Table 2). Moreover, in the diagrams of Figure 6 it is possible to see that the Cpx of natural starting material runs show nucleation rates smaller than those of glassy starting material runs. The presence of these pre-existing crystals, thus, influencing the nucleation rate, consequently, also affects the growth rate. As shown in Figure 5b, indeed, the Cpx growth rates of natural starting material runs are higher than those of the other series. Since the series were performed with similar time and water content conditions, the only different parameters able to affect the growth rate are temperature and undercooling (e.g., Bonechi et al., 2020a, 2020b). However, neither can justify the higher growth rate of natural starting material runs, since both temperature and undercooling ($\Delta T = T_{liquidus} - T_{experiment}$) of natural starting material series (1225 °C and 55 °C, respectively) are quite similar to those of glassy starting material series (1250-1220 °C and 45-50 °C, respectively). Indeed, considering how the nucleation should vary with the undercooling, in absence of pre-existing crystals, the nucleation values should be slightly lower than those measured for lower ΔT (i.e., 45-50 °C) but not so different as those measured in natural starting material runs (~3 order of magnitude of difference; Figure 7a). The same interpretation is applicable to the growth rate (Figure 7d): indeed, in absence of pre-existing nuclei, the growth rate should be slightly higher than those measured for lower ΔT (i.e., 45-50 °C) but with a difference lower than an order of magnitude. The influence of pre-existing crystals on nucleation and growth rate has also been observed for plagioclase crystals in the work of Arzilli et al. (2015), comparing the

natural rhyolite of Hammer and Rutherford (2002) with the vitrified rhyolite of Mollard et al. (2012). Therefore, the different values of nucleation and growth rates in the natural starting material series seems to be linked to the presence of pre-existing nuclei rather than to the different undercooling.

Influence of Time on Nucleation and Growth Rates

Time is an important factor since it plays a crucial role in the crystallization processes of silicate melts (e.g., Hammer and Rutherford, 2002; Couch et al., 2003; Arzilli and Carroll, 2013; Arzilli et al., 2015). As shown in Figure 6, the runs of this study show a decrease of the Cpx nucleation rate with increasing the duration of the experiments as well as those (single-step cooling runs) of Shea and Hammer (2013). *J* is relatively high during the initial nucleation event (0.25 and 3 h), from 10^4 to 10^5 $mm^{-3} \cdot s^{-1}$, and rapidly decreases increasing the dwell time (6 and 9 h) remaining quite constant (10^3 and 10^4 $mm^{-3} \cdot s^{-1}$ for glassy starting material runs, respectively). This suggests that the main event of nucleation occurred within the first three hours of the experiment, probably in the first minutes at the beginning of the experiment as observed by Ni et al. (2014) for a basaltic composition through in situ experiments. According to the results of Bonechi et al. (2020b), the Cpx growth rate calculated for the natural starting material series follow the trend of the glassy starting material one, varying by an order of magnitude between the runs with the shortest and those with the longest durations (Figure 5b), in agreement with what has been observed in other studies available in literature (e.g., Burkhard, 2002; Allwardt et al., 2005; Orlando et al., 2008; Shea and Hammer, 2013; Pontesilli et al., 2019). In particular, starting from a dwell time ≥ 3 h, the runs begin to achieve conditions close

to the textural equilibrium, at which point an overall decay of the growth rate occurs (Hammer, 2008; Orlando et al., 2008; Masotta et al., 2020). The influence of time on crystal growth rate, indeed, results to be strictly related to the equilibration time of the growing phases, as observed by previous studies (e.g., Couch, 2003; Couch et al., 2003; Orlando et al., 2008; Arzilli et al., 2015; Bonechi et al., 2020b).

Influence of Undercooling on Nucleation and Growth Rates

Arzilli et al. (2015) comparing plagioclase nucleation rates in a variety of experimental studies on water-saturated compositions ranging from basaltic through rhyolitic, noted that nucleation rates of 8-h runs in basaltic melts increase with increasing ΔT_{eff} (i.e., the difference between the phase liquidus temperature and the nominal temperature of the runs), whereas the 1-h runs show an opposite trend, because the nucleation process was not able to be accomplished due to the limited experimental dwell time. The authors, indeed, suggest that for the same ΔT_{eff} the nucleation could be completed within 2 h. The increase of the nucleation rate with the undercooling has also been observed for clinopyroxene by Masotta et al. (2020) in a trachybasaltic melt in long-lasting runs (dwell time of 24 h). Although in this study it was possible to calculate the nucleation rates at 0.25 h only for low undercoolings, it is reasonable to assume that the ≤ 3-h runs behave like the 1-h runs of Arzilli et al. (2020), in accordance with what stated above. As shown in Figure 7c, the nucleation rate decreases with increasing the undercooling up to 50 °C while for higher undercooling the nucleation first increases (up to 100 °C) and then decreases, similarly to the trend of the runs of Shea and Hammer (2013) (Figure 7b). At effective

degrees of undercooling ≤ 50 °C, indeed, most phases fail to nucleate significantly probably due to the dominance of crystal growth (Lofgren, 1983; Shea and Hammer, 2013), rather than to a nucleation lag or incubation period as typically considered (Gibb, 1974; Sato et al., 1981; Fokin et al., 2006). Moreover, according to Shea and Hammer (2013), at low undercoolings (≤ 50 °C) it is possible to hypothesize the occurrence of a heterogeneous nucleation due to the high energy barrier required by homogeneous nucleation. The lack of the latter process in the natural starting material runs is related to the presence of pre-existing nuclei in the starting melt, that favor growth over nucleation. For undercoolings > 50 °C (data from Bonechi et al., 2020b), instead, the nucleation has a bell shape suggesting that it probably occurs homogeneously (Figure 7c). As regards the growth rate, crystal growth occurred both on pre-existing crystals as well as on new forming nuclei during the experiments. As shown in Figure 7d, the growth rate follows a bell-shaped trend with increasing the undercooling, in agreement with what observed by previous studies (e.g., Shea and Hammer, 2013; Arzilli et al., 2015). Moreover, the Cpx growth rates of the run with pre-existing nuclei (natural starting material series) are higher than those of the other runs (glassy starting material series) at similar T and time conditions, according to what previously observed for the nucleation rate (i.e., pre-existing nuclei in the starting melt favor growth over nucleation).

Application

In Bonechi et al. (2020b), data of Cpx growth rates have been combined with thermobarometric data of natural Cpx (SCE and SOG samples) in order to

provide an estimate of deep-level ascent rate for CFVD primitive magmas. In particular, they assumed that a deep episode of magmatic crystallization occurred at low undercooling, a condition verified by CSD investigations of SCE and SOG samples that highlighted the presence of three main Cpx population: larger phenocrysts (sizes ~0.32 mm), smaller phenocrysts and microlites (sizes < 0.32 mm). The range of temperatures and pressures of crystallization estimated for the larger population of Cpx are between 1141–1178 °C and 0.7–0.9 GPa (20–25 km of depth assuming an average crustal density of 2.8 g/cm^3), suggest together with CSD analysis that this population formed during a crystallization stage at deep level. According to the approach of Armienti et al. (2013), for a ΔT of 37 °C (ΔT = 1178–1141 °C), a ΔL of ~ 0.3 cm and a growth rate of 2×10^{-8} cm·s^{-1}, the cooling rate during the ascent of Procida K-basaltic magmas was estimated to be 0.3×10^{-5} °C/s. This value, combined with the dP/dT from thermobarometry, provided a deep level ascent velocity of ~0.5×10^{-4} m·s^{-1}. In this work using the same crystallization parameters but the growth rate obtained for the natural starting material series, influenced by the presence of pre-existing nuclei (1.2×10^{-7} cm s^{-1}), a deep-level ascent velocity of ~6×10^{-4} m·s^{-1} was obtained. However, the Ol/Cpx ratio (~1) of the SCE and SOG samples suggests, in accordance with the experimental phase relations at 0.2–0.8 GPa (Granati, 2016), that primitive magmas of Procida pond at relatively shallow level before the Solchiaro hydromagmatic eruption. This is validated by barometric estimation on the smaller phenocrysts, whose crystallization occurred at 0.3-0.5 GPa (8–14 km of depth; Bonechi et al., 2020b). Therefore, the assessed residence time for the larger Cpx population (i.e., at least 5 months for a G_L of 2×10^{-8} cm·s^{-1} and 1 months for a G_L of 1.2×10^{-7} cm·s^{-1})

multiplied for the magma volume erupted from the CFVD tuff ring (0.1-1 km^3; e.g., Mastrolorenzo et al., 2017) could represent the minimum recharge rate of the large magmatic reservoir, whose top is situated in the CFVD at about 8 km of depth (Rapolla et al., 1989; Cecchetti et al., 2001; Auger et al., 2001; Zollo et al., 2008; Esposito et al. 2011; Pappalardo and Mastrolorenzo, 2012; Fanara et al., 2015; Fedi et al., 2018). Considering the mass balance model of Fedi et al. (2018), according to which the source of the Campania Active Volcanic Area has a total volume of about 40,000 km^3, an estimated recharge rate of 0.2–2 $km^3 \cdot year^{-1}$ (absence of pre-existing nuclei) or 1-10 $km^3 \cdot year^{-1}$ (in presence of pre-existing nuclei) suggests that a deep reservoir of primitive parental magma similar to those had feeding the Campanian Ignimbrite eruption (39 ka), could be formed in a time interval ranging from 10^4 to 10^5 years (absence of pre-existing nuclei) or 10^3 to 10^4 years (presence of pre-existing nuclei). In the case of Solchiaro eruption, the absence of plagioclase phenocrysts and the primitive composition of scoriae indicate that the magma does not stop at 8 km or shallower reservoirs but continue its ascent, going directly to feed the hydromagmatic eruption (De Astis et al., 2004). Moreover, the composition of the Cpx populations with $L < 0.32$ mm in the SOG and SCE scoriae indicates that the late stage of crystallization of the Solchiaro magma takes places in conditions of disequilibrium probably caused by the eruptive regime of ascent. Thus, by taking a grain growth of ~0.32 mm and a G_L of 2×10^{-7} $cm \cdot s^{-1}$, that as indicated by Bonechi et al. (2020b) experiments it is suitable for disequilibrium conditions of Cpx-crystallization, the resulting minimum sin-eruptive time of magma ascent from ~8 km of depth is on the order of 2 days and it results to be very similar to the ascent time estimated by Piochi et al. (2005),

Calzolaio et al. (2010) and Arzilli et al. (2016) in their works on feldspar bearing products of Monte Nuovo eruption (1538 AD). Noteworthy, this time interval is equivalent to that during which occurred the more intense precursor phenomena (i.e., earthquakes, uplift, lowering, increase of the flow of wells) of the Monte Nuovo eruption (Guidoboni and Ciuccarelli, 2011), that is the last of the CFVD and whose VEI (≤4) is comparable to that of Solchiaro eruption (Mastrolorenzo et al., 2017).

Conclusions

This study provides constraints on the effect of pre-existing nuclei on clinopyroxene growth and nucleation rates. In particular, the growth rates calculated in the run performed using natural starting material with pre-existing nuclei are higher than those calculated in the runs performed using the vitrified starting material, while the nucleation rates show the opposite behavior with lower values for the run containing pre-existing nuclei. These differences are due to the structural similarities between the pre-existing nuclei and the nucleating phases that concentrate the supply of chemical elements in the liquid surrounding the new growing crystals, limiting in this way the formation of new nucleation sites. Moreover, the influence of time and undercooling on growth and nucleation rate has been investigated. Concerning the time, regardless of the starting material, for all the series both growth and nucleation rates decrease with increasing dwell time from ~10^{-7} to ~10^{-8} cm·s^{-1} and from 10^5 to 10 mm^{-3}·s^{-1}, respectively, as time decreases from 0.16 to 12 h. In regard to the undercooling, instead, the nucleation rate decreases with increasing the undercooling up to 50 °C while for higher undercooling the nucleation first increases (up to 100 °C) and then

decreases. At $\Delta T_{eff} \leq 50$ °C, indeed, most phases fail to nucleate significantly probably due to the dominance of crystal growth, as it is possible to observe for the runs containing pre-existing nuclei. For $\Delta T_{eff} > 50$ °C, instead, the nucleation has a bell shape as that observed for the growth rate. Finally, the application of the calculated growth rate, combined with the thermobarometric estimates and the crystal size analysis of natural samples from Procida island (CFVD), allow to estimate the recharge rate of the large magmatic reservoir, whose top has been located in the CFVD at about 8 km of depth. These data (0.2-2 $km^3 \cdot year^{-1}$ in absence of pre-existing nuclei or 1-10 $km^3 \cdot year^{-1}$ in presence of pre-existing nuclei) suggests that a deep reservoir of primitive parental magma similar to those had feeding the Campanian Ignimbrite eruption (39 ka), could be formed in a time interval ranging from 10^4 to 10^5 years (absence of pre-existing nuclei) or 10^3 to 10^4 years (presence of pre-existing nuclei).

Acknowledgments

I would like to thank the anonymous Reviewers for their comments helpful in improving the manuscript. I thank Luca Ziberna (BGI Bayreuth) for preparing APR16GL sample, M. Albano (CNR-IGAG) for help in electronic backscattered images and M. Serracino (CNR-IGAG) for help in EMP analyses. I also thanks M. Gaeta and C. Perinelli for their support in the preparation of this work.

Supplementary data

Supplementary data to this article can be found online at

https://doi.org/10.3390/min10030234

Chapter 1.3

Amphibole growth from a primitive alkaline basalt at 0.8 GPa: Time dependent compositional evolution, growth rate and competition with clinopyroxene

Barbara Bonechi [a*], Cristina Perinelli [a], Mario Gaeta [a], Vanni Tecchiato [a], Alessandro Fabbrizio [b]

[a] Dipartimento di Scienze della Terra, Sapienza Università di Roma, P. le Aldo Moro 5, 00185 Rome, Italy

[b] Institute of Petrology and Structural Geology, Faculty of Science, Charles University, Albertov 6, 12843, Prague, Czech Republic

Published in *Lithos*, 2020, vol. 354-355, 105272

Abstract

Amphibole growth rates were experimentally determined at hydrous (3.3-4.2 wt% H_2O), isobaric (0.8 GPa) conditions, variable temperature (1030 and 1080 °C) and dwell time (0.25, 3, 6, and 9 h), using as starting material a primitive alkaline basalt from Procida island (Campi Flegrei Volcanic District, south Italy). Amphibole growth rates decrease from $1.5 \cdot 10^{-7}$ to $2.9 \cdot 10^{-8}$ cm s^{-1} as the duration of the experiments increase from 0.25 to 9 h. Moreover, increasing both temperature and water content leads to similar growth rate increase at constant dwell time. The comparison between amphibole and clinopyroxene growth rates determined at the same experimental conditions reveals for amphibole a faster growth relatively to the coexisting clinopyroxene, regardless of the dwell time. Furthermore, the experimental time appears to be a critical parameter for the composition of synthetic amphiboles; specifically, edenite is the dominant composition in short experiments (≤ 3 h), particularly, at low temperature (1030 °C), whereas the magnesiohastingsitic amphibole becomes progressively more important shifting towards longer duration and higher temperature run conditions. The magnesiohastingsite, on the basis of the amphibole-liquid Fe-Mg exchange coefficient values, results to be the compositional term representative of amphibole-melt equilibrium at the investigated *P*-*T*-H_2O conditions. Finally, experimental growth rates from this study have been used to investigate the crystallization time of natural amphiboles and clinopyroxenes from the Oligo-Miocene cumulates of north-western Sardinia (i.e., Capo Marargiu Volcanic District, Italy), yielding crystallization times of 1.46-3.12 yr.

Keywords: Amphibole growth rate, High pressure, Primitive alkaline basalt, Campi flegrei

Introduction

Amphibole is a typical phase of mafic to felsic hydrous magmas (Arculus and Wills, 1980; Cawthorn et al., 1973; Davidson et al., 2007). By virtue of the high physico-chemical sensitivity of amphibole texture and composition, magmatic crystallization pressure and temperature as well as magma storage, mixing and ascent processes have been qualitatively and quantitatively inferred in a number of studies (e.g. Bachmann and Dungan, 2002; De Angelis et al., 2013; Ridolfi et al., 2010, 2008; Rutherford and Devine, 2008; Rutherford and Hill, 1993; Shane and Smith, 2013; Thornber et al., 2004; Turner et al., 2013; Zhang et al., 2017). It is also widely documented that amphibole is stable in hydrous basalts stalling at the roots of arc crust, influencing the chemical evolution of derivative liquids obtained by fractionation of amphibole bearing cumulates (e.g., Abd El-Rahman et al., 2012; Davidson et al., 2007; Foden and Green, 1992; Green and Ringwood, 1968; Larocque and Canil, 2010; Li et al., 2017; Melekhova et al., 2015). However, investigations on the kinetics of amphibole crystallization (e.g., growth rate) from siliceous liquids are scarce and all addressed to investigate calc-alkaline rocks affinity (i.e., Shea and Hammer, 2013; Simakin et al., 2009; Zhang et al., 2019), implying negligible or misleading interpretation of the timescales on which magmatic processes act at depth. Indeed, the only experimentally determined growth rates for amphibole were obtained at 0.1-2.7 GPa and 860-970 °C from hydrous basaltic to andesitic melts (i.e., Shea and Hammer, 2013; Simakin et al., 2009; Zhang et al., 2019). In this framework, using as starting material a primitive

alkaline basalt from Procida island (Campi Flegrei Volcanic District; south Italy), we investigated the amphibole crystal growth rate at a pressure corresponding to the crustal-mantle boundary in this area (~25 km of depth; Fedi et al., 2018). Aimed to this, we performed hydrous (3.3-4.2 wt% H_2O), isobaric (0.8 GPa), timeseries (dwell time 0.25, 3, 6, 9 h) experiments at temperatures of 1030 and 1080 °C. These T were chosen on the basis of previous high pressure experimental investigations on the APR16GL composition (Bonechi et al., 2019, 2017; Perinelli et al., 2019) demonstrating that for an initial water content in the system of ~4 wt%, amphibole is stable at T < 1100 °C. At the selected temperatures the undercooling, expressed as the difference between liquidus and experimental temperatures (ΔT = $T_{liquidus}$ - $T_{experiment}$), is of ~200 and ~150 °C, respectively. The imposed ΔT coupled to the variable time at isothermal conditions will also allow to highlight how, after an early stage of significant undercooling, the equilibration processes affect the amphibole crystal growth with increasing the dwell time (i.e., relaxation kinetics; Arzilli et al., 2018; Mollo et al., 2012; Pontesilli et al., 2019). The calculated growth rates were used to investigate the crystallization process of natural products from Sardinia. Our findings may be useful to correctly interpret the textural features of amphibole-bearing mafic cumulates and rocks, and for a better constraining of the timescales of magmatic processes at upper mantle-lower crustal depths.

Methods

Starting material

The APR16 sample (Table 1) is a primitive alkaline basalt found as scoria clast in the deposits of the Solchiaro hydromagmatic centre located in

Procida island (Campi Flegrei, Italy). Detailed textural and compositional information about this product are provided by D'Antonio et al. (1999). The starting material is an anhydrous glass (APR16GL; Table 1) prepared by first crushing pieces of the natural APR16 sample in a mortar under ethanol, then by melting the resulting powder at 1400 °C and atmospheric pressure for 15 min and oxygen fugacity buffered at Nickel-Nickel Oxide level by means of a CO/CO_2 gas mixture fluxed inside the furnace at the Bayerisches Geoinstitut, Germany. The melting temperature (i.e., 1400 °C) was chosen so as to be above the liquidus temperature of the APR16 natural sample (i.e., 1290 °C) at 0.8 GPa as calculated using MELTS program (Asimow and Ghiorso, 1998; Ghiorso and Sack, 1995) and verified experimentally in the work of Perinelli et al. (2019). Instead, the imposed fO_2 conditions for starting material preparation take into account that at the experimental conditions (1080-1030 °C and 0.8 GPa) the initial oxygen fugacity is ~NNO - 1, close to in the range of fO_2 previous estimates from runs performed with the same kind of CaF_2 cell assemblages (Conte et al., 2009; Weaver et al., 2013).

Experimental techniques

Experiments were performed at isobaric conditions (~0.8 GPa) as function of temperature and time by using the ½ inch end loaded piston cylinder apparatus at the HP-HT Laboratory of the Earth Sciences Department, Sapienza University of Rome. Assemblies consist of an outer CaF_2 cell, a graphite furnace and MgO crushable spacers. The experimental charges were prepared loading $Au_{75}Pd_{25}$ capsules with ~40 mg of APR16GL powder after that appropriate water amount was added into the capsules by using

a microsyringe. The H_2O/rock ratio was of 1:25 (~4 wt% of H_2O added to the starting material; Table 2). Then the capsule was arc welded while keeping it cooled to avoid loss of water. The welded capsule was weighed, stored in a furnace at 110 °C, and then weighed again to confirm the absence of water leaks. Moreover, to prevent possible loss of H_2 the charges were surrounded by pyrophyllite powder (Freda et al., 2001). The ~0.8 GPa experiments were carried out at 1030 and 1080 °C (i.e., APR16-C3A and APR16-C3B series, respectively) for different dwell time (0.25, 3, 6 and 9 h). The choice of the temperature conditions is based on the phase diagram obtained by Perinelli et al. (2019). The temperature was measured using a type D W_3Re_{97}-$W_{25}Re_{75}$ thermocouple and maintained with an estimated accuracy of ±5 °C. We performed a total of 8 experiments, whose experimental conditions are reported in Table 2. The experimental assembly was first pressurized to the target pressure by piston-out procedure (Johannes et al., 1971; Presnall et al., 1978), that consists in applying an overpressure of ~10% of the run pressure gradually increasing the temperature up to the working temperature and correcting for pressure drops due to stress relaxation within the assembly during heating. The sample is maintained at the pressure and temperature for a given duration (nominal duration), and then quenched down by turning off the power. The temperature drops below 500 °C was of < 5 s (average cooling rate of 150 °C/s). The oxygen fugacity (fO_2) was not controlled, however, an estimation of experimental fO_2 was made using the theoretical model of Barr and Grove (2010) which is based on the temperature-and fO_2-dependent partitioning of Fe between the AuPd capsule and coexisting melt. Thus, we measured the post run Fe content in the sample-holder as closer as possible to the capsule-sample boundary of a

near-liquidus anhydrous experiment (1295 °C; see Table 2 of Perinelli et al., 2019) and of 1080-1030 °C longest experiments. Applying the Barr and Grove (2010) approach the calculated fO_2 were of NNO -0.5 for the near-liquidus run and NNO -0.8 and NNO -1.1 for the longest runs of this study. Finally, being the undercooling a parameter that influence the kinetics of magma crystallization, for both amphibole and clinopyroxene we also determined the effective undercooling (ΔT_{eff}) defined as the difference between the equilibrium amphibole (clinopyroxene) liquidus temperature (T_L) and the experimental temperature (Hammer and Rutherford, 2002). Using as starting material the APR16GL composition we performed the Rhyolite-MELTS equilibrium crystallization calculations to determine the T_L value of clinopyroxene and amphibole. However, for amphibole the thermodynamic modelling provided dubious results. This is probably due to the poor reliability of Rhyolite-MELTS in dealing with hydrous phases, therefore, we extrapolated the T_L value (1095 °C) on the basis of T vs. H_2O in melt phase diagram of Perinelli et al. (2019) reported in Figure A1 in the supplementary materials. T_L and ΔT_{eff} are listed in Table 2.

Table 2 Experimental run conditions melt water contents, phases assemblage and proportions in run products.

Run #	T (°C)	T_L (°C)	$T_{L\text{-}Amph}$ (°C)	ΔT(°C)	$\Delta T_{eff\text{-}Amph}$ (°C)	Time (h)	H_2O_i (wt%)	Phases	H_2O_f EPMA (wt%)	H_2O_f Raman (wt%)	Σr^2	% $\Delta Fe^{\S}$
APR16-C3A												
APR16-C3Aa*	1080	1218	1095	138	15	0.25	4	Gl + Amph + Cpx + Plg + Ox				
APR16-C3Ab*	1080	1218	1095	138	15	3	4	Gl + Amph + Cpx + Plg + Ox	7.5			
APR16-C3Ac	1080	1224	1095	144	15	6	3.8	Gl(60) + Cpx(37) + Ol(3)	6.5		0.62	-10
APR16-C3Ad	1080	1233	1095	153	15	9	3.3	Gl(55) + Amph(24) + Cpx(20) + Ox(1)	10.2	9.9	0.41	-1
APR16-C3B												
APR16-C3Ba*	1030	1224	1095	194	65	0.25	3.8	Gl + Amph + Cpx + Plg + Ox	10.6			
APR16-C3Bb*	1030	1225	1095	195	65	3	3.7	Gl + Amph + Cpx + Plg + Ox	9.5			
APR16-C3Bc*	1030	1232	1095	202	65	6	3.4	Gl + Amph + Cpx + Opx + Ox				
APR16-C3Bd	1030	1216	1095	186	65	9	4.2	Gl(40) + Cpx(24) + Amph(35) + Ox(1)	8.3	7.6	0.18	-1

Gl = glass; Amph = amphibole; Cpx = clinopyroxene; Opx = orthopyroxene; Ol = Olivine; Plg = plagioclase; Ox = oxide minerals. T_L is the liquidus temperature (°C) determined on the basis of phase relations experimental data from Perinelli et al. (2019) and on the calculations by using MELTS software (Ghiorso and Sack, 1995; Asimow and Ghiorso, 1998). ΔT_{eff} is the difference between the liquidus temperature and the nominal temperature of the runs. H_2O_i is nominal content (wt.%) of water added to the charge. $H_2O_{f\ EPMA}$ = water content in the melt determined by the by-difference calculation method (respect to the total of EMP analyses); $H_2O_{f\ Raman}$ = water content in the melt determined by Raman spectroscopy analyses. §Percent of relative Fe loss from starting material based on difference between the starting material and calculated bulk composition of experiment obtained from mass-balance calculations. Σr^2 values from mass balance calculation. *Crystals too small for analysis and not considered for mass balance calculation.

Analytical methods

The recovered samples have been mounted in epoxy resin, ground flat and polished. Textural aspect of the recovered samples was analysed by Scanning Electron Microscopy (SEM) using a FEI quanta 400 equipped for microanalysis with an EDAX Genesis system at the Earth Sciences Department, Sapienza University of Rome and a TESCAN Vega equipped with EDS (energy dispersive X-ray spectrometry) system at the Institute of Petrology and Structural Geology (Charles University in Prague). Phase compositions were analysed at the CNR-Istituto di Geologia Ambientale e Geoingegneria di Roma, with a Cameca SX50 electron microprobe equipped with five wavelength dispersive spectrometers (WDS) and at the Institute of Petrology and Structural Geology (Charles University in Prague) with a Jeol JXA-8530F equipped with five WDS. Quantitative analyses were performed using 15 kV accelerating voltage and 15 nA beam current. As standards we employed metals for Mn and Cr, Jadeite for Na, Wollastonite for Si and Ca, Orthoclase for K, Corundum for Al, Magnetite for Fe, Rutile for Ti and Periclase for Mg. Counting times were 20 s per element and 10 s for backgrounds. Light elements were counted first to prevent loss by volatilization. The PAP correction method was used. Minerals were analysed using a beam diameter of 1 mm whereas for glasses a defocused electron beam from 10 to 15 mm was used. Water contents of experimental glasses were estimated according to the by-difference method of Devine et al. (1995). Due to the uncertainty (±0.5 wt% H_2O) of this approach, the water content of those glasses with ≤ 1 wt% H_2O has been more accurately measured (±0.15 wt% H_2O) by micro-Raman spectroscopy (Di Genova et al., 2017; Le Losq et al., 2012, Table 2). Raman spectra were acquired from

mineral- and/or bubble-free glass portions large enough to be analysed with a Horiba Lab Ram HR 800 spectrometer at the Department of Science, Roma Tre University. Data were collected using a 600 grooves/mm spectrometer grating and CCD detector.

Growth rate calculation

In the collected SEM images, crystal dimensions were measured using the measure tool in ImageJ® software. Because we are interested in determining the maximum growth rate following a method reported in the literature (Couch, 2003 and reference therein), the length (L, cm) and the width (W, cm) of the 10 largest crystals of amphibole from each experimental products were measured. The maximum growth rate (G_L, cm·s^{-1}) values were calculated using the following formula (Hammer and Rutherford, 2002 and reference therein):

$$G_L = (L \cdot W)^{0.5}/t^*2 \quad (1),$$

where t (s) is the duration of the experiments.

Experimental results

Crystal abundance, shape and growth rates

All the experimental products show a high crystallinity (Fig. 1 and Table 2) as a result of the imposed undercooling (ΔT = 150-200 °C). Indeed, this produces strong supersaturation conditions in the K-basaltic melt and enhances the nucleation kinetics in the sample during the early stage of experiments (e.g., Cashman, 1993; Hammer, 2008; Hammer and Rutherford, 2002; Iezzi et al., 2011; Lofgren, 1983; Shea et al., 2015; Simakin et al., 2003)

possibly also influencing the phase modal proportions. Amphibole (Amph) occurs in seven of the eight experiments, followed by clinopyroxene (Cpx), orthopyroxene (Opx) and oxide (Ox). Moreover, Amph is always the most abundant phase, even in the highest temperature experiments (1080 °C) despite its low ΔT_{eff} of ~15 °C (Table 2) that would suggest abundances significantly lower than those of Cpx (ΔT_{eff} ~140 °C). The large experimental undercooling can account for this discrepancy considering that reached the target experimental temperature, it triggered an important nucleation phenomenon in the sample causing an increase of the water content in the system, establishing the conditions suitable for the amphibole crystallization. Notably, the APR16-C3Ac experiment (1080 °C-6 h run), in which Amph does not crystallize, the different phase relations obtained (Gl + Cpx + Ol; Table 2) with respect to the other experiments performed at the same *P*-*T*-H_2O_i (H_2O_i = nominal content of water added to the charge) conditions, can be explained considering the lower final water content in the melt (H_2O_f). Indeed, in this run the residual melt contains ~6.5 wt% of H_2O_f, whereas the residual melt of the APR16-C3Ad experiment, performed at the same *P*-*T*-H_2O_i conditions and showing a comparable crystallization degree, has a H_2O_f amount of ~10.2 wt%. This indicates that probably the H_2O in the APR16-C3Ac charge is partially lost, resulting in insufficient water for the crystallization of amphibole (Table 3), as also observed in the phase relation diagram of Perinelli et al. (2019). Glass is present in all the experimental runs, but it was analysed only in those with glass portions large enough to be examined.

Amphibole. In the runs with short duration (0.25-3 h), Amph are clustered (Fig. 1a and b) with *L* and *W* sizes up to 10 μm. In the 6 h run, Amph shows

frequently well-formed outer faces and occurs as ≤ 20 μm sized isolated grains. Finally, in the 9 h experiments, Amph is euhedral with maximum *L* and *W* size of ~40 and 20 μm, respectively (Fig. 1c), sometimes hosting small Cpx in the inner region of the crystal (Fig. 1d).

Other mineral phases. All the observed pyroxene and oxide crystals have, respectively, euhedral habit with sizes up to ~5 and 40 μm, in agreement with the experimental results of Bonechi et al. (2019) obtained from the same starting material at $P = 0.8$ GPa, $T = 1170$-1250 °C ($\Delta T_{eff} = 45$-100 °C) and $H_2O_f \leq 5$ wt%. Olivine crystallized only in the run APR16-C3Ac and it is characterized by euhedral habit and maximum size of 30 μm. Finally, in the 0.25-3 h run with high degree of crystallization (Table 2), subhedral to euhedral plagioclase with dimension ≤ 10 μm occurs. Amphibole growth rates calculated by using equation (1) are reported in Table 3, together with Cpx and Ox growth rates determined by Bonechi et al. (2019). Amph-G_L vary between $1.5 \cdot 10^{-7}$ cm s^{-1} (APR16-C3Aa, 0.25 h) to $2.9 \cdot 10^{-8}$ cm s^{-1} (APR16-C3Bd, 9 h), showing an inverse correlation with time.

Phases composition and approach to equilibrium

Amphibole. Chemical compositions of Amph are reported in Table 4. According to the Hawthorne et al. (2012) classification, all the crystallized Amph is calcic and its composition varies from magnesiohorneblende and edenite (Fig. 2a and b) to pargasite and magnesiohastingsite (Fig. 2b and c) with increasing time.

Other phases. Chemical compositions of the other phases crystallized in the experimental runs are reported in Table A1. Clinopyroxene compositions are augitic (Wo_{42}-En_{41}-Fs_{18}) and diopsidic (Wo_{47}-En_{43}-Fs_{10}), whereas the

orthopyroxene crystals found in the APR16-C3Bc run is enstatitic (Wo_{4}-En_{73}-Fs_{23}). Oxide crystals are generally hercynites, while in the APR16-C3Aa run Cr-rich spinels also occur. Olivine is present only in the run APR16-C3Ac and is characterized by compositions of Fo_{84} while plagioclase grains occurring in the shorter runs (0.25-3 h) are bytownitic and labradoritic in composition.

Where possible we calculated the equilibrium conditions between the mineral phases crystallized in the investigated runs (i.e., Amph, Cpx, Plg and Ol) and the corresponding melts (Table 4 and A1). As regards Amph, the calculated Amph-melt Fe-Mg exchange coefficient (i.e., $^{Amph\text{-}liq}K_{DFe\text{-}Mg} = (FeO/MgO)^{Amph}/(FeO/MgO)^{liq}$) varies between ~0.3 and ~1, showing an almost linear decrease with increasing time (Fig. 3). According to the Putirka (2016) $^{Amph\text{-}liq}K_D^{Fe\text{-}Mg}$ value (i.e., 0.28±0.11), only the magnesiohastingsites crystallized in the runs at 9 h (APR16-C3Ad and APR16-C3Bd), characterized by the lowest $^{Amph\text{-}liq}K_D^{Fe\text{-}Mg}$ values (0.34 and 0.40, respectively) attained Amph-liquid equilibrium conditions. Similar $K_D^{Fe\text{-}Mg}$ trend towards equilibrium with increasing run times has been observed by Mollo et al. (2013) also for clinopyroxene phase. As regards the other phases, instead, Cpx and Plg results to be always in disequilibrium conditions. Particularly, since Cpx-melt Fe-Mg exchange coefficient (i.e., $^{Cpx\text{-}liq}K_D^{Fe\text{-}Mg} = (FeO/MgO)^{Cpx}/(FeO/MgO)^{liq}$) is 0.41±0.01 and 0.43±0.02 in the APR16-C3Ad and APR16-C3Bb runs, respectively, Cpx result to be in disequilibrium with the melt, according to the Putirka (2008) $^{Cpx\text{-}liq}K_D^{Fe\text{-}Mg}$ value (i.e., 0.28±0.08). Similarly, Plg are not in equilibrium with the melt according to the (Putirka, 2008) K_D $(An\text{-}Ab)^{Plg\text{-}liq}$ value (0.1±0.05 for $T < 1050$ °C). Indeed, plagioclase-liquid equilibrium (i.e., K_D $(An\text{-}Ab)^{Plg\text{-}liq}$) is 0.46 and 0.47±0.02 in the APR16-

C3Ba and APR16-C3Bb runs, respectively. Different case is the APR16-C3Ac run (1080 °C, 6 h), in which both Ol and Cpx results to be in equilibrium with the melt. In this run, indeed, both $^{Cpx\text{-}liq}K_D^{Fe\text{-}Mg}$ (0.36±0.04) and $^{Ol\text{-}liq}K_D^{Fe\text{-}Mg}$ (0.30±0.01) are in agreement with the Putirka (2008) reference values (0.28±0.08 and 0.29±0.06, respectively).

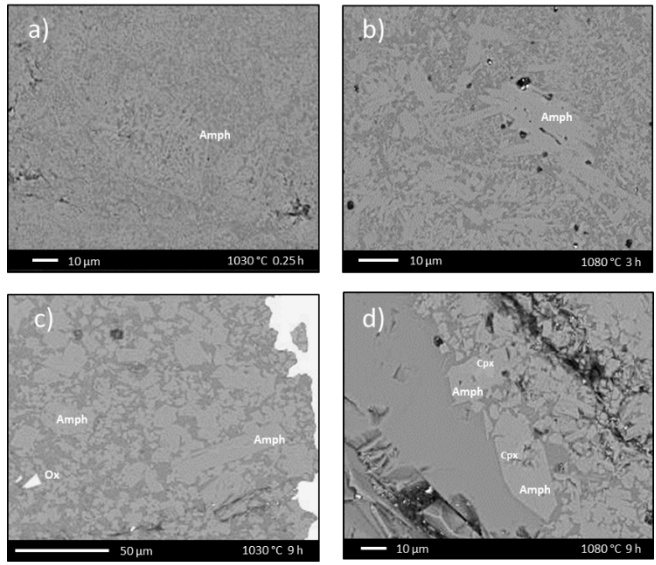

Fig. 1. *- Backscattered (BSE) images of selected run products, showing the textural variation as a function of time and temperature. a) clustered Amph with sizes <10 µm; b) clustered Amph and isolated grains (sizes > 10 µm); c) euhedral Amph with maximum size of ~40 µm; d) euhedral Amph hosting small Cpx in their inner region. Abbreviation: Cpx: clinopyroxene; Ox: oxide; Amph: amphibole; Gl: glass.*

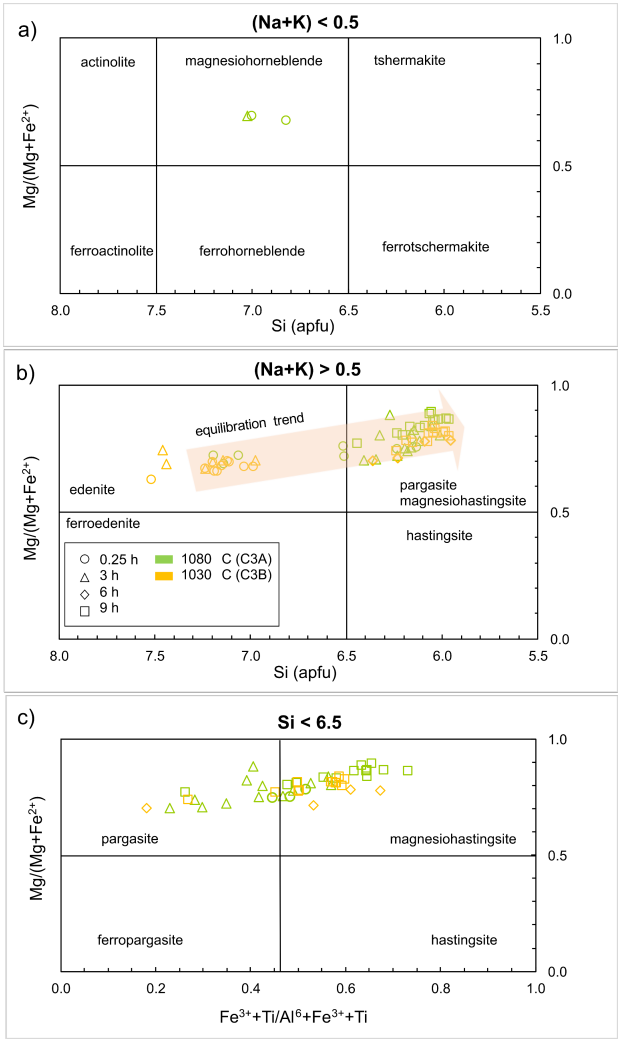

***Fig. 2**. - Classification diagram of calcic amphiboles (Hawthorne et al., 2012). Cation abundances are calculated by using the Ridolfi et al. (2018) "AMFORM Calc" and expressed in apfu (atoms per formula unit). Runs of APR16-C3A series are reported in green while those of APR16-C3B series in yellow. Circle indicates 0.25 h runs, triangle 3 h runs, diamond 6 h runs and square 9 h runs. Orange arrow in b) shows the time-controlled equilibration trend from edenite to magnesiohastingsite.*

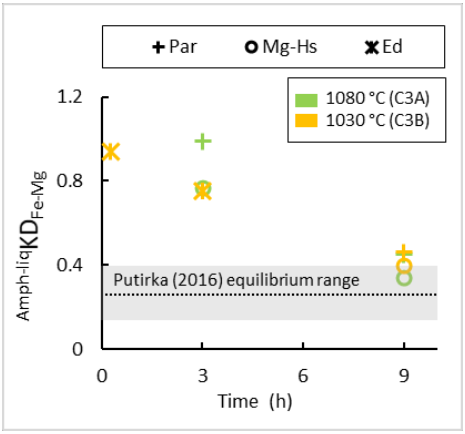

***Fig. 3**. - Amph-melt Fe-Mg exchange coefficient vs time diagram. Only the magnesiohastingsites of the 9 h runs match the grey field representing the Putirka (2016) equilibrium range (0.28±0.11). Runs of APR16-C3A series are reported in green while those of APR16-C3B series in yellow. Asterisk indicates edenite (Ed), plus pargasite (Par) and circle magnesiohastingsite (Mg-Hs). Grey dashed line indicates the linear regression of the experimental data.*

Discussion

Amphibole growth rate dependence on time and temperature

Studies of amphibole growth rate at high-pressure conditions are scarce in the literature. The only data available are obtained at 0.1-2.7 GPa, 860-970 °C, undercooling between 100 and 600 °C from hydrous basaltic to andesitic melts (i.e., Shea and Hammer, 2013; Simakin et al., 2019, 2009; Zhang et al., 2019) and range from 10^{-5} to 10^{-8} cm s^{-1}. Amphibole growth rates from this study decrease from $1.5 \cdot 10^{-7}$ to $2.9 \cdot 10^{-8}$ cm s^{-1} with increasing the duration of the experiments (Fig. 4), since longer runs allow to attain conditions close to equilibrium under which kinetic processes (i.e., growth) slow down.

Notably, textural variations, observed starting from 6 h of dwell time, that from widely dispersed cluster of tiny amphiboles (<10 μm in size; Fig. 1a and b) change in well-formed to euhedral isolated grains (Fig. 1c and d), point out the recrystallization of the set of small crystals with decreasing of the crystal density number and increasing of the average and maximum size over time. This dissolution reprecipitation process may be induced from small temperature fluctuations unavoidable in experiments of long durations (Simakin and Bindeman, 2008) and therefore, the G_L determined for long-lasting experiments may be apparent or reflect a recrystallization process (Simakin et al., 2019). However, it should be emphasized that the Amph growth rate calculated in this work varies of about an order of magnitude between the runs with the shortest duration and those with the longest one (Table 3). Concerning the effect of water in the system on the Amph growth rate, Fig. 5 shows that the G_L value of Amph in run 1080 °C (APR16-C3Ad) with 10.2 wt% H_2O_f (i.e., water content dissolved in the melt) is higher than that of crystals in 1030 °C run (APR16-C3Bd) with 8.3 wt% H_2O_f, testifying that melt depolymerization, viscosity reduction, and element diffusivity increase by increasing both temperature and water content. Since Zhang et al. (2019) also show that amphibole growth rate depends upon time and temperature, we applied their regression equation calibrated on 1-100 h long experiments, to calculate amphibole growth rate (G_{CSD}) as a function of temperature and (also) pressure:

$$G_{CSD}(T,P) = 7.4(\pm3.8)\cdot10^{-10}\cdot T + 1.4(\pm0.2)\cdot10^{-7}\cdot P - 7.0(\pm3.5)\cdot10^{-7} \quad (2)$$

At the isobaric conditions of 0.8 GPa, this method yields growth rate values of $2.11\cdot10^{-8}$ cm s^{-1} at 1080 °C and $1.74\cdot10^{-8}$ cm s^{-1} at 1030 °C, keeping in line

with those experimentally obtained from 3 to 9 h long experiments (2.9-6.4 $\cdot 10^{-8}$ cm s^{-1}) mismatching instead the *G* values determined for the shortest experiments ($1.5 \cdot 10^{-7}$ cm s^{-1}). The quite good correspondence of *G* values between our medium-long experiments and those calculated by Zhang et al. (2019) equation probably reflects the action of textural equilibration process driven by surface energy reduction, that affected our 3-9 h experiments. Indeed, as stated by Zhang et al. (2019) their experiments have time for crystals to undergo textural maturation (Ostwald ripening; Voorhees, 1992) or coarsening (Marsh, 1988) during which smaller crystals, with higher surface energy, dissolve and larger crystals grow. However, it should be emphasized that in our study only the longest experiments approach also to the chemical equilibrium.

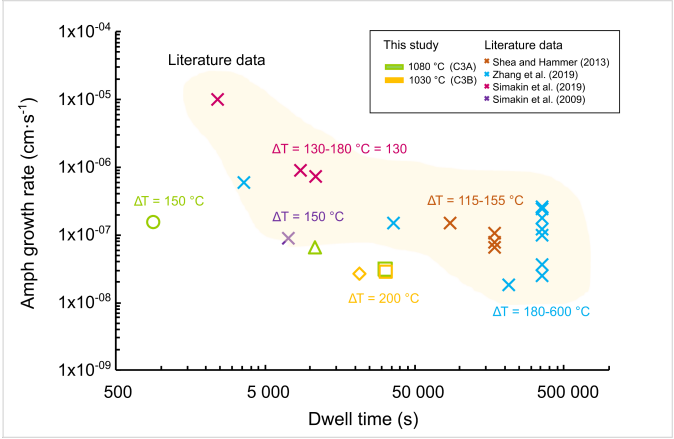

Fig. 4. *- Amphibole growth rate (cm·s^{-1}) vs dwell time (s) diagram. The yellow area shows literature data: red crosses indicate Shea and Hammer (2013) growth rate values obtained for ΔT of ~115-155 °C; light blue crosses indicate Zhang et al. (2019) growth rates obtained for ΔT of ~180-300 °C for runs at 0.6-1 GPa experiments and ΔT of ~500-600 °C at 2.1-2.6 GPa; magenta crosses indicate Simakin et al. (2019) growth rates obtained for ΔT of ~130-180 °C; and purple cross indicates Simakin et al. (2009) one obtained for a ΔT of ~150 °C. Symbols for data from this study are as in Fig. 2.*

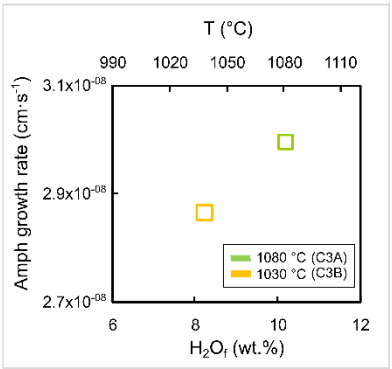

Fig. 5. *- Amphibole growth rate (cm s^{-1}) vs final water content in the melt (H_2O_f wt%) and T (°C) diagram, revealing that the positive correlation is possibly due to melt depolymerization, viscosity reduction, and element diffusivity increase. Symbols are as in Fig. 4.*

Antagonism with clinopyroxene

As for amphibole, clinopyroxene growth rate determined at the same experimental conditions (Bonechi et al., 2019) decrease from $2.0 \cdot 10^{-8}$ to $8.2 \cdot 10^{-9}$ cm s^{-1} with increasing time (Fig. 6; Table 3), paralleling the trend described by data of Bonechi et al. (2019) for synthetic clinopyroxene crystallized from the same starting material at P = 0.8 GPa, T = 1170-1250 °C and $H_2O_f \leq 5$ wt%. However, these Cpx-G_L values are in general slightly higher than those determined in this study (e.g., ~$2.0 \cdot 10^{-8}$ and ~$0.8 \cdot 10^{-8}$ cm s^{-1} for a same dwell time), but it should be noted that the temperatures and the H_2O-melt contents of Bonechi et al. (2019) experiments are, respectively, higher and lower than our investigated conditions and not suitable for Amph formation.

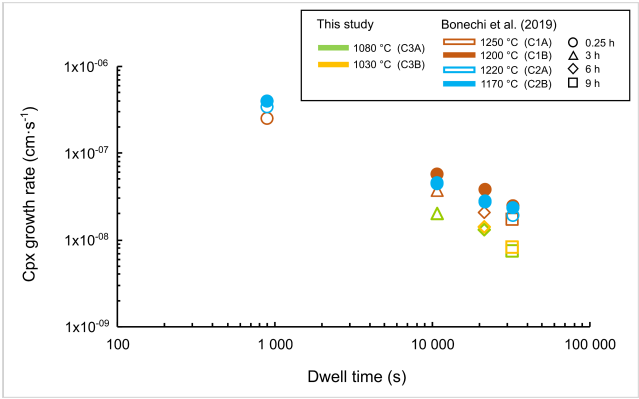

***Fig. 6**. - The decrease of clinopyroxene growth rate (cm s^{-1}) with increasing dwell time (s). Literature data from Bonechi et al. (2019). Symbols are as in Fig. 4.*

Thus, the above small differences in Cpx-GL values can be explained by the contemporary amphibole-clinopyroxene crystallization in our experiments and by the strikingly evidences of the faster growth of amphibole relatively to clinopyroxene (Fig. 7). Such phenomenon is readily explained by the chemical and structural similarities of these minerals (e.g., Kennedy, 1935; Wones and Gilbert, 1982), that compete for Mg, Fe, Ca and to a lesser extent Al and Na. The occurrence of amphibole at high water content, therefore, not only reduces the abundance of clinopyroxene (Fig. 8), but also the rates of clinopyroxene nucleation and growth (Fig. 7), as previously observed by Shea and Hammer (2013).

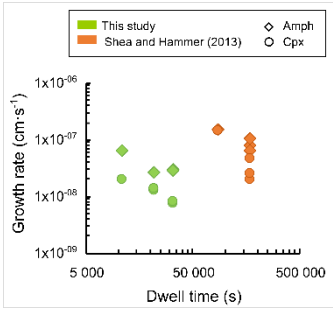

Fig. 7. *- Clinopyroxene and amphibole growth rate vs dwell time (s) diagram, showing the faster growth of amphibole (diamonds) relatively to coexisting clinopyroxene (circles). Literature data (orange symbols) from Shea and Hammer (2013) are in agreement with our observation.*

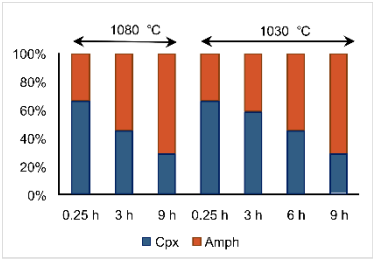

Fig. 8. *- Histogram showing the clinopyroxene (blue) and amphibole (red) modal percentage variation from 0.25 to 9 h runs at both 1030 and 1080 °C. Amphibole becomes progressively more abundant with increasing time at the expense of clinopyroxene.*

Chemical evolution of amphibole with time

Synthetic amphibole from this study shows compositional variability from edenite to magnesiohastingsite with increasing time (Fig. 2). According to our chemical data (Table 4), the percentage of amphibole species at different dwell time (Fig. 9a) shows that edenite is the dominant term in short (≤ 3 h), low-temperature (1030 °C) runs, whereas the magnesiohastingsite abundance progressively increases shifting towards longer experimental

duration and higher temperature. Coherently with the amphibole-liquid Fe-Mg exchange coefficient values (Fig. 3), magnesiohastingsite is therefore identified as the compositional term representative of amphibole-melt equilibrium at the investigated *P-T*-H_2O conditions. Specifically, we consider the formation of magnesiohastingsitic amphibole as the final product of a reaction process that begins with the crystallization of metastable edenite, whose early nucleation is probably promoted by the pressure conditions. Indeed, the formation of Na-Ca amphiboles is favoured by the increase of pressure but hampered by the elevated temperatures that stabilize the pargasite amphibole type (Ernst and Liu, 1998 and reference therein). Therefore, the variation of Si and Al^{IV} in the tetrahedral site with time (Fig. 9b) depicts the overall tendency of amphibole to preferably incorporate Al rather than Si in four-fold coordination, mirroring the time-dependent chemical evolution from more siliceous (i.e., edenite) to more aluminous (i.e., magnesiohastingsite) species. At the same time, the SiO_2/Al_2O_3 ratio of amphibole keeps always constant around the value of 3 (Fig. 9c), suggesting that the transition from metastable edenite to magnesiohastingsite is not driven by any change of Si and Al activities in the melt. Graham and Navrotsky (1986) observe that a reduction of albite activity from 1.0 to 0.5, corresponding to a change in plagioclase composition from albite to andesine, is responsible for the compositional deviation of coexisting amphibole from edenite to tremolite. Alternatively, under equilibrium conditions, the crystallochemistry of coexisting experimental phases potentially acts as a buffer for cation exchange substitutions between the different amphibole structural sites (Graham and Navrotsky, 1986; Holland and Blundy, 1994; Spear, 1981). On this basis, by

exemplifying the edenite and magnesiohastingsite activity as a function of the exchange reaction

$(Na_ASi_T) = ((Ca; Mg)_{A\text{-}M}Al_T)$

where the subscripts indicate the A, M and T sites of amphibole structure, we can qualitatively conclude that the absence of plagioclase (Table 2) and the minor abundance of clinopyroxene (Fig. 8) in the 6-9 h experiments drive the reaction to the right, stabilizing magnesiohastingsite.

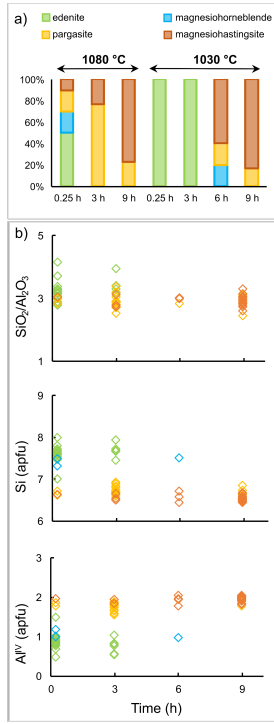

Fig. 9. *- a) Histogram showing the time-dependent variation of amphibole species percentage at different temperature conditions, and b) variation of SiO_2/Al_2O_3 ratio, Si (apfu) and Al^{IV} (apfu) against time (s). Edenite is reported in green, magnesiohorneblende in light blue, pargasite in yellow and magnesiohastingsite in orange.*

Crystallization timing for capo marargiu Oligo-Miocene igneous products

Experimental growth rates from this study have been applied to investigate the crystallization time of natural amphiboles and clinopyroxenes from the Oligo-Miocene products of north-western Sardinia (i.e., Capo Marargiu Volcanic District; CMVD). According to Tecchiato et al. (2018b), these minerals crystallize at P = 0.2-0.7 GPa, T = 960-1140 °C and H_2O = 5-6 wt% during the polybaric differentiation of a primitive basalt towards andesitic terms by olivine + Cr-spinel + clinopyroxene + amphibole + plagioclase (i.e., crystallization sequence) fractionation. Intriguingly, amphibole crystals are found as millimetre-to centimetre-sized relicts either dispersed in the groundmass of porphyritic, magmatic enclaves (Fig. 10a) entrapped in basaltic andesitic domes, or as plutonic textured, plagioclase-bearing crystal clots disrupted within andesitic dikes, representing the lower (enclave amphibole) and upper (crystal clots) levels of a crustal-scale cumulitic pile variably sampled and disaggregated upon eruption of basaltic andesitic to andesitic magmas (Tecchiato et al., 2018b, 2018a). Therefore, they always show coronas due to resorption under crystal-melt disequilibrium conditions, where amphibole is replaced by an anhydrous paragenesis of clinopyroxene + plagioclase + titanomagnetite/ilmenite ± low-Ca pyroxene (Tecchiato et al., 2018b).

Based on Simakin and Shaposhnikova (2017), the bimodal distribution of amphibole from enclaves and crystal clots in the $Fe^{3+}+Ti^{4+}$ vs. Al^{VI} diagram (Fig. 10b) implies the calculation of different regression equations. The intercepts of these lines with the y-axis provide two Al^{VI}_{max} parameters, that according to the Simakin and Shaposhnikova (2017) barometric formulation

$$P = (-7.819 \pm 0.359) + (16.051 \pm 0.773) \cdot Al_{max}^{VI} \quad (3)$$

testifies to crystallization pressures of 0.91±0.12 GPa and 0.32±0.09 GPa, respectively, confirming the polybaric nature of these minerals and providing a slightly higher crystallization pressure for enclave crystals. Tecchiato et al. (2018a) also identify three types of clinopyroxenes into the CMVD porphyritic enclaves, but only the first and the second population show disequilibrium dissolution features (i.e., spongy texture and rounded corners) ascribable to crystal recycling and/or uptake from a deep cumulate region. Specifically, while the $Mg\#_{83\text{-}93}$ Type 1 is a near-liquidus mineral crystallizing along with early olivine and Cr-spinel, the $Mg\#_{75\text{-}84}$ Type 2 is texturally associated to amphibole (Fig. 10a), representing a colder stage of the magmatic history (Tecchiato et al., 2018a). An approximate estimation of the minimum growth time and then, a minimum residence time of the Type 1 and Type 2 amphiboles can be obtained using a growth rate of $2.9 \cdot 10^{-8}$ cm s^{-1} that is the average experimental G_L from 9 h runs (Table 3), and that on the basis of K_D $(Fe\text{-}Mg)^{Cpx\text{-}liq}$ fall in the field representing equilibrium conditions. We are aware that this G_L probably better represent a recrystallization rate, however, it is in the order of the effective growth rate determined from amphiboles in the 3 h runs (see Amphibole growth rate dependence on time and temperature section) and can be confidently used to provide an estimation of the crystallization time of natural Type 1 and Type 2 amphiboles. Thus, depending on the crystallographic orientation, the maximum dimension of the five biggest amphibole crystals measurable from thin sections ranges from 1.340 to 2.850 cm (Table 5), translating to crystallization times of 1.5-3.1 yr at a growth rate of $2.9 \cdot 10^{-8}$ cm s^{-1} (i.e., the average experimental growth rate from 9 h runs; Table 3). In turn,

clinopyroxene measurements yield maximum dimension of 1.375 cm for Type 1, and 0.380 cm for Type 2 crystals. Crystallization time for Type 1 clinopyroxene (i.e., 2.18 yr) is comparable to that from enclave amphibole (1.46-2.03 yr; Table 5) only when the $2.0 \cdot 10^{-8}$ cm s^{-1} growth rate from amphibole-free experiments of Bonechi et al. (2019) is adopted. In contrast, the lowest growth rate of $7.4 \cdot 10^{-9}$ cm s^{-1} from amphibole-bearing runs (Table 3) is necessary to retrieve a consistent Type 2 crystallization time (i.e., 1.62 yr). In conclusion, these results suggest that at the lower crustal pressures typical of enclave paragenesis, the bigger, more primitive Type 1 population crystals coexisting with olivine and Cr-spinel at higher temperature grow faster than the smaller, more evolved Type 2 clinopyroxene crystals associated with amphibole at colder conditions, reflecting the coupled effect of amphibole crystallization and temperature on clinopyroxene growth rate.

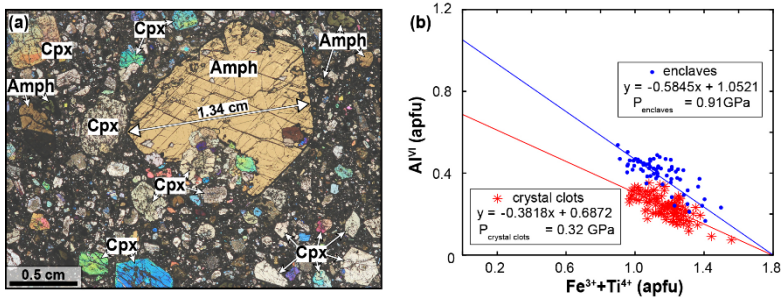

Fig. 10. - a) A centimetre-sized amphibole crystal as appear in a porphyritic, magmatic enclave from CMVD (Tecchiato et al., 2018a). Smaller Type 2 clinopyroxene is included in this amphibole megacryst (see text for further details). Abbreviations are as in Fig. 1b) The bimodal distribution of amphibole from enclaves and crystal clots in the $Fe^{3+}+Ti^{4+}$ vs. Al^{VI} diagram (Fig. 10b) testifies to different crystallization pressures (cf. Simakin and Shaposhnikova, 2017), with enclave amphibole belonging to lower crustal environments. Data from Tecchiato et al. (2018b).

Conclusions

New amphibole growth rate data from this study improve knowledge of amphibole growth kinetics at high pressure (~0.8 GPa). At the investigated *P*-*T*-H_2O conditions, amphibole growth rate decreases from $1.5 \cdot 10^{-7}$ to $2.9 \cdot 10^{-8}$ cm s^{-1} with increasing time (from 0.25 to 9 h), temperature (from 1030 to 1080 °C) and water content in the melt (from 8.3 to 10.2 wt%), reflecting time-dependent equilibration, melt depolymerization, viscosity reduction, and element diffusivity increase. Comparison between amphibole and clinopyroxene growth rates provide evidence for the faster growth of amphibole with respect to clinopyroxene, which we surmise is due to chemical and structural similarities between these minerals that cause a "kinetic competition". According to our chemical data, edenite is the dominant term in short (≤3 h), low temperature (1030 °C) runs, whereas magnesiohastingsite is progressively more important in longer experimental duration and higher temperature runs. Coherently with the amphibole-liquid Fe-Mg exchange coefficient values, magnesiohastingsite is likely representative of amphibole-melt equilibrium at the investigated *P*-*T*-H_2O conditions. The results obtained by applying our growth rate data to amphiboles and clinopyroxenes from the Oligo-Miocene products of Capo Marargiu Volcanic District (Sardinia, Italy) suggest that the biggest, more primitive Type 1 population of clinopyroxenes co-existing with olivine and Cr-spinel at higher temperature grow over a longer period of time (2.18 yr) than the smaller, more evolved Type 2 clinopyroxene (1.62 yr) associated to amphibole (1.46-3.12 yr) at colder conditions, reflecting the coupled effect of amphibole crystallization and temperature on clinopyroxene growth rate.

Acknowledgments

We are grateful to Keith Daniel Putirka and Alexander Simakin for their useful and constructive comments. The Editor, Michael Roden, is acknowledged for the editorial work. We thank Luca Ziberna (BGI Bayreuth) for preparing APR16GL sample. We thank M. Albano (CNR-IGAG), Dr. R. Jedlicka (Institute of Petrology and Structural Geology, Charles University of Prague) and M. Serracino (CNR-IGAG) for assistance during SEM and EMPA analytical sessions. This article is a contribution of the project "Dipartimenti di Eccellenza" of the Earth Science Department, Sapienza University of Rome, supported by the Italian Ministry of Education, University and Research.

Supplementary data

Supplementary data to this article can be found online at **https://doi.org/10.1016/j.lithos.2019.105272**

Chapter 1.4

Experimental investigation of high pressure clinopyroxene dissolution in a K-basaltic melt

Barbara Bonechi[1], Cristina Perinelli[1], Mario Gaeta[1], Vincenzo Stagno[1,2], Alessandro Fabbrizio[3], Silvio Mollo[1,2], Rostislav Hrubiak[4]

1: Dipartimento di Scienze della Terra, Sapienza Università di Roma, P. le Aldo Moro 5, 00185, Rome, Italy

2: Istituto Nazionale di Geofisica e Vulcanologia, Roma - Via di Vigna Murata 605, 00143 Roma, Italy

3: Institute of Petrology and Structural Geology, Faculty of Science, Charles University, Albertov 6, 12843 Prague, Czech Republic

4: High Pressure Collaborative Access Team, X-ray Science Division, Argonne National Laboratory, 9700 S. Cass Avenue, Argonne, IL 60439, United States

Under review in *Chemical Geology*

Abstract

In this experimental work, the dissolution of clinopyroxene (cpx) in a K-basaltic melt from Campi Flegrei Volcanic District (Italy) have been investigated in terms of diffusive dissolution, dissolution-crystallization, and melting. The dissolution rate of cpx has been determined through piston cylinder experiments conducted at pressure of 0.8 GPa, superliquidus temperature of 1350 °C, and dwell times between 0.5 and 1 h. The obtained dissolution rates range from $7.9 \cdot 10^{-6}$ cm s^{-1} to $6.1 \cdot 10^{-6}$ cm s^{-1} as a function of dwell time. In the dissolution-crystallization experiment (1300 °C; 0.8 GPa; 2 h), the formation of overgrowth rims accompanied by new cpx crystals suggests that the injection of recharge magmas in basaltic reservoir may lead to inverse or oscillatory zonation. A high temperature experiment at 1570 °C was monitored in real time by *in-situ* radiography using synchrotron radiation combined with the Paris-Edinburgh press. We document that kinetic melting of cpx does not occur linearly with time but, rather, depends on crystal size and shape. The calculated cpx melting rates of ~$5 \cdot 10^{-2}$ cm s^{-1} (crystal face) and ~$3 \cdot 10^{-1}$ cm s^{-1} (sub-rounded shape) are systematically higher than those (10^{-5}-10^{-6} cm s^{-1}) determined by previous quench experiments conducted at 1 atm. The effective binary diffusivities of MgO and CaO resulting from dissolution experiments confirm classical Arrhenian dependence of D_{MgO} and D_{CaO} on temperature and anisotropy with maximum parallel to c-axis. The role of crystal dissolution in the estimation of magma residence times has been also tested for a natural magmatic system by interpolating the dissolution rates (~10^{-5}-10^{-6} cm s^{-1}) with the textural data of cpx phenocrysts from the Agnano-Monte Spina pyroclastic deposit at Campi Flegrei caldera (Campanian region, Italy).

Results from calculations indicate that the time required for partial or complete resorption of phenocrysts varies from ~0.5 to ~40 h, and that the effect of crystal dissolution may be relevant to estimate magma residence times whether significant dissolution occurs during magma mixing processes.

Keywords: clinopyroxene; dissolution rate; in-situ synchrotron; chemical diffusion; dissolution-crystallization process; Campi Flegrei

Introduction

Dissolution is a fundamental process in igneous petrology and it often occurs, for instance, during xenolith and/or xenocryst digestion by magma assimilation and transport processes (e.g., Edwards and Russell 1998). Knowledge of dissolution kinetics of minerals is important to provide information and develop models on the crystal-liquid interaction during melt transport (Navon and Stolper 1987; Kelemen 1990; Reiners 1998). Among the studies available in literature on mineral dissolution in silicate melts, those focusing on clinopyroxene (cpx) are few and sparse (Kutolin and Agafonov 1978; Scarfe et al. 1980; Kuo and Kirkpatrick 1985; Zhang et al. 1989; Van Orman and Grove 2000; Chen and Zhang 2009) (Fig. 1), and only those by Scarfe et al. (1980) and Brearley and Scarfe (1986) report data on cpx dissolution in alkali basaltic compositions. Crystal dissolution in silicate melts can be controlled by interface reaction and mass transfer, with this latter mechanism being both convective (e.g., Kerr 1995; Liang 2003; Zhang and Xu 2003) and diffusive (e.g., Zhang et al. 1989; Liang 1999). Crystal dissolution in nature often occurs under convective conditions

driven by density differences between crystal and melt, or density differences between interface and far-field melts (e.g., Kerr 1995; Shaw 2000; Chen and Zhang 2008, 2009). Convective dissolution has been investigated in some early experimental works (e.g., Donaldson 1985; Kuo and Kirkpatrick 1985; Brearley and Scarfe 1986) showing that the dissolution rate does not depends on the crystallographic orientation but scales with dwell time. However, as pointed out by Zhang et al. (1989) convective dissolution cannot be used to quantify chemical diffusivities, and the application of dissolution rate is restricted to natural systems with similar convection regimes. To overcome this limitation, more recent authors have investigated the effects of non-convective dissolution (e.g., Watson 1982; Zhang et al. 1989; Finnila et al. 1994; Liang 1999, 2000; Morgan et al. 2006; Shaw 2006), pinpointing that diffusive mass transfer and dissolution rates are inversely proportional to the square root of time. Generally, the crystal dissolution rate is studied by assuming an effectively semi-infinite or infinite reservoir. However, crystal dissolution measured in a finite geometry (e.g., partially molten system) can provide useful information about specific magmatic processes such as melt-rock reactions occurring at the edges of magmatic reservoirs between melt and cumulitic rocks (e.g., Liang 2000; Morgan and Liang 2003; Tursack and Liang 2012). Together with dissolution, melting of crystals is another important process in some geological events, such as magma production, assimilation of crustal materials, and melting of high-pressure phenocrysts in ascending magmas (Tsuchiyama and Takahashi 1983). However, there are only a few experimental studies describing melting kinetics of silicate minerals (Wagstaff 1969; Johannes 1978; Scarfe et al. 1980; Tsuchiyama and Takahashi 1983; Tsuchiyama 1986). Differently

from dissolution that is governed by mass transfer and concentration gradients (e.g., Woods 1992), the melting rate is mostly controlled by heat transfer and/or rearrangement of atoms at the crystal-melt interface (Tsuchiyama and Takahashi 1983).

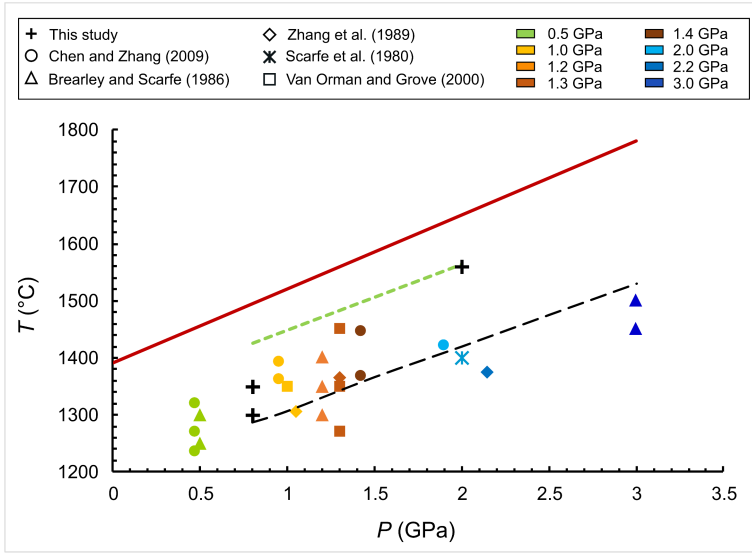

Fig. 1. *T and P conditions of cpx dissolution experiments. Data sources: black cross this study (49 wt.% SiO_2); star Scarfe et al. (1980), convective cpx dissolution in alkali basalt (47 wt.% SiO_2); triangle Brearley and Scarfe (1986), cpx dissolution in alkali basalt (49 wt.% SiO_2); diamond Zhang et al. (1989), diffusive diopside dissolution in andesite (56.3 wt.% SiO_2); square Van Orman and Grove (2000), diffusive diopside dissolution in lunar ferrobasalt (47 wt.% SiO_2); circle Chen and Zhang (2009) (51.2 wt.% SiO_2). Colours indicate pressure ranges: green 0.5 GPa, yellow 1 GPa, orange 1.2 GPa, red 1.3 GPa, brown 1.4 GPa, light blue 2 GPa, blue 2.2 GPa, dark blue 3 GPa. The solid red curve is the pure diopside melting curve by Yoder (1952), Boyd and England (1963) and Williams and Kennedy (1969). The dashed green curve is the Vesuvius cpx seed melting curve while the dashed black curve is the rough liquidus of the alkaline basalt used in this study, both estimated by MELTS program (Asimow and Ghiorso 1998; Ghiorso and Sack 1995).*

In this study, we report the results from three different types of experiments: 1) dissolution experiment in a semi-infinite reservoir, 2) dissolution-crystallization experiment in a finite reservoir, and 3) melting experiment. Through experiments 1) and 2), we investigated clinopyroxene dissolution and dissolution-crystallization in an alkali basalt in anhydrous conditions, at the pressure of 0.8 GPa, superliquidus temperatures of 1300 and 1350 °C, and dwell times between 0.5 and 2 h. Through experiment 3), we monitored in real time the cpx melting at 1570 °C and 2 GPa. Data obtained from dissolution experiments were used to quantify crystal dissolution rates and cation diffusion rates in a K-basaltic melt. Cpx dissolution rates from this study were also employed to determine phenocryst residence times and magma chamber dynamics at Campi Flegrei caldera (Campanian region, Italy).

Experimental and analytical methods

Starting material and seed placement

The starting material used in this study (Table 1) is a natural rock powder obtained from a K-basaltic rock (APR16; D'Antonio et al. 1999) found as scoria clast in the deposits of Solchiaro hydromagmatic eruption (between 19±6 ka and 14±3 ka; Morabito et al. 2014) located in Procida island (Campi Flegrei, Italy). It is characterized by 12 vol.% of forsteritic olivine (ol) and diopsidic cpx phenocrysts dispersed in a groundmass of ol, cpx, plagioclase (plg), oxide (ox), alkali feldspar (afs) and glass (D'Antonio et al. 1999; De Astis et al. 2004). The powder, used as starting material in the APR16-D1Ab run, was obtained by grinding the APR16 rock sample in an agate mortar under acetone. The APR16GL, used as starting material in the others runs,

was prepared by melting for 15 min the APR16 natural powder in a 1 atm gas-mixing (CO-CO_2) furnace installed at the Bayerisches Geoinstitut (Bayreuth, Germany) at 1400 °C and oxygen fugacity corresponding to the NNO (nickel-nickel oxide) buffer. The experiments were performed using the "seeding technique" which consisted in placing both the starting material and a cpx seed in an $Au_{75}Pd_{25}$ capsule. We selected, as suitable seeds, natural homogeneous diopsidic cpx crystals (hereafter cpx Ves; Wo_{48}-En_{46}-Fs_6 and Mg# = 0.90, with Mg# = MgO/(MgO+FeO_{tot}) on molar basis by assuming all iron as FeO_{tot}) from the 1944 Vesuvius eruption (Morgan et al. 2004) (Table 1). These crystals were chosen because *i*) they are not in equilibrium with the APR16 melt (Perinelli et al. 2019), thus simulating dissolution mechanisms due to the effect of temperature change and mixing between magmas with different degrees of differentiation, and *ii*) can be easily hand-picked as idiomorphic single crystals and further worked into the desired shape. Thus, cpx crystals were cut and ground in small parallelepiped shapes (~1×1×0.5 mm) and polished. For all the experimental runs performed with the piston cylinder and the Paris-Edinburgh press, we used the same procedure to place the seed, with a set up that does not allow to control convection but guarantees isothermal-isobaric conditions. In particular, we filled the capsule from the bottom to the top with a thin layer of powdered starting material, the cpx seed and a further thicker layer of powdered starting material (Fig. S1 and S2 in Online Resource 1). For each experiment, the cpx seed was oriented placing it with the c-axis parallel to the bottom of the capsule in the APR16-D1Aa and APR16-D1Ab runs, and perpendicular to it in APR16-D1A run, in order to point out possible anisotropies of the cpx–melt interface reaction. The orientation of the

crystals was marked by welding a Pt-wire on the outer wall of capsule. This procedure allowed to recognize possible shifts from the pristine orientation of crystal during the experiment (see § *Analytical methods*). In APR16-D1Ab run, we used a cpx seed with larger dimensions (1.4 x 2.2 x 2.3 mm) than the other ones, reducing the powdered starting material/cpx seed ratio (Table 2). This latter experimental procedure implies a finite geometry system, and the chemical system shifts towards the cpx composition. The increase of the cpx components activity (i.e., chemical components) in the melt phase, due to variable cpx dissolution, holds to an increase of the liquidus temperature of the system (according to the depression of the melting point). Consequently, the system is forced to stay close to the liquidus temperature and small variations of the melt composition, due to the diffusion of dissolved components, can produce local crystallization of cpx whose composition is stable at high temperature (i.e., Mg-rich cpx).

Experimental procedure

Experiments were performed by using the ½ inch end loaded piston cylinder apparatus (PC) at the HP-HT Laboratory of the Department of Earth Sciences of Sapienza - University of Rome (Italy), and the VX-3 Paris–Edinburgh press (PE) at the 16-BM-B beamline at the Advanced Photon Source (Argonne National Laboratory, Illinois). Four anhydrous experiments were carried out with the PC at the isobaric pressure of 0.8 GPa, dwell times between 0.5 and 2 h, and temperatures of 1300 and 1350 °C, corresponding to ΔT of 20 and 70 °C, where ΔT ($T_{experiment}$ - $T_{liquidus}$) is the difference between the nominal temperature of the runs and the APR16 liquidus temperature (Table 2). One of the experiments was failed and

excluded. Temperature conditions were chosen to be *i*) higher than the liquidus temperature of the basalt (i.e., 1280 °C for the APR16 sample at 0.8 GPa, as reported in Perinelli et al. (2019)) to avoid crystallization in the bulk melt that disturbs the diffusion and dissolution processes, and *ii*) lower than the melting temperature of the diopsidic cpx at 0.8 GPa (i.e., 1495 °C for pure diopside, in agreement with Yoder (1952), Boyd and England (1960) and Williams and Kennedy (1969), as well as 1425 °C for the cpx seed according to Ghiorso and Sack (1995)) (Fig. 1). The PC assembly (Fig. S1a in Online Resource 1) consists of an outer CaF_2 cell, graphite furnace and MgO crushable spacer. The two starting materials were dried at 110 °C for at least 2 h to remove the moisture before being loaded in the $Au_{75}Pd_{25}$ capsules. Temperature was measured using a D-type W_3Re_{97}-$W_{25}Re_{75}$ thermocouple and manually controlled within an uncertainty of ±5 °C. Capsules of less 7-mm long were used in order to maintain the samples in the furnace hot spot. The experimental assembly was first pressurized to the target pressure by piston-out procedure (Johannes et al. 1971; Presnall et al. 1978). An overpressure of ~10% was applied with increasing temperature and corrected for pressure drops due to stress relaxation within the assembly during heating. The assembly was heated up to the target temperature with a rate of 150 °C min^{-1}. The sample was maintained at the pressure and temperature for a given duration (nominal duration), and then quenched down by turning off the power. The in-situ experiment was performed using the PE press at 2 GPa, 1570 °C and dwell time of 4 s (Table 2). The PE cell assembly (Fig. S1b in Online Resource 1) mainly consists of boron-epoxy (BE) gaskets, MgO ring, ZrO_2 cap, graphite heater, and BN capsule. Graphite inner capsule was used for silicate melt experiments inside BN sleeve (Kono

et al. 2014). A ring-shaped BE (boron: epoxy = 4:1 in weight ratio) is used as gasket with a supporting outer polycarbonate plastic (Lexan) ring. The BE gasket and ZrO_2 caps in the assembly provide good thermal insulation for high temperature experiments. The MgO ring is placed between BE gasket and graphite heater to increase the stability of the cell assembly and maintain anvil gap. The MgO ring is also used as the pressure standard, according to the thermal equation of state by Kono et al. (2010). The pressure uncertainty is ±0.15 GPa. The loaded cell was first brought to the target pressure by a hydraulic system connected to the Paris-Edinburgh press. After pressurization, the sample was heated rapidly at a rate of ~100 °C s^{-1}. The temperature was estimated using the electrical power vs. temperature calibration curve reported in Kono et al. (2014). The experiment was quenched by shutting down the electrical power to the heater.

Table 2 Experimental run conditions, phase assemblages and clinopyroxene seed features.

Run#	Experimental device	P (GPa)	T (°C)	ΔT (°C)	Time (s)	Phases	Cpx seed size (L x W x Z; mm)	Cpx seed weight (g)	Powder/cpx seed ratio
APR16-D1	PE	2	1570	-	4	Gl	0.60 x 0.40 x 0.31	0.0004	n.d.
APR16-D1A	PC	0.8	1350	70	3600	Gl + cpx* + ol + ox	1.48 x 0.80 x 0.46	0.0008	0.95
APR16-D1Aa	PC	0.8	1350	70	1800	Gl + cpx*	1.10 x 0.93 x 0.34	0.0009	0.96
APR16-D1Ab	PC	0.8	1300	20	7200	Gl + cpx* + cpx	2.32 x 2.19 x 1.43	0.0238	0.59

PE = Paris-Edinburgh press; PC = piston cylinder apparatus; ΔT is difference between the nominal temperature of the runs and the APR16 liquidus temperature; *cpx seed used for the experiments; [y] cpx loss during polishing of the run. Ol and Ox crystallized in APR16-D1A run occur in a small reservoir present in one side of the capsule.

Ultrafast X-ray imaging with the Paris Edinburgh press

For the PE experiment, a white X-ray radiography was used to photomicrograph the interior of the capsule at high pressure. In particular, the melting rate of the cpx seed in the APR16-D1 run was measured by a collimated (1.5x1.5 mm) white X-ray beam and radiographic photomicrographs captured by a high-speed camera (Photron FASTCAM SA3), located approximately 1.2 m downstream from the PE cell, with 250 frame per second (fps) recording time and pixel resolution of 2.5 μm/pixel (Kono et al. 2014). The use of thick (100 μm thick) Ce-doped LAG provides sufficiently high brightness for ultrafast X-ray imaging through the PE cell assembly. Figure S2 in Online Resource 1 is a radiographic photomicrograph showing the initial position of the cpx seed in the middle part of the starting sample, and inside the graphite cap at the top of the capsule. Movie 1 (https://drive.google.com/file/d/16APRp5k5CwZA32TbLzboFLe3hKty2n0S/view?usp=sharing) shows, in real time, the melting of the cpx seed in the APR16 melt at 2 GPa and 1570 °C over a time duration of ~4 s. Since the contrast between clinopyroxene seed and surrounding melt was not much marked, in order to highlight it, we adjusted the contrast/brightness of the collected frames by using the ImageJ software package.

Analytical methods

The recovered samples were mounted in epoxy resin, ground flat, and polished. Textural features of the experimental runs were analyzed by scanning electron microscopy (SEM) using a FEI-quanta 400 equipped for microanalysis with an EDAX Genesis system at the Department of Earth

Sciences of Sapienza - University of Rome and a TESCAN Vega equipped with EDS (energy dispersive X-ray spectrometry) system at the Institute of Petrology and Structural Geology of the Charles University in Prague (Czech Republic). We also analyzed the phase compositions by electron probe micro-analysis (EPMA) using a Cameca SX50 equipped with five-wavelength dispersive spectrometer (WDS) and installed at CNR - Istituto di Geologia Ambientale e Geoingegneria in Rome (Italy). A 15 kV accelerating voltage, 15 nA beam current, and the following standards were used: metals for Mn and Cr, jadeite for Na, wollastonite for Si and Ca, orthoclase for K, corundum for Al, magnetite for Fe, rhodonite for Mn, rutile for Ti, periclase for Mg, apatite for P. Counting times were 20 s for elements and 10 s for backgrounds. Light elements were counted first to prevent loss by alkali migration. Raw data were corrected using the PAP method. We analyzed minerals using a beam diameter of 1 μm, and glasses with a defocused beam from 10 to 15 μm of diameter. For each experiment, multiple compositional profiles were measured by using a Jeol JXA-8530F equipped with five wave dispersive spectrometers (WDS) at the Institute of Petrology and Structural Geology. The operating conditions were 15 kV and 15 nA beam current. Standards were quartz for Si, corundum for Al, periclase for Mg, magnetite for Fe, rhodonite for Mn, calcite for Ca, rutile for Ti, chromium oxide for Cr, albite for Na, apatite for P. Profiles across cracks are re-connected smoothly. First, we made preliminary profiles by measuring points with a distance of 5 μm and a beam diameter of 1 μm. Subsequently, to better define the area at the cpx-melt interface, we made other profiles parallel and close to the first ones using a distance and a beam diameter of 1 μm. Crystallographic orientations of the polished cpx seeds

were obtained by electron backscatter diffraction (EBSD) at the Institute of Petrology and Structural Geology. EBSD patterns were collected with an accelerating voltage of 20 kV, beam current 6 nA, working distance of 33 mm, and tilt angle of 70°. On each seed, 10 points were analyzed, all of which produced a good indexed solution for diopside using AZtec software, with a mean angular deviation <0.5°. Averaged results are shown in Figures 2, 3 and S3 in Online Resource 1 as equal-area upper-hemisphere projections of the crystallographic axes.

Results

Textural and chemical features of the experimental runs

Textural and chemical aspects of the experimental runs are described in the following two sections: "Dissolution and melting experiments" and "Dissolution-crystallization experiment". In the first section we focused on the APR16-D1A, APR16-D1Aa, and APR16-D1 runs. In the second section, instead, we focused on the APR16-D1Ab run, that is characterized by a more complex dissolution-crystallization process. The compositions of minerals and those of glasses far from the residual seed (at distance $x \geq 500$ μm) for all the runs are reported in Table S1 in Online Resource 3. Compositional profiles conducted at the interface ($x = 0$ μm) between cpx seed and glass for the APR16-D1Aa, APR16-D1A, and APR16-D1Ab runs are reported in the Electronic Appendix in Online Resource 4. The compositional profiles show that SiO_2, MgO, and CaO of the glass increase, whereas TiO_2, Al_2O_3, FeO, Na_2O, and K_2O decrease towards the cpx-melt interface. In the far-field melt, instead, the compositional profiles are flat, and no compositional gradients can be observed.

Dissolution and melting experiments

Cpx seed of APR16-D1Aa run (1350 °C; 0.8 GPa; 0.5 h) shows subrounded edges without reaction texture. This suggests that dissolution occurred during the experiment according to Tsuchiyama (1986). One side of the crystal displays some indentations (Fig. S4a in Online Resource 1). Similarly, in APR16-D1A run (1350 °C; 0.8 GPa; 1 h) the cpx seed shows a subrounded shape with indentations on one side, in front of which the formation of ol and ox occurred (Fig. S4b in Online Resource 1), probably linked to the presence of small inclusions in the cpx seed. As regards the APR16-D1 (1570 °C; 2 GPa) experiment, the radiographic Movie 1 (https://drive.google.com/file/d/16APRp5k5CwZA32TbLzboFLe3hKty2n0S/view?usp=sharing) shows the complete melting of cpx seed. Crystal melting starts from the edges and the corners of the seed, leading to a round shape before its complete disappearance.

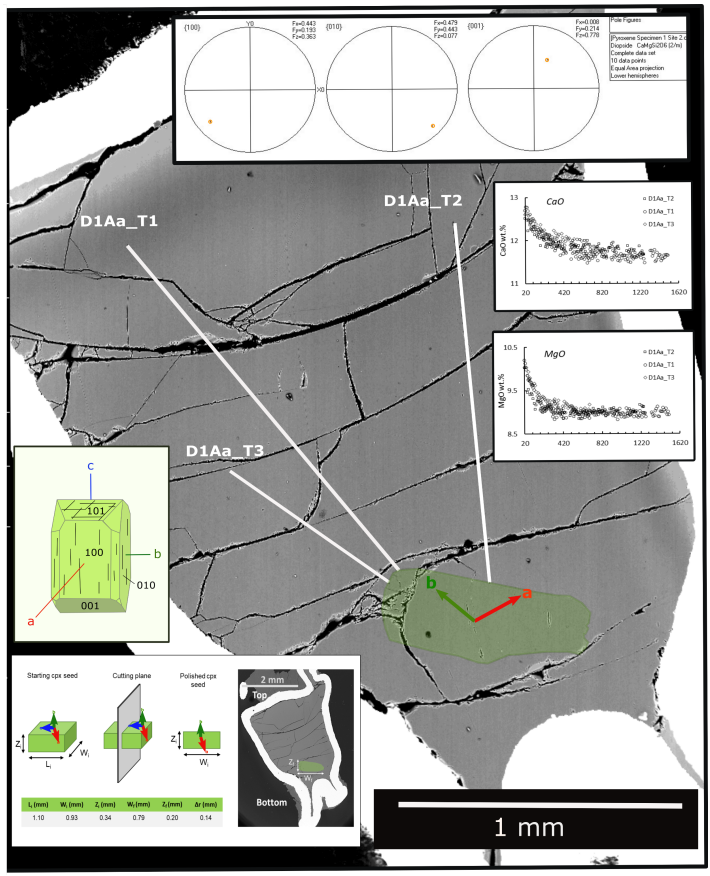

Fig. 2. *Backscattered image of APR16-D1Aa run. Polished cpx seed is indicated in green. Inside the cpx seed the crystallographic axes are reported (a in red, b in green, c in blue) following the orientations showed by the upper-hemisphere projections (inset in the upper side of the figure). As possible to see from these projections the polished surface is approximately perpendicular to the c-axis (001). In the figure the profiles along which we measured the variation of the major elements concentration in the melt are indicated with white lines. An example is reported in the insets on the right, where the concentration profiles of MgO and CaO are shown. Finally, in the lower left part of the figure is reported a cartoon showing the sizes, the placement, and the orientation of the seed before and after the experiment. The table reports the initial (i) sizes, the final (f) sizes and the difference between them (Δr). Cartoon not in scale.*

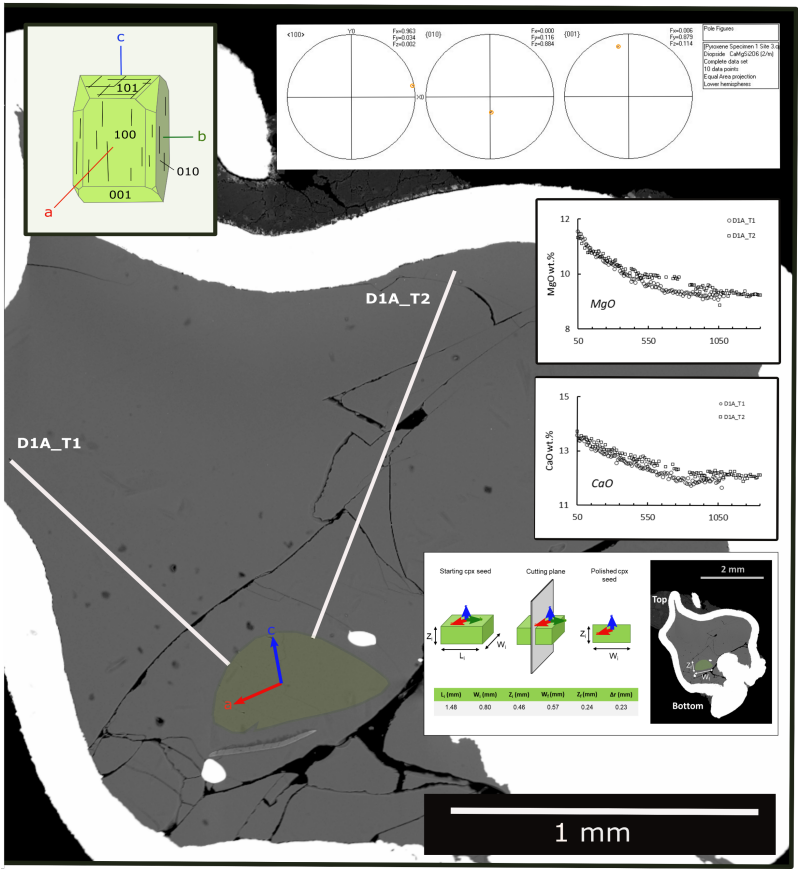

Fig. 3. *Backscattered image of APR16-D1A run. Polished cpx seed is indicated in green. Inside the cpx seed the crystallographic axes are reported (a in red, b in green, c in blue) following the orientations showed by the upper-hemisphere projections (inset in the upper side of the figure). As possible to see from these projections the polished surface is approximately perpendicular to the b-axis (010). In the figure the profiles along which we measured the variation of the major elements concentration in the melt are indicated with white lines. An example is reported in the insets on the right, where the concentration profiles of MgO and CaO are shown. Finally, in the lower left part of the figure is reported a cartoon showing the sizes, the placement, and the orientation of the seed before and after the experiment. The table reports the initial (i) sizes, the final (f) sizes and the difference between them (Δr). Cartoon not in scale.*

The composition of the residual cpx seed in APR16-D1Aa run (1350 °C; 0.5 h) does not differ significantly from the original one (Fig. 4). Conversely, the residual cpx seed in the APR16-D1A run (1350 °C; 1 h) shows higher Mg# (0.91) and lower TiO_2 (0.29 wt.%), Al_2O_3 (1.43 wt.%), and Cr_2O_3 (0.22 wt.%) than the original cpx Ves (Table 1 and Table S1 in Online Resource 3).

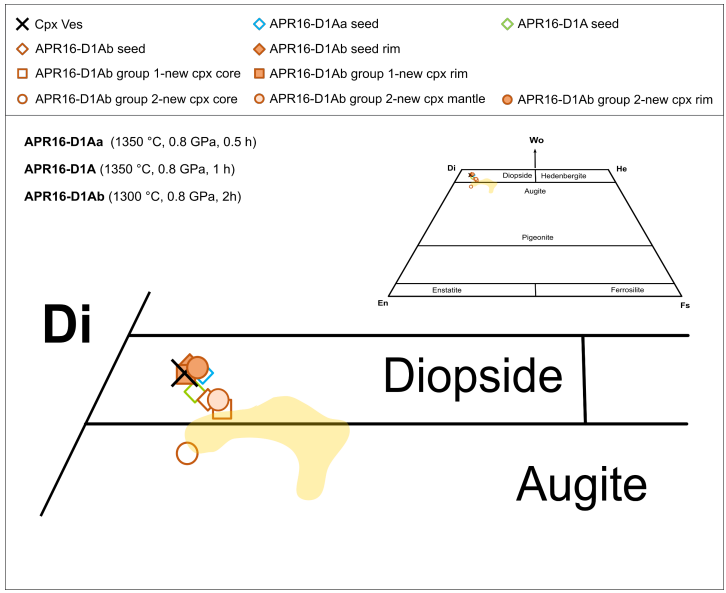

Fig. 4 *Clinopyroxene compositions plotted into a magnification of the pyroxene classification diagram (Morimoto et al. 1998). Wo: wollastonite; En: enstatite; Fe: ferrosilite; Di: diopside, He: hedenbergite. The inset shows the whole diagram. Cross indicates the Vesuvius cpx, diamonds the cpx seeds, squares the group 1-new cpx and circles the group 2-new cpx. Empty symbols indicate cpx core, while filled symbols indicate cpx rim. For group-2-new cpx the lighter filled symbols indicate the mantle while the darker filled symbols the rim. New cpx unzoned of D1Ab run is not reported since its composition matches that of the cpx seed rim. Yellow field shows cpx composition from Bonechi et al. (2020b).*

Concerning the experimental glasses, those analyzed far from the residual seed of APR16-D1A and APR16-D1Aa runs have major oxide concentrations similar to those of the starting material (APR16GL; Fig. 5), while the composition of APR16-D1 glass exhibits higher Mg# (0.73) and CaO abundances (12.9 wt.%) reflecting the complete melting of the cpx seed in the melt (Movie 1 in https://drive.google.com/file/d/16APRp5k5CwZA32TbLzboFLe3hKty2n0S/view?usp=sharing).

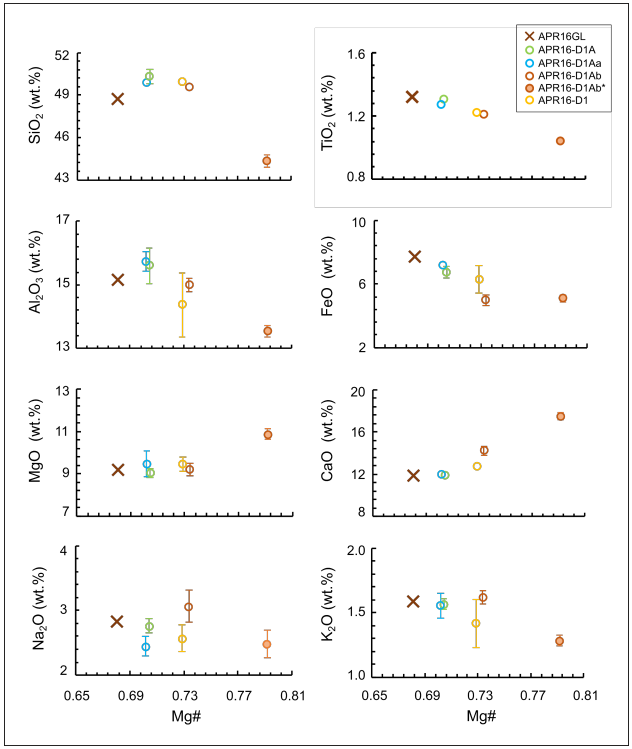

Fig. 5 *Variation diagrams of major element with Mg# for residual glasses far from the residual cpx seeds. Cross indicates the starting material (SM) and circles the compositions of synthetic glasses. Error bars not reported are within the symbols size.*

The Fe–Mg exchange between cpx and melt ($K_D(Fe\text{-}Mg)^{cpx\text{-}liq}$ = $Fe_{cpx} \times Mg_{liq}/Mg_{cpx} \times Fe_{liq}$, calculated assuming all Fe as Fe^{2+} in both phases) for APR16-D1Aa and APR16-D1A runs is 0.26±0.01 and 0.24±0.01, respectively. These values indicate that cpx seeds are in equilibrium with the coexisting melt according to the equilibrium criteria ($K_D(Fe\text{-}Mg)^{cpx\text{-}liq}$ = 0.28±0.08) proposed by Putirka (2008). Finally, in the APR16-D1A experiment, ol and ox crystallize during cpx dissolution. Ol is characterized by a homogeneous composition (Fo_{93}). Conversely, Ox is compositionally zoned, with core enriched in Fe_2O_3 and MgO relative to the magnesioferritic rim. The Fe–Mg distribution coefficient between ol and melt ($K_D(Fe\text{-}Mg)^{ol\text{-}liq}$ = $Fe_{ol} \times Mg_{liq}/Mg_{ol} \times Fe_{liq}$, calculated assuming all Fe as Fe^{2+} in both phases) is 0.17±0.03, thereby in disequilibrium with the melt according to the criteria ($K_D(Fe\text{-}Mg)^{ol\text{-}liq}$ = 0.30±0.03) proposed by Roeder and Emslie (1970) and Putirka (2008).

Dissolution-crystallization experiment

The APR16-D1Ab run (1300 °C; 0.8 GPa; 2 h) exhibits textural features resulting from dissolution-crystallization processes. In particular, the large cpx seed displays smoothed edges on which a 10-50 μm-thick layer (i.e., cpx seed rim) overgrew (Fig. 6a, b, d). Notably, a precipitation layer with cellular texture overgrew on the cpx seed rim along the lateral faces of the residual crystal (Fig. 6d). Moreover, new euhedral cpx crystals with size up to 200 μm formed towards the top of the capsule adjacent to the overgrown rim (Fig. 6a, c). Some of these new cpx, are zoned and, depending on the crystal size and zoning pattern, can be divided in two groups: group 1-new cpx are characterized by large crystals (~100 μm in size; Fig. 6a) formed by euhedral

layer grown on anhedral cores (up to 30 μm in size), that probably represent restitic of natural starting material. Group 2-new cpx are characterized by small newly-growing cpx crystals (~20 μm in size; Fig. 6c) showing concentric oscillatory zoning with euhedral shape.

The overgrown rim is a diopside ($Wo_{49}En_{48}Fs_3$; Fig. 4) as for the residual seed, but with higher Mg# (0.93 vs. 0.89) and Al_2O_3 (4.88 wt.% vs. 1.53 wt.%) and lower SiO_2 (51.16 wt.% vs. 53.12 wt.%) contents. In the new zoned cpx crystals both cores and rims are still classified as diopside (Wo_{46}-En_{47}-Fs_7 and Wo_{48}-En_{48}-Fs_4, respectively; Fig. 4) but their compositions are distinct from that of the residual seed. In particular, the cores of the group 1-new cpx have Mg# (0.88), SiO_2 (49.48 wt.%), and CaO (21.15 wt.%) lower than those of the rims (0.92, 51.21 wt.%, 23.13 wt.%, respectively) (Table S1 in Online Resource 3). Moreover, the crystal cores are enriched in TiO_2, Al_2O_3, FeO, Na_2O, and Cr_2O_3 (Table S1 in Online Resource 3). The group 2-new cpx are characterized by different oxide contents in relationship with the concentric oscillatory zonations (Fig. 6 and Table S1 in Online Resource 3). Their core composition falls in the augite field (Morimoto et al. 1988; Fig. 4) next to the boundary with diopside, while the mantle and the outer parts are both diopside. The gradual increase of CaO (from 20.6 to 22.6 wt. %) towards the crystal rim is counterbalanced by the decrease of FeO (from 3.7 to 2.6 wt.%). MgO clearly decreases from the core to the mantle (from ~17 to 15.5 wt.%) and then shows a limited change (MgO = ~16 wt.%) in the outermost portion (~10 mm far) of the grains, while the mantles of these new cpx are enriched in Al_2O_3, TiO_2, Na_2O_3, and Cr_2O_3 (Table S1 in Online Resource 3). Notably, the chemistry of the mantle of the group 2-new cpx and that of the cores of the group1-new cpx (i.e., restitic cpx phenocrysts of the APR16-starting

material) compare well with the composition of the cpx crystallized at 0.8 GPa in equilibrium with the APR16 residual melt, as reported in Bonechi et al. (2020b) (Fig. 4; Table S1 in Online Resource 3). Finally, the composition of the large unzoned new cpx is diopsidic ($Wo_{49}En_{47}Fs_4$; Fig. 4) and closely approaches that of the cpx seed rim and those of the crystal rims from group 1- and group 2-new cpx (Table S1 in Online Resource 3).

The chemical composition of the glass in this run is heterogeneous showing marked differences between the portion near the top of the capsule (hereafter identified as APR16-D1Ab) and that in the new-cpx zone (i.e., APR16-D1Ab*). Figure 5 shows that the composition of APR16-D1Ab glass is in the trend outlined by the glasses of the dissolution experiments. Conversely, the APR16-D1Ab* glass shows lower SiO_2 (~46 wt.%), TiO_2 (~1 wt.%) and Al_2O_3 (~14 wt.%), as well as higher Mg# (0.79) and CaO (~18 wt.%) than those of the APR16-D1Ab glass (~50 wt.%, ~1.2 wt.%, 0.77, ~14 wt.%, respectively). Both glass compositions were used to calculate $K_D(Fe\text{-}Mg)^{cpx\text{-}liq}$ in order to identify the possible equilibrium condition among the different types of cpx crystallized during this experiment. Using the APR16-D1Ab glass, the obtained values are: 0.38±0.02 for the cpx seed, 0.25±0.01 for the cpx seed rim and for the unzoned, new cpx, 0.49±0.03 for the group 1-new cpx core, 0.28±0.01 for the group 1-new cpx rim, 0.40±0.02 for the group 2-new cpx core, 0.44±0.02 for the group 2-new cpx mantle, and 0.31±0.01 for the group 2-new cpx rim. Using the APR16-D1Ab* glass, the obtained values are: 0.44±0.03 for the cpx seed, 0.29±0.01 for the cpx seed rim and for the unzoned, new cpx, 0.56±0.04 for the group 1-new cpx core, 0.33±0.01 for the group 1-new cpx rim, 0.46±0.02 for the group 2-new cpx core, 0.51±0.03 for the group 2-new cpx mantle, and 0.35±0.01 for the group 2-new cpx rim.

According to the equilibrium range of Putirka (2008), the cpx seed and the new cpx cores are in disequilibrium with both APR16-D1Ab and APR16-D1Ab* melts, whereas the cpx seed rim, the unzoned, new cpx, group 1- and group 2-new cpx rims are in equilibrium with APR16-D1Ab* composition.

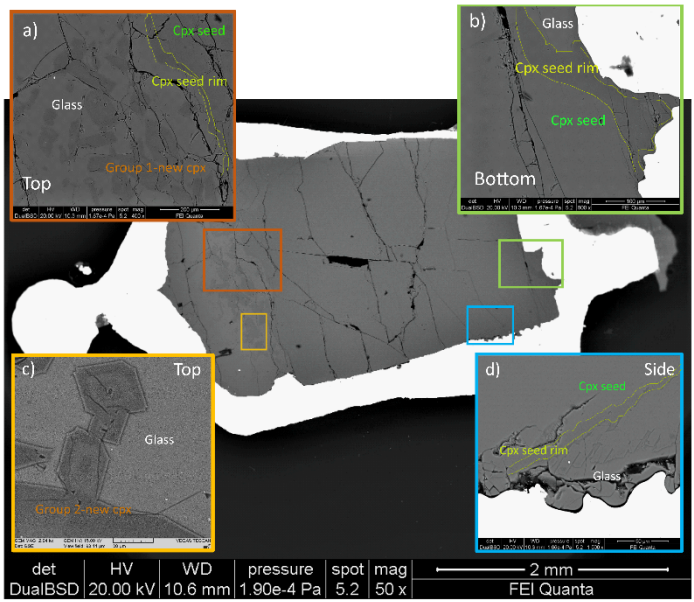

Fig. 6 *Backscattered photomicrographs of the APR16-D1Ab run. Insights show a-c) the top, b) the bottom and d) the side of the capsule. Cpx, clinopyroxene, Rim, reaction rim between cpx seed and glass.*

Dissolution rates

Dissolution rates have been calculated by the difference between initial and final length of cpx seed before and after the experiment (Δr) divided by the time duration of experimental run (e.g., Chen and Zhang 2009). Data reported in Table 3 are $7.9 \cdot 10^{-6}$ cm s^{-1} for APR16-D1Aa (1350 °C; 0.8 GPa; 0.5 h) and $6.1 \cdot 10^{-6}$ cm s^{-1} for APR16-D1A (1350 °C; 0.8 GPa; 1 h).

For the APR16-D1Ab run (1300 °C; 0.8 GPa; 2 h), it was not possible to directly calculate the dissolution rate due to the effect of crystallization during the experiment. These dissolution rates are consistent with those (from 10^{-5} to 10^{-7} cm s^{-1}) obtained by previous authors (e.g., Brearley and Scarfe 1986; Zhang et al. 1989; Van Orman and Grove 2000; Chen and Zhang 2009) at temperatures (1236-1500 °C), ΔT (5-125 °C), pressures (0.47-3 GPa) and dwell time (0.14-2.6 h) comparable with those employed in our experiments (Table S2 in Online Resource 3).

Melting rate

Radiographic photomicrographs collected during the APR16-D1 run (1570 °C; 2 GPa) made possible to estimate the time taken by the cpx seed to melt and the process through which it occurred. In particular, by processing the collected frames, we evaluated the change of the cpx dimensions as a function of time. Figure 7 shows that the crystal size decreases with increasing time, following a non-linear trend characterized by apparent slope increase at around 2.5 s, after which crystal dissolution proceeds until the complete disappearance of cpx crystal. Due to this different behavior, we calculated average melting rates of $4.8 \cdot 10^{-2}$ cm s^{-1} up to 2.5 s and $3.2 \cdot 10^{-1}$ cm s^{-1} after 2.5 s. These calculated melting rates result to be about three

orders of magnitude higher than that ($6.5 \cdot 10^{-5}$ cm s^{-1}) estimated by Tsuchiyama (1986) in quench experiments conducted at 1 atm, 1190-1307 °C, and 1.5-192 h of dwell time, during gabbroic-xenolith digestion by basaltic melts.

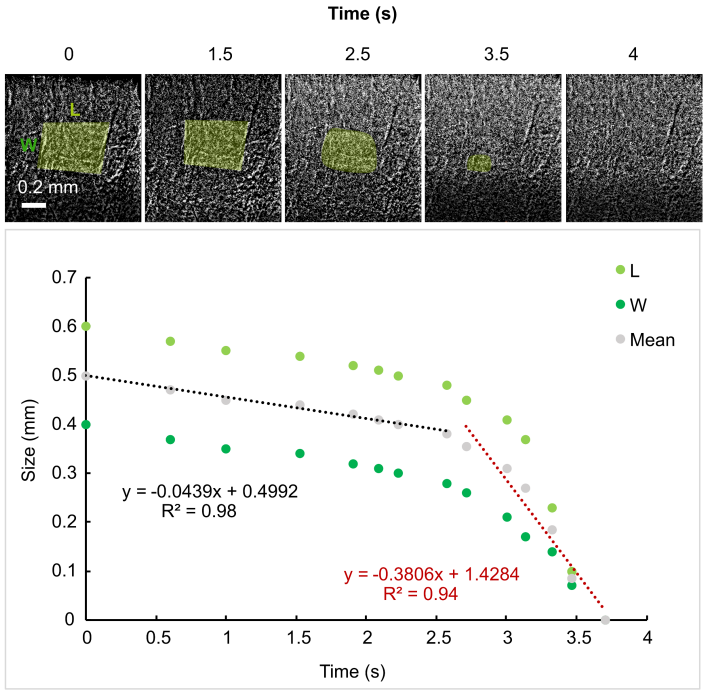

Fig. 7 *X-ray radiography frames of melting cpx seed (in green) in APR16GL melt at 2 GPa and 1570 °C. Scale bar 0.2 mm. The diagram reports the variation of the crystal sizes L (light green circles), W (dark green circles) and their mean value (M; grey circles) with time for each frame (0.5 s interval).*

Discussion

Photomicrographs of experimental runs show that cpx dissolution occurs by consumption of crystalline faces with the formation of subrounded shapes and/or indentations (Fig. S4 in Online Resource 1). Radiographic movie from APR16-D1 run documents that the melting process develops by symmetric consumption of the crystalline faces. According to our experimental data, textural changes typical of patchy, sieve or spongy cpx phenocrysts that often characterize natural magmatic environments, may be the result not only of mineral dissolution or melting but also of overgrowth processes (Tsuchiyama 1986; Perinelli et al. 2008), as observed for example in natural plagioclase phenocrysts (e.g., Viccaro et al. 2010; Fornaciai et al. 2015). In the following paragraphs, melting, dissolution, and dissolution-crystallization mechanisms are examined and discussed.

Melting experiment

Although experimental temperature (1570 °C) and pressure (2 GPa) of APR16-D1 run are not representative of magmatic conditions, we note that this technique offers the possibility to monitor in real time the kinetics of crystal dissolution. More specifically, the non-linearity of melting process is characterized by a faster crystal melting with increasing time, as shown in Figure 7. This acceleration seems to be strictly related to the disappearance of the crystal euhedrality, with development of a sub-rounded morphology after 2.5 s. As the cpx volume decreases, the specific crystal surface in contact with the melt increases, thus reducing the energetic barrier of melting. As observed by Liang et al. (2002) for nanocrystals, the surface/volume ratio increases with decreasing crystal size. Consequently,

the potential energy of surface atoms increases due to bond losing and the internal energy of crystal increases. In this scenario, the melting enthalpy and melting temperature depression as a function of crystal size is essentially induced by the surface contribution related to the large surface/volume ratio and breaking bonds (Liang et al., 2002).

Dissolution experiments

Evidence of convection-free dissolution

Although the experimental set up used in this study is not able to control convection, such as those presented in previous works (Zhang et al. 1989; Chen and Zhang 2008, 2009), we can evaluate the absence of convection by employing different approaches. According to Yu et al. (2016), we have performed four analytical traverses across distinct portions of the cpx seed-melt interface. These analytical traverses closely overlap attesting the absence of convection (Fig. S5 in Online Resource 1). Moreover, as observed by Zhang et al. (1989), in absence of convection the dissolution rate is inversely proportional to the square root of time. At the same *P-T* conditions, we note that the measured dissolution rates are inversely correlated with the square root of time (Fig. 8a), whereas the dissolution distances (Δr) are proportional to the square root of time (Fig. 8b), in agreement with a diffusion-controlled dissolution (Zhang et al. 1989). When controlled by diffusion, Δr is a function of $\sqrt{t}$, as also mentioned in Eq. 3 of this study. Therefore, the dissolution rate calculated via $\Delta r/t$ results to be purely empirical and dependent on experiment duration. In a perfectly executed time-series of experiments, for instance, an experiment with twice the duration of the other would give a dissolution rate 50% lower (Fig. 8a).

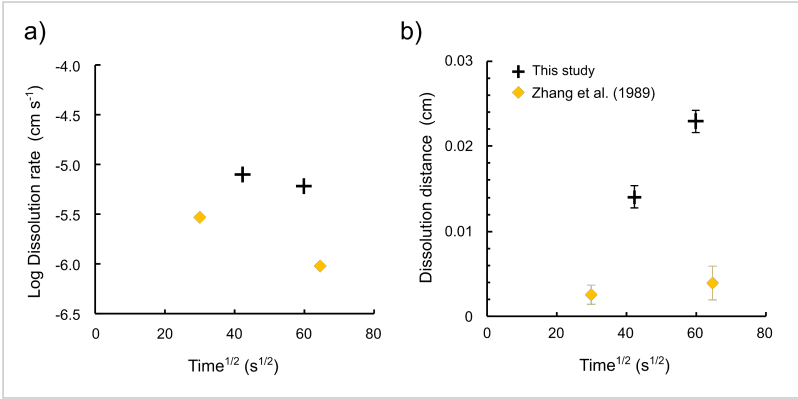

Fig.8 *Diagrams showing the absence of convection in the runs of this study: dissolution distance (a) and Log dissolution rate (b) vs square root of time. Black plus indicates the runs of this study while yellow diamond those of Zhang et al. (1989).*

Influence of temperature and pressure on cpx dissolution

Cpx dissolution rates from this study are comparatively combined with those from previous works (Brearley and Scarfe 1986; Zhang et al. 1989; Van Orman and Grove 2000; Chen and Zhang 2009) and plotted in Fig. 9 as function of ΔT (a) and temperature (b). As already demonstrated by previous authors (Brearley and Scarfe 1986; Zhang et al. 1989; Van Orman and Grove 2000; Chen and Zhang 2009), T and ΔT exercise a major control on cpx dissolution, according to their influence on diffusivity of chemical species in the melt phase. In particular, the dissolution rate increases with increasing both ΔT (Fig. 9a) and T (Fig. 9b). The dissolution rate can be also modelled by integrating data from this study with those of Chen and Zhang (2009) and Zhang et al. (1989):

$$\text{Log Diss. rate} = 0.014 \cdot \Delta T - 6.349 \quad (1),$$

$$\text{Log Diss. rate} = 0.009 \cdot T - 17.916 \quad (2).$$

For comparable values of T and ΔT, we also note that pressure does not show any apparent influence on the dissolution rate at $P < 2$ GPa. Conversely, at $P > 2$ GPa, the dissolution rate increases with increasing pressure.

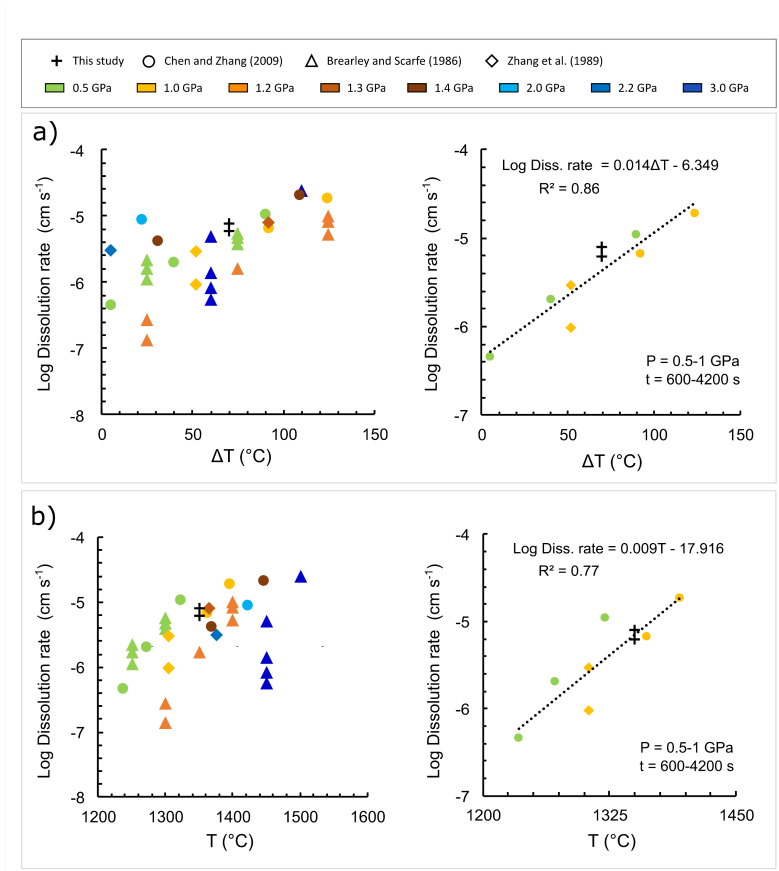

Fig. 9 *Dissolution rate diagrams as function of a) ΔT (°C) and b) temperature (°C). Data from previous studies:Brearley and Scarfe (1986), Zhang et al. (1989), Van Orman and Grove (2000), Chen and Zhang (2009). Pressure values of the reported experiments are between 0.5 and 3 GPa while time values vary between 500 and 7200 s. In the diagrams on the right are reported only data with similar P conditions (0.5-1 GPa) and diffusive dissolution. Symbols are as in Figure 1. Error bars fall inside the symbols.*

Chemical diffusion

The knowledge of chemical diffusion coefficients is extremely important to correctly constrain the time scale of magma dynamics (Cherniak and Dimanov 2010). The composition of cpx is highly sensitive to *P-T* and melt composition feeding the crystal growth (Perinelli et al. 2016, 2018; Mollo et al. 2018) as well as the diffusion of chemical species in its crystal lattice (Petrone et al. 2016). Diffusion coefficient (*D*) in silicate melts is controlled by several parameters, such as temperature, pressure, melt-water content, bulk chemical composition, and oxygen fugacity (Zhang et al. 2010).

In this context, we have calculated the effective binary diffusion coefficients of some major elements in the melt from APR16-D1A and APR16-D1Aa runs (Table 4), by employing the one-dimensional diffusive dissolution equation (Crank 1975; Zhang et al. 1989; Chen and Zhang 2009):

$$C = C_\infty + (C_0 - C_\infty)\frac{erfc\left(\frac{x}{2\sqrt{Dt}} - \alpha\right)}{erfc(-\alpha)} \quad (3)$$

C is the variable concentration of the oxide in the diffusive melt, C_0 is the concentration of the oxide at the crystal–melt interface, C_∞ is the constant concentration of the oxide in the far-field melt, x is the distance from the crystal–melt interface, t is the dwell time, and α is a parameter calculated as:

$$exp(\alpha^2)erfc(-\alpha)\sqrt{\pi}\alpha = \frac{C_0 - C_\infty}{C_C - C_0} \quad (4)$$

C_C is the concentration of the oxide in the crystal. Following the study of Chen and Zhang (2009), we have also derived the cpx dissolution distance (Δr_1) as:

$$\Delta r_1 = 2\alpha \frac{\rho_m}{\rho_c} \sqrt{Dt} \quad (5),$$

where ρ_m (2.8 g·cm^{-3}; Sakamaki et al. 2013) and ρ_c (3.2 g·cm^{-3}; Thompson et al. 2005) are the density of the melt and crystal, respectively. D and α obtained by Eqns. (3) and (4) were substituted into Eqn. (5), in order to compare the calculated Δr_1 with the measured Δr (Table 3). This calculation is independent of direct measurements and provides cross-check to experimental diffusion profiles. The fitted profiles of SiO_2, TiO_2, Al_2O_3, MgO, CaO, Na_2O, and K_2O from APR16-D1A and APR16-D1Aa runs are reported in the Electronic Appendix. According to Zhang et al. (1989) and Chen and Zhang (2008, 2009), we observe a bent profile very close to the cpx-melt interface that can be attributed to the overgrowth of tiny cpx crystals on the pre-existing crystalline surface at the time of quench (Fig. 10). The bent part of the profile is indeed consistent with cryptic overgrowth of cpx, as the interface melt becomes supersaturated with newly-formed cpx crystals during quench (Yu et al. 2016). The composition of this melt layer near the interface (~1 μm or less) is not part of the normal concentration profile derived during crystal dissolution. For this motivation, the bent part of the profile near the interface (~6 μm in length) was not considered in our calculations (cf. Zhang et al. 1989; Chen and Zhang 2008, 2009). We focused only on Ca and Mg diffusivity, as these cations are much more compatible with cpx than Mn, P, Al, Ti, Na, and K. Moreover, the concentrations of MnO and P_2O_5 are extremely low, scattered and not clearly quantifiable. FeO chemical profiles are also affected by apparent uphill diffusion which can be treated by a specific diffusion matrix approach (Zhang 1993) beyond the scope of this study.

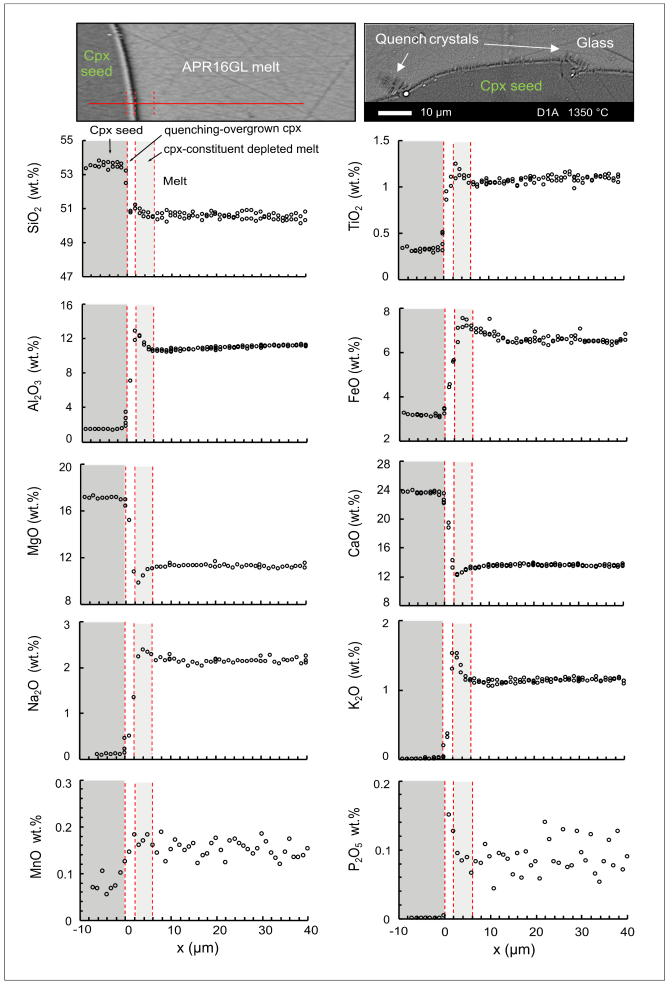

Fig.10 *Backscattered photomicrographs of the experimental run APR16-D1A and analysis across the cpx–melt interface. BSE photomicrographs shows the cpx-melt interface (on the left) and quench crystals occurring close to the cpx edge (on the right). From the cpx seed into the basaltic melt (from left to right), four units can be recognized: the original cpx seed (gray), the quenching-overgrown cpx (narrow bright area), the cpx-constituent depleted melt due to quench growth (narrow darker area), and basaltic melt with the normal diffusion profile. Cpx seed-melt interface is at x = 0 µm. Cpx analyses were controlled to test their correct stoichiometry and the analyses including both cpx and melt were discarded.*

Effective binary diffusion coefficients of Mg and Ca

Since diffusion is a thermally-activated process, temperature is the most critical parameter controlling the chemical diffusivity of cations in minerals and melts (e.g., Zhang et al. 2010b; Petrone et al. 2016). The effect of pressure is appreciable only when it changes on the order of several GPa or causes changes in crystal symmetry and order-disorder cation redistributions (Dimanov and Wiedenbeck 2006). Chemical diffusion is also a time-independent process due to fast development of interface reactions within 0.0002-0.2 s (Zhang et al. 1989). Figure 11a-d shows the influence of pressure and temperature on D_{MgO} and D_{CaO} for either the K-basalt object of this study or other melt compositions from literature (Brearley and Scarfe 1986; Zhang et al. 1989; Chen and Zhang 2009). Pressure does not show any trend (Fig. 11a-b), suggesting no effect on cation diffusion due to melt/cpx volume changes. Conversely, D_{MgO} and D_{CaO} are positively correlated with temperature (Fig. 11c-d). A such temperature dependency is the expression of an Arrhenian relation $D = D_0 \exp(-E/RT)$, where D_0 is a constant and E is the activation energy of diffusion, R is the gas constant and T is the absolute temperature. Figure 11e-f shows the Arrhenius plots of D_{MgO} and D_{CaO} from this study compared with diffusion coefficients from previous works (Zhang et al., 1989; Kress and Ghiorso 1995; LaTourrette et al. 1996; Morgan et al. 2006; Chen and Zhang 2009). Since the concentration of SiO_2 in the melt phase strongly controls the diffusivity of cations (e.g., Cheng and Zhang 2009), we have compared diffusion coefficients from experiments conducted on a restricted melt compositional range of 41-57 wt.% SiO_2.

D_{MgO} and D_{CaO} from APR16-D1A run are similar to those estimated by Chen and Zhang (2009), while those from APR16-D1Aa run are characterized by

lower values similar to diffusion coefficients by Zhang et al. (1989). However, as previously mentioned, while low *D* values from Zhang et al. (1989) can be explained by the high SiO_2 concentration of the melt, this is not valid for our experiments conducted on the same k-basaltic composition. Therefore, since both APR16-D1Aa and APR16-D1A runs were performed at the same conditions, their different D_{MgO} and D_{CaO} values can be ascribed to the different orientation of the cpx seed (Fig. 2 and 3). In particular, the polished surface of the cpx seed of APR16-D1Aa run (Fig. 2) results to be approximately perpendicular to the c-axis, while that of the cpx seed of APR16-D1A run (Fig. 3) is approximately parallel to c-axis. Bearing in mind the directions of the crystallographic axes in diopside, cpx seed dissolution in APR16-D1Aa run occurred approximately parallel to the b-axis (010), corresponding to the consumption of the prism faces. Conversely, the cpx seed dissolution in APR16-D1A run occurred approximately parallel to the c-axis (001), with the consequent consumption of the pinacoid faces. In other words, CaO and MgO diffusion at *D*//c was faster than that at *D*//b, in agreement with the anisotropic diffusion of ^{44}Ca and ^{26}Mg observed in natural diopside (Cherniak and Dimanov 2010, and reference therein).

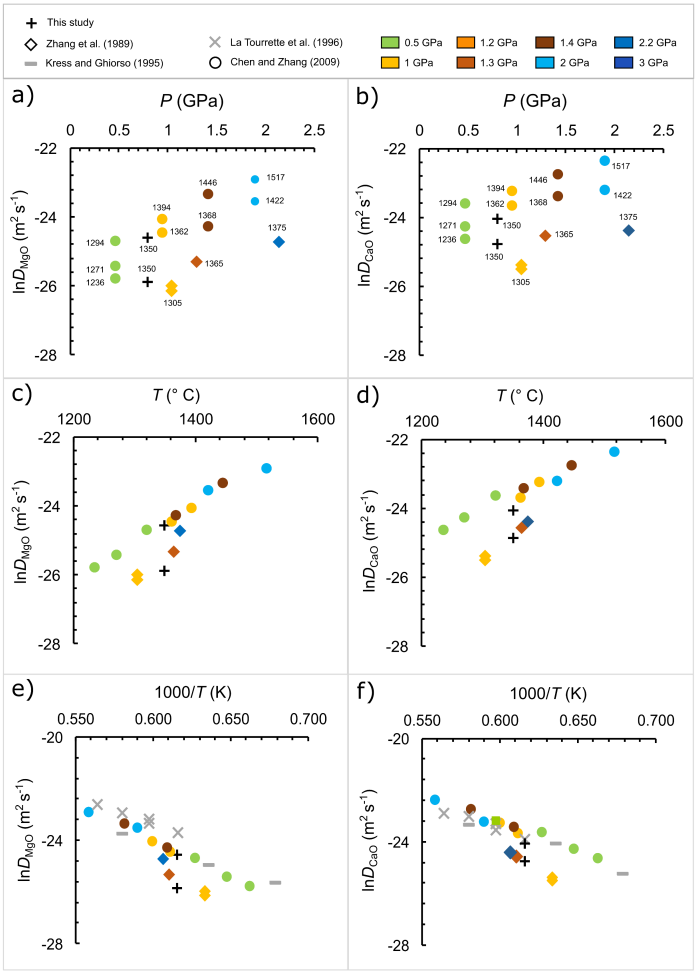

Fig.11 *lnD_{MgO} and lnD_{CaO} vs a-b) pressure, c-d) temperature and e-f) reciprocal absolute temperature diagrams. Literature data from (Kress and Ghiorso 1995; Zhang et al. 1989; LaTourrette et al., 1996;Chen and Zhang 2009). Symbols are as in Figure 1. Error bars fall inside the symbols. Numbers reported near the symbols indicate temperature values in °C.*

Dissolution-crystallization experiment

APR16-D1Ab run is characterized by a dissolution-crystallization process due to a low APR16-powder/cpx seed ratio (Table 2). As a consequence, $T_{liquidus}$ of the bulk composition (APR16+cpx Ves) increases to 1384 °C (ΔT = -84 °C), as estimated by Rhyolite-MELTS software (Asimow and Ghiorso 1998; Gualda et al. 2012). Indeed, $T_{liquidus}$ is lower for experiments at higher APR16-powder/cpx seed ratios (i.e., 1314-1316 °C, $\Delta T \approx$ -15 °C on average; Table S3 in Online Resource 3). Textural and compositional data indicate that the crystallization process is preceded by a dissolution process (Fig. 6). Figure 12 and Table 5 show a step-by-step schematic model which reconstructs the process of early seed dissolution and late formation of new cpx crystals. At the beginning of the experiment (t_0), the system is formed by the cpx Ves and the APR16 starting material which contains some restitic natural phenocrysts. At t_1, the dissolution is triggered by the destabilization of the cpx seed whose chemistry is in disequilibrium with that of K-basalt at 0.8 GPa (Perinelli et al. 2019). During cpx Ves dissolution, the diffusion of cations in the melt does not substantially change the far-field melt composition of APR16, from which new cpx crystal portions (i.e., the core and mantle of group 2-new cpx; Fig. 12) start to crystallize. Notably, both core and mantle of group 2-new cpx are in local equilibrium with APR16 melt as testified by the $K_D(Fe\text{-}Mg)^{cpx\text{-}liq}$ values (~0.25 for the core and ~0.27 for the mantle; Fig. S6 in Online Resource 1). At t_2, the diffusion of cations in the melt becomes more effective and the composition of APR16 melt progressively changes. Accordingly, the chemistry of newly-formed cpx crystals also changes, leading to the formation of a further type of cpx, either as single crystals (unzoned new cpx) or overgrowth rims (cpx seed rim,

group 1-new cpx and group 2-new cpx rims; Fig. 12). At t_3 (corresponding to the end of the experiment), the bulk system is composed of 1) partially resorbed cpx Ves characterized by a seed rim, 2) new cpx crystals both oscillatory and inversely zoned, 3) unzoned new cpx crystals (Fig. 6), and 4) the inhomogeneous glass. The Mg# value of glass increases from 0.68 (APR16-Mg# value at t_0) to 0.79 near to the residual cpx Ves or to 0.77 at ~500 μm far from it (Table S1 in Online Resource 3). The glass results in equilibrium with the cpx seed rim and the new cpx rims ($K_D(\text{Fe-Mg})^{cpx\text{-}liq}$ = 0.29-0.35; Fig. S6 and Table S1 in Online Resource 1 and 3, respectively). The effective time lapse during which the dissolution operates (t_1 step, see above) is unknown. However, a rough time estimation can be provided by using literature data on mineral dissolution rates determined at ΔT between 20 and 40 °C (Fig. 9), and comparable to ΔT = 20 °C of APR16-D1Ab run. At these conditions, the dissolution rate covers a range of values of three orders of magnitude ($2.5 \cdot 10^{-5}$ and $1.4 \cdot 10^{-7}$ cm s^{-1}; Fig. 9), and the time required to dissolve ~0.02 cm of cpx Ves (Fig. 12 and Table 3) varies from ~0.5 to ~1.4 h using dissolution rates (i.e., $1 \cdot 10^{-5}$ and $4 \cdot 10^{-6}$ cm s^{-1}) compatible with the experimental dwell time (i.e., 2 h; Table 2). Therefore, the crystallization of the seed and new cpx rims and unzoned new cpx crystals occurred in a maximum time of 1.44 h with a growth rate of ~$1.35 \cdot 10^{-6}$ cm s^{-1}. Noteworthy, this value is lower than those experimentally determined by Bonechi et al. (2020b) at the same pressure conditions and using APR16GL composition as starting material (e.g., ~10^{-7}-10^{-8} cm s^{-1} for dwell time in the range of 0.25-9 h). Conversely, it is comparable with the cpx growth rates (~$1 \cdot 10^{-6}$ cm s^{-1}) obtained from kinetic experiments performed at high cooling rates (i.e., ≥ 80 °C min^{-1}; Burkhard 2002; Pontesilli et al. 2019) and high degrees of

undercooling (i.e., the difference between the phase-in temperature of the melt and the quench temperature $\Delta T^* \geq 80$ °C; Burkard 2002; Pontesilli et al. 2019). This latter correspondence can be related to the compositional change of the APR16 melt caused by the dissolution of cpx Ves. The liquidus temperature of the melt increases from 1280 °C for APR16 to 1332 °C for APR16-D1Ab* (Table S3 in Online Resource 3). However, the limited variation of T_{liquidus} indicates low-to-moderate undercooling conditions during steps t_2 and t_3 (maximum ΔT^* = 52 °C), with maintenance of low degrees of cpx supersaturation in the melt and high cation mobilities (Hammer, 2008 and reference therein). Despite high crystal growth rates are more commonly associated with high degrees of undercooling and development of anhedral to dendritic/skeletal crystal morphologies (e.g., Cashman 1993; Conte et al. 2006; Hammer 2008), these conditions were suitable for the formation of euhedral, unzoned new cpx (up to ~200 mm in size) in chemical equilibrium with the APR16-D1Ab* melt (Fig. 12).

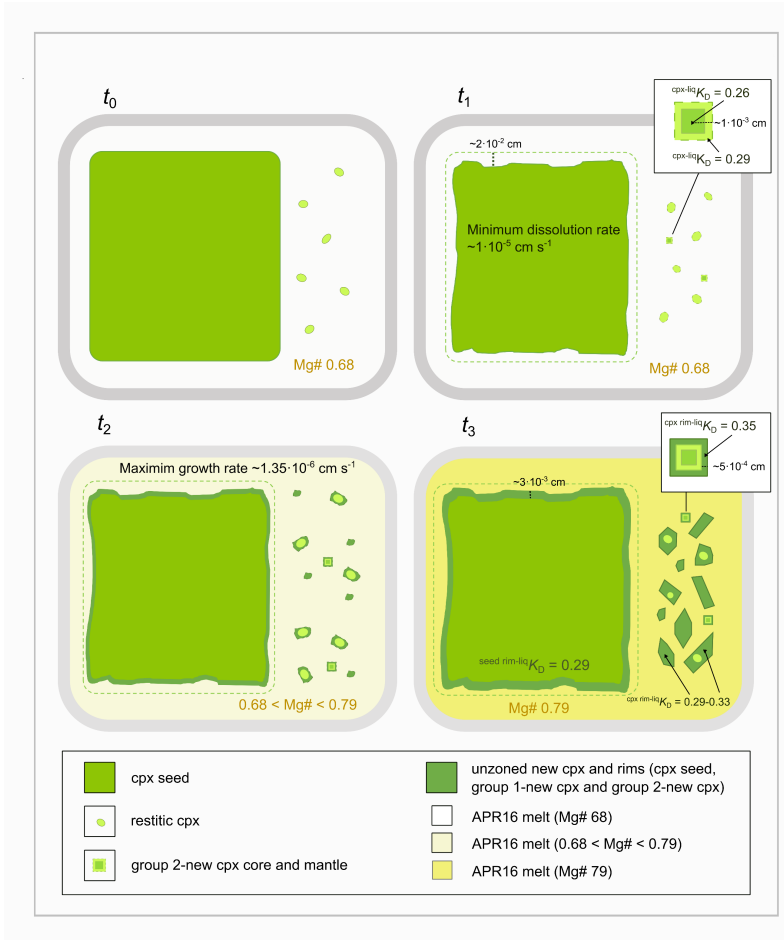

Fig.12 *Cartoon showing the sequence of steps occurring during the APR16-D1Ab experiment, that from the dissolution lead to the formation of the new cpx. Insights show group 2-new cpx at t_1 and t_3 with the Fe-Mg partition coefficient between core, mantle and rim and the coexisting melt.*

Implications to magma dynamics

Mineral dissolution and/or re-crystallization phenomena due to magma mixing, often produce phenocryst assemblages with disequilibrium textures and mineral zoning. In this context, intracrystalline cation exchange models are commonly used to calculate crystal residence times and magma ascent rates (e.g., Viccaro et al. 2016; Petrone et al. 2018), as well as the time elapsed between the refilling of a new and more mafic magma into sub-volcanic reservoirs and eruptions (e.g., Perugini et al. 2015; Ubide and Kamber 2018; Rossi et al. 2019). Only sporadic studies have also considered the role played by crystal dissolution phenomena during crystal-melt interaction and crystal growth (e.g., Liang 2003). If magma mixing is accompanied by crystal dissolution, then it is likely that most of retrieved residence times are potentially underestimated. The refilling of sub-volcanic reservoirs by a new magma batch is proposed as one of the major processes capable of triggering explosive volcanic eruptions due to abrupt changes of the intensive-extensive variables of the system (e.g., Nakamura 1977; Sparks et al. 1977; Viccaro et al. 2006). Understanding the timing of volcanic eruptions is a central issue, particularly to densely populated, active volcanic settings, such as Campi Flegrei caldera (Southern Italy). Many authors identified in the eruptive products of Campi Flegrei several textural and compositional features that can be traced back to mingling-mixing processes (e.g., Orsi et al. 1995; D'Antonio et al. 2007; Arienzo et al. 2010; Di Renzo et al. 2011). Through basalt-phonolite mixing experiments, it has been suggested that the time-scales of mixing for some recent eruptions (namely, Astroni, Averno and Agnano Monte Spina) is in the order of tens of minutes (Perugini et al. 2015). We are aware that *P-T* conditions investigated in this

study are quite different from those encountered at shallow crustal depths where magma mixing takes place (e.g., Orsi et al. 1995; D'Antonio et al. 2007; Arienzo et al. 2010; Di Renzo et al. 2011). However, our experimental data may be combined with the textural information gained by using natural cpx phenocrysts from the pyroclastic deposits of Agnano-Monte Spina eruption (4100 BP; de Vita et al. 1999) to obtain a rough estimation for the crystal dissolution time. This approach may be reasonable considering that *i*) the pressure has negligible influence on the dissolution rate (see in the above § *Influence of temperature and pressure on cpx dissolution*), *ii*) the investigated *T* range is high (1300-1350 °C), and *iii*) the temperature of basaltic magmas intruding into the shallow reservoirs is high too (*T* >1150 °C; Fowler et al., 2007). This comparatively approach provides a preliminary evaluation for the effect of crystal dissolution on mixing time scales, by calculating the dissolution time of cpx phenocrysts whose morphological and chemical features testify to magma mixing processes (Fig. 13). The selected zoned crystals were separated from trachytic crystal-rich pumice. The mineral composition is diopsidic with maximum values of Mg# (80-89) restricted to the crystal portions with shapes suggesting crystal-resorption events (dark gray areas in BSE photomicrographs showed in Fig. 13). These Mg#-rich crystal portions are relicts of early-formed cpx phenocrysts (hereafter named AMS-Cpx1) from a more primitive magmas rising from greater depths (depths ≥ 8 km; Arienzo et al. 2010 and references therein) and mixing with the resident evolved magma. Relict crystals show maximum and minimum sizes in the order of ~1 mm and ~150 μm, respectively. According to the dissolution rates of ~10^{-5}-10^{-6} cm s^{-1} experimentally derived for the basaltic end-member of Campi Flegrei

caldera (i.e., APR16 sample), the minimum dissolution time for a resorption of 150 μm ranges from ~25 min to ~4 h. This time interval is slightly higher than the time scales of mixing of 15±4, 18±5, and 13±4 min proposed by Perugini et al. (2015) for Agnano-Monte Spina, Averno, and Astroni eruptions, respectively. It is not possible to know if magma mixing caused the partial or complete dissolution of larger AMS-cpx1 phenocrysts. For this reason, we have considered for the calculation a maximum length that corresponds to largest AMS-cpx1 (0.15 cm; Fig. 13a). This phenocryst results to be less affected by dissolution. The time required for partial (ΔL ~0.08 cm where ΔL is the difference between the initial and the final crystal length) or complete resorption (ΔL ~0.15 cm) of AMS-cpx1 varies from at least ~2 to ~23 h or from ~4 to ~39 h, by assuming dissolution rates of ~10^{-5} cm·s^{-1} and ~10^{-6} cm s^{-1}, respectively.

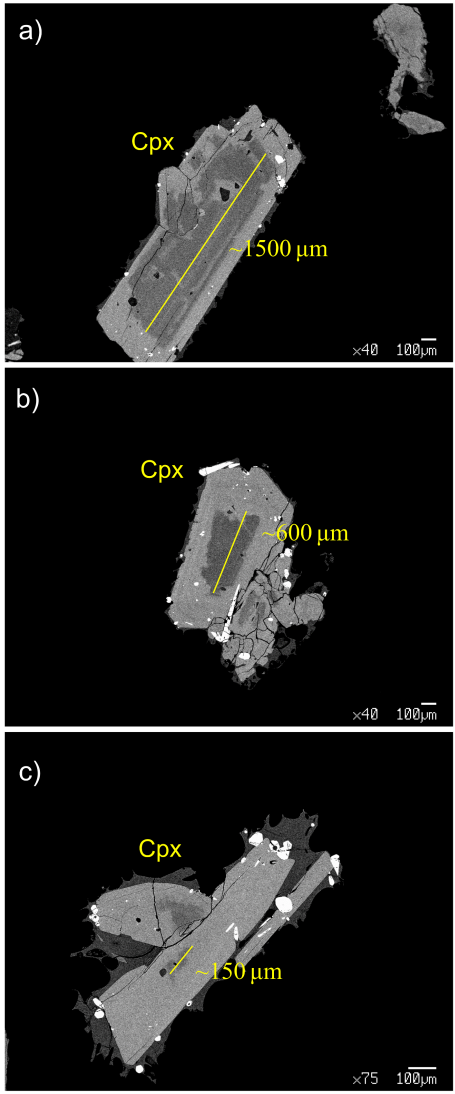

Fig.13 *Selected zoned cpx crystals from Agnano Monte Spina eruption (Campi Flegrei; 4100 BP; de Vita et al. 1999); dark gray areas (Mg# 80-89), indicated with a yellow line, correspond to the portion of grain whose shape is attributable to crystal-resorption event.*

Conclusions

In this experimental work, we have determined the dissolution rate of cpx interacting with a K-basaltic composition. Values calculated at pressure of 0.8 GPa, temperature of 1350 °C, and dwell times between 0.5 and 1 h are in the order of ~10^{-5}-10^{-6} cm s^{-1}. By in-situ experiment at 2 GPa and 1570 °C, we have evaluated the cpx melting rate, showing a non-linear trend over time, with apparent acceleration after consumption of crystal faces. The melting rates shift from $4.8 \cdot 10^{-2}$ cm s^{-1} in presence of crystal faces to $3.2 \cdot 10^{-1}$ cm s^{-1} in presence of a sub-rounded crystal morphology. The effective binary diffusivities of Mg and Ca cations show a classical Arrhenian dependence on temperature and anisotropy with maximum parallel to the c-axis. Textural features of the quenched runs indicate that the dissolution process occurs by consumption of crystalline faces independently of the crystal orientation, leading to rounded shapes and indentations. In the dissolution-crystallization experiment, the formation of overgrowth rims and new cpx crystals with different textures and compositions suggests that injection of basaltic melts in a cold magma chamber may produce crystals with inverse or oscillatory zonation. This disequilibrium crystallization process is also related to the dissolution of pristine crystals resident in the magma reservoir. The growth rate ($1.35 \cdot 10^{-6}$ cm s^{-1}) extrapolated from this dissolution-crystallization experiment, confirms that dynamic conditions favor rapid crystal growth rates. By applying the experimental dissolution rates calculated in this study to products of Agnano-Monte Spina eruption (4100 BP) at Campi Flegrei caldera (Campanian region, Italy), we have estimated maximum cpx dissolution time-scale of ~40 h.

Acknowledgment

We thank Luca Ziberna (BGI Bayreuth) for preparing APR16GL sample. We thank D. Mannetta (Dipartimento Scienze della Terra, Sapienza Università di Roma) for his help in preparing the cpx seeds, M. Albano (CNR-IGAG), Dr. R. Jedlicka (Institute of Petrology and Structural Geology, Charles University of Prague) and M. Serracino (CNR-IGAG) for assistance during SEM and EPMA analytical sessions.

Funding

This research has been conducted with the financial support of the HP-HT Laboratory at the Department of Earth Sciences of Sapienza - University of Rome and with the financial support of the project M_011177_14_D_MAGRI_10-MIUR funded to B.B. A.F. acknowledges support from the GACR (Project 18-01982S). The experiment with PE was performed at HPCAT (Sector 16), Advanced Photon Source (APS), Argonne National Laboratory. HPCAT operations are supported by DOE-NNSA's Office of Experimental Sciences. The Advanced Photon Source is a U.S. Department of Energy (DOE) Office of Science User Facility operated for the DOE Office of Science by Argonne National Laboratory under Contract No. DE-AC02-06CH11357. V.S. acknowledges financial support from the DeepCarbon Observatory and Fondi di Ateneo Sapienza (2016).

Chapter 2

Rheological constraints on the pre-eruptive system of Campi Flegrei (Naples, Italy) from viscosity and melt structure measurements of primitive alkaline basalts

Barbara Bonechi[1], Vincenzo Stagno[1], Yoshio Kono[2], Rostislav Hrubiak[3], Luca Ziberna[4], Cristina Perinelli[1], Mario Gaeta[1]

1 Dipartimento di Scienze della Terra, Sapienza Università di Roma, P. le Aldo Moro 5, 00185, Rome, Italy

2: Geodynamics Research Centre, Ehime University, 2-5 Bunkyo-cho, Matsuyama Ehime 790-8577, Japan

3: High Pressure Collaborative Access Team, X-ray Science Division, Argonne National Laboratory, 9700 S. Cass Avenue, Argonne, IL 60439, United States

4: Dipartimento di Matematica e Geoscienze, Università degli Studi di Trieste, Via Weiss, 2 34128 Trieste, Italy

To be submitted

Abstract

Geochemical and seismic surveys are generally used as precursor of the volcanic hazard as they allow to infer the presence of magmatic bodies in depth. Volcanic eruptions are, however, shallow phenomena resulting from density- and viscosity- driven processes that affect the melt migration and ascent velocity from mantle regions. In this study, we investigated the effect of pressure and temperature on the viscosity and the atomic structure of liquid primitive K-basalts representative of the least-evolved magmas of the Campi Flegrei Volcanic District. Measured viscosities (~0.3-2 Pa·s) along with modelled rock parameters (e.g., permeability, porosity and mineral grain size) show that magmas underneath Campi Flegrei are characterized by a mobility (0.1-1 g $cm^3 \cdot Pa^{-1} \cdot s^{-1}$) and a migration velocity (1-25 $m \cdot y^{-1}$) higher than those of basalts from mid-ocean ridges. Our results support current geochemical and geophysical predictions of Campi Flegrei undergoing magma recharge in depths in favor of a new period of volcanic activity. Finally, the viscosity data at the lowest pressure is used to constrain the ascent velocity of K-basaltic magmas from Procida island within dikes, estimating the time scale for the ascent of magma from two different paths: from the deep reservoir (Moho level; ~24 km depth) to the shallower reservoir located at ~8 km depth, and from the deep reservoir to the surface. Results show time scales in the order of minutes.

Keywords: viscosity, melt structure, Paris-Edinburgh press, high pressure, magma ascent velocity, Campi Flegrei

Introduction

The monitoring of volcanic unrest is of primary importance to predict the possibility of eruptions that might have dramatic consequences for human life. Among the most dangerous and, therefore, monitored examples of volcanic areas, Campi Flegrei is of particular interest because of its multiple unrest episodes in the recent last 100 years (Del Gaudio et al., 2010) accompanied by historical large eruptions (Albert et al., 2019), and characterized by geochemical and geophysical observations like long-term record of degassing fumaroles, perturbation of the hydrothermal circulation (Petrillo et al., 2013), chemistry and high temperatures of groundwaters (Aiuppa et al., 2006), and uplift/subsidence cycles the latter of which tightly associated to changes in the CO_2/steam ratio of the released fluids (Todesco et al., 2014). All these precursors have been interpreted as due to an increase in the production of magmatic gases released by shallow plumbing system (Calò and Tramelli, 2018) sustained by an evolving magmatic body extending down to sub-crustal depths (Fedi et al., 2018), the activity of which follows the last eruption occurred in 1538 AD (Mt. Nuovo; Barberi and Carapezza, 1996), and suggest a severe volcanic hazard of the area as characterized by high density of population (1.5 million; Orsi et al. (2004)).

The volcanic hazard has been generally linked with the explosivity of a volcano due to differentiation processes at shallow conditions. However, there is evidence that the re-activation of volcanic areas is supported by an input of deeply formed magmatic batches (Burgisser and Bergantz, 2011; Folch and Martı, 1998; Pallister et al., 1992; Rizzo et al., 2015; Sparks et al., 1977). This, in turn, implies that the eruptive style at surface is influenced by the physical and chemical conditions of magmas at depths of the upper

mantle. In the case of Campi Flegrei, several studies have pointed out the geochemical and seismic signature for the presence of mantle-derived magmas, the rheological properties of which remained unexplored so far. To date, several studies have investigated the viscosity of natural (Kani, 1934; Murase and McBirney, 1973; Scarfe, 1973) and synthetic magmas (Behrens and Schulze, 2003; Kozu and Kani, 1935) at various pressure conditions from atmospheric to low pressure (~0.4 GPa). Additional studies have provided empirical numerical models to determine the viscosity of natural lavas spreading in composition from basalts to trachytes (Giordano et al., 2008b), rhyolites and granitic melts (Shaw, 1972). These studies are, however, applicable mostly at differentiated lavas in open-conduit scenarios, i.e., the pressure dependence and mantle origin of primitive magmas is not considered. Experimental studies have provided the pressure dependence of viscosity first by performing quench experiments in multi anvil and piston cylinder (Kushiro et al., 1976) although limited to viscosities > 1 Pa·s. More recent experimental studies performed at high pressure and temperature representative of mantle regions by means of in situ radiographic techniques combined with high-pressure apparatus have allowed to explore a wider range of silicate melt compositions like basaltic (Sakamaki et al., 2013), trachy-andesitic (Suzuki et al., 2005), albitic (Suzuki et al., 2002) and dacitic (Tinker et al., 2004) melts. Although such studies highlight differences in viscosity up to three order of magnitude within a pressure interval of ~1.5 to ~6.5 GPa for melts that have SiO_2 content varying between 51.7 wt% and 67.51 wt%, none of them can be taken as reference values to infer the rheological behaviour of mantle-derived magmas on interest for the Campi Flegrei Volcanic District (CFVD; Italy). In fact, the

primitive magmas at Campi Flegrei are characterized by less silica content (~49.3 wt%), more TiO_2 (1.33 wt%) and almost twice the alkali abundance (~4.5 wt% of $Na_2O + K_2O$; see TAS diagram in Figure S1) than the basaltic composition used by Sakamaki et al. (2013) strictly representative of MOR basalts. To date, experimental studies on the rheological properties of magmas of interest for the Campi Flegrei Volcanic District (CFVD; Italy) investigate only differentiated compositions from latites to trachytes at low (< 0.5 GPa) and atmospheric pressure (Caricchi et al., 2008; Giordano et al., 2004b, 2009; Misiti et al., 2006, 2011; Romano et al., 2003).

Here, we investigate experimentally the viscosity of a primitive composition at pressures and temperatures that are representative of the source rock depth to shed light on the migration rate and ascent velocity of deep magmas confined to a closed system. At this aim, we investigated the viscosity of K-basaltic glass (APR16 rock sample; D'Antonio et al., 1999) as representative of source magma of the CFVD at pressure of 0.7-7 GPa and temperatures between 1300 °C and 2000 °C by the falling sphere technique using the Paris-Edinburgh press combined with in situ X-ray radiography, an advanced technique of viscosity measurement with ultrafast synchrotron X-ray imaging.

Results

Viscosity measurements of APR16 K-basalt at HP-T by falling Pt sphere technique

Viscosity measurements were performed using a glassy powder of the natural APR16 K-basalt as starting material after being melted at 1400 °C under controlled oxygen fugacity (Perinelli et al., 2019). The falling-sphere

technique (Leblanc et al., 1999) was employed assisted by in situ X-ray radiography and a Paris–Edinburgh press installed at Beamline 16BM-B (HPCAT) at the Advanced Photon Source (Kono et al., 2014a). Runs were carried out at pressures and temperatures of 0.7 GPa/1335 ºC, 1.4 GPa/1440 ºC, 2.3 GPa/1600 ºC, 3.7 GPa/1650 ºC, 5.5 GPa/1835 ºC, 7 GPa/2000 ºC.

Figure 1 summarizes our determined viscosities plotted as function of pressure and temperature, compared with the few experimental data available in literature (Sakamaki et al., 2013; Suzuki et al., 2002, 2005; Tinker et al., 2004; Wang et al., 2014). The viscosity obtained here varies between 1.7 Pa·s at 0.7 GPa/1335 ºC and 0.1 Pa·s at 3.7 GPa/1650 ºC as result of the combined effects of pressure and temperature. As shown in Figure 1a, our data interestingly reproduce the same trend observed from MOR basalts by Sakamaki et al. (2013), but with APR16 being constantly less viscous by about 0.1 Pa·s. Two isobaric runs at 0.7 GPa showed viscosities varying from 1.1 to 1.7 within a ΔT of 105 ºC suggesting a strong temperature dependence of the obtained viscosity values (Figure 1b).

As already noted by Wang et al. (2014) the response of viscosities to pressure is dissimilar between polymerized (NBO/T < 1) and depolymerized (NBO/T ≥ 2) melts. Indeed, while the viscosity of a diopsidic depolymerized melt (NBO/T ≥ 2; Cochain et al., 2017) increases with pressure, that of polymerized melts such as MOR basalts (Sakamaki et al., 2013; NBO/T = 0.7) first decrease with increasing pressure (abnormal) to, then, increase linearly. Similarly to Sakamaki et al. (2013), our data (NBO/T = 0.82) show a pressure effect on the viscosity considering that in high-P runs the glass-liquid transition temperature increases as well as the liquidus resulting, therefore, to lower viscosity values (Figure 1).

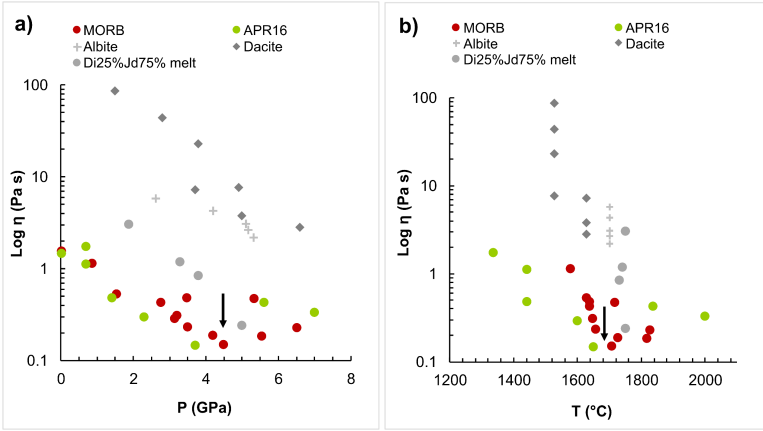

Fig.1 *a) Log viscosity vs pressure diagram; b) log viscosity vs temperature diagram. Red circles indicate MORB (Sakamaki et al., 2013), green circles indicate K-basalt of this study, grey circles indicate Di 25%–Jd 75% melt (Suzuki et al., 2005), grey plus indicate albitic melt (Suzuki et al., 2002), grey diamond indicate dacitic melt (Tinker et al., 2004). Black arrow shows the P (~4 GPa) and T (~1700 °C) at which viscosity change trend due to variation in the Al coordination.*

Melt structure measurements

The viscosity of a magma is known to reflect changes in the interatomic distances of the amorphous structure (Kono et al., 2014b; Yamada et al., 2011a). Hence, to better understand the rheological properties of APR16 at mantle-deep crustal conditions, melt structure measurements were performed immediately after the fall of the Pt sphere using the multi-angle energy-dispersive X-ray diffraction technique (Kono et al., 2014b; see Methods for details). To avoid crystallization caused by increasing thermal pressure of the cell during the 3h of acquisition, these measurements were performed by increasing slightly the target temperature to keep it above the liquidus conditions. The structure factors, $S(Q)$, were obtained from the

measured X-ray diffraction data using the in-house *aEDXD* analytical program (see Methods for details) and converted to the pair distribution function *G(r)*. Figure 2 shows the acquired spectra at 2.3 GPa/1600 ºC, 4.6 GPa/1650 ºC and 5.4 GPa/1835 ºC. The displayed peaks are relative to the tetrahedral-coordinated cation T-T and T-O interatomic distances. More in detail, according to previous studies (Sakamaki et al., 2013; Yamada et al., 2011b), the peaks located at ~1.65, 1.67 and 1.67 Å can be assigned to the T-O bond length, the basic unit of the silicate melt. The distinct peak at r = 1.65 Å gradually becomes more intense and shifts toward higher r with increasing pressure (Figures 2).

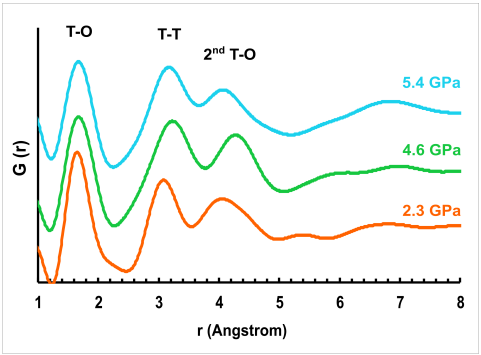

Fig.2 *Radial distribution function G(r) of the APR16 melt at different investigated pressures. The peak positions indicate the average bond length of the atomic pairs in the melt. The peak positions indicate T-O, T-T and 2nd T-O bond length.*

Figures 3a-c show the pressure dependence of T-O and T-T interatomic distances, and T-O-T angle in APR16 K-basaltic melt. In general, the T-O bond length decreases when depolymerization of the SiO_4 network

structure occurs (Yamada et al., 2007, and refernce therein). The reason why the Si-O distance increased increasing the pressure may be related to the gradual change in coordination state of Si atoms (Yamada et al., 2007). The peaks at ~ 3.08, 3.23 and 3.17 Å are, instead, corresponding to the T-T bond length and reflect the distance between TO_4 tetrahedron units. The T-O-T angle was calculated using the relationship between T-O bond length and T-T bond length (T-O-T angle = 2arcsin{[T-T]/2[T-O]}) proposed in case of corner-sharing TO_4 tetrahedra forming a 3D framework structure. We obtained 138º at 2.3GPa/1600 ºC, 151º at 4.6GPa/1650 ºC and 143º 5.4GPa/1835 ºC (Figure 3c). These angles are closely related to the intermediate-range network structure and, for this reason, a decrease in T-O-T angle indicates that the atomic structure becomes more compact as observed also by Yamada et al. (2011b) for the $NaAlSi_3O_8$ albitic composition.

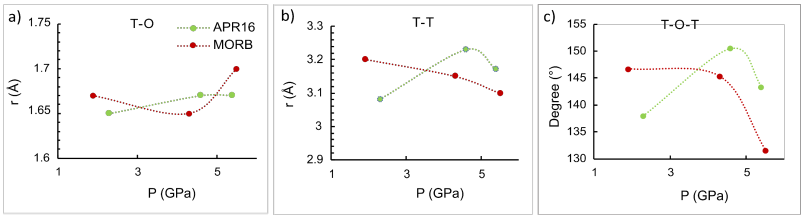

Fig.3 *Pressure dependence of T-O (a) and T-T (b) interatomic distances, and T-O-T angle (c) in APR16 K-basaltic melt (green circles) and in MOR basalt (red circles) of Sakamaki et al. (2013).*

Discussion

Effect of pressure and temperature on the viscosity

As known in literature, pressure does not have a significant influence on viscosity, at least up to 2.0 GPa, respect to other parameters like temperature, but at high pressure (>2 GPa) this influence is evident. The influence of high pressure on viscosity of silicate melts has been studied by several authors (Allwardt et al., 2007; Brearley and Scarfe, 1986; Kushiro, 1980; McMillan and Wolf, 1995; Persikov, 1991; Persikov and Bukhtiyarov, 2004). In Figure 1 we plotted our data and those of Sakamaki et al. (2013) relative to MORB composition, which is the most similar composition to the alkaline basalt studied in this work. We observed the influence of pressure on the viscosity with a decrease of viscosity increasing *P* up to 4 GPa while for *P* >4 GPa we noted an inversion of the trend with an increase of viscosity increasing *P*. Such rapid densification is consistent with previous studies on quenched alumino-silicate melts, which showed that Al coordination number increases rapidly between 3 and 5 GPa (Allwardt et al., 2007). The same behavior is observable for the MORB, that show values slightly higher. The temperature dependence of the viscosity is one of the most important characteristics of magmas since knowledge of this physical property allows one to quantify their transport capacities and heat and masses transfer processes under different geodynamic settings in the Earth's interior (Persikov et al., 2017). Some equations of temperature dependences of viscosity of silicate and magmatic melts have been suggested (Giordano et al., 2004a, 2008a; Giordano and Dingwell, 2000, 2003; Hui and Zhang, 2007; Liebske et al., 2005; Richet, 1984; Shaw, 1972; Whittington et al., 2001, 2004). In APR16-PE3 run we used a double Pt sphere to obtain two different

viscosity values at the same *P* but a different *T*, observing a difference of ~0.4 Pa·s for a variance of ~100 °C. Since temperatures of the runs are super liquidus temperatures, necessary to observe a regular fall of the sphere without directional variation, it is very difficult to obtain great amount of data on *T* dependence at high pressure. For this reason, we decided to estimate this effect at atmospheric pressure taking in consideration our samples, the MORB of Sakamaki et al. (2013) and other differentiated composition typical of the Campi Flegrei area (Giordano et al., 2004b; Giordano and Dingwell, 2003; Misiti et al., 2011) by using the calculation model proposed by Giordano et al. (2008b). In Figure S2a-b it was possible to note that viscosity decrease increasing temperature and that viscosity values are higher for the differentiated compositions.

Migration rate of K-basalts from the mantle source rock beneath Campi Flegrei

Our data can be used to model the mobility and migration rate of APR16 melts at upper mantle conditions corresponding to a scenario of new batches of magma that form in the mantle source and move upward creating the conditions of re-felling of the chamber at crustal depths. Recent petrographic and geochemical observations of the Campanian Ignimbrite products of Campi Flegrei supported by thermo-mechanical models of magma ascent provide evidence of magma chambers located at ~7 km in depth (e.g., Moretti et al., 2017; Forni et al., 2018). The location of a shallow magmatic chambers that cause unrest of the area has been matter of investigation in the last 3 decades both from the seismological (Bagagli et

al., 2017; Chiodini et al., 2017) and geochemical point of view (Caliro et al., 2014; Chiodini et al., 2016; Moretti et al., 2017). However, there are geochemical evidence in favor of the potential involvement of deep reservoir likely associated to subducted sedimentary crust (Allard et al., 1991). Our results represent an integrated set of data that shed light on the possible role of new raising magma through time as represented by APR16 sample (D'Antonio et al., 1999, 2013; D'Antonio and Di Girolamo, 1994). Our viscosity measurements allow to model the magma mobility and migration rate as done by previous authors who performed similar experiments (Kono et al., 2014a; Sakamaki et al., 2013). We used the equation (McKenzie, 1989),

$$\phi w_0 = \frac{kg\Delta\rho}{\eta} \quad (2),$$

with,

$$k = \frac{a^2\phi^n}{C} \quad (3),$$

where k is the permeability, a is the characteristic grain diameter, ϕ is the melt fraction, while n (equal to 3) and C (equal to 1000) are numerical constants (McKenzie, 1984), g is the gravitational acceleration constant, and w_0 is the melt ascent velocity. In equation (3) for low porosities ($\phi \leq 0.5$), when melt first exceeds the percolation threshold and becomes interconnected along grain edges (Connolly et al., 2009), is appropriate to use a quadratic dependence (n = 2 and C = 1600). Conversely, for higher porosities ($\phi \geq 0.5$) the appropriate dependence is the cubic one (n = 3 and C = 1000; Connolly et al., 2009; McKenzie, 1984). For the permeability and grain size we used parameters for mantle rocks as proposed in literature (McKenzie, 1984, 1985). The mobility ($\Delta\rho/\eta$) and the migration velocity of

APR16 melt obtained in this study are summarized in Figure 4a-b, respectively. The study by Sakamaki et al. (2013) discussed the mobility of the basalt melt in the upper mantle and showed that $\Delta\rho/\eta$ changes from 0.03 to 0.58 $g \cdot cm^{-3} \cdot Pa^{-1} \cdot s^{-1}$ at 0–210 km depth. To compare the mobility of K-basaltic melt with that of MOR basalt, we calculated the mobility of K-basaltic melts by adopting the density of upper mantle and cumulitic rocks by Fedi et al. (2018) as density of solid rock. As shown in Figure 4a, we obtained a melt mobility of 0.1-1 $g \cdot cm^{-3} \cdot Pa^{-1} \cdot s^{-1}$ for the runs of this study, that is higher than those calculated for MOR basalts (0.03 to 0.25 $g\ cm^3\ Pa^{-1}\ s^{-1}$) of Sakamaki et al. (2013). Moreover, similarly to MOR basalts of Sakamaki et al. (2013), melt mobility of APR16 basalt decreases rapidly from 100 to 180 km depth, as a consequence of the coordination change of Al in the melt with an unusually large compressibility almost five times higher than usual above and below this depth range (Sakamaki et al., 2013). According to the melt zone model of Schubert et al. (2001), which takes into account the compaction of the solid mantle as the melt migrates (McKenzie, 1984), where mobility is low, melt fraction must be high. For this reason, melt mobility play a fundamental role in controlling magma transport. Moreover, we tried to estimate the migration velocity of this alkaline melt from the source rock (~60-80 km depth; Mazzeo et al., 2014) to the Moho (~ 25 km of depth in the Campi Flegrei area) by assuming three different melt fractions of 5, 10 and 15 %. Indeed, according to Mazzeo et al. (2014), in order to generate the Procida primary magmas, it is necessary ~6% degree partial melting of the source. As shown in Figure 4b, the obtained values of ~1-25 $m \cdot yr^{-1}$ are higher than those estimated beneath mid-ocean ridges (~0.3-7 $m \cdot yr^{-1}$), although a decrease of velocity at shallow depths for each

simulation tends to flatten for the lower melt fraction percentage (i.e., < 5 %).

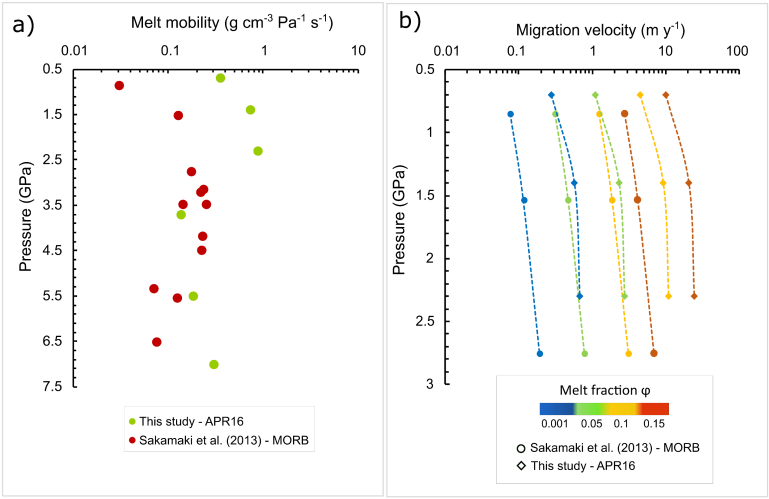

***Fig. 4 a**) Melt mobility and b**) migration velocity of K-basaltic and MOR basalts as function of pressure. a) The mobility of alkaline melt was calculated by using viscosity determined in this study and density of upper mantle and cumulitic rocks by Fedi et al. (2018) as density of solid rock for APR16 basalt. For MORB we used data from Sakamaki et al. (2013). b) to model migration velocity, we used different melt fraction (φ) from 0.001 to 0.15. Melt fraction is indicated with the scale bar. Circle indicates MORB of Sakamaki et al. (2013) while diamond indicates APR16 basalt of this study.*

Ascent rate of K-basalts in the Campi Flegrei Volcanic District

Despite the magma migration underneath a volcano is usually accompanied by geophysical precursors (e.g., volcano-tectonic earthquakes, tremors, and deformations), these signals alone are not enough to forecast volcanic eruptions. In this context, the viscosity data represent a useful tool as they allow to estimate flow regime and magma ascent rate from deep to shallow reservoirs, and up to the surface (Misiti et al., 2011, 2009; Vetere et al., 2007).

This approach has been already successfully used to estimate the ascent velocities of shoshonitic, latitic and trachytic magmas belonging to the Campi Flegrei caldera (Misiti et al., 2011), basaltic magmas of Stromboli (Misiti et al., 2009) and shoshonitic magmas of Vulcanello (Aeolian Islands; Vetere et al., 2007). On the basis of melt inclusion studies (Moretti et al., 2013; Mormone et al., 2011), seismic data interpretations (Chiarabba et al., 2008; Di Stefano et al., 1999; Piochi et al., 2005), gravimetric and petrological modelling (Fedi et al., 2018), and experimental data (Bonechi et al., 2020b; Perinelli et al., 2019), has been hypothesized the presence beneath the CFVD of a deep magmatic reservoir at ~25 km depth (at about Moho depth, Di Stefano et al., 2011), that corresponds to 0.7-0.8 GPa. From this reservoir the K-basaltic magma can rise directly to the surface or ponds at shallower depth. The direct ascent of magma to the surface can generate effusive eruptions with the emplacements of lava flows as those historically occurred in the Campi Flegrei Volcanic District (e.g., 1302 Arso eruption, Ischia island), or hydromagmatic eruptions when magma interacts either groundwater or surface water. Although these eruptions are classified as low-magnitude eruptions, they might have dramatic effects in a densely inhabited area as Campi Flegrei is (~1.5 million of people; Orsi et al., 2004). The ponding of the K-basaltic magma should occur at ~8 km of depth, as suggested by thermobarometric estimates on clinopyroxene microlites of scoria clasts from Procida Island (Bonechi et al., 2020b). Therefore, on the basis of these evidence, we tried to estimate the APR16 K-basaltic magma ascent velocity for two different paths: the first from the deep reservoir to the shallower reservoir located at ~8 km depth (hereafter path 1), while the second from the deep reservoir to the surface (hereafter path 2). For both the

paths we assumed that the rise of the magma occurs through dikes without constraining their geometry in depth. Although the dike geometry plays a key role in controlling the mass flux, however, it does not significantly influence the average ascent velocity (Giberti and Wilson, 1990). Assuming that magma ascent is driven by buoyancy, we calculated the overpressure ΔP at ~25 km depth where the K-basaltic melt resides by using the following equation (Misiti et al., 2011, and reference therein):

$$\Delta P = \Delta \rho g h \quad (4),$$

where ρ is the density, g is the gravitational acceleration, and h is the vertical lengths of the dike. $\Delta \rho$ are the difference between 3150 kg/m^3, which is the seismically and gravity constrained average density of the crustal rocks beneath the CFVD (Fedi et al., 2018), and the density of the dry (ρ = 2730 kg/m^3; 0.6 wt.% H_2O) and hydrous (ρ = 2643 kg/m^3; 2.0 wt.% H_2O) K-basaltic melt estimated at 1250 °C (dry) and 1235 °C (hydrous), and 0.7 GPa following Iacovino and Till (2019). Temperatures and water contents selected were chosen as representative conditions of the magma at ~25 km depth based on experimental evidence (Perinelli et al., 2019) and melt inclusion studies (Moretti et al., 2013), respectively. The calculated $\Delta \rho$ is 420 kg/m^3 for the dry melt and 507 kg/m^3 for the hydrous melt. Concerning the vertical lengths of the dike (h), they are 17 and 25 km for path 1 and 2, respectively. Using Eq. (4) and the above parameters, we obtained a ΔP(dry) of 70 and 103 MPa and a ΔP(hydrous) of 85 and 124 MPa for path 1 and path 2, respectively. Since the viscosity value measured in this study at 0.7 GPa and 1335 °C ($10^{1.76}$ Pa s) is an absolute value, it is necessary to correct it considering the temperature, the water content and the number of crystals

of the APR16 K-basalt magma in natural conditions. Therefore, considering temperatures of 1250 °C (dry) and 1235 °C (hydrous), and water contents up to ~2 wt.%, we calculated viscosity values of $10^{1.9}$ and $10^{1.4}$ Pa s for dry and hydrous conditions, respectively, by using the modified VFT equation of Vetere et al. (2007). Furthermore, taking into account that the APR16 K-basalt have a maximum crystal content of ~12 vol.% (Bonechi et al., 2020b; Perinelli et al., 2019), we recalculated the viscosity through the model of Sato et al. (2005), obtaining $10^{2.2}$ and $10^{1.6}$ Pa s for the dry and hydrous melt, respectively. Before the calculation of the ascent velocity, it is necessary to estimate the Reynolds number (*Re*) within the dike, to know if the magma moves in laminar (*Re* <10), turbulent (*Re* >1000), or transitional (10<*Re*<1000) flow regime. In this regard we measured the critical value of the viscosity (η_c), using the following relation (Sparks et al., 2006):

$$\eta_c = [(2\Delta P \rho w^3)/(3hRe_c)]^{1/2} \quad (5),$$

where Re_c is the critical Reynolds number, ρ is the density of the melt, w is the width of the dike. We selected w = 2 m based on the value assumed by Misiti et al. (2011) for the Campi Flegrei, and w = 10 m as maximum value of the dike width. We also select 10 and 1000 as representative values of Re_c. Considering both dry (H_2O = 0.6 wt.%) and hydrous (H_2O = 2 wt.%) melts, for a dike width of 2 m the critical viscosities are $10^{2.1}$ Pa s for Re_c = 10 and $10^{0.8}$ Pa s for Re_c = 1000; for a dike width of 10 m, instead, they are $10^{3.0}$ Pa s for Re_c = 10 and $10^{1.9}$ Pa s for Re_c = 1000. In the case of the dry melt, these effective viscosity values are higher than those estimated using Eq. (5) at Re_c = 1000 and 10, and w = 2 m while the difference is less evident at Re_c = 10 and w = 10 m. Conversely, in the case of the hydrous melt, the effective viscosity

values are lower than those estimated using Eq. (5) at Re_c = 1000 and 10, and w = 10 m whit a less evident difference at Re_c = 1000 and w = 2 m. According to these data we can assume that the APR16 magma moves within the dike in a laminar flow regime for water content up to 0.6 wt.% while it switches to a turbulent flow regime with the increase of the amount of water (2 wt.%). At this point, we calculated the ascent velocity (u) for the dry and hydrous magmas by using the relations of Lister and Kerr (1991) for laminar (Eq. 6) and turbulent (Eq. 7) flows, respectively:

$$u = (w^2/3\eta)\Delta\rho g \quad (6),$$

$$u = 7.7\ [w^5/\{\eta(\rho g\Delta\rho)^3\}]^{1/7} g\Delta\rho \quad (7).$$

By setting w = 2 m, $\Delta\rho$(dry) = 420 kg/m^3, $\Delta\rho$(hydrous) = 507 kg/m^3, η(dry) = $10^{2.2}$ Pa s and η(hydrous) = $10^{1.6}$ Pa s, we obtained the following values: u(dry) = 36 m/s and u(hydrous) = 33 m/s. These values are consistent with the ascent velocities estimated by Misiti et al. (2011) for shoshonitic, latitic and trachytic magmas of the Campi Flegrei, that vary between 3 and 19 m/s (Fig. 5). Moreover, they result in agreement also with the ascent rate estimated for Stromboli basalts (Misiti et al., 2009), that is ~32 m/s at T = 1150 °C, H_2O = 3.76 wt.% and a crystal content of ~10 vol.%.

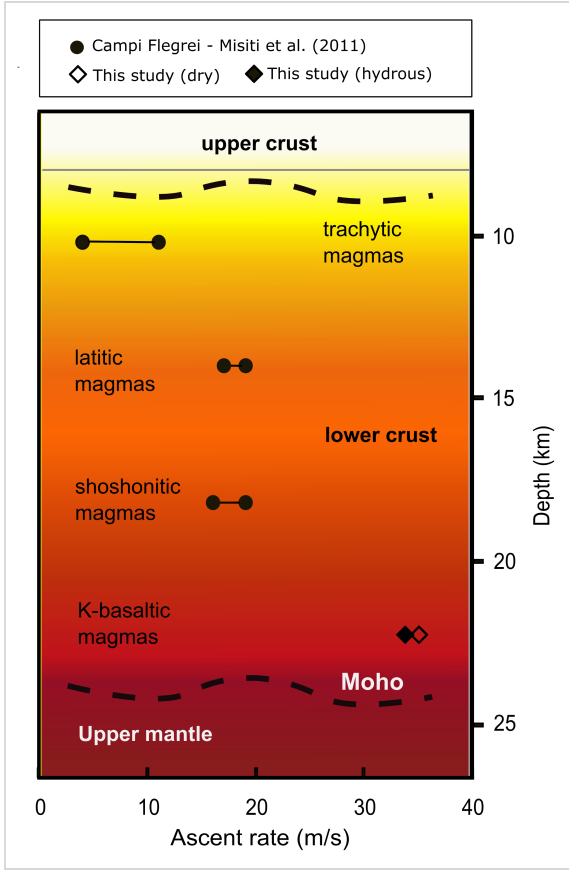

Fig. 5 Comparison *among ascent rate estimates for trachyte (Agnano Monte Spina), latite (Fondo Riccio), shoshonite (Minopoli) by Misiti et al. (2011), indicated with black circles; diamonds indicate K-basalt magmas from this study: empty symbol for dry (0.6 wt.% H_2O) magma while full symbol for hydrous (2 wt.% H_2O) one. Modified after Fedi et al. (2018).*

Finally, we estimated the ascent time for K-basaltic magma between 25 and 8 km of depth (path 1) and between 25 km of depth and the surface (path 2) for dry and hydrous conditions. For the path 1, the ascent times are in the

order of 7.9 min (dry) and 8.4 min (hydrous), while for the path 2, they are 11.7 min (dry) and 12.4 min (hydrous). As stated by previous authors (Misiti et al., 2011 and reference therein), the estimated velocity does not represent an absolute value but rather an order of magnitude. Indeed, the used model does not consider some processes, such as i) freezing at the walls, which can locally increase the viscosity (Wylie et al., 1999); ii) the variation of the dike geometry in depth (Giberti and Wilson, 1990); and iii) possible vesiculation able to decrease the magma viscosity (Manga and Loewenberg, 2001). The model used in this study to estimate the ascent velocity is confidently valid for an open conduit system, as in the case of Stromboli. Indeed, the ascent of magma from the 7–8 km deep reservoir to the 3 km shallower one in few minutes, as estimated by Misiti et al. (2009), results to be in good agreement with the seismic surveillance (Martini et al., 2007), according to which, at Stromboli the eruptions triggered by the sudden arrival of new magma from a deep reservoir show evident precursory signals of a new batch of volatile-rich ascent magma only few minutes before the occurrence of the paroxysm (Misiti et al., 2009). In order to observe the behaviour of the ascent velocity in a closed conduit system, in which $w \rightarrow 0$ m, we modelled the ascent velocity in both laminar and turbulent flow regime as a function of the width of the dike (from 0 to 10 m) varying the water content of the melt (from 0 to 4 wt.%), for different T conditions (1150, 1200 and 1250 °C), $\Delta\rho$ = 350-600 kg/m^3 and ~10-12 vol.% of crystal content (Figure 6). As possible to see in Figure 6, overall, the ascent velocity tends to decrease with decreasing the width of the dike, and for the same widths it increases with increasing water content. Moreover, the width of the dike at which the shift from laminar to turbulent flow regime occurs, decreases with increasing

temperature for each considered water contents, and for same T it decreases with increasing water content. Thus, for example, considering a dry melt at 1250 °C and a dike with of 4 m, it will start to rise in a turbulent regime with u ~32 m/s. If the system is a closed conduit, during the ascent there will be a decrease in the width of the dike with consequent passage to laminar regime (w = 3 m; u = 26 m/s), after which the ascent velocity will exponentially decrease until the complete stop (w = 0 m).

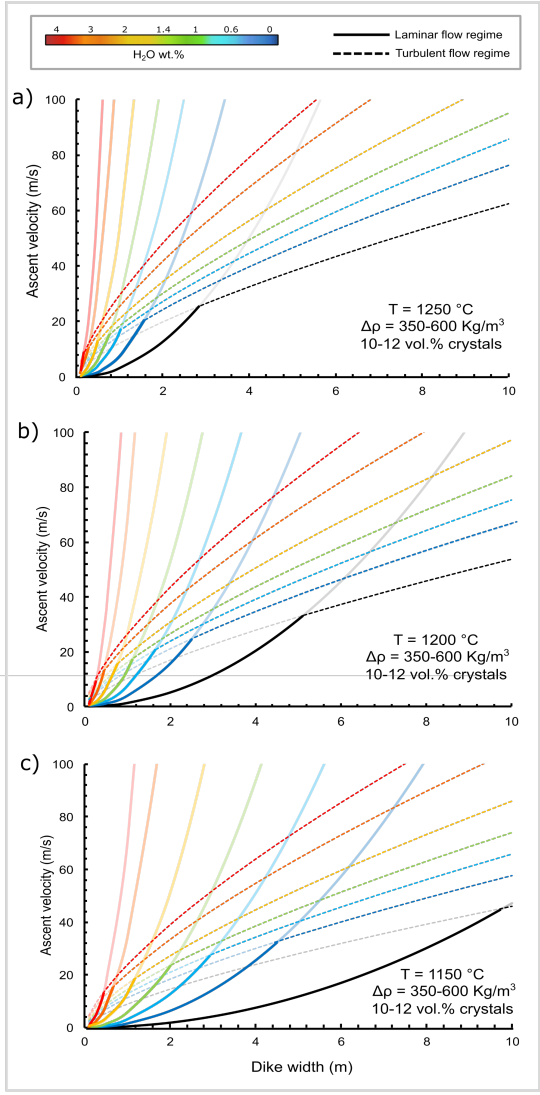

Fig. 6 *Ascent velocity vs dike width for APR16 melt at a) 1250 °C, b) 1200 °C and c) 1150 °C. For all the simulations we selected Δρ = 350-600 Kg/m³ and 10-12 vol.% of crystals. Coloured scale bar indicates the amount of water in the melt. Continuous lines represent laminar flow regime while dotted lines turbulent one. at the point where the two lines intersect, the transition from laminar to turbulent regime occurs.*

Materials and Methods

Starting material

The choice of APR16 for this study is mainly motivated by the fact that this sample represent the near-primary melt of the CFVD on the basis of its geochemical and isotopic features (D'Antonio et al., 1999).

The APR16 sample, indeed, is a primitive alkaline basalt found as scoria clast in the deposits of the Solchiaro hydromagmatic centre located in Procida island (Campi Flegrei, Italy), previously investigated in the literature (Bonechi, 2020; Bonechi et al., 2017, 2020a, 2020b; Perinelli et al., 2019). The starting material used in this work is an anhydrous glass (APR16GL) prepared by melting the APR16 natural powder in a gas-mixing furnace at 1400 °C and atmospheric pressure for 15 min to reduce all Fe^{3+} to Fe^{2+} using a CO/CO_2 gas mixture at the Bayerisches Geoinstitut (Bayreuth, Germany). The starting material did not contain crystalline phases, as analyzed by both microprobe and image analyses.

High-pressure and high-temperature experiments

Experiments were performed using the VX-3 Paris–Edinburgh (PE) press (Besson et al., 1992; Klotz et al., 2004) available at the 16BM-B beamline at the Advanced Photon Source (Argonne National Lab, Illinois; Kono et al., 2014a, 2015; Figure S3). Our PE cell allowed the compression of large 3.53 mm^3 sample volumes (up to) at high pressures and high temperatures. Cup shaped WC anvils with the cup diameter of 12 mm and the bottom diameter of 3 mm are used to generate high pressures (Yamada et al., 2011b). The cell assembly design for liquid structure measurement and/or viscosity measurement mainly consists of boron–epoxy (BE) gaskets, a MgO ring,

ZrO_2 caps, a graphite heater, and a BN capsule. Graphite inner capsule were used for silicate melt experiments inside BN sleeve (Sakamaki et al., 2012; Yamada et al., 2011b). A ring-shaped BE (boron: epoxy = 4:1 in weight ratio) is used as gasket with a supporting outer polycarbonate plastic (Lexan) ring. The BE gasket and ZrO_2 caps in the assembly provide good thermal insulation for high temperature experiments. A MgO ring is placed between BE gasket and graphite heater to increase stability of the cell assembly and maintain anvil gap. The MgO ring is also used as the pressure standard by using an equation of state (Kono et al., 2010). Uncertainty of the pressure calculation using the MgO ring was typically up to 0.15 GPa. The loaded cell was first compressed to the target pressure by a hydraulic system connected to the Paris-Edinburgh press. After compression, the sample was heated quickly (~100 °C/s), and the temperature estimated using a power vs. temperature calibration curve reported by Kono et al. (2014b). Finally, experiments were quenched by shutting down the electrical power to the heater.

Ultrafast X-ray imaging

White X-ray radiography is used to image the interior of the cell assembly at high pressures and is mainly used for travel distance determination for elastic wave velocity measurements or falling sphere viscosity measurement (Kono et al., 2015). The beamline utilizes two cameras for X-ray imaging experiments. High spatial-resolution X-ray imaging measurements are conducted using a CCD camera (Prosilica GC1380H) placed roughly 30 cm from the sample position (Figure S3). A thin scintillator (5 μm thick Eu-doped lutetium aluminum garnet (LAG)) is used

with a 45° mirror and a 10 times infinity-corrected objective lens mounted on a 127 mm long tube. By using the Eu-doped LAG scintillator, it is possible typically obtain a reasonable image with a 0.5 s exposure time. The other camera, a high-speed camera Photron SA3, is located approximately 1.2 m downstream from the PE cell (Figure S3). The use of thick (100 μm thick) Ce-doped LAG provides sufficiently high brightness for ultrafast X-ray imaging through the PE cell assembly. The pixel resolution of the ultrafast X-ray imaging is typically 2.5 μm/pixel, and the full field of view is larger than the maximum sample size available in the PE cell (up to 2 mm in both diameter and height; Kono et al., 2015)

Falling-sphere viscosity measurement

The falling sphere velocity, necessary to determine the viscosity using Stokes equation, was determined from the collected radiographic images with the Tracker plugin in the ImageJ software package. Experimental measurements of the viscosity were performed using unfocused white X-ray beam with radiographic images captured by a high-speed camera (Photron FASTCAM SA3) with 250 and 500 frame per second recording time (250 fps for the runs APR16-PE5, PE6, PE7; 500 fps for the runs APR16-PE1, PE2 and PE3). The image resolution of the ultrafast camera used for the viscosity measurements was 2.5 μm m/pixel. The measured fall velocity of the Pt sphere was converted into melt viscosity using the general Stokes law,

$$\eta = \frac{g d_s^2 (\rho_s - \rho_l)}{18v} \frac{F}{E} \quad (8)$$

including the proper correction factors for the effect of the wall (F) and for the end effect (E), where v is the terminal velocity (mm·s^{-1}) of the probing sphere, ρ_s and ρ_l are the densities (g·cm^{-3}) of the Pt sphere at high P and T (Dorogokupets and Dewaele, 2007) and melt, respectively; d is the diameter (in mm) of the sphere determined from radiographic image. Particularly, the diameter of the spheres was measured by using a high-resolution camera (Prosilica GC1380) with a pixel size of 0.85 μm per pixel (Kono et al., 2014b). A fixed value of 2.8 g·cm^{-3} was chosen for the density of molten APR16 according to the work by Sakamaki et al. (2013) considering, however, that a difference up to ±1 g cm^{-3} would affect the viscosity value by 0.02 Pa·s. In addition, the uncertainty in the diameter of the probing sphere contributes to errors in viscosity due to the small sphere size. Our high-resolution X-ray radiography has a ±2 μm resolution in imaging (Kono et al., 2014b), which causes ±2.1-4.1% uncertainty in viscosity. Therefore, the overall uncertainty in our viscosity determination is <±9.3%. Supplementary Movie 1 (https://drive.google.com/file/d/18NH0TIpK8Bmx1lfJeM56-AzH7SCD6JQ9/view?usp=sharing) shows the falling Pt sphere in APR16 melt at ~ 1.4 GPa and ~ 1440 °C in real time. The radiographic images were collected during heating of the run until the fall of the sphere could be observed. Supplementary Figures S4-S10 show diagrams of the falling distance versus time and falling velocity versus distance of the Pt sphere for the runs of this study.

Melt structure measurements

Liquid structure studies are conducted by the multi-angle energy-dispersive X-ray diffraction technique. A large Huber stage holding a Ge solid state

detector (Ge-SSD) allows precise control 2θ angle from 2° to 39.5°. For diffracted X-rays, two slits are located on the diffractometer arm: one near the sample (around 60 mm from the centre) and the other in front of the detector (at around 480 mm distance). The detector arm also supports the Ge-SSD with a liquid nitrogen dewar. The collimation depth control is important to liquid scattering measurement for discriminating sample signal from background scattering caused by surrounding materials. Diffraction patterns were collected at 10 fixed diffraction angles (2θ = 3°, 4°, 5°, 7°, 9°, 12°, 16°, 22°, 28°, 35°) to cover a wide range of scattering vectors (Q). Interference functions and structure factors were calculated using the scattering intensity and atomic scattering factors. In particular, the factor structure S(Q) was calculated using the following formula:

$$S(Q) = \{I^{coh}(Q) - \sum_{i=1}^{m} f_i{}^2(Q)\}/\{\sum_{i=1}^{m} f_i(Q)\}^2 \quad (9),$$

where $I^{coh}(Q)$ is the coherent intensity resulting from the correlations of atoms, $f_i(Q)$ is the atomic scattering factors of the i-th atom, and the summation is taken over the formula unit. Q is scattering vector. The local structures in real space (Figure 2 and Supplementary Figures S11-S13) are given by the radial distribution function, G(r), as proposed by Kaplov et al. (1965), obtained by taking the Fourier transform of $S(Q)$:

$$G(r) = \frac{2}{\pi}\int_0^{Q_{max}} Q\{S(Q) - 1\}\sin(Qr)dQ \quad (10),$$

where r is the radial distance. More details of this methods are described in Yamada et al. (2011b). The peaks position, finally, was obtained by Gaussian fitting of the peaks.

Acknowledgments

This work was performed at HPCAT (Sector 16), Advanced Photon Source (APS), Argonne National Laboratory. HPCAT operation is supported by DOE-NNSA under Award No. DE-NA0001974, with partial instrumentation funding by NSF. The Advanced Photon Source is a U.S. Department of Energy (DOE) Office of Science User Facility operated for the DOE Office of Science by Argonne National Laboratory under Contract No. DE-AC02-06CH11357.

Chapter 3

Trace element partitioning between clinopyroxene and alkali basaltic melt: investigation at high pressure on a primitive composition from the Campi Flegrei Volcanic district (Italy)

Barbara Bonechi[a], Cristina Perinelli[a], Mario Gaeta[a], Alessandro Fabbrizio[b], Maurizio Petrelli[c], Ladislav Strnad[d]

a: Dipartimento di Scienze della Terra, Sapienza Università di Roma, P. le Aldo Moro 5, 00185, Rome, Italy

b: Institute of Petrology and Structural Geology, Faculty of Science, Charles University, Albertov 6, 12843 Prague, Czech Republic

c: Department of Physics and Geology, University of Perugia, Piazza Università, Perugia 06100, Italy

d: Laboratories of the Geological Institutes, Charles University, Albertov 6, Prague 2, CZ-12843, Czech Republic

Under review in *Geochimica et Cosmochimica Acta*

Abstract

We present new experimental data on major and trace element partition coefficients (*D*) between clinopyroxene and a K-basaltic melt from Procida Island (Campi Flegrei Volcanic District, south Italy). Time-series experiments were conducted at 0.8 GPa and 1080-1250 °C aiming to investigate the role of the crystallization kinetics on trace elements partitioning behaviour at a pressure relevant for deep magmatic reservoirs. Results indicate that large ion lithophile elements (LILE) are incompatible (e.g., $D_{Sr} \leq 0.15$), light rare elements (LREE; e.g., $D_{La} \leq 0.20$) are always more incompatible than heavy rare elements (HREE), which in some cases result to be compatible with clinopyroxene (e.g., $D_{Dy} = 1.40$); high field strength elements (HFSE) are generally incompatible ($D_{HFSE} \leq 0.8$), while transition elements (TE) range from slightly incompatible (e.g., $D_{V} = 0.6$) to highly compatible (e.g., $D_{Cr} = 63$). The calculated *D* values for LILEs, REEs, HFSEs, and TEs tend to decrease with the increase of temperature and to increase with increasing tetrahedrally-coordinated aluminium content, in agreement with the previous studies. Moreover, we observed the influence of the growth rate on the partition coefficients, with the highest D_{REE} values calculated in the runs with the highest growth rate (~10^{-7} cm s^{-1}), due to the less efficient rejection of incompatible elements during rapid crystal growth, that in this study is not linked to disequilibrium conditions, but to the presence of pre-existing nuclei. Finally, the apparent increase in D_{REE} values with time observed in some runs is not referable to a change in time but rather to the different degrees of polymerization, expressed as the ratios NBO/T of these melts, strictly related to a loss of Fe occurred during the experiments, and thus to a different melt viscosity. Finally, the application

of the experimental clinopyroxene/melt partition coefficients highlights that the deepest step of the magmatic differentiation in the Campi Flegrei Volcanic District is represented by the fractionation of about 20-30% of a clinopyroxenitic mineral assemblage from a basaltic parental magma.

Keywords: clinopyroxene; trace element partition coefficient; lattice strain model; order-disorder crystal growth; fractional crystallization

1. Introduction

A central factor in the evolution of an igneous body is the partitioning of elements between the melt and the crystallizing minerals. The partition coefficient of an element *i* (D_i) has been defined as its concentration in a mineral divided by the concentration of that element in the coexisting melt (Blundy and Wood, 1994; Jones, 1995) and describes the chemical distribution between coexisting phases under equilibrium conditions. Most partition coefficients, indeed, are usually investigated presupposing equilibrium conditions, assuming thus that natural systems are characterized by chemical homogeneity of melt and crystals and that these systems evolve slowly enough to allow for continuous re-equilibration between melt and growing crystals (e.g., Onuma et al., 1968; Higuchi and Nagasawa, 1969; Philpotts and Schnetzler, 1970; Schnetzler and Philpotts, 1970). However, disequilibrium conditions are not unusual in natural systems affecting thus crystal-melt partitioning and relative partition coefficients, as observed by Albarede and Bottinga (1972). The resulting disequilibrium partition coefficients can be used as sensitive monitors of magmatic processes such as fractional crystallization, assimilation, mixing

and partial melting of crustal or mantle rocks (e.g., Leeman and Phelps, 1981; Mahood and Hildreth, 1983; Drexler et al., 1983; White, 2003; Henderson and Pierozynski, 2012; Arzilli et al., 2018). Indeed, as shown in several studies, in some natural igneous systems, events of rapid crystal growth (driven by the undercooling degree) can produce an excessive accumulation or depletion of elements, depending on their degree of compatibility or incompatibility, at the crystal-melt interface with a consequent disequilibrium element uptake during crystal growth (e.g., Albarede and Bottinga, 1972; Watson, 1996; Morgan and London, 2003; Watson and Müller, 2009; Mollo et al., 2011, 2013; Arzilli et al., 2018) with respect to under equilibrium conditions (e.g., Morgan and London, 1996; Lofgren et al., 2006; Mollo et al., 2011, 2013). Therefore, trace elements partitioning results to be controlled by kinetic effects such as diffusive re-equilibration and undercooling degree (Arzilli et al., 2018; Shea et al., 2019) as well as by temperature and pressure (Shimizu, 1974; Green and Pearson, 1983; Ray et al., 1983; Green and Pearson, 1985; Gallahan and Nielsen, 1992; Jones, 1995; Blundy and Wood, 2003; McDade et al., 2003; Sun and Liang, 2012; Yao et al., 2012; Bédard, 2014; Mollo et al., 2018), mineral composition (Yagi and Onuma, 1967; Onuma et al., 1968; Colson et al., 1988; Blundy and Wood, 1991, 1994; Skulski et al., 1994; Lundstrom et al., 1998; Hill et al., 2000; Bédard, 2010; Mollo et al., 2016), melt composition (Mysen and Virgo, 1980; Ray et al., 1983; Nielsen, 1985; Gallahan and Nielsen, 1992; Bennett et al., 2004; Gaetani, 2004), and redox conditions (Aigner-Torres et al., 2007; Cartier et al., 2014; Dygert et al., 2020). Furthermore, among the works focused on the influence of the crystallization kinetics on the partition coefficients (Albarede and Bottinga, 1972; Morgan and London, 2003;

Lofgren et al., 2006; Milman-Barris et al., 2008; Mollo et al., 2011, 2013; Arzilli et al., 2018; Shea et al., 2019), only a few are relative to clinopyroxene (Shimizu, 1981; Lofgren et al., 2006; Mollo et al., 2013). The work of Shimizu (1981) investigates the kinetics effect on sector-zoned augite phenocrysts being a clear case of disequilibrium crystallization. Lofgren et al. (2006) performed equilibrium and dynamic crystallization experiments at cooling rates in the range 5-1000 °C/h to explore the effects of kinetics on *D*-values. Mollo et al. (2013), instead, determined trace element partition coefficients at the interface between clinopyroxene rims and co-existing glasses resulting from isothermal and cooling rate experiments. The study of the factors influencing trace element partitioning is of paramount importance since the latter are frequently used in petrological and geochemical studies to better understand magmatic processes, like fractional or equilibrium crystallization, assimilation, and partial melting (e.g., Mollo et al., 2016). This is because clinopyroxene has crystal-melt REE partition coefficients approximately up to 4 orders of magnitude higher than other mafic rock-forming minerals (e.g., olivine and orthopyroxene; Chen and Zhang, 2009; Sun, 2018), exerting, therefore, a strong control on the overall partitioning of the crystallising assemblage. In this study, we present a new set of partition coefficient data derived from synthetic clinopyroxenes in equilibrium and in disequilibrium with a K-basaltic composition from the Campi Flegrei Volcanic District (CFVD) as a function of temperature and time. The investigated pressure condition is of 0.8 GPa that for the CFVD area represents the depth of the crustal-mantle boundary (~25 km of depth; Fedi et al., 2018). Moreover, for having a comparison term we measured the trace element concentrations in some natural clinopyroxene phenocrysts

belonging to some scoria clasts from Procida island. The main aim of this work, indeed, is to fill the following lacks: *i*) the scarcity of quantitative experimental data on the role of the crystallization kinetics on trace elements partitioning behaviour relative to high-pressure conditions and relevant for deep magmatic reservoirs; *ii*) the absence of clinopyroxene-melt partition coefficient experimental data for primitive compositions in the CFVD area. Furthermore, based on the evidence relating to the stages of deep crystallization of the Campi Flegrei Volcanic District parental magmas (Di Stefano et al., 1999; Piochi et al., 2005; Chiarabba et al., 2008; Mormone et al., 2011; Moretti et al., 2013; Fedi et al., 2018), we explored the mineral assemblage involved in the magmatic differentiation at the deepest ponding level, by using the experimental results of this study.

2. Methods

2.1. Samples description

Synthetic samples were obtained through crystallization experiments performed by using the ½ inch end loaded piston cylinder apparatus at the HP-HT Laboratory of the Earth Sciences Department (Sapienza University, Rome, Italy) at 0.8 GPa, 1080-1250 °C, $1 \leq H_2O \leq 4$ wt.%, with durations of 0.25, 3, 6 and 9 hours. For these experiments we used two different starting materials: the APR16 powder and the APR16GL glass (Table 1), both obtained from a natural primitive K-basalt (APR16 sample) found as scoria clast in the deposits of the Solchiaro hydromagmatic eruption (~22 ka ago; Morabito et al., 2014) located in Procida island (Campi Flegrei, Italy). This K-basalt is characterized by 12 vol.% of forsteritic olivine and diopsidic clinopyroxene phenocrysts dispersed in a groundmass made of olivine,

clinopyroxene, plagioclase, Ti-magnetite, alkali feldspar and glass (D'Antonio et al., 1999; De Astis et al., 2004). The APR16 powder, already used as starting material in the experimental runs of Bonechi (2020) (Table 2), was obtained by grinding the natural APR16 rocky sample in an agate mortar under acetone. The APR16GL, instead, used as starting material in the runs of Bonechi et al. (2020b) (Table 2), was prepared by melting for 15 min the APR16 natural powder in a 1 atm gas-mixing (CO-CO_2) furnace installed at the Bayerisches Geoinstitut (Bayreuth, Germany) at 1400 °C and oxygen fugacity corresponding to the NNO (nickel-nickel oxide) buffer. Then, the obtained glassy starting material was grinded in an agate mortar under acetone. Compositions of synthetic clinopyroxenes were compared with natural clinopyroxene phenocrysts occurring in the SCE and SOG scoria clasts, belonging to the Solchiaro eruption. The SCE and SOG samples (Table 1 and Supplementary Material 1) are porphyritic, scarcely vesiculated rocks containing ~10-20 vol.% of medium-grained olivine and clinopyroxene phenocrysts (olivine/clinopyroxene ratio ~1). A detailed description of these samples is reported in Bonechi et al. (2020b).

2.2. Experimental techniques

The detailed experimental procedure is described by Perinelli et al. (2019) and by Bonechi et al. (2020a, 2020b). Here we report the main aspects. The assembly consists of an outer CaF_2 cell, graphite furnace and MgO crushable spacers. The experimental charges were prepared loading $Au_{75}Pd_{25}$ capsules with ~40 mg of sample powder. For hydrous experiments we added water in known amounts by using a 1.0 μL microsyringe (Table 2). Loss of H_2O by vaporization during welding was prevented by freezing the crucible with

nitrogen. The welded capsule was weighed, stored in a furnace at 110 °C, and then weighed again to confirm the absence of water leaks. Moreover, to prevent possible loss of H_2 the charges were surrounded by pyrophyllite powder (Freda et al., 2001). Capsules of less 7-mm long were used in order to maintain the samples in the furnace hot spot. Temperature was measured using a type D W_3Re_{97}-$W_{25}Re_{75}$ thermocouple and maintained with an uncertainty of ± 5 °C. The experimental assembly was first pressurized to the target pressure by a piston-out procedure (Johannes et al., 1971; Presnall et al., 1978) that applies an overpressure of ~ 10 % of the run pressure and then gradually increases the temperature to the final temperature, while correcting for pressure drops due to stress relaxation within the assembly during heating. The heating rate was imposed at 150 °C/min. The sample was maintained at the pressure and temperature for a given duration (nominal duration), and then quenched by turning off the power. The temperature drop below 500 °C was of <5 s (average cooling rate of 150 °C/s). All the runs were self-buffered; an estimation of experimental oxygen fugacity (fO_2) was made through the equation of Kress and Carmichael (1991). To use this equation, where possible, we first assessed the FeO content of experimental residual glass, and then its Fe^{2+}/Fe_{tot} mole ratio; to do this we used the value of iron and magnesium partitioning between olivine and liquid (K_D Fe-Mg ol/liq) calculated according to the procedure proposed by Toplis (2005). Therefore, the application of Kress and Carmichael (1991) equation residual glass of each experiment, yielded fO_2 values between of -1.9 and +0.9 log-bar units with respect the nickel-nickel oxide buffer. As a whole the estimated range of fO_2 value is in agreement with those estimated for similar furnace assemblages (Conte et al., 2009;

Weaver et al., 2013; Perinelli et al., 2019; Bonechi et al., 2020a). Finally, we determined the effective undercooling (ΔT_{eff}) that is the difference between the equilibrium clinopyroxene liquidus temperature (T_{CpxL}) and the experimental temperature (Bonechi et al., 2020a, 2020b; Bonechi, 2020). The T_{CpxL} values used to calculate ΔT_{eff} for each experiment were taken from Procida K-basalt experimental data (Perinelli et al., 2019) and from calculations using MELTS software (Ghiorso and Sack, 1995; Asimow and Ghiorso, 1998).

Table 2 Experimental conditions of the experimental samples

Runs	Starting material	P (GPa)	T (°C)	ΔT (°C)	Time (h)	G_{LCpx} (cm s^{-1})	H_2O_i (wt.%)	H_2O_f (wt.%)	NBO/T	Phases	% ΔFe§	References
APR16-1C	APR16	0.8	1225	55	3	$1.59 \cdot 10^{-7}$	NWA	0.96	0.82	Gl(94) + Cpx(6) + Ol# + Ox#	-5	Bonechi (2020)
APR16-35	APR16	0.8	1225	55	6	$8.34 \cdot 10^{-8}$	NWA	1.7	0.80	Gl(96) + Cpx(4) + Ol#	-22	
APR16-C1Ac	APR16GL	0.8	1250	45	6	$2.06 \cdot 10^{-8}$	NWA	2.03	0.78	Gl(83) + Cpx(15) + Ol(2)	-20	Bonechi et al. (2020b)
APR16-C1Ad	APR16GL	0.8	1250	45	9	$1.73 \cdot 10^{-8}$	NWA	1.95	0.85	Gl(90) + Cpx(10)	-19	
APR16-C2Aa	APR16GL	0.8	1220	50	0.25	$3.24 \cdot 10^{-7}$	2	1.92	0.92	Gl(91) + Cpx(4) + Ol(1) + Ox(4)	-25	
APR16-C2Ab	APR16GL	0.8	1220	50	3	$3.04 \cdot 10^{-8}$	1.9	1.56	0.61	Gl(72) + Cpx(23) + Ol(4) + Plg(1) + Ox*	-17	
APR16-C2Ac	APR16GL	0.8	1220	50	6	$2.67 \cdot 10^{-8}$	2.1	2.47	0.60	Gl(65) + Cpx(27) + Ol(5) + Plg(3)	-25	
APR16-C2Ad	APR16GL	0.8	1220	50	9	$1.93 \cdot 10^{-8}$	1.9	1.3	0.70	Gl(80) + Cpx(17) + Ol(3) + Ox*	-26	
APR16-C2Bc	APR16GL	0.8	1170	100	6	$2.77 \cdot 10^{-8}$	2	3.77	0.67	Gl(58) + Cpx(33) + Ol(5) + Plg(1)	-27	
APR16-C2Bd	APR16GL	0.8	1170	100	9	$2.34 \cdot 10^{-8}$	1.8	2.02	0.61	Gl(57) + Cpx(34) + Ol(2) + Plg(3) + Ox(4)	-4	
APR16-C3Ac	APR16GL	0.8	1080	144	6	$1.31 \cdot 10^{-8}$	3.8	6.5	1.00	Gl(60) + Cpx(37) + Ol(3)	-10	Bonechi et al. (2020a)

Notes: Gl glass; Cpx clinopyroxene; Ol Olivine; Plg plagioclase; Ox oxide. ΔT is the difference between the Cpx liquidus temperature and the nominal temperature of the runs; G_L is the growth rate taken from Bonechi et al. (2020b); H_2O_f = water content in the melt determined by the by-difference calculation method (respect to the total of EMP analyses); NBO/T is the ratio of non-bridging oxygens to number of structural tetrahedra in the liquid calculated as in Mysen (1985). § Percent of relative Fe loss from starting material based on difference between the starting material and calculated bulk composition of experiment obtained from mass-balance calculations. * crystals present in trace; # pre-existing crystals.

2.3. Analytical techniques

2.3.1. Textural investigations and major element determinations

Back-scattered electron (BSE) images used to investigate textural aspects of both natural and experimental samples were collected by Scanning Electron Microscopy (SEM) using a FEI-quanta 400 equipped for microanalysis with an EDAX Genesis system at the Earth Sciences Department, Sapienza University of Rome. Major elements were analysed at the CNR-Istituto di Geologia Ambientale e Geoingegneria di Roma, with a Cameca SX50 electron microprobe equipped with five wavelength dispersive spectrometers (WDS). Quantitative analyses were performed using 15 kV accelerating voltage and 15 nA beam current. As standards we employed metals for Mn and Cr, Jadeite for Na, Wollastonite for Si and Ca, Orthoclase for K, Corundum for Al, Magnetite for Fe, Rutile for Ti, Periclase for Mg, Apatite for P. Counting times for all elements were 20 s on peak and half time on both backgrounds. Light elements (Na, K) were counted first to prevent loss by volatilization. The PAP correction method was used. Minerals were analysed using a beam diameter of 1 μm whereas to minimize alkali loss during glass analysis, the beam was defocused to 15 μm. In order to evaluate the accuracy of the analyses, repeated analyses of three international secondary standard (Kakanui augite, Iceladic Bir-1 and rhyolite RLS132 glasses from USGS) were made prior to any series of measurements. The mean precision from the standard value was about 1% for SiO_2, 2% for Al_2O_3, 5% for K_2O, CaO and FeO, and 8-10% for other elements. Moreover, the analytical precision (2 sigma error) is ≤ 1% for elements in the concentration range > 10 wt% oxide, 5% for elements in the range 2–10 wt% oxide and better than 10% for elements in the range 0.5–2

wt% oxide. From chemical analyses, the water contents of experimental glasses were estimated according to the by-difference method (Devine et al., 1995; Humphreys et al., 2006). We are aware that this method fully reliable given the estimation is affected by *i*) element concentrations not measured by EMPA and *ii*) surface charge effects (Hughes et al., 2019) leading to an overestimation of H_2O concentration. However, the obtained H_2O values are close to those determined by micro-Raman spectroscopy measurements on residual melts of equilibrium experiments performed on the same composition, at the same *P*, *T* and initial hydrous conditions (see Perinelli et al., 2019, for details).

2.3.2. Laser ablation-inductively coupled plasma mass spectrometry (LA-ICP-MS)

LA-ICP-MS analyses were performed on both natural (SCE and SOG samples) and experimental samples. LA-ICP-MS analyses of SCE and SOG natural samples were performed on a quadrupole–based ICP-MS iCAP-Q instrument (Thermo Fisher Scientific, Bremen) coupled to a modified NewWave UP 213 laser microprobe (NewWave, USA) installed at Charles University, Prague. Analyses of natural clinopyroxene crystals were performed using a circular laser beam of 100 μm diameter, a frequency of 10 Hz and a laser density on the sample surface of 3.5 J/cm^2. External calibration of the laser ablation analyses was done using Standard Reference Materials NIST (National Institute of Standards and Technology, USA) 612 with internal standardisation using Si, based on electron microprobe measurements. The concentration values for NIST of all measured elements were taken from Pearce et al. (1997). The external reproducibility of this

method was checked on repeated analyses of USGS BCR-2G glass as reference material (e.g., Strnad et al., 2005 and reference therein; Table S1 in Supplementary Material 2). The isotopes used were selected with respect to their most abundant species, free from isobaric overlap and minimum interferences. Formation of oxides (MO^+/M^+) was monitored using U in NIST 612 directly from ablation and the measured ratios ($^{254}UO^+/^{238}U^+$) was below 10^{-2}. Further details about the analytical protocol and correction strategy have been described by Strnad et al. (2005) and Skála et al. (2009). Detection limits for all elements were calculated as 3σ level of the gas blank (Table S1 in Supplementary Material 2). LA-ICP-MS analyses of the experimental samples were performed at the Department of Physics and Geology, University of Perugia (Italy). The instrumentation consisted of a Teledyne/Photon Machine G2 LA device equipped with a Two-Volume ANU HelEx 2 cell coupled with a Thermo Fisher Scientific quadrupole-based iCAP-Q ICP-MS. Analyses of clinopyroxene crystals and glasses were performed using a circular laser beam of 8-20 μm diameter, a frequency of 10-15 Hz and a laser density on the sample surface of 3.5 J/cm^2. Oxide formations was measured on the NIST SRM 612 monitoring and maintaining the ratio ThO/Th below 0.005. The NIST SRM-610 standard reference material was used as calibrant and Ca, previously analysed by EPMA, as internal standard. Under these operating conditions precision and accuracy are better than 10% for most of the elements (Petrelli et al., 2007, 2008, 2016). In detail, at beam sizes equal or larger than 15 μm, precision (measured as one sigma) and accuracy (expressed as relative deviation from the reference value) are of the order of 10% (Petrelli et al., 2016). At a smaller beam size of 8 um, precision decreases to 15% for

concentration above 1.7 μg g^{-1} (Petrelli et al., 2016). Accuracy is better or equal to 10% and 13% at beam sizes of 15 and 10 μm, respectively (Petrelli et al., 2016). When the spatial resolution is increased to 8 μm, accuracy remains better than 15% (Petrelli et al., 2016).

3. Results

3.1 Phase relations

Experimental samples investigated in this study are described in detail in previous works (Perinelli et al., 2019; Bonechi et al., 2020a, 2020b; Bonechi, 2020). Here we briefly report a description of the paragenesis of these samples given the importance of the coexistence of several phases for the fractionation of some trace elements, like the presence of plagioclase for the fractionation of Eu. Overall, the experimental products consist of glass and microlites of clinopyroxene (Cpx) ± olivine (Ol) ± plagioclase (Plg) ± oxide (Ox). In particular, the APR16-1C and APR16-35 runs (1225 °C), performed using the natural starting material APR16, are characterized by the presence of glass (Gl) and Cpx plus restitic Ol and Ox. In the runs performed at 1250 °C (APR16-C1Ac and APR16-C1Ad), the dominant phase is Cpx while olivine (Ol) crystallizes only in the APR16-C1Ac run. The mineral phases crystallized in the runs at 1220 °C (APR16-C2Aa, APR16-C2Ab, APR16-C2Ac, APR16-C2Ad) are Cpx + Ol + Plg + Ox. Clinopyroxene and Ol are ubiquitous in these runs, whereas Plg is present only in the runs at 3 and 6 hours (i.e., APR16-C2Ab, APR16-C2Ac) and Ox is absent in the run APR16-C2Ac. The runs at 1170 °C (APR16-C2Bc and APR16-C2Bd) show a higher degree of crystallization and the mineral assemblage is Cpx + Ol + Plg ± Ox. Finally, the hydrous run at 1080 °C (APR16-C3Ac; 6.5 wt.% H_2O) shows a

degree of crystallization similar to that of the runs at 1170 °C and the phases crystallized are Cpx and Ol.

3.2. Texture and chemical composition of experimental samples

Clinopyroxene. Chemical compositions of Cpx are given in Table S2 in Supplementary Material 2. Overall synthetic Cpx crystals are characterized by homogeneous composition and euhedral habits (Fig. 1a-c). In particular, in the runs performed using the glassy starting material (i.e., APR16GL) habit and sizes vary with time: subhedral with sizes of ~5 μm in the shortest run (e.g., APR16-C2Aa; 0.25 h; Fig.1a) and euhedral with sizes up to ~20 μm in the longest run (≥ 3 h; Fig. 1b). The runs APR16-1C and APR16-35, performed using the natural starting material (i.e., APR16 natural powder), instead, are characterized by euhedral habit and sizes up to ~50 μm (Fig. 1c) (Bonechi, 2020).

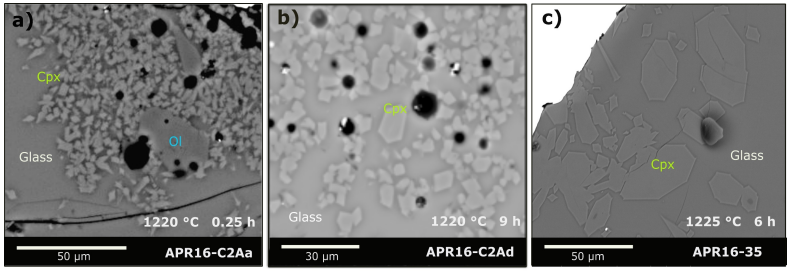

Fig. 1. *Backscattered (BSE) images of experimental samples. Details of the experimental conditions are reported at the bottom of each image. Figures a) and b) show the variation of habit and sizes with time in the runs performed using the glassy starting material (i.e., APR16GL): a) subhedral Cpx with sizes of ~5 μm in the shortest run APR16-C2Aa (0.25 hours) and b) euhedral Cpx with sizes up to ~20 μm in the longest run APR16-C2Ad (9 hours); c) Cpx with euhedral habit and size up to ~50 μm crystallized in the APR16-35 run performed using the natural starting material (i.e., APR16 natural powder). Abbreviation: Cpx: clinopyroxene; Ol: olivine; Gl: glass.*

These Cpx crystals are augitic ($Wo_{42}En_{41}Fs_{18}$) and diopsidic ($Wo_{47}En_{43}Fs_{10}$) in composition according to the classification scheme of Morimoto et al. (1998) (Fig. 2a). Overall, the Mg# of Cpx (calculated as the molar $MgO/(MgO+FeO_{tot})$ ratio) varies between 0.81 and 0.92, the TiO_2 contents are between 0.58 and 1.18 wt.% while those of Al_2O_3 are between 5.00 and 9.49 wt.%. The Fe–Mg distribution coefficients between clinopyroxene and melt ($K_D(Fe\text{-}Mg)^{Cpx\text{-}liq} = Fe_{Cpx} \times Mg_{liq}/Mg_{Cpx} \times Fe_{liq}$, calculated assuming all Fe as Fe^{2+} in both phases), for the longest runs ≥ 3 hours lie in the equilibrium range of 0.28±0.08 (Putirka, 2008) whereas the shortest experiment (APR16-C2Aa) shows significant deviation from the equilibrium (Table S2 in Supplementary Material 2).

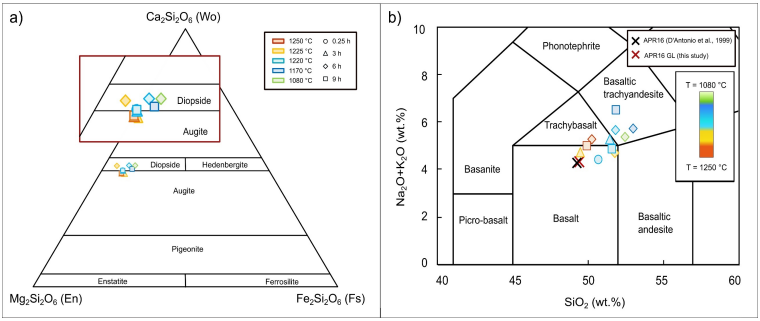

Fig. 2. *a) Clinopyroxene compositions plotted into the pyroxene classification diagram (Morimoto et al., 1998). Wo: wollastonite; En: enstatite; Fe: ferrosilite. The inset show a magnification of the area of interest. Synthetic samples are indicated with different colours: in orange the runs at 1250 °C, in yellow the runs at 1225 °C, in light blue the runs at 1220 °C, in blue the runs at 1170 °C, in light green the run at 1080 °C. Duration of the experimental runs is indicated with different symbols: circle for 0.25 hours, triangle for 3 hours, diamond for 6 hours and square for 9 hours. b) Composition of the experimental glasses plotted in the TAS diagram (Le Maitre et al., 2002). Coloured bar indicates the variation of temperature of the runs that decreases from red to green. Symbols are as in Fig. 2a. Crosses indicate the APR16 (in black) and the APR16GL (in red) starting materials.*

Glass. Chemical compositions of experimental glasses are given in Table S3 in Supplementary Material 2. Glass composition of anhydrous and hydrous experiments varies from K-basalt to K-trachybasalt up to shoshonite compositions with decreasing temperature (Fig. 2b). In particular, in the anhydrous runs, before reaching the temperature at which plagioclase significantly crystallizes, the glass composition is controlled by clinopyroxene crystallization thus leading to a very limited SiO_2 increase in the residual glasses (Perinelli et al., 2019). In the hydrous experiments, the earlier crystallization of olivine ± spinel causes a slightly more marked increase of SiO_2 abundance in the residual glasses (from ~52 to ~53 wt.%; Table S3 in Supplementary Material 2).

3.3. Trace and REE content

Average compositions of trace elements concentrations analysed by LA-ICP-MS technique in synthetic clinopyroxene and coexisting glass are reported in Table 3.

3.3.1. Clinopyroxene

Figure 3 shows the trace elements concentrations in synthetic and natural clinopyroxene normalized to chondrite C1 after Anders and Grevesse (1989) for LILEs (Large-Ion Lithophile Elements), REEs + Y (Rare Earth Elements plus Yttrium), HFSEs (High Field Strength Elements) and TEs (Transition Elements). In this diagram some LIL elements (e.g., Rb and Ba) of synthetic Cpx crystals display different relative abundances depending on experimental conditions unlike the REEs that instead, show quite uniform high contents. In particular, the chondrite-normalised REE patterns have a

general L/HREE (Light/Heavy rare earth element) enrichment (i.e., La_N/Yb_N = 0.85-1.20, where the subscript *N* denotes chondrite-normalized values) with a maximum at Sm_N (~20-37). The REE profiles from the crystallized cpx are comparable to each other with the exception of the clinopyroxene in the APR16-C2Bd charge that shows an evident Eu negative anomaly (Eu/Eu* = 0.58; $Eu/Eu^* = Eu_N/(Sm_N \times Gd_N)^{1/2}$), likely due to the crystallization of plagioclase in this run. Indeed, the lack of plagioclase in the hydrous experiment APR16-C3Ac, justifies the absence of troughs at Eu (Eu/Eu* = 0.95), despite both crystallization degree and amount of Cpx crystallized in this experiment are similar to that of APR16-C2Bd run (40 wt.% and 43 wt.%, and 33 wt.% and 34 wt.%, respectively; Table 2). Finally, tetravalent HFSEs (i.e., Zr and Hf) have a higher concentration than pentavalent cations (i.e., Ta and Nb), while as regards TEs, it is possible to see evident troughs at Co and Ni.

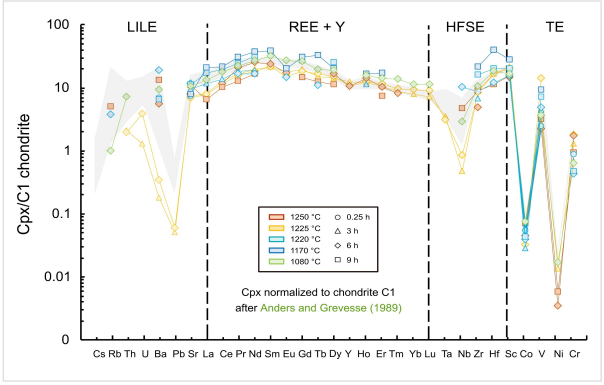

Fig. 3. *C1-normalized (Anders and Grevesse, 1989) trace elements abundances for synthetic clinopyroxenes. Symbols are as in Fig. 2. For comparison we reported C1-normalized trace elements abundances for natural Cpx (SCE and SOG samples; Supplementary Material 1), indicated with the grey field.*

3.3.2 Glass

Figure 4 shows the trace elements concentration in the experimental glasses normalized to chondrite C1 after Anders and Grevesse (1989) for LILEs, REEs + Y, HFSEs and TEs. Generally, all the experimental glasses match the trend of the APR16 sample (Mazzeo et al., 2014), with evident troughs at Pb, Co and Ni. C1-normalized trace element diagrams are L-MREE enriched (La_N = 58-90, La_N/Sm_N = 2.09-2.66, La_N/Yb_N = 5.30-8.58) and nearly flat in the HREE region (Ho_N/Yb_N 1.01-1.48). All the considered glasses have absent or slightly positive Eu anomaly (Eu/Eu* 0.95-1.10; inset of Fig. 4). Eu/Eu* ratio decreases with increasing degree of chemical evolution with the lowest values observed in APR16-C2Bd run (see TAS diagram in Fig. 2b). Moreover, pentavalent HFSEs (i.e., Ta and Nb) are more abundant than tetravalent cations (i.e., Zr and Hf), unlike what was observed for Cpx crystals.

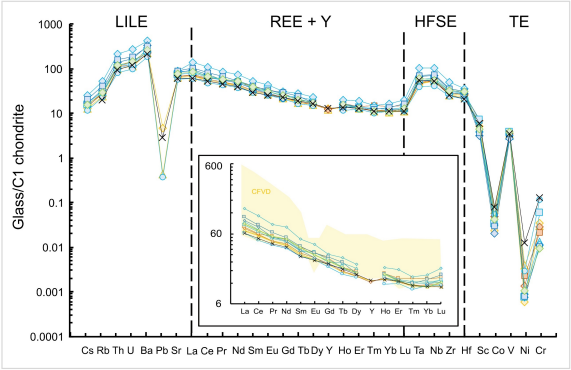

Fig. 4. *C1-normalized (Anders and Grevesse, 1989) trace elements abundances for analysed synthetic glasses. Symbols are as in Fig. 2. Black crosses indicate data for the APR16 natural samples from Mazzeo et al. (2014). The inset shows a magnification of REE + Y abundances. Yellow field represents REE abundances for natural glasses of Campi Flegrei Volcanic District (CFVD) products (data from GEOROC database; http://georoc.mpch-mainz.gwdg.de/georoc/Start.asp).*

3.4. Partition coefficients

The *D*-values for the REEs and other trace elements between minerals and melt (quenched to glass) for the reported experiments are given in Table 4. Figure 5 shows the partition coefficients between clinopyroxene and melt for LILEs, REEs + Y, HFSEs and TEs. LILEs are incompatible (e.g., $D_{Sr} \leq 0.15$, $D_{Ba} \leq 0.05$). LREEs (e.g., $D_{La} \leq 0.20$) are always more incompatible than HREEs, which in some cases result to be compatible with cpx (e.g., D_{Tb} and D_{Dy} = 1.30-1.40 for APR16-C2Bd and APR16-C2Ad experiments). It should be noted that any clear relationships are observed between D_i variation and dwell time for LREEs. In general, for MREE and HREE longest duration experiments (e.g., APR16-35 and APR16-C1Ad) are characterized by lower partitioning coefficients. In some cases, it was possible to note evident differences of D_i values as function of experimental time, as shown for instance by Dy behaviour in the runs at 1250 °C, where it results a compatible element in the 6 h-experiment (APR16-C1Ac; D_{Dy} = ~1) while it is moderately incompatible in the run at 9 hours (APR16-C1Ad; D_{Dy} = ~0.6). Furthermore, we observed that, except for the APR16-C3Ac run (the most hydrated run), the Eu behaves to a more incompatible extent than the adjacent REEs (i.e., Sm and Gd, Fig. 5). Given the low plagioclase abundance, this behaviour reflects only the Eu^{3+}/Eu^{2+} ratio variation caused by changing the redox conditions. As regards HFSEs, tetravalent and pentavalent-charged cations are always incompatibles (D_{Nb} and $D_{Ta} \leq 0.1$; D_{Zr} and D_{Hf} between 0.2 and 0.8), except for D_{Hf} measured in the cpx of the APR16-C2Bd run (D_{Hf} ~1.2). Finally, trace element partition coefficients of TEs (i.e., D_{Co}, D_{Cr}, D_{Ni}, D_{Sc} and D_V) range from slightly incompatible to highly

compatible. In particular, D_{Co} and D_{V} vary between 0.7 and 3, whereas D_{Sc}, D_{Ni} and D_{Cr} are between 2 and 63.

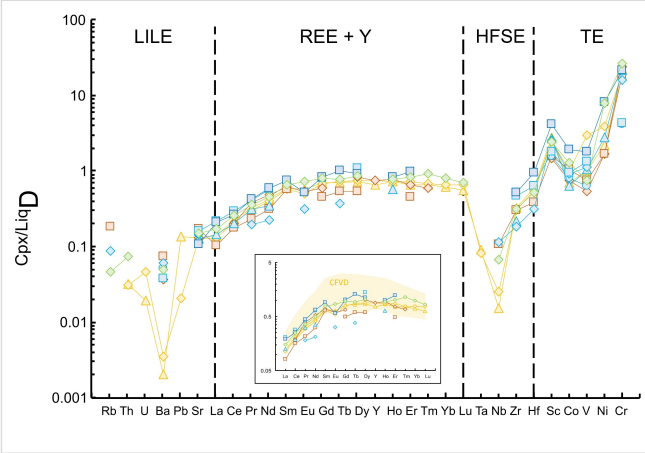

Fig. 5. *Calculated* $^{Cpx/L}D$ *values for trace elements in experimental samples. Symbols are as in Fig. 2. Yellow field represents* $^{Cpx/L}D_{REE}$ *values for natural Campi Flegrei Volcanic District (CFVD) products (data from Pappalardo et al. (2008), Fedele et al. (2009) and Mollo et al. (2016)).*

4. Discussion

4.1. Lattice strain model (LSM)

Assuming equilibrium, the cpx/melt partition coefficient is quantitatively described by the near-parabolic relationship (Brice, 1975; Blundy and Wood, 1994; Wood and Blundy, 1997; Sun and Liang, 2012):

$$D_j^{cpx-melt} = D_0 exp\left[\frac{-4\pi E N_A}{RT}\left(\frac{r_0}{2}\left(r_0 - r_j\right)^2 - \frac{1}{3}\left(r_0 - r_j\right)^3\right)\right] \quad (1),$$

where D_0 is the clinopyroxene-melt partition coefficient for the strain-free substitution; r_0 is the optimum radius for the lattice site; r_j is the ionic radius of the element of interest in the appropriate co-ordination taken from Shannon (1976) (Table S4 in Supplementary Material 2); E is the effective Young's modulus for the lattice site (GPa); R is the gas constant (8.3144 J mol^{-1} K^{-1}); N_A is Avogadro constant and T is temperature in K. The effective Young's modulus E controls the tightness of the parabola, and D_0 determines the apex of the parabola with corresponding ideal lattice site r_0. Cpx crystals are characterized by the general formula XYT_2O_6. The T site could contain tetrahedrally coordinated Si^{4+} and $^{VI}Al^{3+}$, whereas X and Y refer to two octahedral sites, a larger M2 site and a smaller M1 site (Sun, 2018). The M1 site is occupied by small cations in VI-fold coordination, including divalent Ni, Mg, Co and V, trivalent Al, Cr and Sc, tetravalent Ti, Hf and Zr, and pentavalent cations (e.g., Nb^{5+} and Ta^{5+}) (Blundy and Wood, 2003; Sun and Liang, 2012; Sun, 2018; Baziotis et al., 2019). The M2 site, instead, could host larger cations in VIII-fold coordination like monovalent Na, K and Rb, divalent Fe, Ca, Eu, Sr, Pb and Ba, trivalent REE (La to Lu) and Y, and tetravalent U and Th (Blundy and Wood, 2003). To apply the lattice strain model (LSM) to both M1 and M2 sites and fit the experimentally determined trace element partition coefficients simultaneously we used the DOUBLE FIT program (Dalou et al., 2018), a lattice strain model fit by a differential-evolution-constrained algorithm (Storn and Price, 1997) adapted to be error weighted. When errors are large, we individually fitted the M1 and M2 sites using the SIMPLE FIT program (Dalou et al., 2018). In presence of a low number of measured trace elements, the program failed to produce good fits. Therefore, following Dalou et al.

(2018), we reduced the parameter space from the default range ($D_0^{M1\text{-}M2}$min and/or $D_0^{M1\text{-}M2}$max; $E^{M1\text{-}M2}$min and/or $E^{M1\text{-}M2}$max; $r_0^{M1\text{-}M2}$min and/or $r_0^{M1\text{-}M2}$max) to overcome this limitation. Best-fit parabolas determined for divalent, trivalent, and tetravalent cations are plotted in Figure 6 and Figure S1 in Supplementary Material 3. Fit parameters E, D_0 and r_0 for trivalent cations in M2 site are reported in Table 5, together with E_c and r_c calculated following equations from Wood and Blundy (1997):

$$r_{0(M2)}^{3+} = 0.974 + 0.067X_{Ca}^{M2} - 0.051X_{Al}^{M1}(\mathring{A}) \quad (2),$$

$$E_{M2}^{3+} = 318.6 + 6.9P - 0.036T\ (GPa) \quad (3),$$

where X_{Ca}^{M2} and X_{Al}^{M1} refer to the atomic fractions of Ca and Al on the clinopyroxene M2 and M1 sites, P is in GPa and T in K. Fit parameters E, D_0 and r_0 for divalent cations in M1 and M2 site, and for trivalent and tetravalent cations in M1 site are reported in Table 5 and compared with E and r calculated using the model of Wood and Blundy (1997) for $M2^{2+}$ and that of Hill et al. (2011) for $M1^{4+}$. Following a method reported in the literature (Aigner-Torres et al., 2007; Padilla and Gualda, 2016), $D_{Eu^{3+}}$ and $D_{Eu^{2+}}$ were calculated using the LSM, based on the measured partition coefficients of other REE^{3+}, ideally close in ionic radius to Eu^{3+} (i.e., Gd and Sm), and Sr, respectively. These data were included in the data set of divalent ($D_{Eu^{2+}}$) and trivalent ($D_{Eu^{3+}}$) cations used for the fitting. For the fitting of trivalent cations in M1 site, Al in the M1 site was calculated as the difference between total Al and the Al^{IV} completing the occupancy of the tetrahedral site. As regards divalent cations, to understand their distribution

between M1 and M2 sites, we performed a preliminary fitting with DOUBLE FIT program, observing that *i*) Mn, Ca, Eu^{2+}, Sr, Pb and Ba partition only in M2 site; *ii*) Ni partitions only in M1 site; *iii*) Mg, Co and Fe, instead, partition in both M1 and M2 sites. At this point we fitted divalent cations entering only in M2 site (i.e., Mn, Ca, Eu^{2+}, Sr and ±Pb). The obtained lattice strain parameters were used to calculate D_{M2} of the elements entering both the M1 and M2 sites (i.e., Fe, Mg, Co). Then, using the concentration of these elements in the melt we calculated the concentrations of the elements in M2 and by difference in M1. Finally, we obtained D_{M1} for these elements (Table 5) dividing their concentration in M1 with that in the melt. In the fitting of the divalent cations in M1 site we constrained r_0 between 0.6 and 0.65 Å, based on the work of Purton et al. (1996).

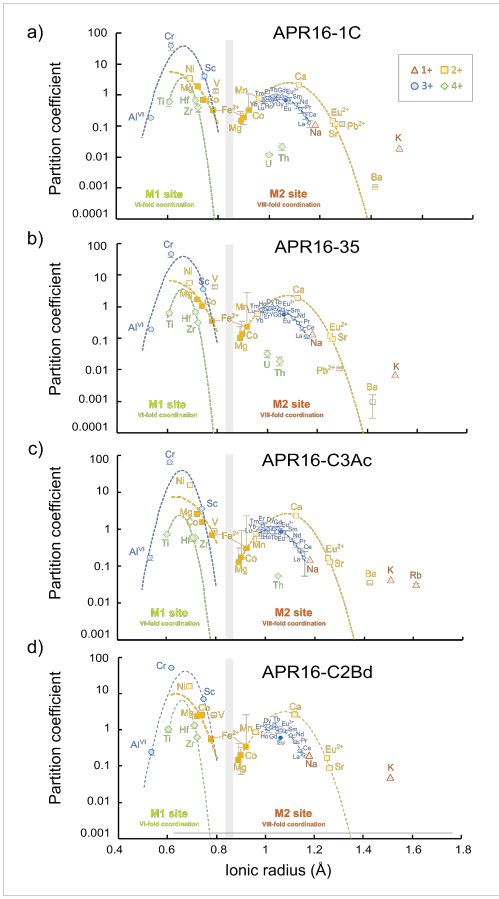

Fig. 6. *Onuma diagrams for clinopyroxene-liquid partition coefficients for mono-, di-, tri-, and tetravalent cations versus ionic radii (in Å; Shannon, 1976) for VI- and VIII-fold coordinated sites along with the results of the lattice strain fits in M1 and M2 sites for samples (a) APR16-1C (1225 °C, 3 hours), (b) APR16-35 (1225 °C, 6 hours), (c) APR16-C3Ac (1080 °C, 6 hours) and (d) APR16-C2Bd (1170 °C, 9 hours). The dotted curves represent the fits of the lattice strain model to* $^{Cpx/L}D_i$ *values while symbols represent measured* $^{Cpx/L}D_i$ *values. Cations are indicated as follow: monovalent with orange triangles, divalent with yellow squares, trivalent with blue circles and tetravalent with green diamonds. Ba and V (yellow empty squares) have not been used in the fit of the LSM for divalent cations. Yellow full squares indicate* D_i *calculated for M1 and M2 site. Blue full circle represents* D_{Eu} *measured in this study, plotted together with the calculated* D_{Eu3+} *and* D_{Eu2+} *values (see text for details).*

4.1.1. Onuma diagrams for divalent, trivalent and tetravalent cations

The partitioning behaviour for cations (D_i) with the same valence is conveniently shown in Onuma diagrams as a function of the ionic radius (Onuma et al., 1968; Leeman and Phelps, 1981; Blundy and Wood, 1994), indicating which elements are compatibles/incompatibles in a given site or which ones are fractionated between two distinct sites.

Divalent cations. Values of D_0, r_0 and E for divalent cations in M1 and M2 site as fitted to the experimental data are given in Table 5. For divalent cations in M1 site we obtained $D_0^{2+} = 6.07 \pm 2.02$, $E^{2+} = 499 \pm 45$ GPa, and $r_0^{2+} = 0.62 \pm 0.01$ Å (Fig. 6 and Fig. S1 in Supplementary Material 3). V^{2+} was excluded from the fitting since it falls outside the parabola, probably due to its presence as V^{5+}. The LSM parameters for the M2 site are $D_0^{2+} = 2.50 \pm 0.37$, $E^{2+} = 256 \pm 26$ GPa, and $r_0^{2+} = 1.08 \pm 0.01$ Å (Fig. 6 and Fig. S1 in Supplementary Material 3). The partitioning of divalent cations into M2 provides a good illustration of the control on partitioning by site size energetics. The linearized regressions for Fe, Ca, Eu^{2+}, Sr and $\pm Pb^{2+}$ produce good fits. Among these divalent cations, Ca^{2+}, that dominantly occupies the M2 site in clinopyroxene (Wood and Blundy, 2001), is the cation closer to the parabolas' apex and Sr is more compatible than Ba. However, the Ba position is far from the fit curve of divalent cations. This anomalous behaviour is probably due to the large ionic radius that produces a displacement of the nearest-neighbour ions in the charged region with an electrostatic work of substitution ($\neq 0$) in spite that of Ba is a fully charge-balanced substitution in the M2 site.

Trivalent cations. Among trivalent cations TEs (i.e., Cr and Sc) are compatible, LREEs are all incompatible, while HREEs are both compatible

and incompatible. Among REEs Dy and Er show the highest distribution coefficients, which tend to decrease with increasing the ionic radius (towards La). Because the HREEs (Dy through Lu) are more compatible than LREEs, clinopyroxene is slightly enriched in HREEs. The LSM parameters for the M1 and M2 sites are D_0^{3+} = 47 ± 18 and 0.85 ± 0.27, E^{3+} = 1456 ± 113 and 311 ± 10 GPa, and r_0^{3+} = 0.66 ± 0.01 and 1.03 ± 0.01 Å, respectively. The values of r_0^{3+} and E^{3+} in the M2 site match within the range of previous studies on basaltic compositions (r_0 = 1-1.05 Å, E = 325–441 GPa; Hill et al., 2011; Dalou et al., 2012; Mollo et al., 2016; Baudouin et al., 2020). Similarly, D_0^{3+} and E for the M1 site display similar values compared to other basaltic compositions ones (Hill et al., 2000; Dalou et al., 2012). Figure 6 and Figure S1 in Supplementary Material 3 show that our apparent partition coefficients for REEs lie on parabola-like curves of Onuma diagrams (Onuma et al., 1968), similar to the trajectories found by Pappalardo et al. (2008), Fedele et al. (2009) and Mollo et al. (2016) for differentiated magmas at Campi Flegrei. From these diagrams, also, it is possible to note the different partitioning behaviour of Eu, which occurs as both 2+ and 3+ cations, depending on fO_2. Particularly, if all Eu is present as Eu^{3+} D_{Eu} lies along the parabola defined by other REE^{3+}, whereas if Eu is present as Eu^{2+}, D_{Eu} lies along the 2+ parabola defined by Mn, Ca, Sr, ±Pb (Aigner-Torres et al., 2007). In all the runs of this study D_{Eu} lies along or close to the parabola defined by other REE^{3+}. In particular, D_{Eu} lies along the parabola in the APR16-C3Ac run (Fig. 6c), slightly below the parabola in APR16-1C, APR16-35 and APR16-C1Ac runs (Fig. 6a, b and Fig. S1 in Supplementary Material 3), and far below the parabola in the APR16-C2Bd runs (Fig. 6d). The Eu-anomaly is due to the presence of some Eu^{2+} in the melt, which is much less compatible in the M2

site than Eu^{3+} because of its larger size (Shearer et al., 2006). Moreover, in the APR16-C2Bd run, it is evident a clean-cut difference between D_{Eu3+} calculated and D_{Eu} measured (Fig. 6d). This latter indeed is much lower (~0.6) than D_{Eu3+} (~1) due to the crystallization of plagioclase in this run. The height of the parabola varies as a function of the crystal composition (Blundy and Wood, 1994, 2003) and the physical conditions of the system (Wood and Blundy, 2001; Sun and Liang, 2012). In the experimental runs the peak position can be alternatively higher or lower than 1 as a function of Al^{IV} content and temperature, in agreement with the observation that these parameters have opposing effects on trace element partitioning (Sun and Liang, 2012). For instance, we noted that the increase of Al^{IV} content, at a given temperature and under similar water content conditions, causes an increase of D_0, and a decrease of r_0 and E (Fig. 7). As a consequence, the parabolic patterns of D_{REE} move upwards and shift toward left, resulting in a more open parabola (Fig. 7a). This suggests that the increase in Al^{IV} content has a greater effect on the D_{HREE} than on D_{LREE}. In fact, HREEs are more easily accommodated in clinopyroxene than LREEs (McKay et al., 1994; Lofgren et al., 2006; Mollo et al., 2013), since their smaller ionic radius can better compensate for the enlargement of the tetrahedral site induced by the replacement of Si with Al (Hill et al., 2000). Consequently, partition coefficients of HREEs, which are on the left side of the parabola, increase with the increase in Al^{IV} content, while partition coefficients of light and middle REEs (LREE and MREE), which are on the right side of the parabola, decrease slightly as the parabola shifts to the left, but increase as the parabola becomes more open, as previously observed by Sun and Liang (2012). Furthermore, even if it was not possible to discriminate the only

effect of the temperature in our runs, we believe that for a constant composition an upward movement of the parabola (e.g., APR16-C3Ac and APR16-C2Ac, APR16-C1Ad and APR16-C2Bd; Fig. 7b) may be due to a decrease in temperature, following the observations of Sun and Liang (2012). Moreover, together with tetrahedrally coordinated Al and temperature, also the undercooling (ΔT = $T_{liquidus}$ - $T_{experiment}$) influence the partitioning of trace element, as shown in Figure 7b. In particular, the increase of the undercooling moves the parabola upwards as observed for Al^{IV} content.

Tetravalent cations. The partition coefficients for Ti, Hf and Zr have been used to obtain E, D_0, and r_0 for the tetravalent cations. Best fits to the data yield D_0^{4+} = 3.35 ± 1.54, E^{4+} = 2600 ± 536 GPa, and r_0^{4+} = 0.657 ± 0.004 Å (Fig. 6 and Table 5). The inferred values for E (~1950-3100 GPa) are consistent with the large values expected for small, highly charged cation sites (~800-2400 GPa; Lundstrom et al., 1998; Baudouin et al., 2020). Th^{4+} and U^{4+} fall off the Ti-Hf-Zr regression suggesting that their ionic radii (1.05 and 1.00 Å, respectively) are too large for incorporation in the M1 site (Lundstrom et al., 1998). The r_0^{4+} of the M1 site is very similar to that calculated in previous studies (r_0^{4+} ~0.65-0.67 Å) (Hill et al., 2000; Mollo et al., 2016, 2018; Baudouin et al., 2020).

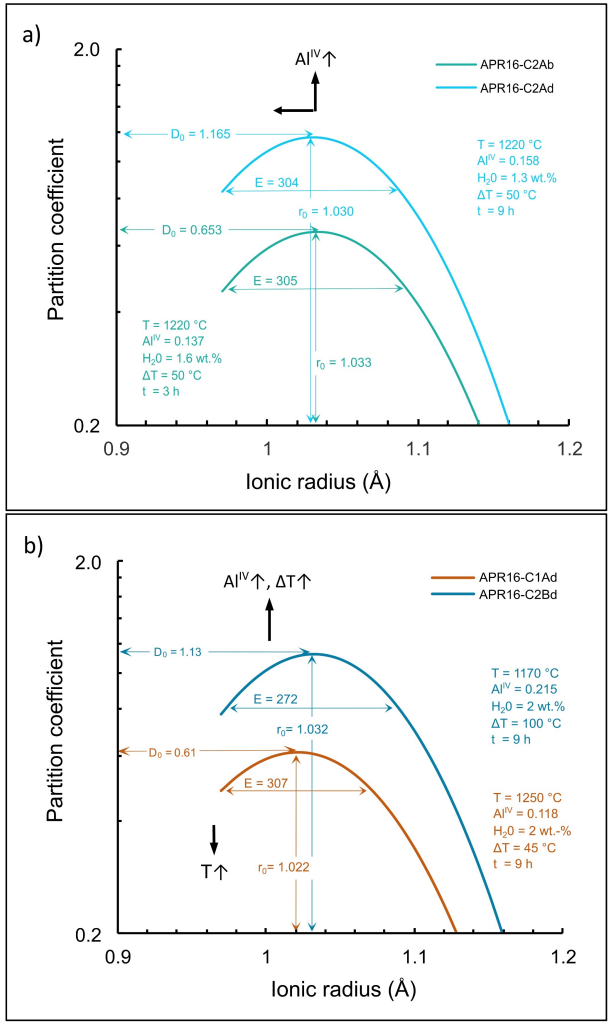

Fig. 7. *Onuma diagrams showing the variation of predicted REE partitioning between cpx and basaltic melt as function of a) composition (Al^{IV}), and b) composition (Al^{IV}), temperature and undercooling. a) The increase in Al^{IV} content shifts the parabola upward (D_0 increases) and towards left (r_0 decreases); b) the increase in undercooling moves the parabola upward like the Al^{IV} content, while the increase in temperature shifts the parabola downward.*

4.2 Factors influencing trace element partitioning

As general rule, partitioning coefficients tend to decrease with the increase of temperature (Wood and Blundy, 1997) and the effect of pressure at $P < 2$ GPa may be negligible for trace element partitioning between clinopyroxene and mafic melts (Sun and Liang, 2012; Mollo et al., 2016). As regards the influence of the chemical composition, it has been observed that in Cpx the tetrahedrally-coordinated aluminium content has a great influence on trace element partitioning (Lindstrom, 1976; Ray et al., 1983; Hart and Dunn, 1993; Forsythe et al., 1994; Lundstrom et al., 1994; Skulski et al., 1994; Lundstrom et al., 1998; Blundy et al., 1998; Hill et al., 2000; Wood and Trigila, 2001; Francis and Minarik, 2008; Sun and Liang, 2012; Yao et al., 2012; Mollo et al., 2013; Sun and Liang, 2013; Scarlato et al., 2014; Mollo et al., 2016). Nevertheless, the magnitude of the T, P and composition effects on the partitioning of trace elements between minerals and melts is not correctly assessed without considering the kinetic effect.

In the literature, the few works investigating the influence of kinetics processes on D_i values are generally focused on the effect of the cooling rates (Albarede and Bottinga, 1972; Watson, 1996; Lofgren et al., 2006; Mollo et al., 2013) and time (Arzilli et al., 2018), showing an increase of REE partition coefficients with increasing cooling rates or with decreasing crystallization times and, consequently, with increasing growth rates. Thus, since growth rates are fast at the beginning of the crystallization process and then decrease with increasing time (Vetere et al., 2013; Arzilli and Carroll, 2013; Iezzi et al., 2014; Vetere et al., 2015; Arzilli et al., 2018; Bonechi et al., 2020b; 2020a; Bonechi, 2020), we would expect a decrease of D_i values with increasing time until equilibrium conditions are reached. As possible to see

in this study, at static conditions (i.e., no cooling rate), D_{REE} values seem to increase with increasing time (Fig. 8), with D_{REE} values calculated in long-duration experiments higher than those calculated in short duration ones, showing thus a behaviour apparently opposite to what would have been expected. This is noticeable considering the group of runs APR16-1C/APR16-C1Ac/APR16-C2Ad (respectively 3, 6 and 9 hours long), characterized by similar T and ΔT conditions and similar Al^{IV} and H_2O contents (Table 2 and Table S2 in Supplementary Material 2), that are the parameters that most affect the partition coefficients. In particular, we observed an increase in D_{REE} values from 3 (APR16-1C) to 9 hours (APR16-C2Ad) experiments, more evident in the right side of the three parabolae (i.e., where the LREEs fall). Along this side, the parabolae tend to widen to the right and upwards as time increases, as confirmed by the increase of r_0 (from 1.0297 to 1.0301 Å; Table 5) and the decrease of E (from 325 to 304 GPa; Table 5) with increasing time. Conversely, there are no appreciable differences for the apical zone (where the HREEs fall) in the 3 and 6 hours experiments. This variation in the shape of the parabolae makes the effect of time on the D values stand out more clearly for the LREEs that fall on the flanks rather than for the HREEs that fall in the apical area. Indeed, D_{HREE} values of the runs at 3 and 6 hours are very similar despite their different duration, and this similarity can be explained by considering their different growth rates. Notably, the APR16-1C run (3 hours) is characterized by a growth rate ($1.6 \cdot 10^{-7}$ cm s^{-1}) higher than that of the other runs with the same duration (e.g., $3 \cdot 10^{-8}$ cm s^{-1}), as a consequence of the use of natural powder containing pre-existing nuclei as starting material, as described in the work of Bonechi (2020). Therefore, the high growth rate of this run yields D_{REE}

values higher than those expected for runs at 3 hours, but similar to those measured in the run at 6 hours (APR16-C1Ac). This agrees with observations made in previous studies (Watson, 1996; Lofgren et al., 2006), according to which, during rapid crystal growth the less efficient rejection of incompatible elements leads to higher *D*-values. Moreover, the greater similarity in D_{HREE} than in D_{LREE} in APR16-1C and APR16-C1Ac runs is due to their different diffusivities, that decrease as the REE size decreases (Zhang et al., 2010), since slow-moving elements (HREE) result more enriched compared with fast moving elements (LREE), as observed for instance during disequilibrium growth (Arzilli et al., 2018). The increase in D_{REE} values with time observed in this work, which would seem to contrast with what was observed in the literature, actually is not referable to a change in time but rather to the different non-bridging oxygens per tetrahedrally co-ordinated cation ratio (NBO/T; Mysen et al., 1982, 1985) of the considered experiments, that seems to inhibit the effect of increasing time which would tend to decrease the partition coefficient values. As stated in the literature, melt composition affects the melt structure, and thus trace element partition coefficients, that generally decrease with decreasing melt polymerization (i.e., increasing the NBO/T ratio) (Mysen and Virgo, 1980; Gaetani, 2004; Huang et al., 2006; Mollo et al., 2016; Michely et al., 2017), while in some cases this influence seems to be negligible in comparison to the effect of mineral chemistry (Beard et al., 2019; Baudouin et al., 2020). Indeed, as observed by Gaetani (2004), the influence of melt structure is significantly evident when NBO/T < 0.49. In this study, despite the NBO/T ratio varies between 0.6 and 1 (Table 2), we observed the influence of this parameter on REE partition coefficients. As shown in Figure 8, there is a negative

correlation between D_{REE} and NBO/T ratio, described by the following equations for a representative LREE (4), MREE (5) and HREE (6) element:

$$D_{Nd} = -1.54 * \frac{NBO}{T} + 1.72 \ (R^2 = 0.98) \quad (4),$$

$$D_{Eu3+} = -2.45 * \frac{NBO}{T} + 2.73 \ (R^2 = 0.92) \quad (5),$$

$$D_{Dy} = -4.54 * \frac{NBO}{T} + 4.58 \ (R^2 = 0.99) \quad (6),$$

where R^2 is the coefficient of determination. In particular, the highest D_{REEs} are those measured in the APR16-C2Ad run characterized by the lowest NBO/T (0.70). The NBO/T ratio represents the degree of polymerization of a melt and thus yields information about its viscosity (Giordano and Dingwell, 2003). The lower NBO/T ratio of the APR16-C2Ad run with respect to that of the other two runs (0.82 and 0.78 for APR16-1C and APR16-C1Ac, respectively) suggests its higher viscosity. High viscosity values imply a lower diffusion of the elements with a consequent increase of *D* values due to the inability of diffusion to keep pace with the crystal growth rate (Lofgren et al., 2006). Moreover, the low NBO/T ratio calculated for the APR16-C2Ad run can be explained by considering its higher loss of Fe (-27 % ΔFe; Table 2) occurred during the experiment with respect to that occurred in the APR16-C1Ac and APR16-1C runs (-20 and -5 % ΔFe, respectively; Table 2). This difference, that suggests a different melt viscosity between the runs, highlights the strong influence of this latter parameter on the partitioning of trace elements between cpx and basaltic melt.

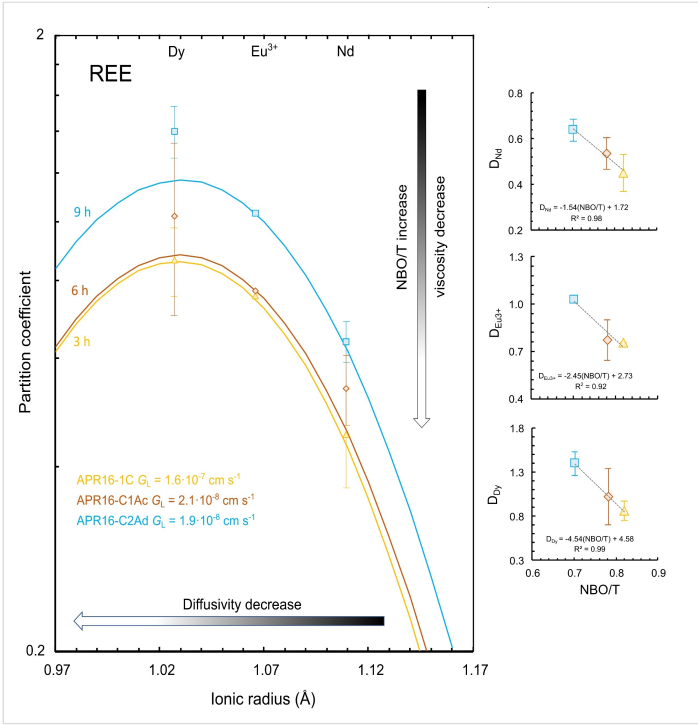

Fig. 8. *Plot of clinopyroxene-liquid partition coefficients for REEs vs ionic radius (Å). The curves represent the fits of the lattice strain model to* $^{Cpx/L}D_i$ *values while symbols represent measured* $^{Cpx/L}D_i$ *values for Dy (HREE),* Eu^{3+} *(MREE) and Nd (LREE) in the APR16-C2Ad (1220 °C; in light blue), APR16-C1Ac (1250 °C; in orange) and APR16-1C (1225 °C; in yellow) runs. Horizontal arrow indicates the diffusivity decrease from LREEs to HREEs, while vertical arrow indicates NBO/T increase and viscosity decrease with decreasing time (from APR16-C2Ad to APR16-1C). On the right side of the figure are reported plots of partition coefficients for Dy,* Eu^{3+} *and Nd vs NBO/T, in which it is possible to see the negative correlation between D values and NBO/T.*

4.3 Deep differentiation of primitive parental K-basaltic magmas of the CFVD

The partitioning of trace elements between crystals and melts provides an important petrogenetic tool for understanding magmatic processes. Trace elements in volcanic rocks tend to fractionate into specific minerals and therefore are useful in formulating models for magmatic differentiation. Nevertheless, phenocrysts formed in deeper magmatic reservoirs are frequently cannibalized during their ascent in the plumbing system (e.g., Tecchiato et al., 2018b, 2018a). In these cases, the experimental phase assemblages obtained from high pressure experiments, as those obtained in this study on the Campi Flegrei primitive compositions (Table 2), represent a powerful tool to validate geochemical models. In the Campi Flegrei Volcanic District mafic products (shoshonitic basalts, trachybasalts, basanites and tephrites) are poorly represented with respect to the differentiated compositions (trachyte or phonolite) that are the largest part of the magma volume erupted (several hundreds of cubic kilometres; e.g., Orsi et al., 1992; Fedele et al. 2003). This suggested that a huge volume of magmas should be differentiated by ponding at variable depths within the crust, producing cumulates joint to the most evolved magmas that have fed the volcanism of the Campania Plain over the past ca. 1.8 Ma (Fedi et al., 2018 and references therein). A first step of differentiation has been supposed at upper mantle-crustal boundary (i.e., at the Moho = ~25 km of depth; Di Stefano et al., 2011) on the basis of the results of melt inclusion studies (Mormone et al., 2011; Moretti et al., 2013), seismic data interpretations (Di Stefano et al., 1999; Piochi et al., 2005; Chiarabba et al., 2008) and gravimetric and petrological modelling (Fedi et al., 2018). As

shown in Perinelli et al. (2019), a stage of high-pressure crystallization is also revealed by the estimate of *T-P* crystallization conditions of clinopyroxenes phenocrysts from the less differentiated CFVD products indicating crystallization temperatures and pressures between 1140 and 1220 °C and between 0.6 and 0.9 GPa, respectively. Fedi et al. (2018) combining gravimetric data with petrological modelling suggest that a first step of differentiation of the Campi Flegrei primary magmas may occur as a result of the underplating at the Moho level. In this deep reservoir K-trachybasalt melts could be originated after about 30 wt% fractionation of gabbrous cumulates. On the other hand, our experimental results along with those reported in Perinelli et al. (2019) indicate that at pressure corresponding to the Moho depth plagioclase has a limited role in the differentiation of K-trachybasalts from parental APR16-like magmas. Indeed, residual melts of trachybasalt can formed after the fractionation of 20-30% of a clinopyroxenitic mineral assemblage (Table 2 of this study and Table 2 in Perinelli et al., 2019) in a range of temperature that depending on water content (1 up to 3 wt%), varies from 1250 and 1150 °C. The role of plagioclase in the deep differentiation process has been evaluated applying the Excel© spreadsheet program for modeling geochemical differentiation of magma proposed by Ersoy and Helvaci (2010) to calculate the concentration of selected elements in remaining trachybasaltic melts, during the fractional crystallization of a primitive parental K-basaltic magma (Fig. 9). Calculations were performed by using: 1) the partition coefficients clinopyroxene/melt determined in this study and 2) a fractionate mineral assemblage formed by clinopyroxene + olivine ± plagioclase. Modelling results indicate that significant amounts of plagioclase crystallization (>10

wt%) did not fully reproduce the composition of CFVD trachybasalts, particularly for the HREEs (Fig. S2 in Supplementary Material 3). Particularly, by increasing the percentage of plagioclase in the fractionated solid, a slight increase in incompatible elements is observed, including the HREEs. Moreover, it is clearly seen that the increase in plagioclase fails to model the Sr. This is a key aspect since Sr is compatible in plagioclase and compatibles elements are much more sensitive than incompatible ones to low degrees of fractionation. On the contrary, the fractionation of 15-26 wt% of clinopyroxene + 2-6 wt% of olivine, according to what resulted from crystallization experiments in which the residual melts had a trachybasalt composition (Table 2 of this study and Table 2 in Perinelli et al., 2019), well mimics the trace element pattern of natural trachybasalts (Fig. 9).

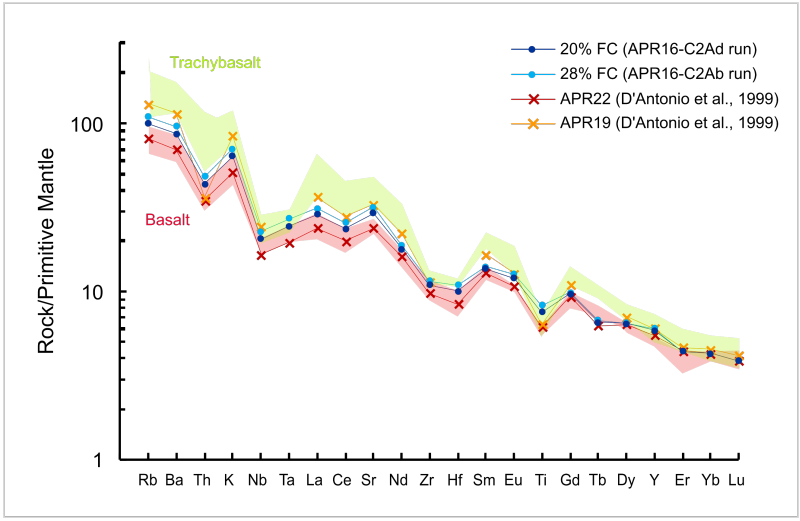

Fig. 9. *Primitive Mantle normalized (McDonough and Sun, 1995) trace elements patterns for primitive basaltic (APR22; D'Antonio et al., 1999) and trachybasaltic (APR19; D'Antonio et al., 1999) rocks, and the predicted composition of differentiated melts obtained after 20 and 28 % of fractional crystallization of APR22 basalt assumed as primitive parental K-basaltic magma. The reported degrees of fractionation (FC) reflect the crystallized phase assemblage and proportions determined for runs APR16-C2Ad ($Cpx_{(17)}$+$Ol_{(3)}$) and AR16-C2Ab ($Cpx_{(23)}$+$Ol_{(4)}$+$Plg_{(1)}$) that produced trachybasaltic residual glass. The modelled compositions were calculated by using the Excel© spreadsheet program of Ersoy and Helvaci (2010) (see §4.3 for details). Normalized patterns for Campi Flegrei Volcanic District basalts and trachybasalts (D'Antonio et al., 1999a; Pappalardo et al., 1999; De Astis et al., 2004), indicated with red and green field, respectively, are shown for comparison.*

5. Conclusions

This study provides new experimental data on trace element partition coefficients between clinopyroxene and a K-basaltic melt, showing the influence of temperature, chemical composition and also kinetic effects like growth rate and order-disorder crystal growth. Particularly, the rapid growth of clinopyroxene under disequilibrium conditions and/or in presence of pre-existing nuclei under near-equilibrium conditions causes less efficient rejection of incompatible elements (e.g., REEs), since disordered crystal growth is the preferred process during the crystallization, yielding higher D_{REE} than those calculated in presence of lower growth rates, generally under equilibrium conditions. Since growth rates are fast at the beginning of the crystallization process and then decrease with increasing time, D_i values should decrease with increasing time. Therefore, the increase in D_{REE} values with time observed in some runs of this work is not related to a change in time but rather to the different NBO/T ratio. The low NBO/T ratio calculated in the run with longer duration (9 hours) is linked to its higher loss of Fe with respect to the other run at 3 and 6 hours, pointing out the strong influence of melt structure and thus of melt viscosity on the partitioning behaviour of trace elements between cpx and basaltic melt. Finally, by using the partition coefficients clinopyroxene/melt determined in this study, geochemical data modelling applied to natural less evolved products of Campi Flegrei Volcanic District, indicate that the differentiation process at mantle-crustal boundary depth is controlled by fractionation of clinopyroxene >> olivine mineral assemblage and that K-trachybasalts can derive from parental APR16-like magmas after the fractionation of about 20-30% of a clinopyroxenitic cumulate.

Acknowledgments

We thank Luca Ziberna (BGI Bayreuth) for preparing APR16GL sample. We thank M. Albano (CNR-IGAG) and M. Serracino (CNR-IGAG) for assistance during SEM and EPMA analytical sessions.

Funding

This research has been conducted with the financial support of the HP-HT Laboratory at the Department of Earth Sciences of Sapienza - University of Rome and with the financial support of the project M_011177_14_D_MAGRI_10-MIUR funded to B.B. A.F. acknowledges support from the GACR (Project 18-01982S).

Chapter 4

Concluding remarks

In this thesis, the investigation of the kinetic and rheological properties of a primitive K-basaltic magma in the deep portion of the CFVD plumbing system allowed to improve the knowledge of the pre-eruptive magmatic processes and magma chamber dynamics, and to provide estimates of magma residence and ascent timescales. Particularly, the following conclusions have been drawn:

1. As regards the kinetic properties (Chapter 1), at 0.8 GPa, 1170-1250 °C and H_2O < 4 wt.%, clinopyroxene growth rate results to be strongly affected by time, with average values that vary from 10^{-7} to 10^{-8} cm·s^{-1} from the shortest (0.25 h) to the longer-lasting (6-9 h) experiments. The growth rates calculated in the run performed using natural starting material with pre-existing nuclei are higher than those calculated in the runs performed using the vitrified starting material, while the nucleation rates show the opposite behavior with lower values for the run containing pre-existing nuclei. These differences are due to the structural similarities between the pre-existing nuclei and the nucleating phases that concentrate the supply of chemical elements in the liquid surrounding the new growing crystals, limiting in this way the formation of new nucleation sites. At 0.8 GPa, 1030-1080 °C and H_2O > 4 wt.%, the growth rate of amphibole, which is the dominant phase, decreases from $1.5 \cdot 10^{-7}$ to $2.9 \cdot 10^{-8}$ cm s^{-1} with increasing time (from 0.25 to 9 h). Comparison between amphibole and clinopyroxene growth rates provides evidence for the faster growth of amphibole with respect

to clinopyroxene, which is due to chemical and structural similarities between these minerals that cause a “kinetic competition”. This "kinetic competition" and consequently the different growth rates observed for the coexisting clinopyroxene and amphibole, could be attributed to a different element diffusivity; however, further targeted experiments are needed to firmly support this assumption. This competition also explains why the growth rates of clinopyroxene calculated in the high water content runs (H_2O_f > 4 wt.%) turn out to be lower than those calculated in the low water content runs (H_2O_f < 4 wt.%). In fact, crystal growth rates should be higher in the presence of high amount of water given its depolymerizing effect on the melt. By the comparison with growth rate data available in the literature, viscosity, composition, undercooling and cooling rate are the factors that most affect crystal growth rate, while pressure appears to have no influence on it. The experimental Cpx growth rate combined with data from CSD and thermobarometry of CFVD clinopyroxenes suggests that recharge by primitive magmas in the deep CFVD reservoirs occurs with a relatively high ascent rate (~$0.5 \cdot 10^{-4}$ m·s^{-1}). The estimated recharge rate (0.2-2 km^3·year^{-1} in absence of pre-existing nuclei or 1-10 km^3·year^{-1} in presence of pre-existing nuclei) suggests that a deep reservoir of primitive parental magma similar to those had feeding the Campanian Ignimbrite eruption (39 ka), could be formed in a time interval ranging from 10^4 to 10^5 years (absence of pre-existing nuclei) or 10^3 to 10^4 years (presence of pre-existing nuclei). Moreover, in the dissolution-crystallization experiment, the formation of overgrowth rims and new cpx crystals with different textures and compositions suggests that

injection of basaltic melts in a cold magma chamber may produce crystals with inverse or oscillatory zonation. This disequilibrium crystallization process is also related to the dissolution of pristine crystals resident in the magma reservoir. The growth rate ($1.35 \cdot 10^{-6}$ cm s^{-1}) extrapolated from this dissolution-crystallization experiment, confirms that chemical dynamic conditions favour an increase in the crystal growth rate. Finally, the application of the calculated experimental dissolution rates to products of Agnano-Monte Spina eruption (4100 BP, Campi Flegrei), results in maximum cpx dissolution time-scales of ~40 h, and that the effect of crystal dissolution may be relevant to estimate magma residence times whether significant dissolution occurs during magma mixing processes. Indeed, if magma mixing is accompanied by crystal dissolution, then it is likely that most of retrieved residence times are potentially underestimated.

2. As regards the rheological properties (Chapter 2), measured viscosities (~0.3-2 Pa·s) along with modelled rock parameters (e.g., permeability, porosity and mineral grain size) show that magmas underneath Campi Flegrei are characterized by a mobility (0.3-3 g $cm^3 \cdot Pa^{-1} \cdot s^{-1}$) and a migration velocity (3-32 $m \cdot y^{-1}$) higher than those of basalts from mid-ocean ridges. Moreover, despite the magma migration underneath a volcano is usually accompanied by geophysical precursors (e.g., volcano-tectonic earthquakes, tremors, and deformations), these signals alone are not enough to forecast volcanic eruptions. In this context, the viscosity measured at the lowest pressure (0.7 GPa; ~ the depth of deep reservoir), corrected for temperature, water and crystals contents, was used to estimate magma ascent rate and time from the

deep reservoir (~25 km depth) to the shallower reservoir located at ~8 km depth (path 1), and from the deep reservoir to the surface (path 2). For both paths, it has been estimated an ascent velocity of 36 and 33 m/s for dry and hydrous conditions, respectively. For the path 1, the magma ascent times are in the order of 7.9 min (dry) and 8.4 min (hydrous), while for the path 2, they are 11.7 min (dry) and 12.4 min (hydrous).

3. In Chapter 3, partition coefficient data derived from synthetic clinopyroxenes in equilibrium and in disequilibrium with a primitive K-basaltic composition from the CFVD were provided since their usefulness in petrological and geochemical studies to better understand magmatic processes, like fractional or equilibrium crystallization, assimilation, and partial melting. The increase in D_{REE} values with time observed in some runs of this work is not related to a change in time but rather to the different NBO/T ratio. Indeed, since growth rates are fast at the beginning of the crystallization process and then decrease with increasing time, D_i values should decrease with increasing time. The low NBO/T ratio calculated in the run with longer duration (9 hours) is linked to its higher loss of Fe with respect to the other run at 3 and 6 hours, pointing out the strong influence of melt structure and thus of melt viscosity on the partitioning behaviour of trace elements between cpx and basaltic melt. Finally, the modelling of a fractional crystallization process of primitive parental K-basaltic magmas, performed by using the partition coefficients determined in this study, highlights that significant amounts of plagioclase crystallization (>10 wt.%) do not fully mimic the composition of CFVD trachybasalts,

which, on the other hand, results to be well reproduced by the fractionation of 15-26 wt.% of clinopyroxene + 2-6 wt.% of olivine.

References

Abd El-Rahman, Y., Helmy, H.M., Shibata, T., Yoshikawa, M., Arai, S., Tamura, A., 2012. Mineral chemistry of the Neoproterozoic Alaskan-type Akarem Intrusion with special emphasis on amphibole: implications for the pluton origin and evolution of subduction-related magma. *Lithos* **155**, 410-425.

Abramoff, M.D., Magalhães, P.J., Ram, S.J., 2004. Image processing with ImageJ. *Biophoton. Int.* **11**, 36–42.

Acocella, V., Salvini, F., Funiciello, R., Faccenna, C., 1999. The role of transfer structures on volcanic activity at Campi Flegrei (Southern Italy). *J. Volcanol. Geotherm. Res*. **91**, 123–139.

Agee, C.B., 1998. Crystal-liquid density inversions in terrestrial and lunar magmas. *Phys. Earth Planet. Inter*. **107**, 63–74.

Agostini, C., Fortunati, A., Arzilli, F., Landi, P., Carroll, M.R., 2013. Kinetics of crystal evolution as a probe to magmatism at Stromboli (Aeolian Archipelago, Italy). *Geochim. Cosmochim. Acta* **110**, 135–151.

Aigner-Torres, M., Blundy, J., Ulmer, P. and Pettke, T., 2007. Laser Ablation ICPMS study of trace element partitioning between plagioclase and basaltic melts: An experimental approach. *Contrib. Mineral. Petrol*. **153**, 647–667.

Aiuppa, A., Avino, R., Brusca, L., Caliro, S., Chiodini, G., D'Alessandro, W., Favara, R., Federico, C., Ginevra, W., Inguaggiato, S., Longo, M., Pecoraino, G., Valenza, M., 2006. Mineral control of arsenic content in thermal waters from volcano-hosted hydrothermal systems: Insights from island of Ischia and Phlegrean Fields (Campanian Volcanic Province, Italy). *Chem. Geol*. **229**, 313–330.

Albarede, F., and Bottinga, Y. (1972) Kinetic disequilibrium in trace element partitioning between phenocrysts and host lava. *Geochim. Cosmochim. Acta* **36**, 141–156.

Albert, P.G., Giaccio, B., Isaia, R., Costa, A., Niespolo, E.M., Nomade, S., Pereira, A., Renne, P.R., Hinchliffe, A., Mark, D.F., Brown, R.J., Smith, V.C., 2019. Evidence for a large-magnitude eruption from Campi Flegrei caldera (Italy) at 29 ka. *Geology* **47**, 595–599.

Allard, P., Maiorani, A., Tedesco, D., Cortecci, G., Turi, B., 1991. Isotopic study of the origin of sulfur and carbon in Solfatara fumaroles, Campi Flegrei caldera. *J. Volcanol. Geotherm. Res*. **48**, 139–159.

Allwardt, J.R., Stebbins, J.F., Terasaki, H., Du, L.S., Frost, D.J., Withers, A.C., Hirschmann, M.M., Suzuki, A., Ohtani, E., 2007. Effect of structural transitions on properties of high-pressure silicate melts:27Al NMR, glass densities, and melt viscosities. *Am. Mineral*. **92**, 1093–1104.

Anders, E., and Grevesse, N., 1989. Abundances of the elements: Meteoritic and solar. *Geochim. Cosmochim. Acta* **53**, 197–214.

Arculus, R.J., and Wills, K.J.A., 1980. The petrology of plutonic blocks and inclusions from the lesser antilles Island arc. *J. Petrol.* **21**, 743-799.

Arienzo, I., Moretti, R., Civetta, L., Orsi, G., Papale, P., 2010. The feeding system of Agnano – Monte Spina eruption (Campi Flegrei, Italy): Dragging the past into present activity and future scenarios. *Chem. Geol.* **270**, 135–147.

Armienti, P., Barberi, F., Bizojard, H., Clocchiatti, R., Innocenti, F., Metrich, N., Rosi, M. and Sbrana, A., 1983. The phlegraean fields: Magma evolution within a shallow chamber. *J. Volcanol. Geotherm. Res.* **17**, 289–311.

Armienti, P., Pareschi, M.T., Innocenti, F., Pompilio, M., 1994. Effects of magma storage and ascent on the kinetics of crystal growth-the case of the 1991-93 Mt. Etna eruption. *Contrib. Mineral. Petrol.* **115**, 402–414.

Armienti, P., Tonarini, S., Orazio, M.D., 2007. Mount Etna pyroxene as tracer of petrogenetic processes and dynamics of the feeding system. *Geol. Soc. Am. Spec. Pap.* 265–276.

Armienti, P., Perinelli, C., Putirka, K.D., 2013. A new model to estimate deep-level magma ascent rates, with applications to Mt. Etna (Sicily, Italy). *J. Petrol.* **54**, 795–813.

Arzilli, F., Agostini, C., Landi, P., Fortunati, A., Mancini, L., Carroll, M.R., 2015. Plagioclase nucleation and growth kinetics in a hydrous basaltic melt by decompression experiments. *Contrib. Mineral. Petrol.* **170**, 55–16.

Arzilli, F., and Carroll, M.R., 2013. Crystallization kinetics of alkali feldspars in cooling and decompression-induced crystallization experiments in trachytic melt. *Contrib. Mineral. Petrol.* **166**, 1011–1027.

Arzilli, F., Piochi, M., Mormone, A., Agostini, C., Carroll, M.R., 2016. Constraining pre-eruptive magma conditions and unrest timescales during the Monte Nuovo eruption (1538 AD; Campi Flegrei, Southern Italy): integrating textural and CSD results from experimental and natural trachy-phonolites. *Bull. Volcanol.* **78**, 72–20.

Arzilli, F., Fabbrizio, A., Schmidt, M.W., Petrelli, M., Maimaiti, M., Dingwell, D.B., Paris, E., Burton, M. and Carroll, M.R., 2018. The effect of diffusive re-equilibration time on trace element partitioning between alkali feldspar and trachytic melts. *Chem. Geol.* **495**, 50–66.

Asimow, P., and Ghiorso, M.S., 1998. Algorithmic modifications extending MELTS to calculate subsolidus phase relations. *Am. Mineral.* **83**, 1127-1132.

Auger, E., Gasparini, P., Virieux, J., Zollo, A., 2001. Seismic evidence of an extended magmatic sill under Mt. Vesuvius. *Science* **294**, 1510–1512.

Avanzinelli, R., Lustrino, M., Mattei, M., Melluso, L., Conticelli, S., 2009. Potassic and ultrapotassic magmatism in the circum-Tyrrhenian region: significance of carbonated pelitic vs. pelitic sediment recycling at destructive plate margins. *Lithos* **113**, 213–227.

Bachmann, O., and Dungan, M.A., 2002. Temperature-induced Al-zoning in hornblendes of the fish canyon magma, Colorado. *Am. Mineral*. **87**, 1062-1076.

Bagagli, M., Montagna, C.P., Papale, P., Longo, A., 2017. Signature of magmatic processes in strainmeter records at Campi Flegrei (Italy). *Geophys. Res. Lett*. **44**, 718–725.

Baker, D.R., 2008. The fidelity of melt inclusions as records of melt composition. *Contrib. Mineral. Petrol.* **156**, 377–395.

Barberi, F., Carapezza, M.L., 1996. The Problem of Volcanic Unrest: The Campi Flegrei Case History, in: Monitoring and Mitigation of Volcano Hazards. Springer Berlin Heidelberg, Berlin, Heidelberg, pp. 771–786.

Barr, J.A., and Grove, T.L., 2010. AuPdFe ternary solution model and applications to understanding the fO_2 of hydrous, high-pressure experiments. *Contrib. Mineral. Petrol.* **160**, 631-643.

Baudouin, C., France, L., Boulanger, M., Dalou, C. and Devidal, J., 2020. Trace element partitioning between clinopyroxene and alkaline magmas: parametrization and role of M1 site on HREE enrichment in clinopyroxenes. *Contrib. Mineral. Petrol*. **175**, 42.

Baziotis, I., Xydous, S., Asimow, P.D., Mavrogonatos, C., Flemetakis, S., Klemme, S. and Berndt, J., 2019. The potential of phosphorus in clinopyroxene as a geospeedometer: Examples from mantle xenoliths. *Geochim. Cosmochim. Acta* **266**, 307–331.

Beard, C.D., Van Hinsberg, V.J., Stix, J. and Wilke, M., 2019. Clinopyroxene/Melt Trace Element Partitioning in Sodic Alkaline Magmas. *J. Petrol*. **60**, 1797–1823.

Beattie, P., 1993. The generation of uranium series disequilibria by partial melting of spinel peridotite: constraints from partitioning studies. *Earth Planet. Sci. Lett*. **117**, 379–391.

Beccaluva, L., Di Girolamo, P., Serri, G., 1991. Petrogenesis and tectonic setting of the Roman Volcanic Province. *Lithos* **26**, 191–221.

Beccaluva, L., Bianchini, G., Mameli, P., Natali, C., 2013. Miocene shoshonite volcanism in Sardinia: Implications for magma sources and geodynamic evolution of the Central-Western Mediterranean. *Lithos* **180–181**, 128–137.

Bédard, J.H., 2010. Parameterization of the Fe=Mg exchange coefficient (Kd) between clinopyroxene and silicate melts. *Chem. Geol*. **274**, 169-176.

Bédard, J.H., 2014. Parameterizations of calcic clinopyroxene - Melt trace element partition coefficients. *Geochem. Geophys. Geosyst*. **15**, 303–336.

Behrens, H., and Schulze, F., 2003. Pressure dependence of melt viscosity in the system $NaAlSi_3O_8$-$CaMgSi_2O_6$. *Am. Mineral*. **88**, 1351–1363.

Bennett, S.L., Blundy, J. and Elliott, T., 2004. The effect of sodium and titanium on crystal-melt partitioning of trace elements. *Geochim. Cosmochim. Acta* **68**, 2335–2347.

Berkebile, C.A., and Dowty, E., 1982. Nucleation in laboratory charges of basaltic composition. *Am. Mineral*. **67**, 886–899.

Besson, J.M., Nelmes, R.J., Hamel, G., Loveday, J.S., Weill, G., Hull, S., 1992. Neutron powder diffraction above 10 GPa. *Phys. B Condens. Matter* **180–181**, 907–910.

Blake, S., and Ivey, G.N., 1986. Magma mixing and the dynamics of withdrawal from stratified reservoirs. *J. Volcanol. Geotherm. Res*. **27**, 153–178.

Blundy, J.D., and Wood, B.J., 1991. Crystal-chemical controls on the partitioning of Sr and Ba between plagioclase feldspar, silicate melts, and hydrothermal solutions. *Geochim. Cosmochim. Acta* **55**, 193–209.

Blundy, J., and Wood, B., 1994. Prediction of crystal-melt partition coefficients from elastic moduli. *Nature* **372**, 452–454.

Blundy, J., and Wood, B., 2003. Partitioning of trace elements between crystals and melts. *Earth Planet. Sci. Lett*. **210**, 383–397.

Blundy, J.D., Robinson, J.A.C. and Wood, B.J., 1998. Heavy REE are compatible in clinopyroxene on the spinel lherzolite solidus. *Earth Planet. Sci. Lett*. **160**, 493–504.

Bonechi, B., 2020. Influence of Pre-Existing Nuclei on the Crystallization Kinetics of Primitive Alkaline Magmas: Insights on the Deep Feeding System of the Campi Flegrei Volcanic District. *Minerals* **10**, 234.

Bonechi, B., Perinelli, C., Gaeta, M., Tecchiato, V., Granati, S.F., 2017. Experimental constraints on amphibole stability in primitive alkaline and calc-alkaline magmas. *Period. Mineral*. **86**, 231–245.

Bonechi, B., Perinelli, C., Gaeta, M., 2019. Clinopyroxene growth and dissolution rates: high-pressure investigation on a primitive alkaline basalt from the Campi Flegrei Volcanic District (south Italy). In: Goldschmidt Conference, p. 324. Barcelona, Spain.

Bonechi, B., Perinelli, C., Gaeta, M., Tecchiato, V. and Fabbrizio, A., 2020a. Amphibole growth from a primitive alkaline basalt at 0.8 GPa: Time-dependent compositional evolution, growth rate and competition with clinopyroxene. *Lithos* **354–355**, 105272.

Bonechi, B., Perinelli, C. and Gaeta, M., 2020b. Clinopyroxene growth rates at high pressure: constraints on magma recharge of the deep reservoir of the Campi Flegrei Volcanic District (south Italy). *Bull. Volcanol*. **82**, 5.

Boyd, F.R., and England, J.L., 1960. Apparatus for phase-equilibrium measurements at pressures up to 50 kilobars and temperatures up to 1750 °C. *J. Geophys. Res.* **65**, 741.

Brearley, M., and Scarfe, C.M., 1986. Dissolution rates of upper mantle minerals in an alkali basalt melt at high pressure: An experimental study and implications for ultramafic xenolith survival. *J. Petrol.* **27**, 1157–1182.

Brice, J.C., 1975. Some thermodynamic aspects of the growth of strained crystals. *J. Cryst. Growth* **28**, 249–253.

Brugger, C.R., and Hammer, J.E., 2010a. Crystal size distribution analysis of plagioclase in experimentally decompressed hydrous rhyodacite magma. *Earth Planet. Sci. Lett.* **300**, 246-254.

Brugger, C.R., and Hammer, J.E., 2010b. Crystallization kinetics in continuous decompression experiments: implications for interpreting natural magma ascent processes. *J. Petrol.* **51**, 1941–1965.

Burgisser, A., and Bergantz, G.W., 2011. A rapid mechanism to remobilize and homogenize highly crystalline magma bodies *Nature* **471**, 212–216.

Burkhard, D.J., 2002. Kinetics of crystallization: example of microcrystallization in basalt lava. *Contrib. Mineral. Petrol.* **142**, 724–737.

Burkhard, D.J.M., 2005. Nucleation and growth rates of pyroxene, plagioclase, and Fe-Ti oxides in basalt under atmospheric conditions. *Eur. J. Mineral.* **17**, 675–686.

Caliro, S., Chiodini, G., Paonita, A., 2014. Geochemical evidences of magma dynamics at Campi Flegrei (Italy). *Geochim. Cosmochim. Acta* **132**, 1–15.

Calò, M., and Tramelli, A., 2018. Anatomy of the Campi Flegrei caldera using Enhanced Seismic Tomography Models. *Sci. Rep.* **8**, 1–12.

Calzolaio, M., Arzilli, F., Carroll, M.R., 2010. Growth rate of alkali feldspars in decompression-induced crystallization experiments in a trachytic melt of the Phlegraean Fields (Napoli, Italy). *Eur. J. Mineral.* **22**, 485–493.

Cannatelli, C., Lima, A., Bodnar, R. J., De Vivo, B., Webster, J. D., and Fedele, L., 2007. Geochemistry of melt inclusions from the Fondo Riccio and Minopoli 1 eruptions at Campi Flegrei (Italy). *Chemical Geology*, **237**, 418-432.

Caricchi, L., Giordano, D., Burlini, L., Ulmer, P., Romano, C., 2008. Rheological properties of magma from the 1538 eruption of Monte Nuovo (Phlegrean Fields, Italy): An experimental study. *Chem. Geol.* **256**, 157–170.

Cartier, C., Hammouda, T., Doucelance. R., Boyet, M., Devidal, J.L. and Moine, B., 2014. Experimental study of trace element partitioning between enstatite and melt in enstatite chondrites at low oxygen fugacities and 5 GPa. *Geochim. Cosmochim. Acta* **130**, 167–187.

Cashman, K.V., 1993. Relationship between plagioclase crystallization and cooling rate in basaltic melts. *Contrib. Mineral. Petrol.* **113**, 126-142.

Cashman, C.V., and Marsh, B.D., 1988. Crystal size distribution (CSD) in rocks and the kinetics and dynamics of crystallisation. *Contrib. Mineral. Petrol.* **99**, 292–305.

Cawthorn, R.G., Curran, E.B., Arculus, R.J., 1973. A petrogenetic model for the origin of the calc-alkaline suite of Grenada, lesser antilles. *J. Petrol.* **14**, 327-337.

Cecchetti, A., Marianelli, P., Sbrana, A., 2001. Prime evidenze della esistenza di un sistema di cristallizzazione profondo ai Campi Flegrei. *Atti Soc. Tosc. Sci. Nat. Mem.*, 1–7.

Chen, Y., and Zhang, Y., 2008. Olivine dissolution in basaltic melt. *Geochim. Cosmochim. Acta* **72**, 4756–4777.

Chen, Y. and Zhang, Y., 2009. Clinopyroxene dissolution in basaltic melt. *Geochim. Cosmochim. Acta* **73**, 5730–5747.

Cherniak, D.J., and Dimanov, A., 2010. Diffusion in Pyroxene, Mica and Amphibole. *Rev. Mineral. Geochemistry* **72**, 641–690.

Chiarabba, C., De Gori, P., Speranza, F., 2008. The southern Tyrrhenian subduction zone: Deep geometry, magmatism and Plio-Pleistocene evolution. *Earth Planet. Sci. Lett.* **268**, 408–423.

Chiodini, G., Paonita, A., Aiuppa, A., Costa, A., Caliro, S., De Martino, P., Acocella, V., Vandemeulebrouck, J., 2016. Magmas near the critical degassing pressure drive volcanic unrest towards a critical state. *Nat. Commun.* **7**, 1–9.

Chiodini, G., Selva, J., Del Pezzo, E., Marsan, D., De Siena, L., D'Auria, L., Bianco, F., Caliro, S., De Martino, P., Ricciolino, P., Petrillo, Z., 2017. Clues on the origin of post-2000 earthquakes at Campi Flegrei caldera (Italy). *Sci. Rep.* **7**, 1–10.

Civetta, L., Orsi, G., Pappalardo, L., Fisher, R.V., Heiken, G., Ort, M., 1997. Geochemical zoning, mingling, eruptive dynamics and depositional processes - the Campanian Ignimbrite, Campi Flegrei caldera, Italy. *J. Volcanol. Geotherm. Res.* **75**, 183–219.

Civetta, L., D'Antonio, M., de Lorenzo, S., Di Renzo, V., Gasparini, P., 2004. Thermal and geochemical constraints on the 'deep' magmatic structure of Mt. Vesuvius. *J. Volcanol. Geotherm. Res.* **133**, 1–12.

Clarke, A.B., Stephens, S., Teasdale, R. Sparks, R.S.J., Diller, K., 2007. Petrologic constraints on the decompression history of magma prior to Vulcanian explosions at the Soufrière Hills volcano, Montserrat. *J. Volcanol. Geotherm. Res.* **161**, 261–274.

Cochain, B., Sanloup, C., Leroy, C., Kono, Y., 2017. Viscosity of mafic magmas at high pressures. *Geophys. Res. Lett*. **44**, 818–826.

Colson, R.O., McKay, G.A., Taylor, L.A., 1988. Temperature and composition dependencies of trace element partitioning: Olivine/melt and low-Ca pyroxene/melt. *Geochim. Cosmochim. Acta* **52**, 539–553.

Connolly, J.A.D., Schmidt, M.W., Solferino, G., Bagdassarov, N., 2009. Permeability of asthenospheric mantle and melt extraction rates at mid-ocean ridges. *Nature* **462**, 209–212.

Conte, A.M., Perinelli, C., Trigila, R., 2006. Cooling kinetics experiments on different Stromboli lavas: effects on crystal morphologies and phases composition. *J. Volcanol. Geotherm. Res.* **155**, 179–200.

Conte, A.M., Dolfi, D., Gaeta, M., Misiti, V., Mollo, S., Perinelli, C., 2009. Experimental constraints on evolution of leucite-basanite magma at 1 and 10^{-4} GPa: implications for parental compositions of Roman high-potassium magmas. *Eur. J. Mineral.* **21**, 763–782.

Conticelli, S., Guarnieri, L., Farinelli, A., Mattei, M., Avanzinelli, R., Bianchini, G., Boari, E., Tommasini, S., Tiepolo, M., Prelević, D., Venturelli, G., 2009. Trace elements and Sr–Nd–Pb isotopes of K-rich, shoshonitic, and calc-alkaline magmatism of the Western Mediterranean Region: Genesis of ultrapotassic to calc-alkaline magmatic associations in a post-collisional geodynamic setting. *Lithos* **107**, 68–92.

Costa, F., Shea, T., Ubide, T., 2020. Diffusion chronometry and the timescales of magmatic processes. *Nat. Rev. Earth Environ.* **1**, 201–214.

Couch, S., 2003. Experimental investigation of crystallization kinetics in a haplogranite system. *Am. Mineral.* **88**, 1471–1485.

Couch, S., Sparks, R.S.J., Carroll, M.R., 2003. The kinetics of degassing induced crystallization at Soufriere Hills Volcano, Montserrat. *J. Petrol.* **44**, 1477–1502.

Crank, J., 1975. The mathematics of diffusion. Oxford University Press, Ely House, London W.I.

D'Antonio, M., and Di Girolamo, P., 1994. Petrological and geochemical study of mafic shoshonitic volcanics from Procida-Vivara and Ventotene Islands (Campanian Region, South Italy). *Acta Vulcanol*. **5**, 69–80.

D'Antonio, M., Tilton, G.R., Civetta, L., 1996. Petrogenesis of Italian alkaline lavas deduced from Pb-Sr-Nd isotope relationships. In: Basu, A., Hart, S.R. (Eds.), Earth Processes. Reading the Isotopic Code - Am. Geophys. Un. Monograph Series vol. 95, pp. 253–267.

D'Antonio, M., Civetta, L. and Di Girolamo, P., 1999a. Mantle source heterogeneity in the Campanian Region (South Italy) as inferred from geochemical and isotopic features of mafic volcanic rocks with shoshonitic affinity. *Mineral. Petrol*. **67**, 163–192.

D'Antonio, M., Civetta, L., Orsi, G., Pappalardo, L., Piochi, M., Carandente, A., De Vita, S., Di Vito, M.A. and Isaia, R., 1999b. The present state of the magmatic system of the campi Flegrei caldera based on a reconstruction of its behaviour in the past 12 ka. *J. Volcanol. Geotherm. Res.* **91**, 247–268.

D'Antonio, M., Tonarini, S., Arienzo, I., Civetta, L., Di Renzo, V., 2007. Components and processes in the magma genesis of the Phlegrean Volcanic District, southern Italy. *Geol. Soc. Am. Spec. Pap.* **418**, 203–220.

D'Antonio, M., Tonarini, S., Arienzo, I., Civetta, L., Dallai, L., Moretti, R., Orsi, G., Andria, M., Trecalli, A., 2013. Mantle and crustal processes in the magmatism of the Campania region: Inferences from mineralogy, geochemistry, and Sr-Nd-O isotopes of young hybrid volcanics of the Ischia island (South Italy). *Contrib. Mineral. Petrol*. **165**, 1173–1194.

Dalou, C., Boulon, J., Koga, K.T., Dalou, R. and Dennen, R.L., 2018. DOUBLE FIT: Optimization procedure applied to lattice strain model. *Comput. Geosci*. **117**, 49–56.

Dalou, C., Koga, K. T., Shimizu, N., Boulon, J. and Devidal, J.L., 2012. Experimental determination of F and Cl partitioning between lherzolite and basaltic melt. *Contrib. Mineral. Petrol*. **163**, 591–609.

Davidson, J., Turner, S., Handley, H., Macpherson, C., Dosseto, A., 2007. Amphibole "sponge" in arc crust? *Geology* **35**, 787-790.

Davis, M.J., and Ihinger, P.D., 2002. Effects of thermal history on crystal nucleation in silicate melt: Numerical simulations. *J. Geophys. Res. Solid Earth* 107, ECV-8.

Davis, M.J., Ihinger, P.D., Lasaga, A.C., 1997. Influence of water on nucleation kinetics in silicate melt. *J. Non. Cryst. Solids* **219**, 62–69.

De Angelis, S.H., Larsen, J., Coombs, M., 2013. Pre-eruptive magmatic conditions at augustine volcano, Alaska, 2006: evidence from amphibole geochemistry and textures. *J. Petrol*. **54**, 1939-1961.

De Astis, G., Pappalardo, L. and Piochi, M., 2004. Procida volcanic history: New insights into the evolution of the Phlegraean Volcanic District (Campania region, Italy). *Bull. Volcanol.* **66**, 622–641.

de Vita, S., Orsi, G., Civetta, L., Carandente, A., D'Antonio, M., Deino, A., di Cesare, T., Di Vito, M., Fisher, R., Isaia, R., Marotta, E., Necco, A., Ort, M., Pappalardo, L., Piochi, M. and Southon, J., 1999. The Agnano–Monte Spina eruption (4100 years BP) in the restless Campi Flegrei caldera (Italy). *J. Volcanol. Geotherm. Res.* **91**, 269–301.

Del Gaudio, P., Mollo, S., Ventura, G., Iezzi, G., Taddeucci, J., Cavallo, A., 2010. Cooling rate-induced differentiation in anhydrous and hydrous basalts at 500 MPa: Implications for the storage and transport of magmas in dikes. *Chem. Geol*. **270**, 164–178.

Devine, J.D., Gardner, J.E., Brack, H.P., Layne, G.D., Rutherford, M.J., 1995. Comparison of microanalytical methods for estimating H_2O contents of silicic volcanic glasses. *Am. Mineral*. **80**, 319–328.

Di Genova, D., Sicola, S., Romano, C., Vona, A., Fanara, S., Spina, L., 2017. Effect of iron and nanolites on Raman spectra of volcanic glasses: a reassessment of existing strategies to estimate the water content. *Chem. Geol*. **475**, 76-86.

Di Renzo, V., Arienzo, I., Civetta, L., D'Antonio, M., Tonarini, S., Di Vito, M.A., Orsi, G., 2011. The magmatic feeding system of the Campi Flegrei caldera: Architecture and temporal evolution. *Chem. Geol*. **281**, 227–241.

Di Stefano, R., Bianchi, I., Ciaccio, M.G., Carrara, G, Kissling, E., 2011. Three-dimensional Moho topography in Italy: new constraints from receiver functions and controlled source seismology. *Geochem. Geophys. Geosyst.* **12**, 1–15.

Di Stefano, R., Chiarabba, C., Lucente, F., Amato, A., 1999. Crustal and uppermost mantle structure in Italy. *Geophys. J. Int.* **139**, 438–498.

Dimanov, A., and Wiedenbeck, M., 2006. (Fe, Mn)-Mg interdiffusion in natural diopside: effect of pO_2. *Eur. J. Mineral*. **18**, 705–718.

Dingwell, D.B., Bagdassarov, N.S., Bussod, G.Y., Webb, S.L., 1993. Magma rheology. In: Luth RH (ed) Short course handbook on experiments at high pressure and applications to Earth's mantle, vol. 21.

Donaldson, C.H., 1985. The Rates of Dissolution of Olivine, Plagioclase, and Quartz in a Basalt Melt. *Mineral. Mag*. **49**, 683–693.

Dorogokupets, P.I., and Dewaele, A., 2007. Equations of state of MgO, Au, Pt, NaCl-B1, and NaCl-B2: Internally consistent high-temperature pressure scales. *High Press. Res*. **27**, 431-446.

Dowty, E., Keil, K., Prinz, M., 1974. Lunar pyroxene-phyric basalts: crystallization under supercooled conditions. *J. Petrol.* **15**, 419–453.

Dowty, E., 1980. Crystal growth and nucleation theory and the numerical simulation of igneous crystallization. In the Physics of Magmatic Processes; Hargraves R.B., Ed.; Princeton University Press: Princeton, NJ, USA, pp. 419–485.

Drexler, J.W., Bornhorst, T.J., Noble, D.C., 1983. Trace-element sanidine/glass distribution coefficients for peralkaline silicic rocks and their implications to peralkaline petrogenesis. *Lithos* **16**, 265–271.

Druitt, T. H., Costa, F., Deloule, E., Dungan, M., Scaillet, B. 2012. Decadal to monthly timescales of magma transfer and reservoir growth at a caldera volcano. *Nature* **482**, 77–80.

Dygert, N., Draper, D.S., Rapp, J.F., Lapen, T.J., Fagan, A.L., Neal, C.R., 2020. Experimental determinations of trace element partitioning between plagioclase, pigeonite, olivine, and lunar basaltic melts and an fO_2 dependent model for plagioclase-melt Eu partitioning. *Geochim. Cosmochim. Acta,* **279**, 258-280.

Edwards, B.R., and Russell, J.K., 1998. Time scales of magmatic processes: New insights from dynamic models for magmatic assimilation. *Geology* **26**, 1103–1106.

Ernst, W.G., and Liu, J., 1998. Experimental phase-equilibrium study of Al- and Ti contents of calcic amphibole in MORB-A semiquantitative thermobarometer. *Am. Mineral*. **83**, 952-969.

Ersoy, Y., and Helvaci, C., 2010. FC-AFC-FCA and mixing modeler: A Microsoft® Excel© spreadsheet program for modeling geochemical differentiation of magma by crystal fractionation, crustal assimilation and mixing. *Comput. Geosci.* **36**, 383–390.

Esposito, R., Bodnar, R.J., Danyushevsky, L.V., De Vivo, B., Fedele, L., Hunter, J., Lima, A., Shimizu, N., 2011. Volatile evolution of magma associated with the solchiaro eruption in the Phlegrean Volcanic District (Italy*). J. Petrol.* **52**, 2431–2460.

Fanara, S., Botcharnikov, R.E., Palladino, D.M., Adams, F., Buddensieck, J., Mulch, A., Beherens, H., 2015. Volatiles in magmas related to the Campanian ignimbrite eruption: experiments vs. natural findings. *Am. Mineral.* **100**, 2284–2297.

Faure, F., and Schiano, P., 2005. Experimental investigation of equilibration conditions during forsterite growth and melt inclusion formation. *Earth. Planet. Sci. Lett.* **236**, 882–898.

Faure, F., Trolliard, G., Nicollet, C., Montel, J.M., 2003. A developmental model of olivine morphology as a function of the cooling rate and the degree of undercooling. *Contrib. Mineral. Petrol.* **145**, 251–263.

Fedele, F.G., Giaccio, B., Isaia, R., Orsi, G., 2003. The Campanian Ignimbrite eruption, Heinrich Event 4, and Palaeolithic change in Europe: a high-resolution investigation. *AGU Geophys. Monogr*.**139**, 301-327.

Fedele, L., Zanetti, A., Morra, V., Lustrino, M., Melluso, L., Vannucci, R., 2009. Clinopyroxene/liquid trace element partitioning in natural trachyte - Trachyphonolite systems: Insights from Campi Flegrei (southern Italy). *Contrib. Mineral. Petrol.* **158**, 337–356.

Fedi, M., Cella, F., D'Antonio, M., Florio, G., Paoletti, V., Morra, V., 2018. Gravity modeling finds a large magma body in the deep crust below the Gulf of Naples, Italy. *Sci. Rep*. **8**, 1–19.

Fenn, P.M. 1977. The nucleation and growth of alkali feldspars from hydrous melts. *Can. Mineral*. **15**, 135–161.

Finnila, A.B., Hess, P.C., Rutherford, M.J., 1994. Assimilation by lunar mare basalts: melting of crustal material and dissolution of anorthite. *J. Geophys. Res*. **99**, 14677–14690.

Fowler, S.J., Spera, F.J., Bohrson, W.A., Belkin, H.E., De Vivo, B., 2007. Phase Equilibria Constraints on the Chemical and Physical Evolution of the Campanian Ignimbrite. *J. Petrol.* **48**, 459-493.

Foden, J.D., and Green, D.H., 1992. Possible role of amphibole in the origin of andesite: some experimental and natural evidence. *Contrib. Mineral. Petrol*. **109**, 479-493.

Fokin, V.M., Zanotto, E.D., Yuritsyn, N.S., Schmelzer, J.W.P., 2006. Homogeneous crystal nucleation in silicate glasses: A 40 years perspective. *J. Non. Cryst. Solids* **352**, 2681–2714.

Folch, A., and Martı, J., 1998. The generation of overpressure in felsic magma chambers by replenishment. *Earth Planet. Sci. Lett*. **163**, 301–314.

Fornaciai, A., Perinelli, C., Armienti, P., Favalli, M., 2015. Crystal size distributions of plagioclase in lavas from the July–August 2001 Mount Etna eruption. *Bull. Volcanol*. **77**, 70.

Forni, F., Petricca, E., Bachmann, O., Mollo, S., De Astis, G., & Piochi, M., 2018. The role of magma mixing/mingling and cumulate melting in the Neapolitan Yellow Tuff caldera-forming eruption (Campi Flegrei, Southern Italy). *Contributions to Mineralogy and Petrology*, **173**, 45.

Forsythe, L., Nielsen, R. and Fisk, M.R., 1994. High-field-strength element partitioning between pyroxene and basaltic to dacitic magmas. *Chem. Geol*. **117**, 107–125.

Francis, D., and Minarik, W., 2008. Aluminum-dependent trace element partitioning in clinopyroxene. *Contrib. Mineral. Petrol*. **156**, 439–451.

Freda, C., Baker, D.R., Ottolin, L., 2001. Reduction of water loss from gold-palladium capsules during piston-cylinder experiments by use of pyrophyllite powder. *Am. Mineral.* **86**, 234–237.

Gaetani, G.A., 2004. The influence of melt structure on trace element partitioning near the peridotite solidus. *Contrib. Mineral. Petrol*. **147**, 511–527.

Gaetani, G.A., Kent, A.J.R., Grove, T.L., Hutcheon, I.D., Stolper, E.M., 2003. Mineral/melt partitioning of trace elements during hydrous peridotite partial melting. *Contrib. Mineral. Petrol.* **145**, 391-405.

Gallahan, W., and Nielsen, R., 1992. The partitioning of Sc, Y, and the rare earth elements between high-Ca pyroxene and natural mafic to intermediate lavas at 1 atmosphere. *Geochim. Cosmochim. Acta* **56**, 2387–2404.

Ghiorso, M.S., and Sack, R.O., 1995. Chemical mass transfer in magmatic processes IV. A revised and internally consistent thermodynamic model for the interpolation and extrapolation of liquid-solid equilibria in magmatic systems at elevated temperatures and pressures. *Contrib. Mineral. Petrol.* **119**, 197–212.

Gibb, F.G.F., 1974. Supercooling and the crystallization of plagioclase from a basaltic magma. *Mineral. Mag*. **39**, 641–653.

Giberti, G., and Wilson, L., 1990. The influence of geometry on the ascent of magma in open fissures. *Bull. Volcanol*. **52**, 515–521.

Giordano, D., and Dingwell, D.B., 2000. Viscosity of a Teide phonolite in the welding interval. *J. Volcanol. Geotherm. Res*. **103**, 239–245.

Giordano, D., and Dingwell. D.B., 2003. Non-Arrhenian multicomponent melt viscosity: A model. *Earth Planet. Sci. Lett*. **208**, 337–349.

Giordano, D., Romano, C., Dingwell, D.B., Poe, B., Behrens, H., 2004a. The combined effects of water and fluorine on the viscosity of silicic magmas. *Geochim. Cosmochim. Acta* **68**, 5159–5168.

Giordano, D., Romano, C., Papale, P., Dingwell, D.B., 2004b. The viscosity of trachytes, and comparison with basalts, phonolites, and rhyolites. *Chem. Geol*. **213**, 49–61.

Giordano, D., Mangiacapra, A., Potuzak, M., Russel, J.K., Romano, C., Dingwell, D.B., Di Muro, A., 2006. An expanded non-Arrhenian model for silicate melt viscosity: a treatment for metaluminous, peraluminous and peralkaline liquids. *Chem Geol* **229**, 42–56.

Giordano, D., Potuzak, M., Romano, C., Dingwell, D.B., Nowak, M., 2008a. Viscosity and glass transition temperature of hydrous melts in the system $CaAl_2Si_2O_8$-$CaMgSi_2O_6$. *Chem. Geol*. **256**, 203–215.

Giordano, D., Russell, J.K., Dingwell, D.B., 2008b. Viscosity of magmatic liquids: a model. *Earth. Planet. Sci. Lett.* **271**, 123–134.

Giordano, D., Ardia, P., Romano, C., Dingwell, D.B., Di Muro, A., Schmidt, M.W., Mangiacapra, A., Hess, K.U., 2009. The rheological evolution of alkaline Vesuvius magmas and comparison with alkaline series from the Phlegrean Fields, Etna, Stromboli and Teide. *Geochim. Cosmochim. Acta* **73**, 6613–6630.

Graham, C.M., and Navrotsky, A., 1986. Thermochemistry of the tremolite-edenite amphiboles using fluorine analogues, and applications to amphibole-plagioclase-quartz equilibria. *Contrib. Mineral. Petrol.* **93**, 18-32.

Granati, S.F., 2016. The architecture of the magmatic feeding system of the Campi Flegrei Volcanic District: constraints from experimental petrology. Sapienza University of Rome, Rome.

Green, T.H., and Ringwood, A.E., 1968. Genesis of the calc-alkaline igneous rock suite. *Contrib. Mineral. Petrol.* **18**, 105-162.

Green, T.H., and Pearson, N.J., 1983. Effect of pressure on rare earth element partition coefficients in common magmas. *Nature* **305**, 414–416.

Green, T.H., and Pearson, N.J., 1985. Rare earth element partitioning between clinopyroxene and silicate liquid at moderate to high pressure. *Contrib. Mineral. Petrol.* **91**, 24–36.

Grove, T.L., and Walker, D., 1977. Cooling histories of Apollo 15 quartz normative basalts. *Proc. Lunar Planet. Sci. Conf.* **8**, 1501–1520.

Grove, T.L., Raudsepp, M., 1978. Effects of kinetics on the crystallization of quartz normative basalt 15597-an experimental study. *Proc. Lunar Planet. Sci. Conf.* **9**, 585–599.

Gualda, G.A.R., Ghiorso, M.S., Lemons, R. V., Carley, T.L., 2012. Rhyolite-MELTS: A modified calibration of MELTS optimized for silica-rich, fluid-bearing magmatic systems. *J. Petrol.* **53**(5), 875-890.

Guidoboni, E., and Ciuccarelli, C., 2011. The Campi Flegrei caldera: Historical revision and new data on seismic crises, bradyseisms, the Monte Nuovo eruption and ensuing earthquakes (twelfth century 1582 ad). *Bull. Volcanol.* **73**, 655–677.

Günther, D., Frischknecht, R., Heinrich, C.A., Kahlert, H.J., 1997. Capabilities of an Argon Fluoride 193 nm excimer laser for laser ablation inductively coupled plasma mass spectometry microanalysis of geological materials. *J. Anal. At. Spectrom.* **12**, 939–944.

Hammer, J.E., 2006. Influence of fO_2 and cooling rate on the kinetics and energetics of Fe-rich basalt crystallization. *Earth Planet. Sci. Lett.* **248**, 618–637.

Hammer, J.E., 2008. Experimental studies of the kinetics and energetics of magma crystallization. In: Putirka KD, Tepley III FJ (eds) Minerals, inclusions and volcanic processes. *Rev. Mineral. Geochemistry*, pp 9–59.

Hammer, J.E., and Rutherford, M.J., 2002. An experimental study of the kinetics of decompression-induced crystallization in silicic melt. *J. Geophys. Res.* **107**, 2021.

Hammer, J.E., Cashman, K.V., Voight, B., 2000. Magmatic processes revealed by textural and compositional trends in Merapi dome lavas. *J. Volcanol. Geotherm. Res.* **100**, 165–192.

Hammer, J.E., Sharp, T.G., Wessel, P., 2010. Heterogeneous nucleation and epitaxial crystal growth of magmatic minerals. *Geology* **38**, 367–370.

Hart, S.R., and Dunn, T., 1993. Experimental Cpx Melt Partitioning of 24 Trace-Elements. *Contrib. Mineral. Petrol.* **113**, 1–8.

Hawthorne, F.C., Oberti, R., Harlow, G.E., Maresch, W.V., Martin, R.F., Schumacher, J.C., Welch, M.D., 2012. Nomenclature of the amphibole supergroup. *Am. Mineral.* **97**, 2031-2048.

Helz, R.T., and Wright, T., 1992. Differentiation and magma mixing on Kilauea's east rift zone A further look at the eruptions of 1955 and 1960. Part I. The late 1955 lavas. *Bull Volcanol* **54**, 361–384.

Henderson, C.M.B., and Pierozynski, W.J., 2012. An experimental study of Sr, Ba and Rb partitioning between alkali feldspar and silicate liquid in the system nepheline-kalsilite-quartz at 0.1 GPa P(H_2O): a revisitation and reassessment. *Mineral. Mag.* **76**, 157–190.

Herzberg, C.T., 1978. Pyroxene geothermometry and geobarometry: Experimental and thermodynamic evaluation of some subsolidus phase relations involving pyroxenes in the system CaO-MgO-Al_2O_3-SiO_2. *Geochim. Cosmochim. Acta*, **42**, 945–957.

Hess, K., and Dingwell, D.D., 1996. Viscosities of hydrous leucogranitic melts: a non-Arrhenian on the nature and efficiency of magmatic processes. As pendence (H_20 concentration in weight percent) for each. *Am. Mineral.* **81**, 1297-1300.

Hess, K.U., Dingwell, D.B., Webb, S.L., 1995. The influence of excess alkalis on the viscosity of a haplogranitic melt. *Am. Mineral.* **80**, 297–304.

Higgins, M.D., 1994. Numerical modeling of crystal shapes in thin section: estimation of crystal habit and true size. *Am. Mineral.* **79**, 113–119.

Higgins, M.D., 1998. Origin of anorthosite by textural coarsening: quantitative measurements of a natural sequence of textural development. *J. Petrol.* **39**, 1307–1323.

Higgins, D.M., 2000. Measurement of crystal size distributions. *Am. Mineral.* **85**, 1105–1116.

Higgins, M.D., 2002. Closure in crystal size distributions (CSD), verification of CSD calculations, and the significance of CSD fans. *Am. Mineral.* **87**, 1242–1243.

Higgins, M.D., and Roberge, J., 2003. Crystal size distribution of plagioclase and amphibole from Soufriere Hills Volcano, Montserrat: evidence for dynamic crystallization-textural coarsening cycles. *J. Petrol.* **44**, 1401–1411.

Higuchi, H., and Nagasawa, H., 1969. Partition of trace elements between rock-forming minerals and the host volcanic rocks. *Earth Planet. Sci. Lett.* **7**, 281–287.

Hill, E., Wood, B.J. and Blundy, J.D., 2000. The effect of Ca-Tschermaks component on trace element partitioning between clinopyroxene and silicate melt. *Lithos* **53**, 203–215.

Hill, E., Blundy, J.D. and Wood, B.J., 2011. Clinopyroxene-melt trace element partitioning and the development of a predictive model for HFSE and Sc. *Contrib. Mineral. Petrol.* **161**, 423–438.

Holland, T., and Blundy, J., 1994. Non-ideal interactions in calcic amphiboles and their bearing on amphibole-plagioclase thermometry. *Contrib. Mineral. Petrol.* **116**, 433-447.

Huang, F., Lundstrom, C.C., McDonough, W.F., 2006. Effect of melt structure on trace-element partitioning between clinopyroxene and silicic, alkaline, aluminous melts. *Am. Mineral*. **91**, 1385-1400.

Hughes, E.C., Buse, B., Kearns, S.L., Blundy, J.D., Kilgour, G.N., Mader, H.M., 2019. Low analytical totals in EPMA of hydrous silicate glass due to sub-surface charging: Obtaining accurate volatiles by difference. *Chem. Geol.* **505**, 48–56.

Hui, H., and Zhang, Y., 2007. Toward a general viscosity equation for natural anhydrous and hydrous silicate melts. *Geochim. Cosmochim. Acta* **71**, 403–416.

Humphreys, M.C.S., Kearns, S.L., Blundy, J.D., 2006. SIMS investigation of electron-beam damage to hydrous, rhyolitic glasses: implications for melt inclusion analysis. *Am. Mineral.* **91**, 667–679.

Iacovino, K., and Till, C.B., 2019. DensityX: A program for calculating the densities of magmatic liquids up to 1,627 °C and 30 kbar Kayla. *Volcanica* **2**, 1–10.

Iezzi, G., Mollo, S., Torresi, G., Ventura, G., Cavallo, A., Scarlato, P., 2011. Experimental solidification of an andesitic melt by cooling. *Chem. Geol*. **283**, 261-273.

Iezzi G., Mollo S., Shahini E., Cavallo A., Scarlato P. (2014) The cooling kinetics of plagioclase feldspar as revealed by electron-microprobe mapping. *Am. Mineral*. **99**, 898–907.

Irvine, T.N., and Baragar, W.R.A., 1971. A guide to the chemical classification of the common volcanic rocks. *Can. J. Earth Sci*. **8**, 523–548.

Johannes, W., 1978. Melting of plagioclase in the system Ab - An – H_2O and Qz - Ab - An - H_2O at P_{H2O} =5 kbars, an equilibrium problem. *Contrib. Mineral. Petrol*. **66**, 295–303.

Johannes, W., Bell, P.M., Mao, H.K., Boettcher, A.L., Chipman, D.W., Hays, J.F., Newton, R.C., Seifert, F., 1971. An interlaboratory comparison of piston-cylinder pressure calibration using the albite-breakdown reaction. *Contrib. Mineral. Petrol*. **32**, 24–38.

Jones, J.H., 1995. Experimental trace element partitioning. In Rock physics and phase relations: A handbook of physical constants pp. 73–104.

Kani, K., 1934. The Measurement of the Viscosity of Basalt Glass at High Temperatures, II. *Proc. Imp. Acad*. **10**, 79–82.

Kaplow, R., Strong, S.L., Averbach, B.L., 1965. Radial distribution functions for liquid mercury and lead. *Phys. Rev*. **138**, A1336.

Kelemen, P.B., 1990. Reaction between ultramafic rock and fractionating basaltic magma I. Phase relations, the origin of calc-alkaline magma series, and the formation of discordant dunite. *J. Petrol*. **31**, 51–98.

Kennedy, W.Q., 1935. The influence of chemical factors on the crystallization of hornblende in igneous rocks. *Mineral. Mag. J. Mineral Soc*. **24**, 203-207.

Kerr, R.C., 1995. Convective crystal dissolution. *Contrib. Mineral. Petrol*. **121**, 237–246.

Kirkpatrick, R.J., 1977. Nucleation and growth of plagioclase, Makaopuhi and Alae lava lakes, Kilauea Volcano, Hawaii. *Geol. Soc. Am. Bull*. **88**, 78–84.

Kirkpatrick, R.J., 1981. Kinetics of crystallization of igneous rocks. *Rev. Mineral.* **8**, 321–395.

Kirkpatrick, R.J., Kuo, L., Melchior, J., 1981. Crystal growth in incongruently-melting compositions: programmed cooling experiments with diopside. *Am. Mineral*. **66**, 223–241.

Klotz, S., Hamel, G., Frelat, J., 2004. A new type of compact large-capacity press for neutron and x-ray scattering. *High Press. Res*. **24**, 219–223.

Kono, Y., Irifune, T., Higo, Y., Inoue, T., Barnhoorn, A., 2010. P-V-T relation of MgO derived by simultaneous elastic wave velocity and in situ X-ray measurements: A new pressure scale for the mantle transition region. *Phys. Earth Planet. Inter*. **183**, 196–211.

Kono, Y., Kenney-Benson, C., Hummer, D., Ohfuji, H., Park, C., Shen, G., Wang, Y., Kavner, A., Manning, C.E., 2014a. Ultralow viscosity of carbonate melts at high pressures. *Nat. Commun*. **5**, 5091.

Kono, Y., Park, C., Kenney-Benson, C., Shen, G., Wang, Y., 2014b. Toward comprehensive studies of liquids at high pressures and high temperatures: Combined structure, elastic wave velocity, and viscosity measurements in the Paris-Edinburgh cell. *Phys. Earth Planet. Inter*. **228**, 269–280.

Kono, Y., Kenney-Benson, C., Shibazaki, Y., Park, C., Wang, Y., Shen, G., 2015. X-ray imaging for studying behavior of liquids at high pressures and high temperatures using Paris-Edinburgh press. *Rev. Sci. Instrum.* **86**, 072207.

Kozu, S., and Kani, K., 1935. Viscosity Measurements of the Ternary System Diopside-Albite-Anorthite at High Temperatures. *Proc. Imp. Acad*. **11**, 383–385.

Kress, V.C., and Carmichael, I.S.E., 1991. The compressibility of silicate liquids containing Fe_2O_3 and the effect of composition, temperature, oxygen fugacity and pressure on their redox states. *Contrib. Mineral. Petrol*. **108**, 82–92.

Kress, V.C., and Ghiorso, M.S., 1995. Multicomponent diffusion in basaltic melts. *Geochim. Cosmochim. Acta* **59**, 313–324.

Kuo, L.C., and Kirkpatrick, R.J., 1985. Dissolution of mafic minerals and its implications for the ascent velocities of peridotite-bearing basaltic magmas. *J. Geol.* **93**, 691–700.

Kushiro, I., 1980. Viscosity, density, and structure of silicate melts at high pressures and their petrological applications, in: Physics of Magmatic Processes. pp. 93–120.

Kushiro, I., Yoder, H.S., Mysen, B.O., 1976. Viscosities of basalt and andesite melts at high pressures. *J. Geophys. Res.* **81**, 6351–6356.

Kutolin, V.A., and Agafonov, L.V., 1978. Composition of the upper mantle in light of the relative stability of ultramafic nodules. *Geol. Geofiz*. **19**, 3–13.

Larocque, J., and Canil, D., 2010. The role of amphibole in the evolution of arc magmas and crust: the case from the Jurassic Bonanza arc section, Vancouver Island, Canada. *Contrib. Mineral. Petrol*. **159**, 475-492.

LaTourrette, T.Z., and Burnett, D.S., 1992. Experimental determination of U and Th partitioning between clinopyroxene and natural and synthetic basaltic liquid. *Earth Planet. Sci. Lett*. **110**, 227–244.

LaTourrette, T., Wasserburg, G.J., Fahey, A.J., 1996. Self-diffusion of Mg, Ca, Ba, Nd, Yb, Ti, Zr, and U in haplobasaltic melt. *Geochim. Cosmochim. Acta* **60**, 1329–1340.

Le Losq, C., Neuville, D.R., Moretti, R., Roux, J., 2012. Determination of water content in silicate glasses using Raman spectrometry: implications for the study of explosive volcanism. *Am. Mineral*. **97**, 779-790.

Le Maitre, R., Streckeisen, A., Zanettin, B., Bas, M., 2002. Igneous rocks: a classification and glossary of terms: recommendations of the International Union of Geological Sciences Subcommission on the Systematics., Cambridge University Press.

Leblanc, G.E., Secco, R.A., Kostic, M., 1999. Viscosity measurement, in: The Measurement, Instrumentation and Sensors Handbook.

Leeman, W.P., and Phelps, D.W., 1981. Partitioning of rare earths and other trace elements between sanidine and coexisting volcanic glass. *J. Geophys. Res.* **86**, 10193–10199.

Lentz, R.C.F., and Mcsween, H.Y., 2000. Crystallization of the basaltic shergottites: insights from crystal size distribution (CSD) analysis of pyroxenes. *Meteorit. Planet. Sci.* **35**, 919–927.

Lesher, C.E., Cashman, K.V., Mayfield, J.D., 1999. Kinetic controls on crystallization of Tertiary North Atlantic basalt and implications for the emplacement and cooling history of lava at site 989, Southeast Greenland Rifted Margn 1. In: *Proceedings of the Ocean Drilling Program, Scientific Results*. pp 135–148.

Li, L., Xiong, X.L., Liu, X.C., 2017. Nb/Ta fractionation by amphibole in hydrous basaltic systems: implications for arc magma evolution and continental crust formation. *J. Petrol*. **58**, 328.

Liang, Y., 1999. Diffusive dissolution in ternary systems: Analysis with applications to quartz and quartzite dissolution in molten silicates. *Geochim. Cosmochim. Acta* **63**, 3983–3995.

Liang, Y., 2000. Dissolution in molten silicates: Effects of solid solution. *Geochim. Cosmochim. Acta* **64**, 1617–1627.

Liang, Y., 2003. Kinetics of crystal-melt reaction in partially molten silicates: 1. Grain scale processes. *Geochem. Geophys. Geosyst*. **4**, 1045.

Liang, L.H., Zhao, M., Jiang, Q., 2002. Melting enthalpy depression of nanocrystals based on surface effect. *J. Mater. Sci. Lett*. **103**, 239–248.

Liebske, C., Schmickler, B., Terasaki, H., Poe, B.T., Suzuki, A., Funakoshi, K. ichi, Ando, R., Rubie, D.C., 2005. Viscosity of peridotite liquid up to 13 GPa: Implications for magma ocean viscosities. *Earth Planet. Sci. Lett*. **240**, 589–604.

Lindstrom, D., 1976. Partitioning of ferric iron between diopside and silicate liquid. Eos, *Trans. Am. Geophys. Union* **57**, 339–339.

Lister, J.R., and Kerr, R.C., 1991. Fluid-mechanical models of crack propagation and their application to magma transport in dykes. *J. Geophys. Res*. **96**, 10049–10077.

Lofgren, G.E., Huss, G.R., Wasserburg, G.J., 2006. An experimental study of trace-element partitioning between Ti-Al-clinopyroxene and melt: Equilibrium and kinetic effects including sector zoning. *Am. Mineral*. **91**, 1596–1606.

Lofgren, G.E., 1974. An experimental study of plagioclase crystal morphology; isothermal crystallization. *Am. J. Sci.* **274**, 243–273.

Lofgren, G.E., 1980. Experimental studies on the dynamic crystallization of silicate melts. *Physics of Magmatic Process* **487**, 551.

Lofgren, G.E., 1983. Effect of heterogeneous nucleation on basaltic textures: a dynamic crystallization study. *J. Petrol.* **24**, 229–255.

Lundstrom, C.C., Shaw, H.F., Ryerson, F.J., Phinney, D.L., Gill, J.B. and Williams, Q., 1994. Compositional controls on the partitioning of U, Th, Ba, Pb, Sr and Zr between clinopyroxene and haplobasaltic melts: implications for uranium series disequilibria in basalts. *Earth Planet. Sci. Lett*. **128**, 407–423.

Lundstrom, C.C., Shaw, H.F., Ryerson, F.J., Williams, Q. and Gill, J., 1998. Crystal chemical control of clinopyroxene-melt partitioning in the Di-Ab-An system: Implications for elemental fractionations in the depleted mantle. *Geochim. Cosmochim. Acta* **62**, 2849–2862.

Mahood, G., and Hildreth, W., 1983. Large partition coefficients for trace elements in high-silica rhyolites. *Geochim. Cosmochim. Acta* **47**, 11–30.

Manga, M., and Loewenberg, M., 2001. Viscosity of magmas containing highly deformable bubbles. *J. Volcanol. Geotherm. Res*. **105**, 19–24.

Mangan, M.T., 1990. Crystal size distribution systematics and the determination of magma storage times: the 1959 eruption of Kilauea volcano, Hawaii. *J. Volcanol. Geotherm. Res*. **44**, 295-302.

Marsh, B.D., 1988. Crystal size distribution (CSD) in rocks and the kinetics and dynamics of crystallization. *Contrib. Mineral. Petrol.* **99**, 277–291.

Marsh, B.D., 1998. On the interpretation of crystal size distributions in magmatic systems. *J. Petrol.* **39**, 553–599.

Martin, V.M., Morgan, D.J. Jerram, D.A., Caddick, M., Prior, D., Davidson, J.P., 2008. Bang! Month-scale eruption triggering at Santorini Volcano. *Science* **321**, 1178.

Martini, M., Giudicepietro, F., D'Auria, P., Esposito, A.M., Caputo, T., Curciotti, R., De Cesare, W., Orazi, M., Scarpato, G., Caputo, A., Peluso, R., Ricciolino, P., Linde, A., Sacks, S., 2007. Seismological monitoring of the February 2007 effusive eruption of the Stromboli volcano, *Annals of Geophysics* **50**(6), 775-788.

Masotta, M., Pontesilli, A., Mollo, S., Armienti, P., Ubide, T., Nazzari, M., Scarlato, P., 2020. The role of undercooling during clinopyroxene growth in trachybasaltic magmas: Insights on magma decompression and cooling at Mt. Etna volcano. *Geochim. Cosmochim. Acta* **268**, 258–276.

Mastrolorenzo, G., Palladino, D.M., Pappalardo, L., Rossano, S., 2017. Probabilistic-numerical assessment of pyroclastic current hazard at Campi Flegrei and Naples city: multi-VEI scenarios as a tool for "full-scale" risk management. *PLoS One* **12**, 1–28.

Mazzeo, F.C., D'Antonio, M., Arienzo, I., Aulinas, M., Di Renzo, V., Gimeno, D., 2014. Subduction-related enrichment of the Neapolitan volcanoes (Southern Italy) mantle source: New constraints on the characteristics of the slab-derived components. *Chem. Geol.* **386**, 165–183.

McDade, P., Blundy, J.D., Wood, B.J., 2003. Trace element partitioning on the Tinaquillo solidus at 1.5 GPa. *Phys. Earth Planet. Inter.* **139**, 129–147.

McDonough, W.F., and Sun, S.s., 1995. The composition of the Earth. *Chem. Geol.* **120**, 223–253.

McKay, G., Le, L., Wagstaff, J., Crozaz, G., 1994. Experimental partitioning of rare earth elements and strontium: Constraints on petrogenesis and redox conditions during crystallization of Antarctic angrite Lewis Cliff 86010. *Geochim. Cosmochim. Acta* **58**, 2911–2919.

McKenzie, D., 1984. The Generation and Compaction of Partially Molten Rock. *J. Petrol.* **25**, 713–765.

McKenzie, D., 1985. The extraction of magma from the crust and mantle. *Earth Planet. Sci. Lett.* **74**, 81–91.

McKenzie, D., 1989. Some remarks on the movement of small melt fractions in the mantle. *Earth Planet. Sci. Lett.* **95**, 53–72.

McMillan, P.F., and Wolf, G.H., 1995. Vibrational spectroscopy of silicate liquids. *Rev. Mineral. Geochem.* **32**, 247–315.

Melekhova, E., Blundy, J., Robertson, R., Humphreys, M.C.S., 2015. Experimental evidence for polybaric differentiation of primitive arc basalt beneath St. Vincent, Lesser Antilles. *J. Petrol*. **56**, 161-192.

Melluso, L., De' Gennaro, R., Fedele, L., Franciosi, L. and Morra, V., 2012. Evidence of crystallization in residual, Cl–F-rich, agpaitic, trachyphonolitic magmas and primitive Mg-rich basalt–trachyphonolite interaction in the lava domes of the Phlegrean Fields (Italy). *Geol. Mag.* **149**, 532–550.

Melnik, O., and Sparks, R.S.J., 2005. Control on conduit magma flows dynamics during lava dome building eruptions. *J. Geophys. Res.* **110**, B02209.

Michely, L.T., Leitzke, F.P., Speelmanns, I.M., Fonseca, R.O.C., 2017. Competing effects of crystal chemistry and silicate melt composition on trace element behavior in magmatic systems: insights from crystal/silicate melt partitioning of the REE, HFSE, Sn, In, Ga, Ba, Pt and Rh. *Contrib. Mineral. Petrol*. **172**, 39.

Milman-Barris, M.S., Beckett, J.R., Baker, M.B., Hofmann, A.E., Morgan, Z., Crowley, M.R., Vielzeuf, D., Stolper, E., 2008. Zoning of phosphorus in igneous olivine. *Contrib. Mineral. Petrol*. **155**, 739–765.

Mishima, N., Ota, R., Wakasugi, T., Fukunaga, J., 1996. Analysis of crystallization behavior in $Li_2O{\cdot}2SiO_2$ glass by DTA method based on a liquid model. J. *Non. Cryst. Solids* **197**, 19–24.

Misiti, V., Freda, C., Taddeucci, J., Romano, C., Scarlato, P., Longo, A., Papale, P., Poe, B.T., 2006. The effect of H_2O on the viscosity of K-trachytic melts at magmatic temperatures. *Chem. Geol*. **235**, 124–137.

Misiti, V., Vetere, F., Freda, C., Scarlato, P., Behrens, H., Mangiacapra, A., Dingwell, D.B., 2011. A general viscosity model of Campi Flegrei (Italy) melts. *Chem. Geol.* **290**, 50–59.

Misiti, V., Vetere, F., Mangiacapra, A., Behrens, H., Cavallo, A., Scarlato, P., Dingwell, D.B., 2009. Viscosity of high-K basalt from the 5th of April 2003 Stromboli paroxysmal explosion. *Chem. Geol*. **260**, 278–285.

Mollard, E., Martel, C., Bourdier, J.L., 2012. Decompression-induced crystallization in hydrated silica-rich melts: Empirical models of experimental plagioclase nucleation and growth kinetics. *J. Petrol*. **53**, 1743–1766.

Mollo, S., Putirka, K., Iezzi, G., Del Gaudio, P., Scarlato, P., 2011. Plagioclase-melt (dis)equilibrium due to cooling dynamics: Implications for thermometry, barometry and hygrometry. *Lithos* **125**, 221–235.

Mollo, S., Misiti, V., Scarlato, P., Soligo, M., 2012. The role of cooling rate in the origin of high temperature phases at the chilled margin of magmatic intrusions. Chem. Geol. 322, 28-46.

Mollo, S., Iezzi, G., Ventura, G., Cavallo, A., Scarlato, P., 2012. Heterogeneous nucleation mechanisms and formation of metastable phase assemblages induced by different crystalline seeds in a rapidly cooled andesitic melt. *J. Non. Cryst. Solids* **358**, 1624–1628.

Mollo, S., Putirka, K., Misiti, V., Soligo, M., Scarlato, P., 2013. A new test for equilibrium based on clinopyroxene-melt pairs: clues on the solidification temperatures of Etnean alkaline melts at post-eruptive conditions. *Chem. Geol*. **352**, 92-100.

Mollo, S., Blundy, J.D., Iezzi, G., Scarlato, P., Langone, A., 2013. The partitioning of trace elements between clinopyroxene and trachybasaltic melt during rapid cooling and crystal growth. *Contrib. Mineral. Petrol*. **166**, 1633–1654.

Mollo, S., Forni, F., Bachmann, O., Blundy, J.D., De Astis, G., Scarlato, P., 2016. Trace element partitioning between clinopyroxene and trachy-phonolitic melts: A case study from the Campanian Ignimbrite (Campi Flegrei, Italy). *Lithos* **252–253**, 160–172.

Mollo, S., Blundy, J., Scarlato, P., De Cristofaro, S.P., Tecchiato, V., Di Stefano, F., Vetere, F., Holtz, F., Bachmann, O., 2018. An integrated P-T-H_2O-lattice strain model to quantify the role of clinopyroxene fractionation on REE+Y and HFSE patterns of mafic alkaline magmas: Application to eruptions at Mt. Etna. *Earth-Sci Rev*. **185**, 32–56.

Morabito, S., Petrosino, P., Milia, A., Sprovieri, M., Tamburrino, S., 2014. A multidisciplinary approach for reconstructing the stratigraphic framework of the last 40 ka in a bathyal area of the eastern Tyrrhenian Sea. *Glob. Planet. Change* **123**, 121–138.

Moretti, R., Arienzo, I., Orsi, G., Civetta, L., D'antonio, M., 2013. The deep plumbing systemof ischia: A physico-chemical window on the fluid-saturated and CO_2-sustained neapolitan volcanism (southern Italy). *J. Petrol*. **54**, 951–984.

Moretti, R., De Natale, G., Troise, C., 2017. A geochemical and geophysical reappraisal to the significance of the recent unrest at Campi Flegrei caldera (Southern Italy). *Geochem. Geophys. Geosyst*. **18**, 1244–1269.

Morgan, Z., and Liang, Y., 2003. An experimental and numerical study of the kinetics of harzburgite reactive dissolution with applications to dunite dike formation. Earth Planet. Sci. Lett. 214, 59–74.

Morgan, VI G.B., and London, D., 1996. Optimizing the electron microprobe analysis of hydrous alkali aluminosilicate glasses. *Am. Mineral*. **81**, 1176–1185.

Morgan, VI. G.B., and London, D., 2003. Trace-element partitioning at conditions far from equilibrium: Ba and Cs distributions between alkali feldspar and undercooled hydrous granitic liquid at 200 MPa. *Contrib. Mineral. Petrol*. **144**, 722–738.

Morgan, D.J., Blake, S., Rogers, N.W., DeVivo, B., Rolandi, G., Macdonald, R., Hawkesworth, C.J., 2004. Time scales of crystal residence and magma chamber volume from modelling of diffusion profiles in phenocrysts: Vesuvius 1944. *Earth Planet. Sci. Lett.* **222**, 933–946.

Morgan, Z., Liang, Y., Hess, P., 2006. An experimental study of anorthosite dissolution in lunar picritic magmas: Implications for crustal assimilation processes. *Geochim. Cosmochim. Acta* **70**, 3477–3491.

Morgan, D.J., Blake, S., Rogers, N.W., De Vivi, B., Rolandi, G., Davidson, J.P., 2006. Magma chamber recharge at Vesuvius in the century prior to the eruption of A.D. 79. *Geology* **34**, 845–848.

Morimoto, N., Fabries, J., Ferguson, A.K., Ginzburg, I.V., Ross, M., Seifert, F.A., Zussman, J., Aoki, K., Gottardi, G., 1998. Nomenclature of pyroxenes Subcommittee. *Am. Mineral*. **73**, 1123–1133.

Mormone, A., Piochi, M., Bellatreccia, F., De Astis, G., Moretti, R., Della Ventura, G., Cavallo A., Mangiacapra A., 2011. A CO_2-rich magma source beneath the Phlegraean Volcanic District (Southern Italy): Evidence from a melt inclusion study. *Chem. Geol.* **287**, 66–80.

Muncill, G.E., and Lasaga, A.C., 1988. Crystal-growth kinetics of plagioclase in igneous systems: Isothermal H_2O saturated experiments and extension of a growth model to complex silicate melts. *Am. Mineral.* **73**, 982–992.

Murase, T., and McBirney, A.R., 1973. Properties of Some Common Igneous Rocks and Their Melts at High Temperatures. *Geol. Soc. Am. Bull*. **84**, 3563–3592.

Mysen, B.O., and Virgo, D., 1980. Trace element partitioning and melt structure: An experimental study at 1 atm pressure. *Geochim. Cosmochim. Acta* **44**, 1917–1930.

Mysen, B.O., Virgo, D., Seifert, F.A., 1982. The structure of silicate melts: Implications for chemical and physical properties of natural magma., *Reviews of Geophysics*, ***20***, 353-383.

Mysen, B.O., Virgo, D., Seifert, F.A., 1985. Relationships between properties and structure of aluminosilicate melts. *Am. Mineral*. **70**, 88–105.

Nakamura, M., 1977. Continuous mixing of crystal mush and replenished magma in the ongoing Unzen eruption. *Geology* **23**, 807–810.

Navon, O., and Stolper, E., 1987. Geochemical Consequences of Melt Percolation: The Upper Mantle as a Chromatographic Column. *J. Geol.* **95**, 285–307.

Ni, H., Hui, H., Steinle-Neumann, G., 2015. Transport properties of silicate melts. *Rev Geophys* **53**, 715–744.

Ni, H., Keppler, H., Walte, N., Schiavi, F., Chen, Y., Masotta, M., Li, Z., 2014. In situ observation of crystal growth in a basalt melt and the development of crystal size distribution in igneous rocks. *Contrib. Mineral. Petrol*. **167**, 1–13.

Nielsen, R.L., 1985. A method for the elimination of the compositional dependence of trace element distribution coefficients. *Geochim. Cosmochim. Acta* **49**, 1775–1779.

Ohtani, E., Maeda, M., 2001. Density of basaltic melt at high pressure and stability of the melt at the base of the lower mantle. *Earth Planet. Sci. Lett*. **193**, 69–75.

Onuma, N., Higuchi, H., Wakita, H., Nagasawa, H., 1968. Trace element partition between two pyroxenes and the host lava. *Earth Planet. Sci. Lett*. **5**, 47–51.

Orlando, A., D'Orazio, M., Armienti, P., Borrini, D., 2008. Experimental determination of plagioclase and clinopyroxene crystal growth rates in an anhydrous trachybasalt from Mt Etna (Italy). *Eur. J. Mineral*. **20**, 653–664.

Orsi, G., D'Antonio, M., de Vita, S., Gallo, G., 1992. The Neapolitan Yellow Tuff, a Large-Magnitude Trachytic PhreatoPlinian Eruption -Eruptive Dynamics, Magma Withdrawal and Caldera Collapse. *J. Volcanol. Geotherm. Res*. **53**(1-4), 275-287.

Orsi, G., Civetta, L., D'Antonio, M., Di Girolamo, P., Piochi, M., 1995. Step-filling and development of a three-layer magma chamber: the Neapolitan Yellow Tuff case history. *J. Volcanol. Geotherm. Res.* **67**, 291–312.

Orsi, G., Di Vito, M.A., Isaia, R., 2004. Volcanic hazard assessment at the restless Campi Flegrei caldera. *Bull. Volcanol*. **66**, 514–530.

Oze, C., and Winter, J.D., 2005. The occurrence, vesiculation, and solidification of dense blue glassy pahoehoe. *J. Volcanol. Geotherm. Res.* **142**, 285–301.

Padilla, A.J., and Gualda, G.A.R., 2016. Crystal-melt elemental partitioning in silicic magmatic systems: An example from the Peach Spring Tuff high-silica rhyolite, Southwest USA. *Chem. Geol.* **440**, 326–344.

Pallister, J., Hoblitt, R., Reyes, A.G., 1992. A basalt trigger for the 1991 eruptions of Pinatubo volcano? *Nature* **356**, 426–428.

Pan, Y., and Batiza, R., 2002. Mid-ocean ridge magma chamber processes: constraints from olivine zonation in lavas from the East Pacific Rise at 9°30′N and 10°30′N. *J. Geophys. Res. Solid Earth* **107**, ECV 9-1–ECV 9-13.

Pappalardo, L., and Mastrolorenzo, G., 2012. Rapid differentiation in a sill-like magma reservoir: a case study from the campi flegrei caldera. *Sci. Rep.* **2**, 712.

Pappalardo L., Civetta L., D'Antonio M., Deino A., Di Vito M., Orsi G., Carandente A., de Vita S., Isaia R., Piochi M. (1999) Chemical and Sr-isotopical evolution of the Phlegraean magmatic

system before the Campanian Ignimbrite and the Neapolitan Yellow Tuff eruptions. *J. Volcanol. Geotherm. Res.* **91**, 141–166.

Pappalardo, L., Ottolini, L., Mastrolorenzo, G., 2008. The Campanian Ignimbrite (southern Italy) geochemical zoning: Insight on the generation of a super-eruption from catastrophic differentiation and fast withdrawal. *Contrib. Mineral. Petrol*. **156**, 1–26.

Pearce, N.J.G., Perkins, W.T., Westgate, J.A., Gorton, M.P., Jackson, S.E., Neal, C.R., Chenery, S.P., 1997. A compilation of new and published major and trace element data for NIST SRM 610 and NIST SRM 612 glass reference materials. *Geostand. Newsl.* **21**, 115–144.

Peccerillo, A., 2017. Cenozoic Volcanism in the Tyrrhenian Sea Region. Springer International Publishing, p. 399.

Perinelli, C., Orlando, A., Conte, A.M., Armienti, P., Borrini, D., Faccini, B., Misiti, V., 2008. Metasomatism induced by alkaline magma in the upper mantle of northern Victoria Land (Antarctica): an experimental approach. *Geol. Soc. London, Spec. Publ*. **293**, 279–302.

Perinelli, C., Mollo, S., Gaeta, M., De Cristofaro, S.P., Palladino, D.M., Armienti, P., Scarlato, P., Putirka, K.D., 2016. An improved clinopyroxene-based hygrometer for Etnean magmas and implications for eruption triggering mechanisms. *Am. Mineral*. **101**, 2774–2777.

Perinelli, C., Mollo, S., Gaeta, M., De Cristofaro, S.P., Palladino, D.M., Scarlato, P., 2018. Impulsive supply of volatile-rich magmas in the shallow plumbing system of Mt. Etna Volcano. *Minerals* **8**, 402.

Perinelli, C., Gaeta, M., Bonechi, B., Granati, S.F., Freda, C., D'Antonio, M., Stagno, V., Sicola, S., Romano, C., 2019. Effect of water on the phase relations of primitive K-basalts: implications for high-pressure differentiation in the Phlegraean Volcanic District magmatic system. *Lithos* **342–343**:530–541.

Persikov, E.S., 1991. The Viscosity of Magmatic Liquids: Experiment, Generalized Patterns. A Model for Calculation and Prediction. Applications, in: Springer (Ed.), Physical Chemistry of Magmas. New York, pp. 1–40.

Persikov, E.S., and Bukhtiyarov, P.G., 2004. Experimental study of the effect of lithostatic and aqueous pressures on viscosity of silicate and magmatic melts. A new structural-chemical model to calculate and predict the viscosity of such melts. Exp. Mineral. Some results Century's Front. 1, 103–122.

Persikov, E.S., Bukhtiyarov, P.G., Sokol, A.G., 2017. Viscosity of hydrous kimberlite and basaltic melts at high pressures. Russ. *Geol. Geophys*. **58**, 1093–1100.

Perugini, D., De Campos, C.P., Petrelli, M., Dingwell, D.B., 2015. Concentration variance decay during magma mixing: A volcanic chronometer. *Sci. Rep.* **5**, 1–10.

Petrelli, M., Caricchi, L., Ulmer, P., 2007. Application of high spatial resolution laser ablation ICP-MS to crystal-melt trace element partition coefficient determination. *Geostand. Geoanalytical Res.* **31**, 13–25.

Petrelli, M., Perugini, D., Alagna, K.E., Poli, G., Peccerillo, A., 2008. Spatially resolved and bulk trace element analysis by laser ablation - Inductively coupled plasma - Mass spectrometry (LA-ICP-MS). *Period. Mineral.* **77**, 3–21.

Petrelli, M., Laeger, K., Perugini, D., 2016. High spatial resolution trace element determination of geological samples by laser ablation quadrupole plasma mass spectrometry: implications for glass analysis in volcanic products. *Geosci. J.* **20**, 851–863.

Petrillo, Z., Chiodini, G., Mangiacapra, A., Caliro, S., Capuano, P., Russo, G., Cardellini, C., Avino, R., 2013. Defining a 3D physical model for the hydrothermal circulation at Campi Flegrei caldera (Italy). *J. Volcanol. Geotherm. Res.* **264**, 172–182.

Petrone, C.M., Bugatti, G., Braschi, E., Tommasini, S., 2016. Pre-eruptive magmatic processes re-timed using a non-isothermal approach to magma chamber dynamics. *Nat. Commun.* **7**, 1-11.

Petrone, C.M., Braschi, E., Francalanci, L., Casalini, M., Tommasini, S., 2018. Rapid mixing and short storage timescale in the magma dynamics of a steady-state volcano. *Earth Planet. Sci. Lett.* **492**, 206–221.

Philpotts, J.A., and Schnetzler, C.C., 1970. Phenocryst-matrix partition coefficients for K, Rb, Sr and Ba, with applications to anorthosite and basalt genesis. *Geochim. Cosmochim. Acta* **34**, 307–322.

Philpotts, A., and Ague, J., 2009. Principles of igneous and metamorphic petrology, Cambridge.

Pichavant, M., Costa, F., Burgisser, A., Scaillet, B., Martel, C., Poussineau, S., 2007. Equilibration scales in silicic to intermediate magmas implications for experimental studies. *J. Petrol.* **48**, 1955–1972.

Pinkerton, H., and Stevenson, R.J., 1992. Methods of determining the rheological properties of magmas at sub-liquidus temperatures. *J. Volcanol. Geotherm. Res.* **53**, 47–66.

Piochi, M., Bruno, P.P., De Astis, G., 2005a. Relative roles of rifting tectonics and magma ascent processes: inferences from geophysical, structural, volcanological, and geochemical data for the Neapolitan volcanic region (southern Italy). *Geochem. Geophys. Geosyst.* 6.

Piochi, M., Mastrolorenzo, G., Pappalardo, L., 2005. Magma ascent and eruptive processes from textural and compositional features of Monte Nuovo pyroclastic products, Campi Flegrei, Italy. *Bull. Volcanol.* **67**, 663–678.

Polacci, M., Arzilli, F., La Spina, G., LeGall, N., Cai, B., Hartley, M.E., Di Genova, D., Vo, N.T., Nonni, S., Atwood, R.C., Llewellin, E.W., Lee, P.D., Burton, M.R., 2018. Crystallisation in basaltic magmas revealed via in situ 4D synchrotron X-ray microtomography. *Sci. Rep.* **8**, 1–13.

Pontesilli, A., Masotta, M., Nazzari, M., Mollo, S., Armienti, P., Scarlato, P., Brenna, M., 2019. Crystallization kinetics of clinopyroxene and titanomagnetite growing from a trachybasaltic melt: new insights from isothermal time-series experiments. *Chem. Geol*. **510**, 113-129.

Pouchou, J.L., and Pichoir, F., 1991. Quantitative analysis of homogeneous or stratified microvolumes applying the model "PAP". In: Heinrich KFJ, Newbury DE (eds) Reserche Aereospatiale, Electron p. Plenum Press, New York, pp 31-75.

Presnall, D.C., Dixon, S.A., Dixon, J.R., O'Donnell, T.H., Brenner, N.L., Schrock, R.L., Dycus, D.W., 1978. Liquidus phase relations on the join diopside-forsterite-anorthite from 1 atm to 20 kbar: their bearing on the generation and crystallization of basaltic magma. *Contrib. Mineral. Petrol.* **66**, 203–220.

Pupier, E., Duchene, S., Toplis, M.J., 2008. Experimental quantification of plagioclase crystal size distribution during cooling of a basaltic liquid. *Contrib. Mineral. Petrol.* **155**, 555–570.

Purton, J.A., Allan, N.L., Blundy, J.D., Wasserman, E.A., 1996. Isovalent trace element partitioning between minerals and melts: A computer simulation study. *Geochim. Cosmochim. Acta* **60**, 4977–4987.

Putirka, K., 1999. Clinopyroxene + liquid equilibria to 100 kbar and 2450 K. *Contrib. Mineral. Petrol.* **135**, 151–163.

Putirka, K.D., 2008. Thermometers and barometers for volcanic systems. In: Putirka, K.D., Tepley III, F.J. (Eds.), Minerals, Inclusions and Volcanic Processes. *Reviews in Mineralogy and Geochemistry*, pp. 61-120.

Putirka, K.D., Mikaelian, H., Ryerson, F., Shaw, H., 2003. New clinopyroxene-liquid thermobarometers for mafic, evolved, and volatile-bearing lava compositions, with applications to lavas from Tibet and the Snake River Plain, Idaho. *Am. Mineral.* **88**, 1542–1554.

Putirka, K.D., 2016. Amphibole thermometers and barometers for igneous systems and some implications for eruption mechanisms of felsic magmas at arc volcanoes. *Am. Mineral*. **101**, 841-858.

Randolph, A.D., and Larson, M.A., 1971. Theory of particulate processes. Academic, New York.

Rapolla, A., Fedi, M., Fiume, M.G., 1989. Crustal structure of the Ischia-Phlegrean geothermal fields, near Naples, Italy, from gravity and aeromagnetic data. *Geophys. J. Int*. **97**, 409–419.

Ray, G.L., Shimizu, N., Hart, S.R., 1983. An ion microprobe study of the partitioning of trace elements between clinopyroxene and liquid in the system diopside-albite-anorthite. *Geochim. Cosmochim. Acta* **47**, 2131–2140.

Reiners, P.W., 1998. Reactive melt transport in the mantle and geochemical signatures of mantle-derived magmas. *J. Petrol*. **39**, 1039–1061.

Richet, P., 1984. Viscosity and configurational entropy of silicate melts. *Geochim. Cosmochim. Acta* **48**, 471–483.

Ridolfi, F., Puerini, M., Renzulli, A., Menna, M., Toulkeridis, T., 2008. The magmatic feeding system of El Reventador volcano (Sub-Andean zone, Ecuador) constrained by texture, mineralogy and thermobarometry of the 2002 erupted products. *J. Volcanol. Geotherm. Res*. **176**, 94-106.

Ridolfi, F., Renzulli, A., Puerini, M., 2010. Stability and chemical equilibrium of amphibole in calc-alkaline magmas: an overview, new thermobarometric formulations and application to subduction-related volcanoes. *Contrib. Mineral. Petrol*. **160**, 45-66.

Ridolfi, F., Zanetti, A., Renzulli, A., Perugini, Di, Holtz, F., Oberti, R., 2018. AMFORM, a new mass-based model for the calculation of the unit formula of amphiboles from electron microprobe analyses. *Am. Min. J. Earth Planet. Mater*. **103**, 1112-1125.

Rizzo, A.L., Barberi, F., Carapezza, M.L., Di Piazza, A., Francalanci, L., Sortino, F., D'Alessandro, W., 2015. New mafic magma refilling a quiescent volcano: Evidence from He-Ne-Ar isotopes during the 2011–2012 unrest at Santorini, Greece. *Geochemistry Geophys. Geosystems* **16**, 267–300.

Roeder, P.L., and Emslie, R.F., 1970. Olivine-liquid equilibrium. *Contrib. Mineral. Petrol*. **29**, 275–289.

Romano, C., Giordano, D., Papale, P., Mincione, V., Dingwell, D.B., Rosi, M., 2003. The dry and hydrous viscosities of alkaline melts from Vesuvius and Phlegrean Fields. *Chem. Geol.* **202**, 23–38.

Rossi, S., Petrelli, M., Morgavi, D., Vetere, F.P., Almeev, R.R., Astbury, R.L., Perugini, D., 2019. Role of magma mixing in the pre-eruptive dynamics of the Aeolian Islands volcanoes (Southern Tyrrhenian Sea, Italy). *Lithos* **324–325**, 165–179.

Rutherford, M.J., and Hill, P.M., 1993. Magma ascent rates from amphibole breakdown: an experimental study applied to the 1980-1986 Mount St. Helens eruptions. *J. Geophys. Res. Solid Earth* **98**, 19667-19685.

Rutherford, M.J., and Devine, J.D., 2008. Magmatic Conditions and Processes in the Storage Zone of the 2004 e 2006 Mount St. Helens Dacite. A Volcano Rekindled Renewed Erupt. Mt. St. Helens 2004-2006. U.S. Geol. Surv. Prof.

Sakamaki, T., Wang, Y., Park, C., Yu, T., Shen, G., 2012. Structure of jadeite melt at high pressures up to 4.9 GPa. *J. Appl. Phys*. 111, 112623.

Sakamaki, T., Suzuki, A., Ohtani, E., Terasaki, H., Urakawa, S., Katayama, Y., Funakoshi, K.I., Wang, Y., Hernlund, J.W., Ballmer, M.D., 2013. Ponded melt at the boundary between the lithosphere and asthenosphere. *Nat. Geosci.* 6, ngeo1982.

Sato, K., Kashima, K., Sunagawa, I., 1981. Measurements of nucleation rates and real growth rates of plagioclase in a solution of basaltic composition. *J. Japan. Assoc. Min. Petr. Econ. Geol*. **76**, 294–307.

Sato, H., Holtz, F., Behrens, H., Botcharnikov, R., Nakada, S., 2005. Experimental petrology of the 1991-1995 Unzen dacite, Japan. Part II: Cl/OH partitioning between hornblende and melt and its implications for the origin of oscillatory zoning of hornblende phenocrysts. *J. Petrol*. **46**, 339–354.

Saunders, K., Blundy, J., Dohmen, R., Cashman, K. 2012. Linking petrology and seismology at an active volcano. *Science* **336**, 1023–1027.

Scarfe, C.M., 1973. Viscosity of Basic Magmas at Varying Pressure. *Nat. Phys. Sci*. **241**, 101–102.

Scarfe, C.M., Takahashi, E., Yoder Jr., H.S., 1980. Rates of dissolution of upper mantle minerals in an alkali-olivine basalt melt at high pressure, in: Carnegie Inst. Washington Yearbook. pp. 290–296.

Scarlato, P., Mollo, S., Blundy, J.D., Iezzi, G., Tiepolo, M., 2014. The role of natural solidification paths on REE partitioning between clinopyroxene and melt. *Bull. Volcanol*. **76**, 1–4.

Schiano, P., Clocchiatti, R., Ottolini, L., Sbrana, A., 2004. The relationship between potassic, calc-alkaline and Na-alkaline magmatism in South Italy volcanoes: a melt inclusion approach. *Earth Planet. Sci. Lett*. **220**, 121–137.

Schneider, C.A., Rasband, W.S., Eliceiri, K.W., 2012. NIH image to ImageJ: 25 years of image analysis. *Nat. Methods* **9**, 671–675.

Schnetzler, C.C., and Philpotts, J.A., 1970. Partition coefficients of rare-earth elements between igneous matrix material and rock-forming mineral phenocrysts-II. *Geochim. Cosmochim. Acta* **34**, 331–340.

Schubert, G., Turcotte, D.L., Olson, P., 2001. Mantle Convection in the Earth and Planets. Cambridge University Press.

Shane, P., and Smith, V.C., 2013. Using amphibole crystals to reconstruct magma storage temperatures and pressures for the post-caldera collapse volcanism at Okataina volcano. *Lithos* **156**, 159-170.

Shannon, B.Y.R.D., 1976. Revised Effective Ionic Radii and Systematic Studies of Interatomic Distances in Halides and Chaleogenides. *Acta Crystallogr*. **A32**, 751.

Shaw, H.R., 1972. Viscosities of magmatic silicate liquids; an empirical method of prediction. *Am. J. Sci*. **272**, 870–893.

Shaw, C.S.J., 2000. The effect of experiment geometry on the mechanism and rate of dissolution of quartz in basanite at 0.5 GPa and 1350 °C. *Contrib. Mineral. Petrol*. **139**, 509-525.

Shaw, C.S.J., 2006. Effects of melt viscosity and silica activity on the rate and mechanism of quartz dissolution in melts of the CMAS and CAS systems. *Contrib. Mineral. Petrol*. **151**, 665–680.

Shea, T., and Hammer, J.E., 2013. Kinetics of cooling- and decompression induced crystallization in hydrous mafic-intermediate magmas. *J Volcanol Geotherm Res* **260**:127–145.

Shea, T., Larsen, J.F., Gurioli, L., Hammer, J.E., Houghton, B.F., Cioni, R., 2009. Leucite crystals: Surviving witnesses of magmatic processes preceding the 79AD eruption at Vesuvius, Italy. *Earth Planet. Sci. Lett.* **281**, 88–98.

Shea, T., Costa, F., Krimer, D., Hammer, J.E., 2015. Accuracy of timescales retrieved from diffusion modeling in olivine: a 3D perspective. *Am. Mineral.* **100**, 2026-2042.

Shea, T., Hammer, J.E., Hellebrand, E., Mourey, A.J., Costa, F., First, E.C., Lynn, K.J., Melnik, O., 2019. Phosphorus and aluminum zoning in olivine: contrasting behavior of two nominally incompatible trace elements. *Contrib. Mineral. Petrol*. **174**, 85.

Shearer, C.K., Papike, J.J., Karner, J.M., 2006. Pyroxene europium valence oxybarometer: Effects of pyroxene composition, melt composition, and crystallization kinetics. *Am. Mineral*. **91**, 1565–1573.

Shimizu, N., 1974. An experimental study of the partitioning of K, Rb, Cs, Sr and Ba between clinopyroxene and liquid at high pressures. *Geochim. Cosmochim. Acta* **38**, 1789–1798.

Shimizu, N., 1981. Trace element incorporation into growing augite phenocryst. *Nature* **289**, 575–577.

Simakin, A.G., and Shaposhnikova, O.Y., 2017. Novel amphibole geobarometer for high-magnesium andesite and basalt magmas. *Petrology* **25**(2), 226-240.

Simakin, A.G., Salova, T.P., Armienti, P., 2003. Kinetics of clinopyroxene growth from a hydrous hawaiite melt. *Geochem. Int*. **41**, 1275-1285.

Simakin, A.G., and Bindeman, I.N., 2008. Evolution of crystal sizes in the series of dissolution and precipitation events in open magma systems. *J. Volcanol. Geotherm. Res*. **177**, 997-1010.

Simakin, A.G., Salova, T.P., Babansky, A.D., 2009. Amphibole crystallization from a water-saturated andesite melt: experimental data at P = 2 kbar. *Petrology* **17**, 591-605.

Simakin, A.G., Devyatova, V.N., Salova, T.P., Shaposhnikova, O.Y., 2019. Experimental study of amphibole crystallization from the highly magnesian melt of Shiveluch volcano. *Петрология* **27**, 476-495.

Skála, R., Strnad, L., McCammon, C. and Čada, M., 2009. Moldavites from the Cheb Basin, Czech Republic. *Geochim. Cosmochim. Acta* **73**, 1145–1179.

Skulski, T., Minarik, W., Watson, E.B., 1994. High-pressure experimental trace-element partitioning between clinopyroxene and basaltic melts. *Chem. Geol*. **117**, 127–147.

Sparks, R. S. J., Sigurdsson, H., Wilson, L. 1977. Magma mixing a mechanism for triggering acid explosive eruption. *Nature* **267**, 315–318.

Sparks, R.S.J., Baker, L., Brown, R.J., Field, M., Schumacher, J., Stripp, G., Walters, A., 2006. Dynamical constraints on kimberlite volcanism. *J. Volcanol. Geotherm. Res*. **155**, 18–48.

Spear, F.S., 1981. Amphibole-plagioclase equilibria: an empirical model for the relation Albite+Tremolite=Edenite+4 quartz. *Contrib. Mineral. Petrol.* **77**, 355-364.

Špillar, V., and Dolejš, D., 2015. Heterogeneous nucleation as the predominant mode of crystallization in natural magmas: Numerical model and implications for crystal–melt interaction. *Contrib. Mineral. Petrol*. **169**, 1–16.

Storn, R., and Price, K., 1997. Differential Evolution - A Simple and Efficient Heuristic for Global Optimization over Continuous Spaces. *J. Glob. Optim*. **11**, 341–359.

Strnad, L., Mihaljevic, M., Sebek, O., 2005. Laser Ablation and Solution ICP-MS Determination of Rare Earth Elements in USGS BIR-1G, BHVO-2G and BCR-2G Glass Reference Materials. *Geostand. Geoanalytical Res*. **29**, 303–314.

Sun, C., 2018. Partitioning and Partition Coefficients. In Encyclopedia of Geochemistry. Encyclopedia of earth sciences series. Springer, Cham.

Sun, C., and Liang, Y., 2012. Distribution of REE between clinopyroxene and basaltic melt along a mantle adiabat: Effects of major element composition, water, and temperature. *Contrib. Mineral. Petrol*. **163**, 807–823.

Sun, C., and Liang, Y., 2013. The importance of crystal chemistry on REE partitioning between mantle minerals (garnet, clinopyroxene, orthopyroxene, and olivine) and basaltic melts. *Chem. Geol*. **358**, 23–36.

Suzuki, A., Ohtani, E., Funakoshi, K., Terasaki, H., Kubo, T., 2002. Viscosity of albite melt at high pressure and high temperature. *Phys. Chem. Miner*. **29**, 159–165.

Suzuki, A., Ohtani, E., Terasaki, H., Funakoshi, K.I., 2005. Viscosity of silicate melts in $CaMgSi_2O_6$-$NaAlSi_2O_6$ system at high pressure. *Phys. Chem. Miner*. **32**, 140–145.

Swanson, S.E., 1977. Relation of nucleation and crystal-growth rate to the development of granitic textures. *Am. Mineral*. **62**, 966–978.

Tecchiato, V., Gaeta, M., Mollo, S., Bachmann, O., Quadt, A. Von, Scarlato, P., 2018a. Snapshots of primitive arc magma evolution recorded by clinopyroxene textural and compositional variations: The case of hybrid crystal-rich enclaves from Capo Marargiu Volcanic District (Sardinia, Italy). *Am. Mineral. J. Earth Planet. Mater*. **103**, 899–910.

Tecchiato, V., Gaeta, M., Mollo, S., Scarlato, P., Bachmann, O., Perinelli, C., 2018b. Petrological constraints on the high-Mg basalts from Capo Marargiu (Sardinia, Italy): Evidence of cryptic amphibole fractionation in polybaric environments. *J. Volcanol. Geotherm. Res.* **349**, 31–46.

Thompson, R.N., 1974. Some High-Pressure Pyroxenes. *Mineral. Mag*. **39**, 768–787.

Thompson, R.M., Downs, R.T., Redhammer, G.J., 2005. Model pyroxenes III: Volume of C2/c pyroxenes at mantle P, T, and x. *Am. Mineral.* **90**, 1840–1851.

Thornber, C.R., 2001. Olivine-liquid relations of lava erupted by Kilauea volcano from 1994 to 1998: implications for shallow magmatic processes associated with the ongoing east-rift-zone eruption. *Can Mineral* **39**, 239–266.

Thornber, C.R., Pallister, J.S., Lowers, H.A., Rowe, M.C., Mandeville, C.W., Meeker, G.P., 2004. Chemistry, mineralogy, and petrology of amphibole in mount St. Helens 2004-2006 dacite. In: A Volcano Rekindled: the Renewed Eruption of Mount St. Helens 2004-2006. *Geological Survey Professional Paper* 1750.

Tiller, W.A., 1977. On the cross-pollenation of crystallization ideas between metallurgy and geology. *Phys. Chem. Miner*. **2**, 125–151.

Tinker, D., Lesher, C.E., Baxter, G.M., Uchida, T., Wang, Y., 2004. High-pressure viscometry of polymerized silicate melts and limitations of the Eyring equation. *Am. Mineral*. **89**, 1701–1708.

Todesco, M., Costa, A., Comastri, A., Colleoni, F., Spada, G., Quareni, F., 2014. Vertical ground displacement at Campi Flegrei (Italy) in the fifth century: Rapid subsidence driven by pore pressure drop. *Geophys. Res. Lett*. **41**, 1471–1478.

Tonarini, S., Leeman, W.P., Civetta, L., D'Antonio, M., Ferrara, G., Necco, A., 2004. B/Nb and δ11B systematics in the Phlegrean Volcanic District, Italy. *J. Volcanol. Geotherm. Res*. **133**, 123–139.

Toplis, M.J., 2005. The thermodynamics of iron and magnesium partitioning between olivine and liquid: criteria for assessing and predicting equilibrium in natural and experimental systems. *Contrib. Mineral. Petrol*. **149**, 22–39.

Tsuchiyama, A., 1986. Melting and dissolution kinetics: application to partial melting and dissolution of xenoliths. *J. Geophys. Res*. **91**, 9395–9406.

Tsuchiyama, A., and Takahashi, E., 1983. Melting kinetics of a plagioclase feldspar. *Contrib. Mineral. Petrol*. **84**, 345–354.

Turner, S.J., Izbekov, P., Langmuir, C., 2013. The magma plumbing system of Bezymianny Volcano: insights from a 54year time series of trace element whole rock geochemistry and amphibole compositions. *J. Volcanol. Geotherm. Res.* **263**, 108-121.

Tursack, E., and Liang, Y., 2012. A comparative study of melt-rock reactions in the mantle: Laboratory dissolution experiments and geological field observations. *Contrib. Mineral. Petrol*. **163**, 861–876.

Ubide, T., and Kamber, B.S., 2018. Volcanic crystals as time capsules of eruption history. *Nat. Commun*. **9**, 1–12.

Uda, S., 1994. Influence of unit cluster size on nucleation rate of $Li_2B_4O_7$ melt. *J. Cryst. Growth* **140**, 128–138.

Van Orman, J.A., and Grove, T.L., 2000. Origin of lunar high-titanium ultramafic glasses: Constraints from phase relations and dissolution kinetics of clinopyroxene-ilmenite cumulates. *Meteorit. Planet. Sci*. **35**, 783–794.

Vetere, F., Behrens, H., Misiti, V., Ventura, G., Holtz, F., De Rosa, R., Deubener, J., 2007. The viscosity of shoshonitic melts (Vulcanello Peninsula, Aeolian Islands, Italy): Insight on the magma ascent in dikes. *Chem. Geol*. **245**, 89–102.

Vetere, F., Iezzi, G., Behrens, H., Cavallo, A., Misiti, V., Dietrich, M., Knipping, J., Ventura, G., Mollo, S., 2013. Intrinsic solidification behaviour of basaltic to rhyolitic melts: A cooling rate experimental study. *Chem. Geol*. **354**, 233–242.

Vetere, F., Iezzi, G., Behrens, H., Holtz, F., Ventura, G., Misiti, V., Cavallo, A., Mollo, S., Dietrich, M., 2015. Glass forming ability and crystallisation behaviour of sub-alkaline silicate melts. *Earth-Sci Rev*. **150**, 25-44.

Viccaro, M., Ferlito, C., Cortesogno, L., Cristofolini, R., Gaggero, L., 2006. Magma mixing during the 2001 event at Mount Etna (Italy): effects on the eruptive dynamics. *J. Volcanol. Geotherm. Res*. **149**, 139–159.

Viccaro, M., Giacomoni, P., Ferlito, C., Lithos, R.C., 2010, U., 2010. Dynamics of magma supply at Mt. Etna volcano (Southern Italy) as revealed by textural and compositional features of plagioclase phenocrysts. *Lithos* **116**, 77–91.

Viccaro, M., Barca, D., Bohrson, W., D'Oriano, C., Giuffrida, M., Nicotra, E., Bradley, W., Pitcher, B.W., 2016. Crystal residence times from trace element zoning in plagioclase reveal changes in magma transfer dynamics at Mt. Etna during the last 400 years. *Lithos* **248–251**, 309–323.

Vitale, S., and Ciarcia, S. 2013. Tectono-stratigraphic and kinematic evolution of the southern Apennines/Calabria–Peloritani Terrane system (Italy). *Tectonophysics*, **583**, 164-182.

Vitale, S., and Isaia, R. 2014. Fractures and faults in volcanic rocks (Campi Flegrei, southern Italy): insight into volcano-tectonic processes. *International Journal of Earth Sciences*, **103**(3), 801-819.

Vona, A., and Romano, C., 2013. The effects of undercooling and deformation rates on the crystallization kinetics of Stromboli and Etna basalts. *Contrib Mineral Petrol* **166**, 491–509.

Voorhees, P.W., 1992. Ostwald ripening of two-phase mixtures. *Annu. Rev. Mater. Sci.* **22**, 197-215.

Wagstaff, F.E., 1969. Crystallization and Melting Kinetics of Cristobalite. *J. Am. Ceram. Soc.* **52**, 650–654.

Walker, D., Powell, M.A., Lofgren, G.E., Hays, J.F., 1978. Dynamic crystallization of a eucrite basalt. In: Lunar and Planetary Science Conference Proceedings. pp 1369–1391.

Wang, Y., Sakamaki, T., Skinner, L.B., Jing, Z., Yu, T., Kono, Y., Park, C., Shen, G., Rivers, M.L., Sutton, S.R., 2014. Atomistic insight into viscosity and density of silicate melts under pressure. *Nat. Commun.* **5**, 1–10.

Watson, E.B., 1996. Surface enrichment and trace-element uptake during crystal growth. *Geochim. Cosmochim. Acta* **60**, 5013–5020.

Watson, E.B., 1982. Basalt contamination by continental crust: Some experiments and models. *Contrib. Mineral. Petrol.* **80**, 73–87.

Watson, E.B., and Müller, T., 2009. Non-equilibrium isotopic and elemental fractionation during diffusion-controlled crystal growth under static and dynamic conditions. *Chem. Geol.* **111**–124.

Weaver, S.L., Wallace, P.J., Johnston, A.D., 2013. Experimental constraints on the origins of primitive potassic lavas from the Trans-Mexican Volcanic Belt. *Contrib. Mineral. Petrol.* **166**, 825–843.

White, J.C., 2003. Trace-element partitioning between alkali feldspar and peralkalic quartz trachyte to rhyolite magma. Part II: Empirical equations for calculating trace-element

partition coefficients of large-ion lithophile, high field-strength, and rare-earth elements. *Am. Mineral*. **88**, 330–337.

Whittington, A., Richet, P., Linard, Y., Holtz, F., 2001. The viscosity of hydrous phonolites and trachytes. *Chem. Geol*. **174**, 209–223.

Whittington, A., Richet, P., Beherens, H., Holtz, F., 2004. Experimental temperature–X(H_2O)–viscosity relationship for leucogranites and comparison with synthetic silicic liquids. *Earth Environ. Sci. Trans. R. Soc. Edinburgh* **95**, 59–71.

Williams, D.W., and Kennedy, G.C., 1969. Melting curve of diopside to 50 kilobars. *J. Geophys. Res*. **74**, 4359–4366.

Wones, D., and Gilbert, M., 1982. Chapter 3, amphiboles in the igneous environment; introduction. Rev. Mineral. Geochem. 9, 355-357.

Wood, B.J., and Blundy, J.D., 1997. A predictive model for rare earth element partitioning between clinopyroxene and anhydrous silicate melt. *Contrib. Mineral. Petrol*. **129**, 166–181.

Wood, B.J., and Blundy, J.D., 2001. The effect of cation on crystal-melt partitioning of trace elements. *Earth Planet. Sci. Lett*. **188**, 59–71.

Wood, B.J., and Trigila, R., 2001. Experimental determination of aluminous clinopyroxene-melt partition coefficients for potassic liquids, with application to the evolution of the Roman province potassic magmas. *Chem. Geol*. **172**, 213–223.

Wood, B.J., Blundy, J.D., Robinson, J.A.C., 1999. The role of clinopyroxene in generating U-series disequilibrium during mantle melting. *Geochim. Cosmochim. Acta* **63**, 1613–1620.

Woods, A.W., 1992. Melting and dissolving. *J. Fluid Mech*. **239**, 429–448.

Wylie, J.J., Helfrich, K.R., Dade, B., Lister, J.R., Salzig, J.F., 1999. Flow localization in fissure eruptions. *Bull. Volcanol*. **60**, 432–440.

Yagi, K., and Onuma, K., 1967. The Join $CaMgSi_2O_6$-$CaTiAl_2O_6$ and its bearing on the Titanaugites. J. Fac. Sci. Hokkaido Univ. Ser. 4, *Geol. Mineral*. **13**, 463–483.

Yamada, A., Inoue, T., Urakawa, S., Funakoshi, K.I., Funamori, N., Kikegawa, T., Ohfuji, H., Irifune, T., 2007. In situ X-ray experiment on the structure of hydrous Mg-silicate melt under high pressure and high temperature. *Geophys. Res. Lett*. **34**, 1–5.

Yamada, A., Inoue, T., Urakawa, S., Funakoshi, K. ichi, Funamori, N., Kikegawa, T., Irifune, T., 2011a. In situ X-ray diffraction study on pressure-induced structural changes in hydrous forsterite and enstatite melts. *Earth Planet. Sci. Lett.* **308**(1-2), 115-123.

Yamada, A., Wang, Y., Inoue, T., Yang, W., Park, C., Yu, T., Shen, G., 2011b. High-pressure x-ray diffraction studies on the structure of liquid silicate using a Paris-Edinburgh type large volume press. *Rev. Sci. Instrum*. **82**, 015103.

Yao, L., Sun, C., Liang, Y., 2012. A parameterized model for REE distribution between low-Ca pyroxene and basaltic melts with applications to REE partitioning in low-Ca pyroxene along a mantle adiabat and during pyroxenite-derived melt and peridotite interaction. *Contrib. Mineral. Petrol*. **164**, 261–280.

Yoder, H.S., 1952. Change of Melting Point of Diopside with Pressure. *J. Geol.* **60**, 364–374.

Yu, Y., Zhang, Y., Chen, Y., Xu, Z., 2016. Kinetics of anorthite dissolution in basaltic melt. *Geochim. Cosmochim. Acta* **179**, 257–274.

Zhang, Y., 1993. A modified effective binary diffusion model. *J. Geophys. Res*. **98**, 11901–11920.

Zhang, Y., 1991. Geochemical Kinetics; Princeton University Press: Princeton, NJ, USA, 2008. 70. Cashman, K.V. Textural constraints on the kinetics of crystallization of igneous rocks. *Rev. Mineral. Geochem*. **24**, 314.

Zhang, Y., Walker, D., Lesher, C.E., 1989. Diffusive crystal dissolution. *Contrib. Mineral. Petrol.* **102**, 492–513.

Zhang, Y., Xu, Z., 2003. Kinetics of convective crystal dissolution and melting, with applications to methane hydrate dissolution and dissociation in seawater. *Earth Planet. Sci. Lett*. **213**, 133–148.

Zhang, Y., Ni, H., Chen, Y., 2010. Diffusion data in silicate melts. *Rev. Mineral. Geochem*. **72**, 311–408.

Zhang, B., Hu, X., Asimow, P.D., Zhang, X., Xu, J., Fan, D., Zhou, W., 2019. Crystal size distribution of amphibole grown from hydrous basaltic melt at 0.6 e 2.6 GPa and 860 e 970 °C. *Am. Mineral.* **104**, 525-535.

Zhang, J., Humphreys, M.C.S., Cooper, G.F., Davidson, J.P., Macpherson, C.G., 2017. Magma mush chemistry at subduction zones, revealed by new melt major element inversion from calcic amphiboles. *Am. Min. J. Earth Planet. Mater*. **102**, 1353-1367.

Zieg, M.J., and Marsh, B.D., 2002. Crystal size distributions and scaling laws in the quantification of igneous textures. *J. Petrol*. **43**, 85–101.

Zieg, M.J., and Lofgren, G.E., 2006. An experimental investigation of texture evolution during continuous cooling. *J. Volcanol. Geotherm. Res*. **154**(1-2), 74-88.

Zollo, A., Maercklin, N., Vassallo, M., Dello Iacono, D., Virieux, J., Gasparini, P., 2008. Seismic reflections reveal a massive melt layer feeding Campi Flegrei caldera. *Geophys. Res. Lett.* **35**, 0–5.

Aknowledgments

Looking back at all the exciting experiences I had, and at all the people that I knew during these three years of hard work, I feel extremely lucky, grateful and thankful to many people.

First of all, I'd like to thank my supervisor Prof. *Mario Gaeta* for his support and for feeding my passion for experimental petrology. Prof, thanks for your sincerity and for the beautiful time spent together. Thank you for trust in me and for all the opportunities you gave me and still gives me today, thanks for the constant presence in times of difficulty, thanks for the laughs and the nice moments shared together during all the activities carried out. I tried to do my best and I hope you are satisfied for our scientific achievements. The first time we talked I was a unsecure and very shy person, but during this experience I've definitely grown a lot both scientifically and personally and this happened also thanks to you.

I'd like to wholeheartedly thank Dr. *Cristina Perinelli*. Cristina, thank you for your sincerity, friendship, scientific but especially moral support. Over these three years you have been among everybody a person who was always available for chatting about a variety of topics, cheering me up, helping me or just listening to me. I thank you so much for being such an amazing colleague and friend.

I am really grateful to Prof. *Vincenzo Stagno*. Vincenzo, thank you for allowing me to collaborate in conducting cutting-edge experiments at the Argonne National Lab in Chicago and to collaborate with foreign researchers from whom I was able to learn new techniques. This experience allowed me to broaden my horizons and get more and more in touch with the world of research.

A special thanks to Dr. *Alessandro Fabbrizio* for his kind and warm hospitality. Thank you, Alessandro, for giving me the privilege of working for several months in you institute. It was a great honour to chat with you and collaborate with you for the

publication of some articles. I really thank you for being an extremely efficient collaborator, on which I can always count.

I am really grateful to Prof. *Silvio Mollo*. Even if I was often scared by your strict revision comments, working with you helped me to grow scientifically and personally. Thank you for involving me in various types of projects allowing me to obtain funds for mobility abroad.

Thanks to my other co-authors: *Dr. Vanni Tecchiato, Dr. Maurizio Petrelli, Prof. Yoshio Kono, Dr. Rostislav Hrubiak, Dr. Luca Ziberna, Dr. Ladislav Strnad*.

Thanks to *Domenico Mannetta* (Mimmo) for his assistance in mounting my experiments in epoxy resin, for the most unlikely attempts devised to cut cpx seeds and for the pleasant chats; to *Marcello Serracino, Marco Albano, Ladislav Strnd, Martin Racek* for their assistance with the electron microprobe and with the scanning electron microscope.
A massive acknowledgement to *Dr. Maurizio Petrelli* and *Dr. Teresa Ubide* for their assistance with laser ablation inductively coupled plasma mass spectrometry analyses and mapping.

Thanks to Prof. *Matteo Masotta* and *Dr. Fabio Arzilli* for the review of this thesis and for their useful and constructive comments.

A huge thank you and a warm hug to my family who have always supported me and to my besties, *Marzia* and *Sonia*, who accompanied me thorough this wonderful journey, in moments of happiness and sadness, stress, anger and craziness. You are the source of my strength and sustenance, thank you for supporting me in everything I do.

Thanks to my friend *Alessandra* faithful companion of lunches and gossip, to all my friends, my speleo-friends of the GGCR and my Ph.D. colleagues.

I truly hope I haven't forgotten anyone. But in case I have, thank you!

Appendix A

Tables

Clinopyroxene growth rates at high pressure: constraints on magma recharge of the deep reservoir of the Campi Flegrei Volcanic District (south Italy)

Barbara Bonechi[1], Cristina Perinelli[1], Mario Gaeta[1]

[1]Dipartimento di Scienze della Terra, Sapienza Università di Roma, P. le Aldo Moro 5, 00185 Rome, Italy

Published in *Bulletin of Volcanology*, 2020, vol. 82(1), 5

Table 1 Composition (wt.%) of APR16 rock sample, APR16GL starting material, SCE and SOG rock samples.

Sample	APR16	APR16GL	SCE	SOG
SiO_2	48.89	49.30	47.62	47.78
TiO_2	1.23	1.33	1.23	1.23
Al_2O_3	15.65	15.31	15.33	15.43
FeO_{tot}	8.08	7.79	8.19	8.24
MnO	0.14	0.14	0.14	0.15
MgO	8.89	9.31	9.78	9.75
CaO	11.64	12.02	11.89	11.59
Na_2O	2.88	2.86	2.69	2.83
K_2O	1.52	1.60	1.58	1.67
P_2O_5	0.31	0.33	0.29	0.29
Sum	99.99	99.23	99.65	99.88
L.O.I.	0.61	nd	0.26	0.28
Mg# [1]	0.66	0.68	0.68	0.68

Notes: [1][MgO/(MgO + FeO_{tot})] molar, assuming all Fe^{2+} and Fe^{3+} as FeO_{tot}. Chemical composition of APR16 is from D'Antonio et al. (1999); APR16GL composition is from Perinelli et al. (2019); SCE from Granati (2016). SOG from this study.

Table 3 Calculated growth rate values for clinopyroxene

Run #	T (°C)	Time (s)	H_2O_f (wt.%)	L (cm)	St. dev. (cm)	W (cm)	St. dev. (cm)	G_L (cm·s^{-1})	St. dev. (cm·s^{-1})
Series 1									
Subseries C1A									
APR16-C1Aa	1250	900	1.61	$6.48\cdot10^{-04}$	$4.4\cdot10^{-05}$	$3.13\cdot10^{-04}$	$6.8\cdot10^{-05}$	$2.50\cdot10^{-07}$	$2.9\cdot10^{-08}$
APR16-C1Ab	1250	10800	2.33	$1.17\cdot10^{-03}$	$2.1\cdot10^{-04}$	$5.30\cdot10^{-04}$	$9.8\cdot10^{-05}$	$3.64\cdot10^{-08}$	$6.8\cdot10^{-09}$
APR16-C1Ac	1250	21600	2.03	$1.35\cdot10^{-03}$	$1.5\cdot10^{-04}$	$5.86\cdot10^{-04}$	$1.5\cdot10^{-04}$	$2.06\cdot10^{-08}$	$2.8\cdot10^{-09}$
APR16-C1Ad	1250	32400	1.95	$1.43\cdot10^{-03}$	$2.1\cdot10^{-04}$	$8.78\cdot10^{-04}$	$1.2\cdot10^{-04}$	$1.73\cdot10^{-08}$	$2.0\cdot10^{-09}$
Subseries C1B									
APR16-C1Ba	1200	900	2.21	$1.05\cdot10^{-03}$	$1.4\cdot10^{-04}$	$4.86\cdot10^{-04}$	$1.6\cdot10^{-04}$	$3.96\cdot10^{-07}$	$7.0\cdot10^{-08}$
APR16-C1Bb	1200	10800	2.92	$1.52\cdot10^{-03}$	$2.5\cdot10^{-04}$	$9.85\cdot10^{-04}$	$2.5\cdot10^{-04}$	$5.67\cdot10^{-08}$	$1.1\cdot10^{-08}$
APR16-C1Bc	1200	21600	2.72	$1.85\cdot10^{-03}$	$1.6\cdot10^{-04}$	$1.50\cdot10^{-03}$	$4.4\cdot10^{-04}$	$3.86\cdot10^{-08}$	$6.8\cdot10^{-09}$
APR16-C1Bd	1200	32400	2.02	$1.93\cdot10^{-03}$	$2.3\cdot10^{-04}$	$1.32\cdot10^{-03}$	$3.9\cdot10^{-04}$	$2.46\cdot10^{-08}$	$5.2\cdot10^{-09}$
Series 2									
Subseries C2A									
APR16-C2Aa	1220	900	1.92	$8.40\cdot10^{-04}$	$1.1\cdot10^{-04}$	$4.05\cdot10^{-04}$	$9.2\cdot10^{-05}$	$3.24\cdot10^{-07}$	$5.2\cdot10^{-08}$
APR16-C2Ab	1220	10800	1.56	$1.07\cdot10^{-03}$	$2.3\cdot10^{-04}$	$4.04\cdot10^{-04}$	$6.5\cdot10^{-05}$	$3.04\cdot10^{-08}$	$3.9\cdot10^{-09}$
APR16-C2Ac	1220	21600	2.47	$1.68\cdot10^{-03}$	$1.3\cdot10^{-04}$	$7.93\cdot10^{-04}$	$3.0\cdot10^{-04}$	$2.67\cdot10^{-08}$	$5.1\cdot10^{-09}$
APR16-C2Ad	1220	32400	1.30	$1.70\cdot10^{-03}$	$1.6\cdot10^{-04}$	$9.22\cdot10^{-04}$	$2.0\cdot10^{-04}$	$1.93\cdot10^{-08}$	$2.2\cdot10^{-09}$
Subseries C2B									
APR16-C2Ba	1170	900	1.61	$9.98\cdot10^{-04}$	$2.1\cdot10^{-04}$	$4.20\cdot10^{-04}$	$9.8\cdot10^{-05}$	$3.60\cdot10^{-07}$	$4.6\cdot10^{-08}$
APR16-C2Bb	1170	10800	1.39	$1.57\cdot10^{-03}$	$1.0\cdot10^{-04}$	$6.06\cdot10^{-04}$	$3.6\cdot10^{-04}$	$4.52\cdot10^{-08}$	$1.2\cdot10^{-08}$
APR16-C2Bc	1170	21600	3.77	$1.80\cdot10^{-03}$	$1.0\cdot10^{-04}$	$7.94\cdot10^{-04}$	$3.5\cdot10^{-04}$	$2.77\cdot10^{-08}$	$5.8\cdot10^{-09}$
APR16-C2Bd	1170	32400	2.02	$1.97\cdot10^{-03}$	$1.8\cdot10^{-04}$	$1.17\cdot10^{-03}$	$6.1\cdot10^{-04}$	$2.34\cdot10^{-08}$	$7.0\cdot10^{-09}$

Table 3 Continued

Run #	T (°C)	Time (s)	H_2O_t (wt.%)	L (cm)	St. dev. (cm)	W (cm)	St. dev. (cm)	G_L ($cm \cdot s^{-1}$)	St. dev. ($cm \cdot s^{-1}$)
Series 3									
Subseries C3A									
APR16-C3Ab	1080	10800		$5.38 \cdot 10^{-04}$	$5.0 \cdot 10^{-05}$	$3.50 \cdot 10^{-04}$	$5.2 \cdot 10^{-05}$	$2.01 \cdot 10^{-08}$	$7.0 \cdot 10^{-10}$
APR16-C3Ac	1080	21600	6.5	$7.45 \cdot 10^{-04}$	$1.8 \cdot 10^{-04}$	$4.28 \cdot 10^{-04}$	$5.7 \cdot 10^{-05}$	$1.31 \cdot 10^{-08}$	$2.5 \cdot 10^{-09}$
APR16-C3Ad	1080	32400	10.2	$5.44 \cdot 10^{-04}$	$7.7 \cdot 10^{-05}$	$4.26 \cdot 10^{-04}$	$4.8 \cdot 10^{-05}$	$7.43 \cdot 10^{-09}$	$8.4 \cdot 10^{-10}$
Subseries C3B									
APR16-C3Bc	1030	21600		$6.43 \cdot 10^{-04}$	$7.8 \cdot 10^{-05}$	$5.55 \cdot 10^{-04}$	$6.0 \cdot 10^{-05}$	$1.38 \cdot 10^{-08}$	$1.3 \cdot 10^{-09}$
APR16-C3Bd	1030	32400	8.3	$5.70 \cdot 10^{-04}$	$6.6 \cdot 10^{-05}$	$5.00 \cdot 10^{-04}$	$3.4 \cdot 10^{-05}$	$8.24 \cdot 10^{-09}$	$5.3 \cdot 10^{-10}$

Notes: NWA natural water rock; H_2O_t as determined by the *by-difference* calculation method (respect to the total of EMP analyses). *L* and *W* are the length and the width of the crystals. G_L is the calculated growth rate. St. dev. Standard deviation

Table 4 Calculated growth rate values for olivine, plagioclase, amphibole and oxide

Run #	T (°C)	Time (s)	H_2O_f (wt%)	Phase	L (cm)	St. dev. (cm)	W (cm)	St. dev. (cm)	G_l (cm·s^{-1})	St. dev (cm·s^{-1})
Series 1										
Subseries C1A										
APR16-C1Ba	1200	900	2.21	Ol	$2.49 \cdot 10^{-03}$	$3.4 \cdot 10^{-04}$	$1.89 \cdot 10^{-03}$	$5.0 \cdot 10^{-04}$	$1.21 \cdot 10^{-06}$	$2.4 \cdot 10^{-07}$
				Plg	$1.38 \cdot 10^{-03}$	$2.3 \cdot 10^{-04}$	$8.48 \cdot 10^{-04}$	$9.4 \cdot 10^{-05}$	$6.01 \cdot 10^{-07}$	$6.5 \cdot 10^{-08}$
APR16-C1Bb	1200	10800	2.92	Ol	$2.96 \cdot 10^{-03}$	$1.8 \cdot 10^{-03}$	$1.01 \cdot 10^{-03}$	$5.7 \cdot 10^{-05}$	$8.00 \cdot 10^{-08}$	$2.7 \cdot 10^{-08}$
				Plg	$1.78 \cdot 10^{-03}$	$4.0 \cdot 10^{-05}$	$8.23 \cdot 10^{-04}$	$4.5 \cdot 10^{-05}$	$5.60 \cdot 10^{-08}$	$2.2 \cdot 10^{-09}$
APR16-C1Bc	1200	21600	2.72	Plg	$1.95 \cdot 10^{-03}$	$3.1 \cdot 10^{-04}$	$9.98 \cdot 10^{-04}$	$8.5 \cdot 10^{-05}$	$3.23 \cdot 10^{-06}$	$3.7 \cdot 10^{-09}$
				Ox	$1.41 \cdot 10^{-03}$	$1.8 \cdot 10^{-04}$	$1.06 \cdot 10^{-03}$	$1.5 \cdot 10^{-04}$	$2.83 \cdot 10^{-08}$	$3.4 \cdot 10^{-09}$
APR16-C1Bd	1200	32400	2.02	Ol	$2.28 \cdot 10^{-03}$	$5.3 \cdot 10^{-04}$	$1.27 \cdot 10^{-03}$	$3.2 \cdot 10^{-04}$	$2.63 \cdot 10^{-08}$	$5.7 \cdot 10^{-09}$
				Plg	$7.82 \cdot 10^{-03}$	$2.2 \cdot 10^{-03}$	$2.71 \cdot 10^{-03}$	$1.1 \cdot 10^{-03}$	$7.11 \cdot 10^{-08}$	$1.7 \cdot 10^{-08}$
				Ox	$1.87 \cdot 10^{-03}$	$2.4 \cdot 10^{-04}$	$1.54 \cdot 10^{-03}$	$2.2 \cdot 10^{-04}$	$2.62 \cdot 10^{-08}$	$3.5 \cdot 10^{-09}$
Series 2										
Subseries C2A										
APR16-C2Aa	1220	900	1.92	Ol	$4.47 \cdot 10^{-03}$	$5.4 \cdot 10^{-04}$	$2.75 \cdot 10^{-03}$	$4.1 \cdot 10^{-04}$	$1.95 \cdot 10^{-06}$	$2.3 \cdot 10^{-07}$
APR16-C2Ab	1220	10800	1.56	Ol	$1.48 \cdot 10^{-03}$	$4.5 \cdot 10^{-04}$	$6.89 \cdot 10^{-04}$	$1.7 \cdot 10^{-04}$	$4.67 \cdot 10^{-08}$	$1.2 \cdot 10^{-08}$
				Plg	$4.56 \cdot 10^{-03}$	$7.0 \cdot 10^{-04}$	$2.03 \cdot 10^{-03}$	$3.5 \cdot 10^{-04}$	$1.41 \cdot 10^{-07}$	$2.2 \cdot 10^{-08}$
APR16-C2Ac	1220	21600	2.47	Ol	$1.49 \cdot 10^{-03}$	$2.0 \cdot 10^{-04}$	$1.18 \cdot 10^{-04}$	$1.1 \cdot 10^{-04}$	$3.07 \cdot 10^{-08}$	$3.0 \cdot 10^{-09}$
				Plg	$5.36 \cdot 10^{-08}$	$1.1 \cdot 10^{-03}$	$1.35 \cdot 10^{-03}$	$1.3 \cdot 10^{-04}$	$5.36 \cdot 10^{-08}$	$9.7 \cdot 10^{-09}$
APR16-C2Ad	1220	32400	1.30	Ol	$1.55 \cdot 10^{-03}$	$2.5 \cdot 10^{-04}$	$1.34 \cdot 10^{-04}$	$2.0 \cdot 10^{-04}$	$2.22 \cdot 10^{-08}$	$1.6 \cdot 10^{-07}$

Table 4 Continued

Run #	T (°C)	Time (s)	H_2O_f (wt%)	Phase	L (cm)	St. dev (cm)	W (cm)	St. dev (cm)	G_L (cm/s)	St. dev (cm·s^{-1})
Subseries C2B										
APR16-C2Ba	1170	900	1.61	Plg	$2.14 \cdot 10^{-03}$	$4.3 \cdot 10^{-04}$	$9.57 \cdot 10^{-04}$	$1.0 \cdot 10^{-04}$	$7.95 \cdot 10^{-07}$	$1.0 \cdot 10^{-07}$
APR16-C2Bb	1170	10800	1.39	Ol	$9.78 \cdot 10^{-04}$	$7.6 \cdot 10^{-01}$	$8.44 \cdot 10^{-04}$	$5.7 \cdot 10^{-05}$	$4.21 \cdot 10^{-08}$	$3.0 \cdot 10^{-09}$
APR16-C2Bc	1170	21600	3.77	Ol Plg	$1.39 \cdot 10^{-03}$ $4.10 \cdot 10^{-03}$	$2.5 \cdot 10^{-04}$ $1.6 \cdot 10^{-03}$	$1.12 \cdot 10^{-03}$ $1.90 \cdot 10^{-03}$	$1.8 \cdot 10^{-04}$ $7.1 \cdot 10^{-04}$	$2.88 \cdot 10^{-08}$ $6.46 \cdot 10^{-08}$	$4.5 \cdot 10^{-09}$ $2.4 \cdot 10^{-08}$
APR16-C2Bd	1170	32400	2.02	Ol Plg	$1.18 \cdot 10^{-03}$ $1.55 \cdot 10^{-03}$	$9.7 \cdot 10^{-05}$ $7.1 \cdot 10^{-05}$	$1.04 \cdot 10^{-03}$ $7.50 \cdot 10^{-04}$	$5.3 \cdot 10^{-05}$ $7.1 \cdot 10^{-05}$	$1.71 \cdot 10^{-08}$ $1.66 \cdot 10^{-08}$	$1.1 \cdot 10^{-09}$ $1.2 \cdot 10^{-09}$
Series 3										
Subseries C3A										
APR16-C3Ab	1080	10800		Amph	$2.59 \cdot 10^{-03}$	$6.8 \cdot 10^{-04}$	$7.50 \cdot 10^{-04}$	$2.1 \cdot 10^{-04}$	$6.45 \cdot 10^{-08}$	$1.4 \cdot 10^{-08}$
APR16-C3Ac	1080	21600	6.5	Ol	$4.52 \cdot 10^{-03}$	$6.4 \cdot 10^{-04}$	$2.15 \cdot 10^{-03}$	$4.9 \cdot 10^{-04}$	$7.21 \cdot 10^{-08}$	$7.4 \cdot 10^{-09}$
APR16-C3Ad	1080	32400	10.2	Amph Ox	$3.26 \cdot 10^{-03}$ $3.09 \cdot 10^{-03}$	$1.3 \cdot 10^{-03}$ $8.7 \cdot 10^{-04}$	$1.16 \cdot 10^{-03}$ $2.57 \cdot 10^{-03}$	$4.1 \cdot 10^{-04}$ $1.1 \cdot 10^{-03}$	$2.99 \cdot 10^{-08}$ $4.34 \cdot 10^{-08}$	$1.0 \cdot 10^{-08}$ $1.5 \cdot 10^{-08}$
Subseries C3B										
APR16-C3Bc	1030	21600		Amph Ox	$1.90 \cdot 10^{-03}$ $8.68 \cdot 10^{-04}$	$2.5 \cdot 10^{-04}$ $1.0 \cdot 10^{-04}$	$6.77 \cdot 10^{-04}$ $8.00 \cdot 10^{-04}$	$7.5 \cdot 10^{-05}$ $9.6 \cdot 10^{-05}$	$2.63 \cdot 10^{-08}$ $1.93 \cdot 10^{-08}$	$1.8 \cdot 10^{-09}$ $2.3 \cdot 10^{-09}$
APR16-C3Bd	1030	32400	8.23	Amph Ox	$3.32 \cdot 10^{-03}$ $1.53 \cdot 10^{-03}$	$6.0 \cdot 10^{-04}$ $2.7 \cdot 10^{-04}$	$1.04 \cdot 10^{-03}$ $1.42 \cdot 10^{-03}$	$2.9 \cdot 10^{-04}$ $2.6 \cdot 10^{-04}$	$2.86 \cdot 10^{-08}$ $2.28 \cdot 10^{-08}$	$4.0 \cdot 10^{-09}$ $4.0 \cdot 10^{-09}$

Notes: NWA natural water rock; Ol olivine; Plg plagioclase; Amph amphibole; Ox oxide. H_2O_f as determined by the *by-difference* calculation method (respect to the total of EMP analyses). *L* and *W* are the length and the width of the crystals. G_L is the calculated growth rate. St. dev. Standard deviation.

Appendix B

Tables

Influence of Pre-Existing Nuclei on the Crystallization Kinetics of Primitive Alkaline Magmas: Insights on the Deep Feeding System of the Campi Flegrei Volcanic District

Barbara Bonechi

Dipartimento di Scienze della Terra, Sapienza Università di Roma, P. le Aldo Moro 5, 00185 Rome, Italy

Published in *Minerals*, 2020, vol. 10(3), 324

Table 1 Composition (wt.%) of APR16 rock sample and APR16GL starting material.

Sample	APR16	APR16GL
SiO_2	48.89	49.30
TiO_2	1.23	1.33
Al_2O_3	15.65	15.31
FeO_{tot}	8.08	7.79
MnO	0.14	0.14
MgO	8.89	9.31
CaO	11.64	12.02
Na_2O	2.88	2.86
K_2O	1.52	1.60
P_2O_5	0.31	0.33
Sum	99.99	99.23
L.O.I.	0.61	nd
Mg# [1]	0.66	0.68

Notes: [1][MgO/(MgO + FeO_{tot})] molar, assuming all Fe^{2+} and Fe^{3+} as FeO_{tot}. Chemical composition of APR16 is from D'Antonio et al. (1999); APR16GL composition is from Perinelli et al. (2019).

Table 3 Calculated growth rate values for clinopyroxene

Run #	T (°C)	Time (s)	H_2O_f (wt.%)	L (cm)	St. dev. (cm)	W (cm)	St. dev. (cm)	G_L ($cm \cdot s^{-1}$)	St. dev. ($cm \cdot s^{-1}$)
APR16-N									
APR16-3B	1225	600	1.77	$1.55 \cdot 10^{-03}$	$6.3 \cdot 10^{-04}$	$9.00 \cdot 10^{-04}$	$1.4 \cdot 10^{-04}$	-	-
APR16-1C	1225	10800	0.96	$4.37 \cdot 10^{-03}$	$5.9 \cdot 10^{-04}$	$2.70 \cdot 10^{-03}$	$6.5 \cdot 10^{-04}$	$1.59 \cdot 10^{-07}$	$3.0 \cdot 10^{-08}$
APR16-35	1225	21600	1.70	$4.64 \cdot 10^{-03}$	$1.5 \cdot 10^{-03}$	$2.83 \cdot 10^{-03}$	$5.8 \cdot 10^{-04}$	$8.34 \cdot 10^{-08}$	$1.9 \cdot 10^{-08}$
APR16-2B	1225	43200	2.13	$6.01 \cdot 10^{-03}$	$2.0 \cdot 10^{-03}$	$4.16 \cdot 10^{-03}$	$8.0 \cdot 10^{-04}$	$5.76 \cdot 10^{-08}$	$1.4 \cdot 10^{-08}$
APR16-C1A									
APR16-C1Aa	1250	900	1.61	$6.48 \cdot 10^{-04}$	$4.4 \cdot 10^{-05}$	$3.13 \cdot 10^{-04}$	$6.8 \cdot 10^{-05}$	$2.50 \cdot 10^{-07}$	$2.9 \cdot 10^{-08}$
APR16-C1Ab	1250	10800	2.33	$1.17 \cdot 10^{-03}$	$2.1 \cdot 10^{-04}$	$5.30 \cdot 10^{-04}$	$9.8 \cdot 10^{-05}$	$3.64 \cdot 10^{-08}$	$6.8 \cdot 10^{-09}$
APR16-C1Ac	1250	21600	2.03	$1.35 \cdot 10^{-03}$	$1.5 \cdot 10^{-04}$	$5.86 \cdot 10^{-04}$	$1.5 \cdot 10^{-04}$	$2.06 \cdot 10^{-08}$	$2.8 \cdot 10^{-09}$
APR16-C1Ad	1250	32400	1.95	$1.43 \cdot 10^{-03}$	$2.1 \cdot 10^{-04}$	$8.78 \cdot 10^{-04}$	$1.2 \cdot 10^{-04}$	$1.73 \cdot 10^{-08}$	$2.0 \cdot 10^{-09}$
APR16-C2A									
APR16-C2Aa	1220	900	1.92	$8.40 \cdot 10^{-04}$	$1.1 \cdot 10^{-04}$	$4.05 \cdot 10^{-04}$	$9.2 \cdot 10^{-05}$	$3.24 \cdot 10^{-07}$	$5.2 \cdot 10^{-08}$
APR16-C2Ab	1220	10800	1.56	$1.07 \cdot 10^{-03}$	$2.3 \cdot 10^{-04}$	$4.04 \cdot 10^{-04}$	$6.5 \cdot 10^{-05}$	$3.04 \cdot 10^{-08}$	$3.9 \cdot 10^{-09}$
APR16-C2Ac	1220	21600	2.47	$1.68 \cdot 10^{-03}$	$1.3 \cdot 10^{-04}$	$7.93 \cdot 10^{-04}$	$3.0 \cdot 10^{-04}$	$2.67 \cdot 10^{-08}$	$5.1 \cdot 10^{-09}$
APR16-C2Ad	1220	32400	1.30	$1.70 \cdot 10^{-03}$	$1.6 \cdot 10^{-04}$	$9.22 \cdot 10^{-04}$	$2.0 \cdot 10^{-04}$	$1.93 \cdot 10^{-08}$	$2.2 \cdot 10^{-09}$

Notes: NWA natural water rock; H_2O_f as determined by the *by-difference* calculation method (respect to the total of EMP analyses). *L* and *W* are the length and the width of the crystals. G_L is the calculated growth rate. St. dev. Standard deviation

Table 4 Calculated nucleation rate values for clinopyroxene.

Run #	T (°C)	Time (s)	Ln n_0 (mm^{-4})	n_0 (mm^{-4})	J ($mm^{-3}s^{-1}$)
APR16-N					
APR16-1C	1225	10800	19.6	$3.25 \cdot 10^{8}$	$5.17 \cdot 10^{2}$
APR16-35	1225	21600	17.86	$5.71 \cdot 10^{7}$	$4.76 \cdot 10^{1}$
APR16-2B	1225	43200	18.02	$6.70 \cdot 10^{7}$	$3.86 \cdot 10^{1}$
APR16-C1A					
APR16-C1Aa	1250	900	25.78	$1.57 \cdot 10^{11}$	$3.93 \cdot 10^{5}$
APR16-C1Ab	1250	10800	26.84	$4.53 \cdot 10^{11}$	$1.65 \cdot 10^{5}$
APR16-C1Ac	1250	21600	24.8	$5.90 \cdot 10^{10}$	$1.21 \cdot 10^{4}$
APR16-C1Ad	1250	32400	25.05	$7.57 \cdot 10^{10}$	$1.31 \cdot 10^{4}$
APR16-C2A					
APR16-C2Aa	1220	900	22.4	$5.35 \cdot 10^{9}$	$1.85 \cdot 10^{4}$
APR16-C2Ab	1220	10800	24.13	$3.00 \cdot 10^{10}$	$1.32 \cdot 10^{4}$
APR16-C2Ac	1220	21600	23.09	$1.06 \cdot 10^{10}$	$2.96 \cdot 10^{3}$
APR16-C2Ad	1220	32400	23.13	$1.10 \cdot 10^{10}$	$2.13 \cdot 10^{3}$

Notes: Ln n_0 is the natural logarithm of nucleation density, n_0 is the nucleation density and *J* is the nucleation rate. Nucleation density and rate were calculated trough the equations: $n_0 = \exp(\ln(n_0))$ and $J = n_0 * G$, respectively. Ln n_0 as derived by CSD Corrections 1.6 program (Higgins, 2000, 2002). Data for APR16-C1A and APR16-C2A from Bonechi et al. (2020)

Appendix C

Tables

Amphibole growth from a primitive alkaline basalt at 0.8 GPa: Time dependent compositional evolution, growth rate and competition with clinopyroxene

Barbara Bonechi [a]*, Cristina Perinelli [a], Mario Gaeta [a], Vanni Tecchiato [a], Alessandro Fabbrizio [b]

[a] Dipartimento di Scienze della Terra, Sapienza Università di Roma, P. le Aldo Moro 5, 00185 Rome, Italy

[b] Institute of Petrology and Structural Geology, Faculty of Science, Charles University, Albertov 6, 12843, Prague, Czech Republic

Published in *Lithos*, 2020, vol. 354-355, 105272

Table 1 Composition (wt%) of APR16 rock sample and APR16GL starting material

Sample	APR16	APR16GL
SiO_2	48.89	49.3 (0.46)
TiO_2	1.23	1.33 (0.03)
Al_2O_3	15.65	15.31 (0.14)
FeO_{tot}	8.08	7.79 (0.13)
MnO	0.14	0.14 (0.05)
MgO	8.89	9.31 (0.07)
CaO	11.64	12.02 (0.09)
Na_2O	2.88	2.86 (0.05)
K_2O	1.52	1.60 (0.02)
P_2O_5	0.31	0.55 (0.02)
Total	99.23	99.31 (0.29)[y]
L.O.I.	0.61	-
Mg# *	0.66	0.68

*[MgO/(MgO+FeO_{tot})] molar, assuming all Fe^{2+} and Fe^{3+} as FeO_{tot}. Chemical composition of APR16 is from D'Antonio et al. (1999); APR16GL composition is from Perinelli et al. 2019. [y]For APR16GL the analysis is normalized to 100 but the original total is reported. Standard deviation is reported in parenthesis.

Table 3 Growth rate calculations for amphibole, clinopyroxene and oxide.

Run #	T (°C)	Time (s)	H_2O_f (wt%)	Phase	L (cm)	W (cm)	G_L (cm·s^{-1})	G_L St. dev (cm·s^{-1})
APR16-C3A								
APR16-C3Aa	1080	900		Amph	$4.26 \cdot 10^{-04}$	$1.80 \cdot 10^{-04}$	$1.54 \cdot 10^{-07}$	$0.02 \cdot 10^{-07}$
APR16-C3Ab	1080	10800	7.5	Amph	$2.59 \cdot 10^{-03}$	$7.50 \cdot 10^{-04}$	$6.45 \cdot 10^{-08}$	$1.40 \cdot 10^{-08}$
				Cpx	$5.38 \cdot 10^{-04}$	$3.50 \cdot 10^{-04}$	$2.01 \cdot 10^{-08}$	$0.07 \cdot 10^{-08}$
APR16-C3Ac	1080	21600	6.5	Cpx	$7.45 \cdot 10^{-04}$	$4.28 \cdot 10^{-04}$	$1.31 \cdot 10^{-08}$	$0.25 \cdot 10^{-08}$
APR16-C3Ad	1080	32400	10.2	Amph	$3.26 \cdot 10^{-03}$	$1.16 \cdot 10^{-03}$	$2.99 \cdot 10^{-08}$	$1.00 \cdot 10^{-08}$
				Ox	$3.09 \cdot 10^{-03}$	$2.57 \cdot 10^{-03}$	$4.34 \cdot 10^{-08}$	$1.50 \cdot 10^{-08}$
				Cpx	$5.44 \cdot 10^{-04}$	$4.26 \cdot 10^{-04}$	$7.43 \cdot 10^{-09}$	$0.84 \cdot 10^{-09}$
APR16-C3B								
APR16-C3Bc	1030	21600		Amph	$1.90 \cdot 10^{-03}$	$6.77 \cdot 10^{-04}$	$2.63 \cdot 10^{-08}$	$0.18 \cdot 10^{-08}$
				Ox	$8.68 \cdot 10^{-04}$	$8.00 \cdot 10^{-04}$	$1.93 \cdot 10^{-08}$	$0.23 \cdot 10^{-08}$
				Cpx	$6.43 \cdot 10^{-04}$	$5.55 \cdot 10^{-04}$	$1.38 \cdot 10^{-08}$	$0.13 \cdot 10^{-08}$
APR16-C3Bd	1030	32400	8.3	Amph	$3.32 \cdot 10^{-03}$	$1.04 \cdot 10^{-03}$	$2.86 \cdot 10^{-08}$	$0.40 \cdot 10^{-08}$
				Ox	$1.53 \cdot 10^{-03}$	$1.42 \cdot 10^{-03}$	$2.28 \cdot 10^{-08}$	$0.40 \cdot 10^{-08}$
				Cpx	$5.70 \cdot 10^{-04}$	$5.00 \cdot 10^{-04}$	$8.24 \cdot 10^{-09}$	$0.53 \cdot 10^{-09}$

Notes: H_2O_f as determined by the by-difference calculation method (respect to the total of EMP analyses). *L* and *W* are the length and the width of the crystals. G_L is the calculated growth rate. St. dev. Standard deviation. Growth rate data of Cpx and Ox from Bonechi et al. (2019). Amph = amphibole; Cpx = clinopyroxene; Ox = oxide minerals.

Table 4 Electron-microprobe analyses and crystal-chemical formulas of amphibole crystallized in the experimental runs.

Amphibole

Run #	C3Aa Amph 1	Amph 2	Amph 3	Amph 4	C3Ab Amph 1	Amph 2	C3Ad Amph 1	Amph 2	C3Ba Amph 1	C3Bb Amph 1	C3Bc Amph 1	Amph 2	Amph 3	C3Bd Amph 1	Amph 2
SiO_2	45.17	42.01	42.00	46.56	42.42	40.77	42.85	40.75	47.43	47.05	42.18	40.79	43.65	42.51	40.45
TiO_2	2.19	2.30	2.57	1.77	2.68	2.58	1.72	1.92	1.22	1.19	3.97	3.71	2.83	2.12	2.25
Al_2O_3	14.27	14.38	14.77	15.17	15.62	14.24	13.96	13.42	14.06	14.08	13.77	12.98	17.73	14.95	13.93
FeO	7.56	10.02	10.55	8.78	7.27	8.43	9.30	7.69	9.15	8.56	10.86	9.90	7.97	10.02	9.11
MnO	0.16	0.11	0.14	0.18	0.16	0.11	0.14	0.12	0.12	0.13	0.15	0.13	0.11	0.09	0.15
MgO	13.46	13.58	13.28	10.35	14.16	14.75	14.74	16.05	10.85	11.82	12.16	14.12	10.55	13.76	14.54
CaO	12.30	11.76	11.21	10.37	11.48	11.48	12.08	11.66	11.81	12.06	11.73	12.44	11.86	11.85	11.88
Na_2O	2.26	2.33	2.49	1.93	2.57	2.26	2.27	2.22	1.99	1.80	1.74	1.46	1.73	2.31	2.32
K_2O	1.21	1.41	1.38	1.61	1.41	1.34	1.26	1.35	1.35	1.62	1.40	1.29	1.32	1.20	1.08
P_2O_5	0.17	0.10	0.12	0.35	0.03	0.00	0.05	0.00	0.16	0.12	0.14	0.00	0.05	0.07	0.00
Total:	99.03	99.01	98.60	97.17	97.90	96.11	98.53	95.32	98.13	98.43	98.32	96.95	97.90	99.09	95.79
Mg#	0.76	0.71	0.69	0.68	0.78	0.76	0.74	0.79	0.68	0.71	0.67	0.72	0.70	0.71	0.74
$^{Amph\text{-}liq}K_{DFe\text{-}Mg}$					1.02	0.77	0.45	0.34	0.88	0.73				0.46	0.40
Species	Ed	Mg-Hs	Par	Mg-Hb	Par	Mg-Hs	Par	Mg-Hs	Ed	Ed	Mg-Hb	Mg-Hs	Par	Par	Mg-Hs

Mg# = [MgO/(MgO+FeO)] molar ratio, assuming FeO = FeO_{tot}. $^{Amph\text{-}liq}K_{DFe\text{-}Mg}$ = (FeO/MgO)Amph/(FeO/MgO)liq calculated according to Putirka (2016). Abbreviations: Ed = edenite; Mg-Hb = magnesiohorneblende; Par = pargasite; Mg-Hs = magnesiohastingsite.

Table 4 Continued

Run #	C3Aa Amph 1	Amph 2	Amph 3	Amph 4	C3Ab Amph 1	Amph 2	C3Ad Amph 1	Amph 2	C3Ba Amph 1	C3Bb Amph 1	C3Bc Amph 1	Amph 2	Amph 3	C3Bd Amph 1	Amph 2
Si	6.5135	6.1538	6.1313	6.8240	6.1432	6.0546	6.2040	6.0645	6.9403	6.8395	6.2312	6.0893	6.3582	6.1477	6.0341
Al	1.4865	1.8462	1.8687	1.1760	1.8568	1.9454	1.7960	1.9355	1.0597	1.1605	1.7688	1.9107	1.6418	1.8523	1.9659
Ti	0.0000	0.0000	0.0000	0.0000	0.0000	0.0000	0.0000	0.0000	0.0000	0.0000	0.0000	0.0000	0.0000	0.0000	0.0000
Sum T	8.0000	8.0000	8.0000	8.0000	8.0000	8.0000	8.0000	8.0000	8.0000	8.0000	8.0000	8.0000	8.0000	8.0000	8.0000
Al	0.9385	0.6358	0.6727	1.4447	0.8093	0.5476	0.5850	0.4181	1.3645	1.2581	0.6286	0.3727	1.4021	0.6967	0.4828
Ti	0.2378	0.2536	0.2825	0.1951	0.2914	0.2880	0.1873	0.2149	0.1340	0.1301	0.4415	0.4169	0.3096	0.2311	0.2530
Cr	0.0000	0.0000	0.0000	0.0000	0.0121	0.0112	0.0000	0.0141	0.0000	0.0000	0.0000	0.0163	0.0101	0.0000	0.0079
Ni+Zn	0.0000	0.0000	0.0000	0.0000	0.0008	0.0057	0.0000	0.0042	0.0000	0.0000	0.0000	0.0007	0.0030	0.0000	0.0025
Fe^{3+}	0.0000	0.4210	0.3449	0.0000	0.2310	0.4184	0.3474	0.5093	0.0000	0.0000	0.2715	0.3492	0.0000	0.3430	0.4641
Mg	2.8924	2.9656	2.8890	2.2623	3.0560	3.2663	3.1805	3.5603	2.3671	2.5615	2.6790	3.1428	2.2912	2.9666	3.2323
Fe^{2+}	0.9120	0.8063	0.9432	1.0760	0.6499	0.6284	0.7789	0.4479	1.1200	1.0406	1.0708	0.8870	0.9706	0.8695	0.6724
Mn	0.0193	0.0134	0.0167	0.0220	0.0191	0.0140	0.0172	0.0146	0.0144	0.0160	0.0184	0.0164	0.0133	0.0109	0.0183
ΔC	0.0000	0.0957	0.1490	0.0000	0.0696	0.1796	0.0963	0.1835	0.0000	0.0000	0.1097	0.2021	0.0000	0.1178	0.1333
Ca	1.9009	1.8449	1.7539	1.6286	1.7820	1.8204	1.8736	1.8165	1.8520	1.8784	1.8560	1.7979	1.8503	1.8356	1.8667
Na	0.0991	0.0594	0.0971	0.3714	0.1484	0.0000	0.0300	0.0000	0.1480	0.1216	0.0344	0.0000	0.1497	0.0466	0.0000
Ca	0.0000	0.0000	0.0000	0.0000	0.0000	0.0057	0.0000	0.0428	0.0000	0.0000	0.0000	0.1913	0.0000	0.0000	0.0319
Na	0.5330	0.6012	0.6079	0.1780	0.5724	0.6504	0.6080	0.6409	0.4163	0.3857	0.4626	0.4215	0.3375	0.6006	0.6707
K	0.2226	0.2640	0.2568	0.3005	0.2607	0.2544	0.2320	0.2557	0.2524	0.3004	0.2629	0.2453	0.2460	0.2210	0.2063
Sum A	0.7555	0.8652	0.8647	0.4785	0.8330	0.9106	0.8399	0.9395	0.6687	0.6861	0.7255	0.8581	0.5835	0.8216	0.9089
OH	1.3022	1.0182	1.4826	1.2023	1.5369	1.4759	1.6218	1.5818	0.9066	1.0840	1.1966	1.2892	1.1766	1.4894	1.5643
F	0.1040	0.4535	0.0286	0.0209	0.0000	0.0000	0.0572	0.0000	0.0000	0.0000	0.0925	0.0000	0.0000	0.0855	0.0000
Cl	0.0098	0.0047	0.0074	0.0109	0.0000	0.0000	0.0000	0.0000	0.0000	0.0000	0.0055	0.0000	0.0000	0.0005	0.0000
O	0.5840	0.5236	0.4814	0.7659	0.4631	0.5241	0.3209	0.4182	1.0934	0.9160	0.7054	0.7108	0.8234	0.4246	0.4357
sum W	2.0000	2.0000	2.0000	2.0000	2.0000	2.0000	2.0000	2.0000	2.0000	2.0000	2.0000	2.0000	2.0000	2.0000	2.0000

AMFORM (an excel worksheet for amph-formula calculation developed by Ridolfi et al., 2018) formula (apfu) reports the final formula calculated from the corrected composition. Fe^{3+}, + Fe^{2+}, WO^{2-} and $^{W}HO^{-}$ values are according to the default method (eq. 3 and 4c; Ridolfi et al. 2018). ΔC represent the total content of Fe^{2+}, Mg and/or Mn that is located in B.

Table 5 Crystal size and estimated crystallization time for natural amphibole and clinopyroxene from the Oligo-Miocene Capo Marargiu Volcanic District (Sardinia, Italy; Tecchiato et al., 2018b).

ROCK TYPE	SAMPLE	MINERAL	SECTION	L (cm)	GROWTH RATE ($cm \cdot s^{-1}$)	CRYSTALLIZATION TIME (yr)
Enclaves	CM40.1	Amph	~ (001)	1.340	$2.9 \cdot 10^{-8}$	1.46
		Type 2 Cpx	~ (110)	0.380	$7.4 \cdot 10^{-9}$	1.62
					$2.0 \cdot 10^{-8}$	0.60
	CM41	Amph	~ (001)	1.860	$2.9 \cdot 10^{-8}$	2.03
	CM42	Type 1 Cpx	~ (001)	1.375	$7.4 \cdot 10^{-9}$	5.89
					$2.0 \cdot 10^{-8}$	2.18
Crystal clots	E1	Amph	~ (110)	2.855	$2.9 \cdot 10^{-8}$	3.12
Crystal clots	E7	Amph	~ (010)	2.700	$2.9 \cdot 10^{-8}$	2.95
Crystal clots	CM47B	Amph	~ (110)	1.505	$2.9 \cdot 10^{-8}$	1.65

Appendix D

Tables and supplementary materials

Experimental investigation of high pressure clinopyroxene dissolution in a K-basaltic melt

Barbara Bonechi[1], Cristina Perinelli[1], Mario Gaeta[1], Vincenzo Stagno[1,2], Alessandro Fabbrizio[3], Silvio Mollo[1,2], Rostislav Hrubiak[4]

1: Dipartimento di Scienze della Terra, Sapienza Università di Roma, P. le Aldo Moro 5, 00185, Rome, Italy

2: Istituto Nazionale di Geofisica e Vulcanologia, Roma - Via di Vigna Murata 605, 00143 Roma, Italy

3: Institute of Petrology and Structural Geology, Faculty of Science, Charles University, Albertov 6, 12843 Prague, Czech Republic

4: High Pressure Collaborative Access Team, X-ray Science Division, Argonne National Laboratory, 9700 S. Cass Avenue, Argonne, IL 60439, United States

Under review in *Chemical Geology*

Table 1 Composition (wt.%) of APR16 rock sample, APR16GL starting material and cpx Ves.

Sample	APR16	APR16GL	Cpx Ves*
SiO_2	48.89	49.30 (0.46)	53.27 (0.33)
TiO_2	1.23	1.33 (0.03)	0.40 (0.03)
Al_2O_3	15.65	15.31 (0.14)	2.19 (0.15)
FeO_{tot}	8.08	7.79 (0.13)	3.56 (0.22)
MnO	0.14	0.14 (0.05)	0.08 (0.04)
MgO	8.89	9.31 (0.07)	16.79 (0.17)
CaO	11.64	12.02 (0.09)	24.63 (0.18)
Na_2O	2.88	2.86 (0.05)	0.14 (0.01)
K_2O	1.52	1.60 (0.02)	-
P_2O_5	0.31	0.55 (0.02)	-
Cr_2O_3	-	-	0.27 (0.14)
L.O.I.	0.61	-	
Total	99.23	99.31 (0.29)[¥]	101.39
Mg#[1]	0.66	0.68	0.89
T_L (°C)	1280	1290	
Wo			48
En			46
Fs			6

[1][MgO/(MgO+FeO_{tot})] molar, assuming all iron as FeO. APR16 composition from D'Antonio et al. (1999); APR16GL composition from Perinelli et al. (2019). Compositions are normalized to 100. Standard deviation is reported in parenthesis. *Representative analysis of cpx from this study. Abbreviation: Cpx clinopyroxene; Wo wollastonite; En enstatite; Fs ferrosilite. T_L liquidus temperature (Perinelli et al., 2019).

Table 3 Clinopyroxene dissolution rates.

Run#	P (GPa)	T (°C)	Time (s)	Δr (cm)	Δr_i (cm)	Dissolution rate (cm s^{-1})	St. Dev. (cm s^{-1})
APR16-D1Aa	0.8	1350	1800	0.014	0.018	$7.89 \cdot 10^{-6}$	$1.60 \cdot 10^{-7}$
APR16-D1A	0.8	1350	3600	0.023	0.072	$6.11 \cdot 10^{-6}$	$2.00 \cdot 10^{-7}$
APR16-D1Ab	0.8	1300	7200	0.016	-	-	-
APR16-D1*	2	1570	4	0.078	-	$1.73 \cdot 10^{-2}$	$3.20 \cdot 10^{-3}$

Δr clinopyroxene dissolution distance calculated by subtracting the final clinopyroxene length from the initial length (both measured under scanning electron microscope). Δr_i is calculated by using Eqn. (3) reported in the text. St. Dev. standard deviation. *melting rate of cpx seed.

Table 4 Effective binary diffusivities (10^{-12} m^2 s^{-1})

Run#	T (°C)	P (GPa)	Time (s)	TiO_2	Al_2O_3	MgO	CaO	Na_2O	K_2O
APR16-D1Aa	1350	0.8	1800	-	3.9 *(1.2)*	5.7 *(2.2)*	18.1 *(3.1)*	6.9 *(1.8)*	5.4 *(1.7)*
APR16-D1A	1350	0.8	3600	16.5 *(2.4)*	18.8 *(1.8)*	20.9 *(1.5)*	36.4 *(3.1)*	27.7 *(2.3)*	25.3 *(1.8)*

Diffusivities values are the mean of the values measured along three different profiles for each run. St. deviation is reported in brackets.

Table 5 Experimental conditions and dissolution-crystallization of steps of the APR16-D1Ab experiment.

<table>
<tr><th colspan="5">Experimental conditions</th></tr>
<tr><td colspan="2">Starting material</td><td colspan="3">Cpx seed (a low pressure cpx from 1944 Vesuvius eruption) + APR16 (powdered natural rock with restitic cpx+ol)</td></tr>
<tr><td colspan="2">Pressure</td><td colspan="3">0.8 GPa</td></tr>
<tr><td colspan="2">Temperature</td><td colspan="3">1300 °C</td></tr>
<tr><td colspan="2">Powder/cpx seed weight ratio</td><td colspan="3">0.59</td></tr>
<tr><td colspan="2">Estimated liquidus temperature of APR16+cpx seed bulk composition (Mg# = 0.83)*</td><td colspan="3">1384 °C</td></tr>
<tr><td colspan="2">Total duration</td><td colspan="3">2 h</td></tr>
<tr><th colspan="5">Timing of experimental processes</th></tr>
<tr><td colspan="2">Time</td><td colspan="2">cpx seed</td><td>APR16 powdered rock</td></tr>
<tr><td colspan="2">t_0</td><td colspan="2">Instability of the cpx seed</td><td>Dissolution + restitic cpx crystals</td></tr>
<tr><td>t_1</td><td>~0.5 h</td><td>Dissolution of ~0.02 cm</td><td>Cation diffusion in the melt is limited and does not change the APR16 composition</td><td>Crystallization of the core + mantle of group 2-new cpx (~10 µm) in local equilibrium with the APR16 composition (Mg# ~0.68)</td></tr>
<tr><td rowspan="2">t_2</td><td rowspan="2">→1.5 h</td><td colspan="3">Cation diffusion produces progressive change of APR16 composition (Mg# changes from ~0.68 to ~0.80)</td></tr>
<tr><td colspan="2">End of cpx seed dissolution and formation of the overgrowth rim</td><td>Overgrowth rims develop on 1) group 2-new cpx cores and on 2) restitic APR16-cpx.
Formation of new unzoned cpx</td></tr>
<tr><td>t_3</td><td>quench</td><td colspan="2">~30-µm-thick cpx seed rim developed</td><td>1) ~70 µm-thick of rims developed on both type of zoned new cpx;
2) unzoned new cpx have reached a maximum size of ~200 µm</td></tr>
</table>

Notes: * the APR16+cpx seed bulk composition has been calculated on the basis of the powder/cpx seed ratio. Liquidus temperatures are determined by the MELTS code (Ghiorso and Sack 1995; Asimow and Ghiorso 1998)

Online Resource 1

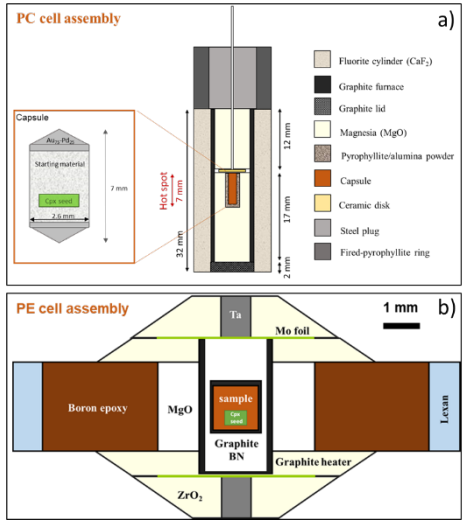

Fig. S1. *Sketch of the experimental assembly in the piston cylinder apparatus (a) and in the Paris Edinburgh press (b). In (a) the zoom-in shows the position of the cpx seed inside the* $Au_{75}Pd_{25}$ *capsule.*

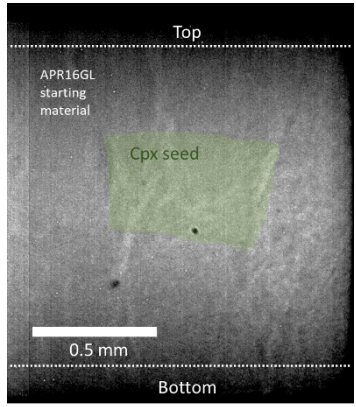

Fig. S2. *Radiographic photomicrograph of the APR16-D1 run in which it is possible to observe the cpx seed (indicated in green) before the experiment.*

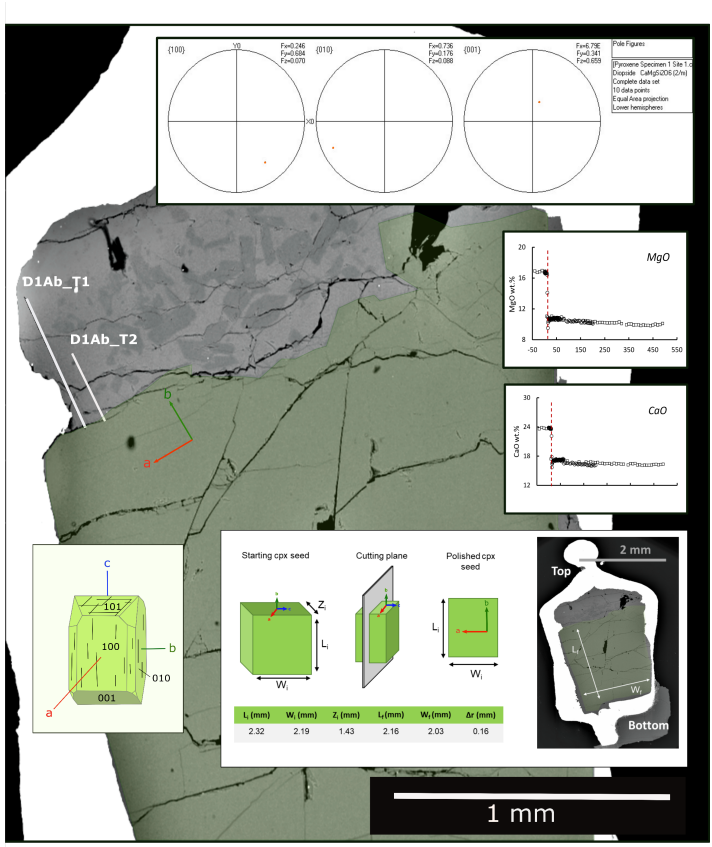

Fig. S3. *Backscattered image of APR16-D1Ab run. Polished cpx seed is indicated in green. Inside the cpx seed the crystallographic axes are reported (a in red, b in green, c in blue) following the orientations showed by the upper-hemisphere projections (inset in the upper side of the figure). As possible to see from these projections the polished surface is approximately perpendicular to the c-axis (001). In the figure the profiles along which we measured the variation of the major elements concentration in the melt are indicated with white lines. An example is reported in the insets on the right, where the concentration profiles of MgO and CaO are shown. In this run, since it represents a finite geometry, diffusion coefficients are not measured. Finally, in the lower left part of the figure is reported a cartoon showing the sizes, the placement, and the orientation of the seed before and after the experiment. The table reports the initial (i) sizes, the final (f) sizes and the difference between them (Δr). Cartoon not in scale.*

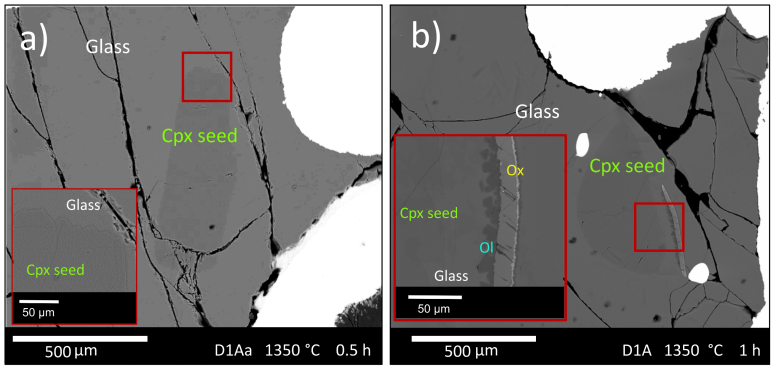

Fig. S4 *Backscattered photomicrograph of the experimental runs: a) APR16-D1Aa (1350 °C, 0.5 h) run; b) APR16-D1A (1350 °C, 1 h) run; cpx clinopyroxene, ol olivine, ox oxide. The red rectangle shows an enlargement of the interface crystal-melt.*

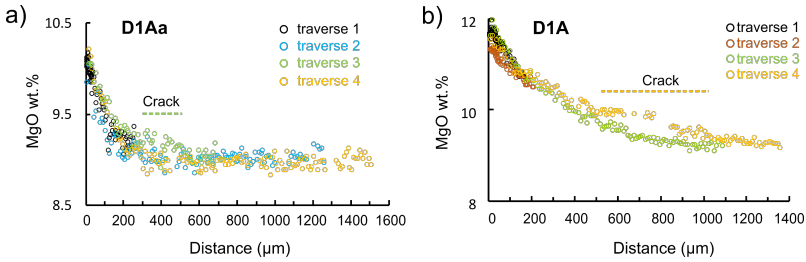

Fig. S5 *Diagrams showing the absence of convection in the runs of this study. a-b) MgO concentration profiles for the APR16-D1Aa (a) and APR16-D1A (b) runs; four traverses were measured across the sample section. Coloured dashed lines indicate the presence of cracks along the traverse 3 in D1Aa run (in green) and along the traverse 4 in D1A run (in yellow).*

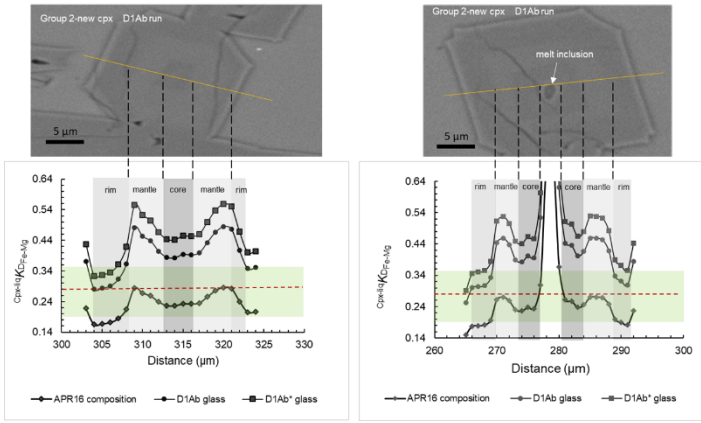

Fig. S6. *Variation of* $^{cpx\text{-}liq}K_{DFe\text{-}Mg}$ *as a function of distance (µm) from core to rim in group 2-new cpx. The green area represents the equilibrium range according to Putirka (2008), while the red dotted lines indicate the mean equilibrium range of 0.28±0.08 (Putirka 2008). Partition coefficients were calculated using the APR16-D1Ab and APR16-D1Ab* glasses and the APR16 composition.*

Online Resource 3

Table S1 EPMA analyses of cpx, glass, olivine and oxide of the experimental runs

Clinopyroxene

	APR16-D1Aa		APR16-D1A		APR16-D1Ab															
	Cpx seed	St. Dev.	Cpx seed	St. Dev.	Cpx seed	St. Dev.	Cpx seed rim	St. Dev.	New cpx Unzoned	St. Dev.	New Cpx core Group 1	St. Dev.	New Cpx rim Group 1	St. Dev.	New Cpx core Group 2	St. Dev.	New Cpx mantle Group 2	St. Dev.	New Cpx rim Group 2	St. Dev.
	40		40		20		5		4		6		6		6		8		5	
SiO_2	52.90	0.48	53.51	0.21	53.12	0.47	51.16	0.66	50.82	0.72	49.48	0.63	51.21	0.79	51.46	0.72	49.20	0.50	50.14	0.17
TiO_2	0.42	0.03	0.29	0.02	0.25	0.09	0.31	0.13	0.32	0.03	0.77	0.11	0.40	0.11	0.52	0.11	0.82	0.12	0.51	0.05
Al_2O_3	2.38	0.07	1.43	0.02	1.53	0.49	4.88	0.75	4.34	0.13	7.14	0.65	5.03	0.80	4.46	0.81	6.54	0.56	5.81	0.24
FeO	3.33	0.08	3.13	0.08	3.55	0.65	2.25	0.80	2.25	0.09	4.17	0.35	2.54	0.27	3.73	0.17	3.72	0.42	2.65	0.06
MnO	0.09	0.02	0.08	0.02	0.10	0.03	0.07	0.03	0.07	0.01	0.10	0.02	0.09	0.02	0.13	0.02	0.11	0.02	0.05	0.03
MgO	16.71	0.31	17.08	0.15	17.21	0.33	16.60	0.52	16.44	0.44	15.80	1.01	16.49	0.30	17.15	0.65	15.48	0.55	15.89	0.07
CaO	23.64	0.17	23.52	0.16	23.47	0.34	23.55	0.48	23.89	0.26	21.15	0.32	23.13	0.42	20.61	0.49	21.28	0.79	22.64	0.11
Na_2O	0.13	0.04	0.08	0.01	0.10	0.06	0.25	0.07	0.23	0.04	0.43	0.03	0.30	0.06	0.31	0.05	0.44	0.04	0.39	0.05
K_2O	0.01	0.02	0.00	0.01	0.00	0.00	0.00	0.00	0.02	0.01	0.00	0.00	0.01	0.01	0.00	0.00	0.01	0.00	0.01	0.00
Cr_2O_3	0.40	0.02	0.22	0.03	0.14	0.02	0.21	0.06	0.20	0.16	0.43	0.20	0.23	0.17	0.29	0.07	0.68	0.10	0.31	0.10
Total:	100.00		99.35		99.47		99.28		98.56		99.47		99.44		98.64		98.27		98.40	
Mg#	0.90		0.91		0.90		0.93		0.93		0.88		0.92		0.89		0.88		0.91	
$^{Cpx-liq}K_{DFe-Mg}$	0.26	0.01	0.24	0.01	0.38	0.02	0.25	0.01	0.25	0.01	0.49	0.03	0.28	0.01	0.40	0.02	0.44	0.02	0.31	0.01
$^{Cpx-liq*}K_{DFe-Mg}$					0.44	0.03	0.29	0.01	0.29	0.01	0.56	0.04	0.33	0.01	0.46	0.02	0.51	0.03	0.35	0.01
Wo	48		47		47		49		49		46		48		44		46		48	
En	47		48		48		48		47		47		48		50		47		47	
Fe	5		5		5		3		4		7		4		6		7		5	

Mg# = [MgO/(MgO+FeO_{tot})] molar, assuming all iron as FeO

St. Dev. standard deviation

$^{Cpx-liq}KD_{Fe-Mg} = Fe_{cpx} \times Mg_{liq} / Mg_{cpx} \times Fe_{liq}$ (calculated assuming all Fe as Fe^{2+} in both phases); liq = glass analysed far from the seed; liq* = glass analysed near the seed.

Table S1 Continued

Glass§										
	APR16-D1Aa		APR16-D1A		APR16-D1Ab		APR16-D1Ab*		APR16-D1	
	Gl	St. Dev.	Gl	St. Dev.	Gl	St. Dev.	Gl	St. Dev.	Gl	St. Dev.
	3		3		2		4		4	
SiO_2	49.88	0.14	50.31	0.50	49.86	0.18	45.87	0.42	50.84	0.17
TiO_2	1.29	0.03	1.31	0.04	1.22	0.04	1.08	0.05	1.24	0.03
Al_2O_3	15.74	0.31	15.60	0.55	15.09	0.21	14.01	0.18	14.62	0.73
FeO	7.18	0.12	6.77	0.36	5.01	0.33	5.28	0.24	6.38	0.86
MnO	0.15	0.02	0.15	0.02	0.15	0.02	0.12	0.03	0.11	0.02
MgO	9.47	0.59	9.04	0.20	9.26	0.31	11.26	0.26	9.62	0.33
CaO	12.01	0.24	11.88	0.20	14.31	0.43	18.09	0.37	12.92	0.13
Na_2O	2.45	0.15	2.76	0.11	3.09	0.25	2.57	0.21	2.62	0.21
K_2O	1.55	0.10	1.56	0.04	1.63	0.05	1.33	0.04	1.44	0.19
P_2O_5	0.28	0.03	0.31	0.03	0.39	0.04	0.40	0.08	0.21	0.08
Total:	98.65		99.73		99.41		96.67		98.39	
Mg#	0.70		0.70		0.77		0.79		0.73	

§ Normalized glass. The original Total are also reported. Glass reported here are analyzed far from the Cpx seed. D1 Ab* glass analysed near the cpx seed. St. Dev. standard deviation.

Table S1 Continued

Olivine			Oxide				
	APR16-D1A			APR16-D1A			
	Ol			core		rim	
	2	St. Dev.		3	St. Dev.	2	St. Dev.
SiO_2	42.58	0.13	SiO_2	0.09	0.02	0.30	0.26
Al_2O_3	0.08	0.02	TiO_2	0.26	0.09	0.23	0.18
FeO	6.27	0.28	Al_2O_3	1.69	0.35	1.75	0.72
MnO	0.17	0.01	FeO	33.39	2.97	71.97	2.11
MgO	50.60	0.11	MnO	0.17	0.01	0.14	0.01
CaO	0.54	0.07	MgO	56.33	2.76	14.09	1.25
			CaO	0.07	0.01	0.28	0.07
			Cr_2O_3	0.05	0.03	0.08	0.03
Total:	100.38		Total:	92.88		88.84	
Fo	93						
$^{Ol\text{-}liq}KD_{Fe\text{-}Mg}$	0.17	0.03					

St. Dev. standard deviation

$^{Ol\text{-}liq}KD_{Fe\text{-}Mg} = Fe_{ol} \times Mg_{liq} / Mg_{ol} \times Fe_{liq}$ (calculated assuming all Fe as Fe^{2+} in both phases)

Table S2 Clinopyroxene dissolution rates of previous works present in literature

	P (GPa)	T (°C)	T_L (°C)	ΔT (°C)	Time (s)	Δr (cm)	Dissolution rate (cm s^{-1})
Brearley and Scarfe (1986)	0.5	1250	1225	25	1800	0.004	$2.22 \cdot 10^{-06}$
	0.5	1250	1225	25	3600	0.004	$1.11 \cdot 10^{-06}$
	0.5	1250	1225	25	7200	0.012	$1.67 \cdot 10^{-06}$
	0.5	1300	1225	75	1800	0.007	$3.89 \cdot 10^{-06}$
	0.5	1300	1225	75	3600	0.02	$5.56 \cdot 10^{-06}$
	0.5	1300	1225	75	7200	0.034	$4.72 \cdot 10^{-06}$
	1.2	1300	1275	25	3600	0.001	$2.78 \cdot 10^{-07}$
	1.2	1300	1275	25	7200	0.001	$1.39 \cdot 10^{-07}$
	1.2	1350	1275	75	1800	0.003	$1.67 \cdot 10^{-06}$
	1.2	1400	1275	125	600	0.006	$1.00 \cdot 10^{-05}$
	1.2	1400	1275	125	1200	0.012	$1.00 \cdot 10^{-05}$
	1.2	1400	1275	125	1800	0.015	$8.33 \cdot 10^{-06}$
	1.2	1400	1275	125	3600	0.019	$5.28 \cdot 10^{-06}$
	3	1450	1390	60	600	0.003	$5.00 \cdot 10^{-06}$
	3	1450	1390	60	1800	0.001	$5.56 \cdot 10^{-07}$
	3	1450	1390	60	3600	0.005	$1.39 \cdot 10^{-06}$
	3	1450	1390	60	7200	0.006	$8.33 \cdot 10^{-07}$
	3	1500	1390	110	600	0.015	$2.50 \cdot 10^{-05}$
Zhang et al. (1989)	1.05	1305	1253*	52	4190	0.004	$9.55 \cdot 10^{-07}$
	1.05	1305	1253*	52	890	0.0026	$2.92 \cdot 10^{-06}$
	1.3	1365	1273*	92	1780	0.0142	$7.98 \cdot 10^{-06}$
	2.15	1375	1370*	5	1810	0.0056	$3.09 \cdot 10^{-06}$
Van Orman and Grove (2000)	1.3	1350			9250	0.0127	$1.37 \cdot 10^{-06}$
	1	1350			3600	0.0178	$4.94 \cdot 10^{-06}$
	1.3	1450			1000	0.0358	$3.58 \cdot 10^{-05}$
Chen and Zhang (2009)	0.47	1271	1231*	40	1807	0.0037	$2.05 \cdot 10^{-06}$
	0.95	1362	1270*	92	732	0.0049	$6.69 \cdot 10^{-06}$
	1.42	1446	1337*	109	732	0.0158	$2.16 \cdot 10^{-05}$
	0.47	1321	1231*	90	613	0.0067	$1.09 \cdot 10^{-05}$
	0.95	1394	1270*	124	733	0.0138	$1.88 \cdot 10^{-05}$
	1.9	1422	1400*	22	494	0.0044	$8.91 \cdot 10^{-06}$
	1.42	1368	1337*	31	732	0.0031	$4.23 \cdot 10^{-06}$
	0.47	1236	1231*	5	2404	0.0011	$4.58 \cdot 10^{-07}$

Δ T is the difference between the nominal temperature of the runs and liquidus temperature (T_L).
*T_L has been calculated by using MELTS software (Asimow and Ghiorso 1998; Gualda et al. 2012).

Table S3 Compositions and liquidus temperature of the bulk starting materials formed by APR16/APR16GL + cpx Ves, as calculated for each experiment. Tliquidus of compositions of APR16-D1Ab and APR16-D1Ab* are also reported.

Sample	APR16-D1A§ (APR16GL+cpx Ves)	APR16-D1Aa§ (APR16GL+cpx Ves)	APR16-D1Ab§ (APR16+cpx Ves)	APR16-D1Ab	APR16-D1Ab*
SiO_2	49.48	49.42	50.67	49.86	45.87
TiO_2	1.28	1.30	0.90	1.22	1.08
Al_2O_3	14.65	14.85	10.20	15.09	14.01
FeO_{tot}	7.58	7.64	6.25	5.01	5.28
MnO	0.14	0.14	0.12	0.15	0.12
MgO	9.68	9.57	12.09	9.26	11.26
CaO	12.64	12.46	16.91	14.31	18.09
Na_2O	2.72	2.76	1.77	3.09	2.57
K_2O	1.52	1.54	0.91	1.63	1.33
P_2O_5	0.31	0.32	0.19	0.39	0.40
Mg#	0.69	0.69	0.78	0.77	0.79
$T_{liquidus}$ at 0.8 GPa (°C)	1316	1315	1384	1326	1332

§ The recalculated compositions of starting materials take into account the powder/cpx seed ratio as reported in the Table 2. $T_{liquidus}$ at 0.8 GPa of the calculated compositions were estimated by MELTS program (Asimow and Ghiorso 1998; Gualda et al., 2012)

Electronic Appendix

Compositional profiles in the glass

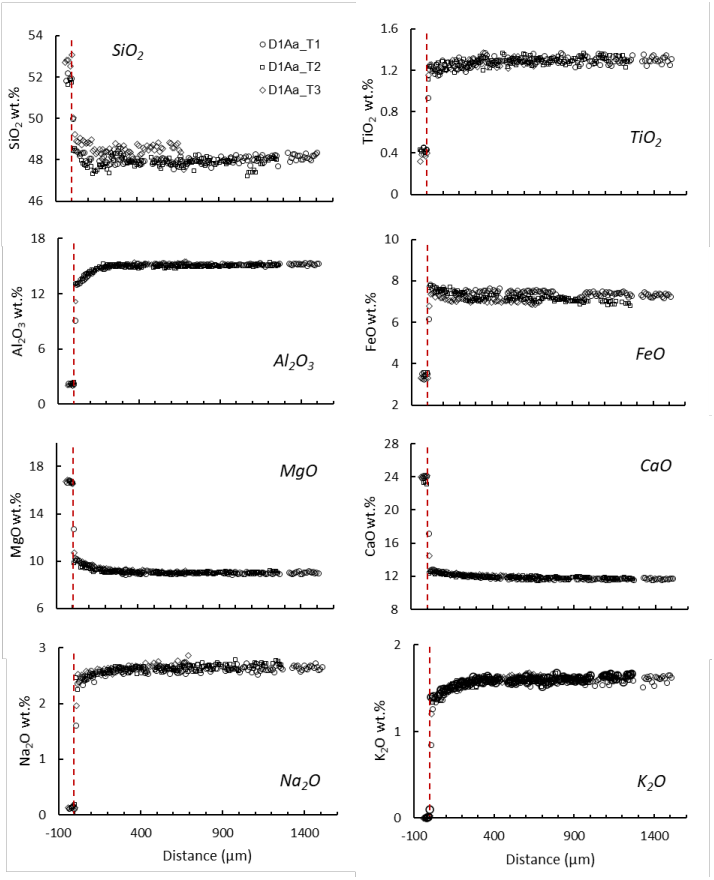

Fig. A1. *Compositional profiles of run APR16-D1Aa (1350 °C, 0.8 GPa, 0.5 h). The vertical axes are major oxides concentrations in wt.%. The horizontal axis is the distance from the clinopyroxene seed to the surrounding glass. Dashed vertical lines indicate the clinopyroxene-glass interface.*

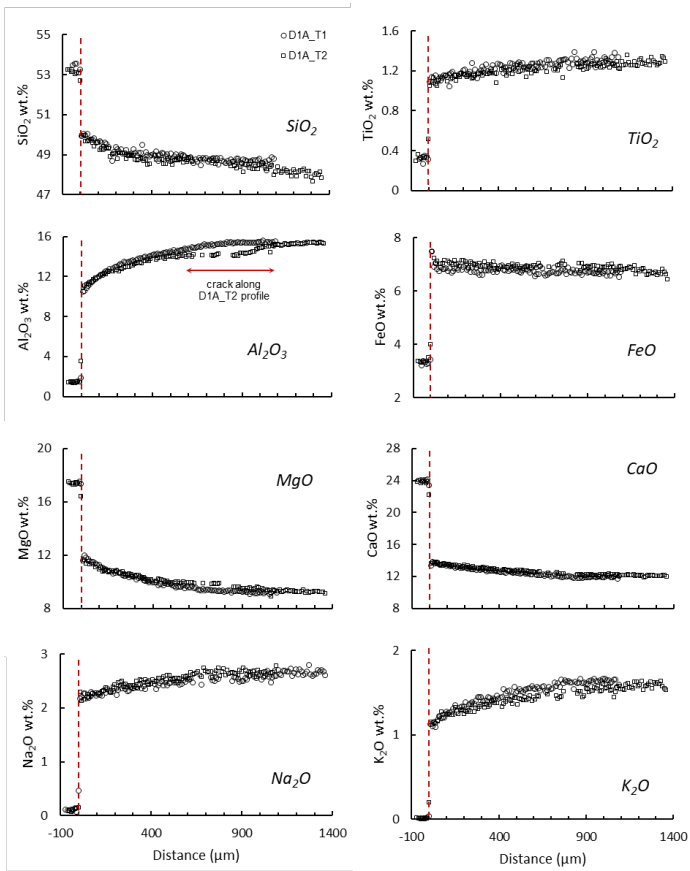

Fig. A2. *Compositional profiles of run APR16-D1A (1350 °C, 0.8 GPa, 1 h). The vertical axes are major oxides concentrations in wt.%. The horizontal axis is the distance from the clinopyroxene seed to the surrounding glass. Dashed vertical lines indicate the clinopyroxene-glass interface.*

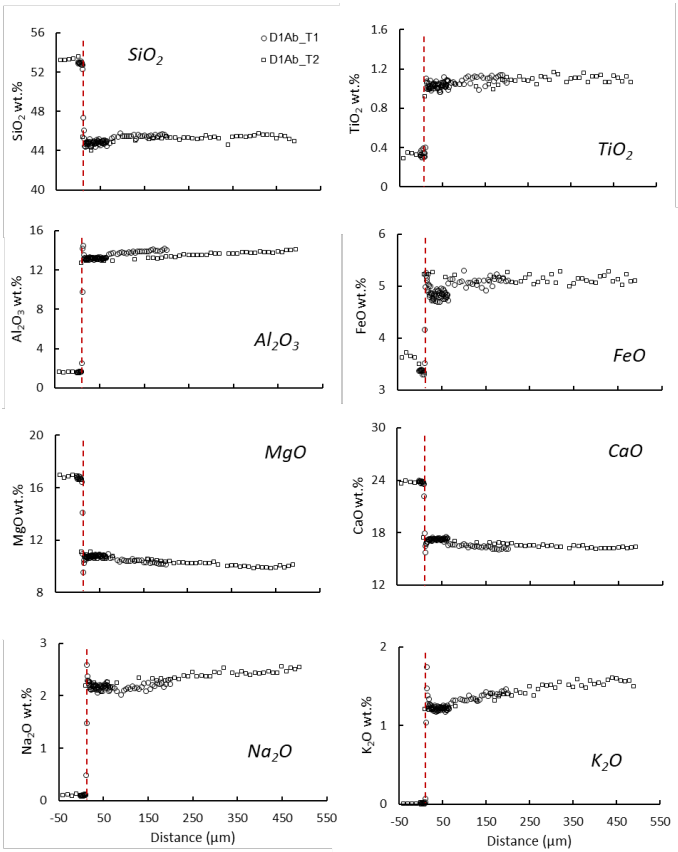

Fig. A3. *Compositional profiles of run APR16-D1Ab (1300 °C, 0.8 GPa, 2 h). The vertical axes are major oxides concentrations in wt.%. The horizontal axis is the distance from the clinopyroxene seed to the surrounding glass. Dashed vertical lines indicate the clinopyroxene-glass interface.*

Fittings to the compositional profiles

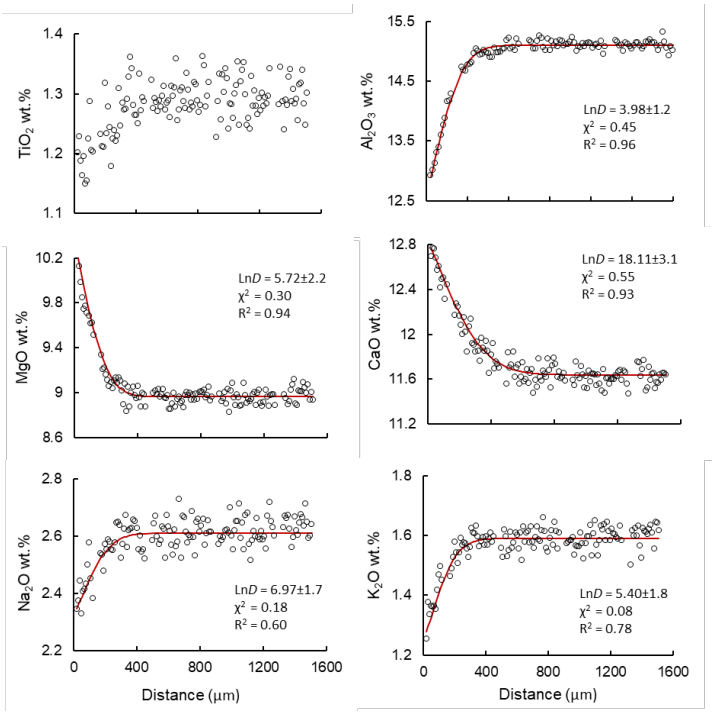

Fig. A4. *Fittings to the compositional profiles of run APR16-D1Aa (1350 °C, 0.8 GPa, 0.5 h). We corrected the values along the cracks, and we performed the calculation using the mean values of the profiles.*

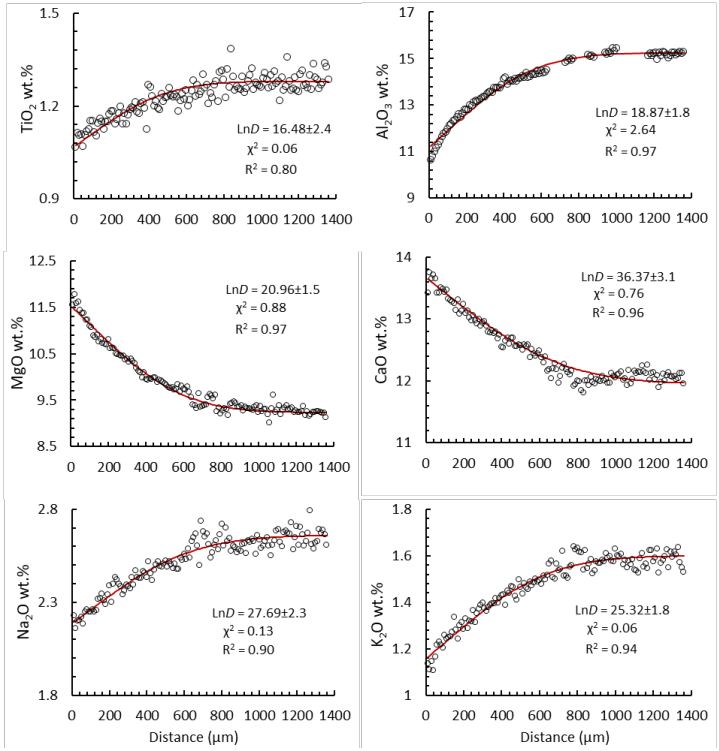

Fig. A5. *Fittings to the compositional profiles of run APR16-D1A (1350 °C, 0.8 GPa, 1 h). We corrected the values along the cracks, and we performed the calculation using the mean values of the profiles.*

Appendix E

Tables and supplementary materials

Rheological constraints on the pre-eruptive system of Campi Flegrei (Naples, Italy) from viscosity and melt structure measurements of primitive alkaline basalts

Barbara Bonechi[1], Vincenzo Stagno[1], Yoshio Kono[2], Rostislav Hrubiak[3], Luca Ziberna[4], Cristina Perinelli[1], Mario Gaeta[1]

1 Dipartimento di Scienze della Terra, Sapienza Università di Roma, P. le Aldo Moro 5, 00185, Rome, Italy

2: Istituto Nazionale di Geofisica e Vulcanologia, Roma - Via di Vigna Murata 605, 00143 Roma, Italy

3: Geodynamics Research Centre, Ehime University, 2-5 Bunkyo-cho, Matsuyama Ehime 790-8577, Japan

4: High Pressure Collaborative Access Team, X-ray Science Division, Argonne National Laboratory, 9700 S. Cass Avenue, Argonne, IL 60439, United States

5: Dipartimento di Matematica e Geoscienze, Università degli Studi di Trieste, Via Weiss, 2 34128 Trieste, Italy

To be submitted

Table S1 Chemical composition of synthetic basalts from this and previous studies

	APR16 (natural rock)	*APR16 (glass)*	*MORB (Sakamaki et al. 2013)*	*Agee (1998)*	*Ohtani and Maeda (2001)*	*de Grouchy et al. (2017)*
SiO_2	48.89	48.76	51.70	49.40	51.81	48.80
TiO_2	1.23	1.32	-	1.43	-	-
Al_2O_3	15.65	15.15	15.80	15.59	15.95	14.70
FeO	8.08	7.70	9.90	9.03	9.97	-
MgO	8.89	9.21	8.10	8.50	7.86	10.20
MnO	0.14	0.13	-	0.17	-	-
CaO	11.64	11.89	11.50	10.86	11.69	22.70
Na_2O	2.88	2.83	2.50	3.11	2.72	-
K_2O	1.52	1.59	-	0.11	-	-
P_2O_5	0.31	0.32	-	0.28	-	-
Lu_2O_3	-	-	-	-	-	3.60
L.O.I.	0.61	-	-	-	-	-
Total (wt%)	99.84	98.91	99.50	98.48	100.00	100.20

Table S2 Experimental conditions and result of viscosity measurements in this study.

Run	P (GPa)	T (°C)	sphere material	sphere diameter (mm)	f.p.s.	terminal velocity	viscosity (Pa·s)
APR16-PE3_top	0.7	1440	Pt	0.0867	23	0.0507	1.118(±0.083)
APR16-PE3_bottom	0.7	1335	Pt	0.1122	21	0.0507	1.756(±0.099)
APR16-PE2	1.4	1440	Pt	0.1326	21	0.0825	0.481(±0.065)
APR16-PE1	2.3	1600	Pt	0.0952	21	0.0848	0.296(±0.075)
APR16-PE7	3.7	1650	Pt	0.0510	21	0.0363	0.147(±0.058)
APR16-PE6	5.6	1835	Pt	0.0833	50	0.1500	0.432(±0.018)
APR16-PE5	7	2000	Pt	0.1137	50	0.2320	0.333(±0.022)

Table S3 Experimental conditions of melt structure measurements in this and previous studies.

Run	P (GPa)	T (°C)	T-O length (Å)	T-T length (Å)	2nd T-O length (Å)	T-O-T (°)
This study						
APR16-PE1	2.3	1600	1.65	3.08	4.05	137.92
APR16-PE7	4.6	1650	1.67	3.23	4.28	150.51
APR16-PE6	5.4	1835	1.67	3.17	4.07	143.28
Sakamaki et al. (2013)						
MOR basalt(+)	1.9	1527	1.67	3.20	4.20	146.70
MOR basalt(+)	4.3	1627	1.65	3.15	4.24	145.32
MOR basalt(+)	5.5	1727	1.70	3.10	4.12	131.50
de Grouchy et al. (2017)						
AnD_Amb1	0.0	17	1.62	-	-	-
AnD_A1b	0.8	1297	1.59	-	-	-
AnD_A2b	2.4	1397	1.61	-	-	-
AnD_A3b	3.5	1447	1.59	-	-	-
AnD_A4b	4.8	1497	1.59	-	-	-
AnD_A5b	6.5	1597	1.60	-	-	-
AnD_A6b	8.0	1797	1.61	-	-	-

Table S4 Chemical composition of experimental runs

	APR16-PE1	σ	APR16-PE2	σ	APR16-PE3	σ	APR16-PE6	σ	APR16-PE7	σ
SiO_2	52.06	0.80	49.73	0.57	52.55	0.43	50.26	0.36	49.39	0.01
TiO_2	1.03	0.12	1.35	0.06	1.27	0.12	1.29	0.07	1.43	0.02
Al_2O_3	19.30	0.44	17.75	0.33	19.78	0.42	15.55	0.03	16.50	0.03
FeO	2.80	0.04	8.44	0.36	8.36	0.46	6.13	0.03	7.08	0.02
MgO	4.17	0.22	5.29	0.43	1.78	0.21	8.96	0.10	9.00	0.06
MnO	0.09	0.01	0.14	0.04	0.14	0.06	0.17	0.02	0.14	0.01
CaO	6.81	0.23	8.85	0.35	8.01	0.72	11.91	0.09	8.82	0.02
Na_2O	4.59	0.12	3.94	0.1	4.46	0.18	2.94	0.10	3.35	0.09
K_2O	2.77	0.12	2.38	0.22	2.42	0.17	1.63	0.05	2.14	0.10
P_2O_5	0.17	0.02	0.45	0.06	0.40	0.03	0.30	0.03	0.44	0.02
Total (wt%)	93.79		98.32		99.17		99.13		98.29	

Note: σ is the standard deviation

Supplementary figures

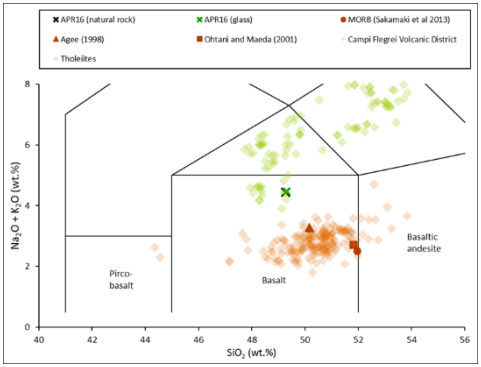

Fig. S1. *Portion of the total alkali (Na_2O+K_2O) vs silica (SiO_2) diagram (TAS, Le Maitre et al., 2002), illustrating the composition of the APR16 K-basalt (this study) and those of the basalt of Sakamaki et al. (2013), Ohtani and Maeda (2001) and Agee (1998). Green diamonds indicate volcanic products from the Campi Flegrei Volcanic District, while the orange ones tholeiites (GEOROC database; http://georoc.mpch-mainz.gwdg.de/georoc/Start.asp).*

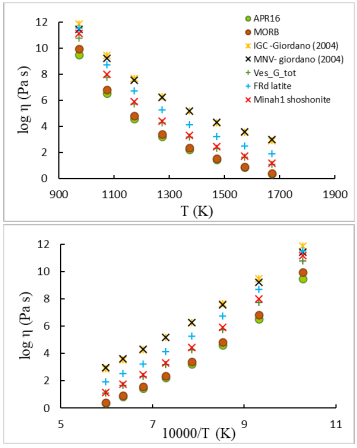

Fig. S2. *Log viscosity vs T (top) and 10000/T (bottom) at atmospheric pressure for differentiated compositions of Campi Flegrei (Giordano et al., 2004a; Giordano and Dingwell, 2003; Misiti et al., 2011), APR16 K-basalt of this study and MORB of Sakamaki et al. (2013). Data were calculated using the Excel spreadsheet of Giordano et al. (2008b).*

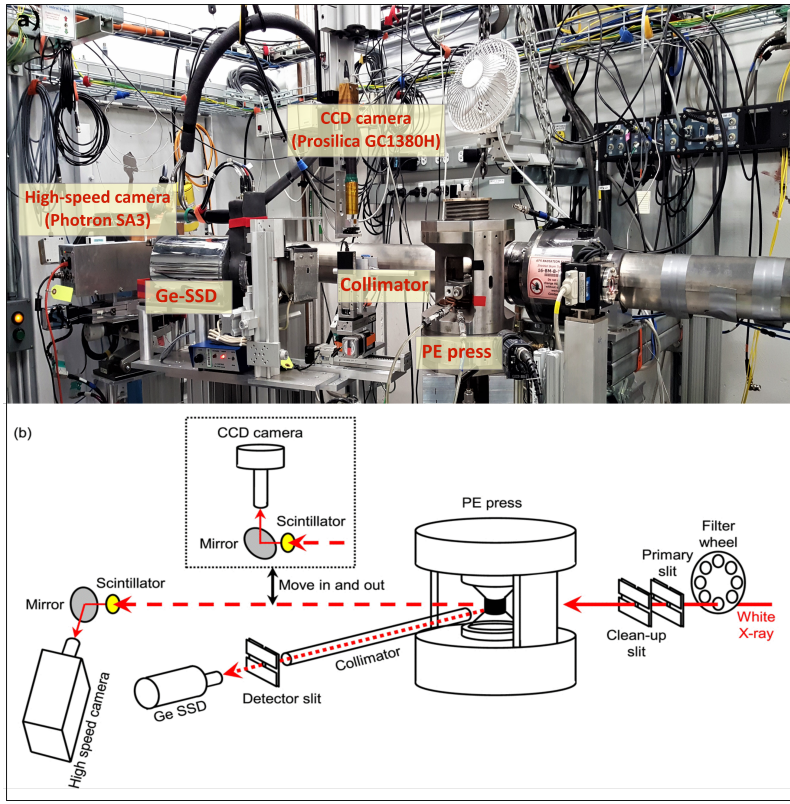

Fig. S3. *A photograph (a) and schematic drawing (b) of the Paris-Edinburgh press experimental setup at the 16-BM-B beamline, HPCAT, at the Advanced Photon Source. Two cameras (Prosilica GC1380H and Photron SA3) are installed for X-ray imaging experiments. Fig S3b from Kono et al. (2015).*

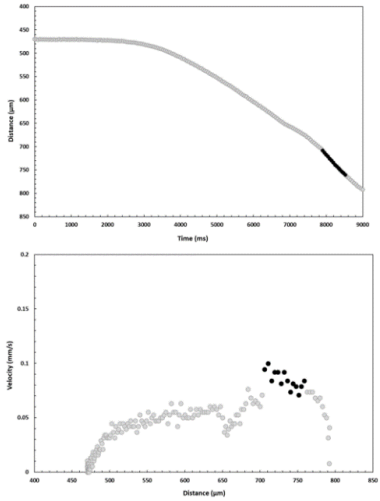

Fig. S4. *Diagrams of the falling distance versus time (top) and falling velocity versus distance (bottom) of the Pt sphere (diameter of 113 µm) for the run at 2.3 GPa and 1600 °C (APR16-PE1).*

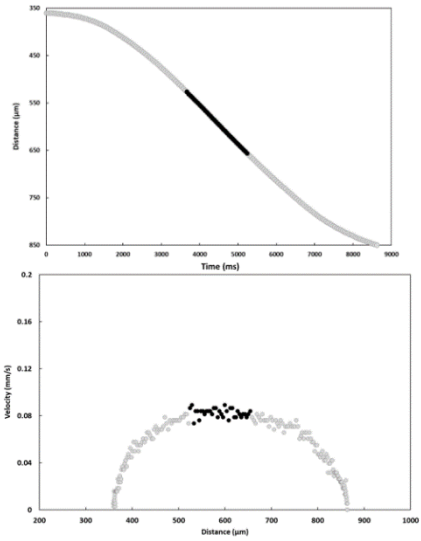

Fig. S5. *Plots of the falling distance as function of time (top) and falling velocity versus distance (bottom) of the Pt sphere (diameter of 155 µm) for the run at 1.4 GPa and 1440 °C (APR16-PE2).*

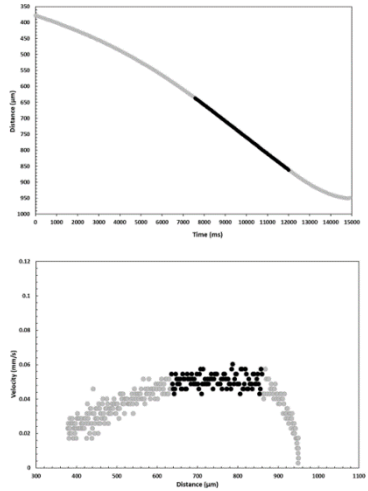

Fig. S6. *The falling distance as function of time (top) and velocity (bottom) of the Pt sphere (diameter of 107 µm) in run at 0.7 GPa and 1440 °C (APR16-PE3 top).*

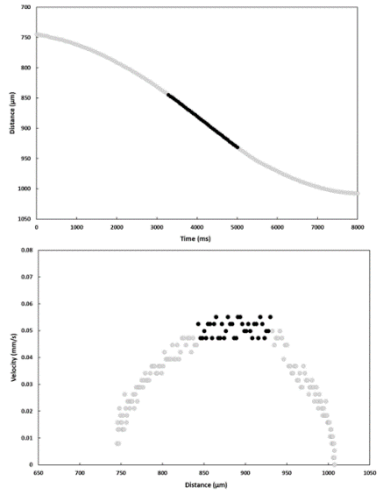

Fig. S7. *Falling distance versus time (top) and velocity (bottom) of the Pt sphere (diameter of 146 µm) recorded for the run at 0.7 GPa and 1335 °C (APR16-PE3 bottom).*

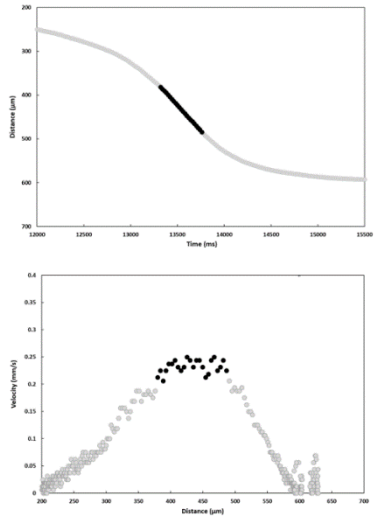

Fig. S8. *The falling vertical distance (top) and velocity profile (bottom) of the Pt sphere (diameter of 124 µm) for the run at 7 GPa and 2000 °C (APR16-PE5).*

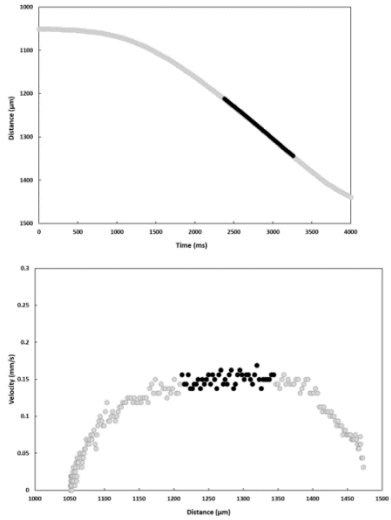

Fig. S9. *The falling distance versus time (top) and velocity profile (bottom) of the Pt sphere (diameter of 126 µm) for the run at 5.6 GPa and 1835 °C (APR16-PE6).*

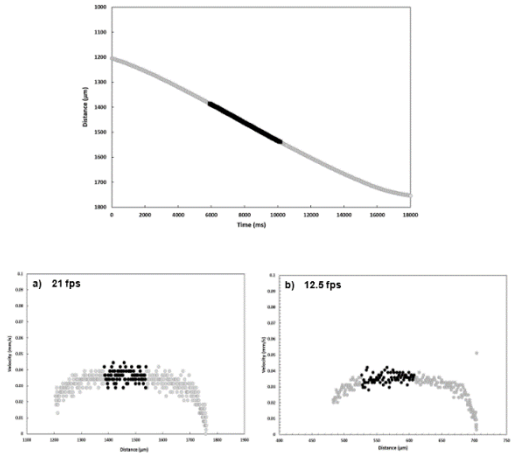

Fig. S10. (top) *The falling distance of the Pt sphere (diameter of 70 µm) for the run at 3.7 GPa and 1650 °C (APR16-PE7) as function of time.* ***(Bottom)*** *Falling velocity profiles are shown at a) 21 fps and b) 12.5 fps.*

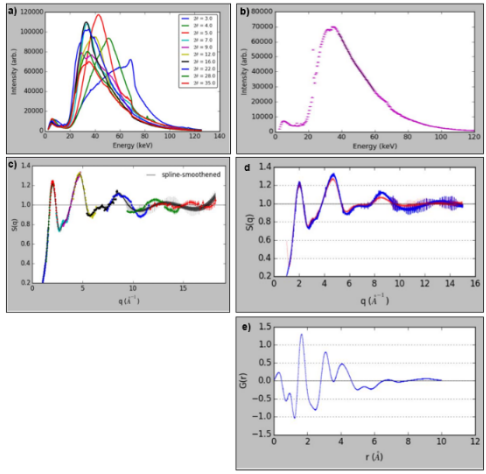

Fig. S11 *a) Multi-angle energy dispersive X-ray diffraction (MA-EDXD) spectra from APR16-PE1 run; b) the effective primary beam estimation for a selected energy range; c) total structure factor S(q) composed of the fragmented structure factor scaled with respect to the highest angle fragment. The solid line is obtained after error-weighted spline-smoothening of the overlapped structure factor fragments; d) structure factor S(q) and e) reduced pair distribution function G(r).*

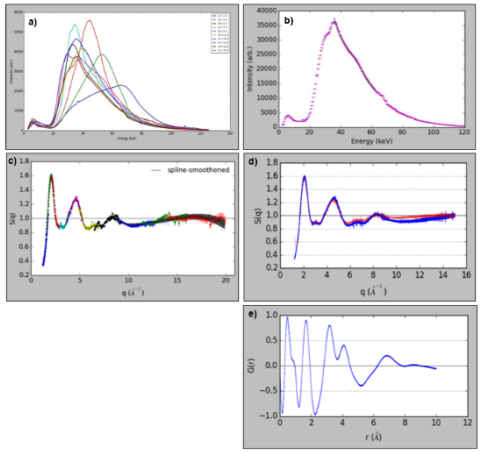

Fig. S12 *a) MA-EDXD spectra from APR16-PE6 run; b) the effective primary beam estimation for a selected energy range; c) total structure factor S(q) composed of the fragmented structure factor scaled with respect to the highest angle fragment. The solid line is obtained after error-weighted spline-smoothening of the overlapped structure factor fragments; d) structure factor S(q) and e) reduced pair distribution function G(r).*

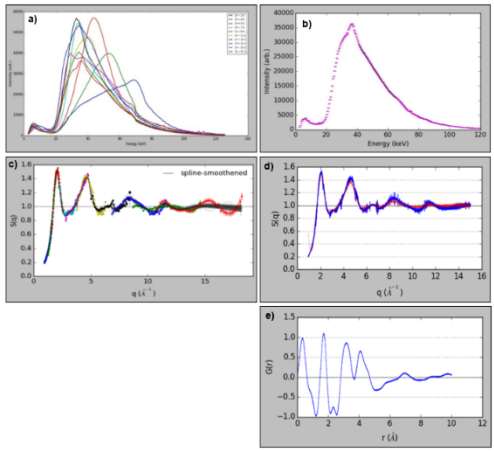

Fig. S13 *a) MA-EDXD spectra from APR16-PE7 run; b) the effective primary beam estimation for a selected energy range; c) total structure factor S(q) composed of the fragmented structure factor scaled with respect to the highest angle fragment. The solid line is obtained after error-weighted spline-smoothening of the overlapped structure factor fragments; d) structure factor S(q) and e) reduced pair distribution function G(r).*

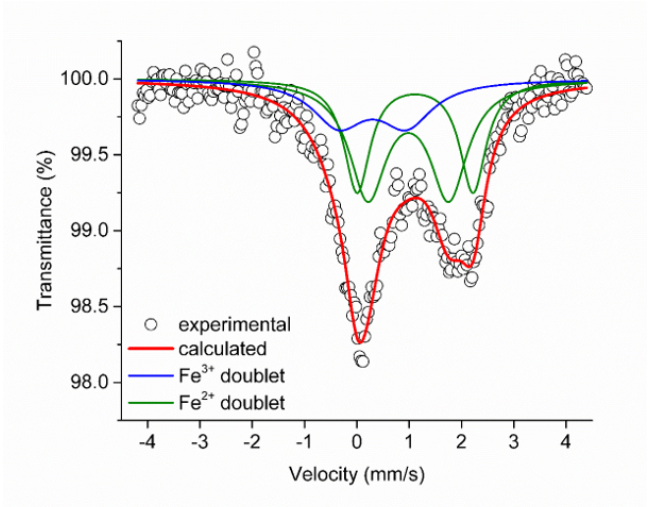

Fig. S14. *Mössbauer spectrum of APR16 starting glass used for our experiments.*

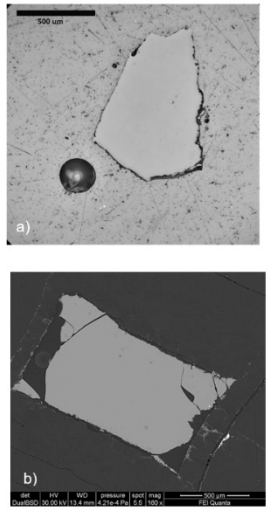

Fig. S15. *a) optical microscope image of APR16GL starting material and b) back-scattered electron image of APR16-PE6 run (1835 °C, 5.6 GPa). From both images, the chemical and textural homogeneity can be inferred.*

Appendix F

Tables

Trace element partitioning between clinopyroxene and alkali basaltic melts: investigation at high pressure on a primitive composition from the Campi Flegrei Volcanic district (Italy)

Barbara Bonechi[a], Cristina Perinelli[a], Mario Gaeta[a], Alessandro Fabbrizio[b], Maurizio Petrelli[c], Ladislav Strnad[d]

a: Dipartimento di Scienze della Terra, Sapienza Università di Roma, P. le Aldo Moro 5, 00185, Rome, Italy

b: Institute of Petrology and Structural Geology, Faculty of Science, Charles University, Albertov 6, 12843 Prague, Czech Republic

c: Department of Physics and Geology, University of Perugia, Piazza Università, Perugia 06100, Italy

d: Laboratories of the Geological Institutes, Charles University, Albertov 6, Prague 2, CZ-12843, Czech Republic

Under review in *Geochimica et Cosmochimica Acta*

Table 1 Composition (wt.%) of APR16 rock sample, APR16GL starting material, SCE and SOG rock samples

Sample	APR16	APR16GL	SCE	SOG
SiO_2	48.89	49.30 (0.46)	47.62	47.78
TiO_2	1.23	1.33 (0.03)	1.23	1.23
Al_2O_3	15.65	15.31 (0.14)	15.33	15.43
FeO_{tot}	8.08	7.79 (0.13)	8.19	8.24
MnO	0.14	0.14 (0.05)	0.14	0.15
MgO	8.89	9.31 (0.07)	9.78	9.75
CaO	11.64	12.02 (0.09)	11.89	11.59
Na_2O	2.88	2.86 (0.05)	2.69	2.83
K_2O	1.52	1.60 (0.02)	1.58	1.67
P_2O_5	0.31	0.55 (0.02)	0.29	0.29
Total	99.99	99.31 (0.29)§	99.65	99.88
L.O.I.	0.61	-	0.26	0.28
Mg# [1]	0.66	0.68	0.68	0.68

Notes: 1[MgO/ (MgO + FeOtot)] molar, assuming all Fe^{2+} and Fe^{3+} as FeO_{tot}. Chemical composition of APR16 is from D'Antonio et al. (1999); APR16GL composition is from Perinelli et al. (2019); SCE and SOG from Bonechi et al. (2020b). § For APR16GL the analysis is normalized to 100 % but the original total is reported. Standard deviation is reported in parenthesis

Table 3 Major and trace element concentrations (ppm) for synthetic clinopyroxene crystals and glasses

Run#	APR16-1C	APR16-35	APR16-C1Ac	APR16-C1Ad	APR16-C2Aa	APR16-C2Ab	APR16-C2Ac	APR16-C2Ad	APR16-C2Bc	APR16-C2Bd	APR16-C3Ac
Phase	cpx glass	cpx glass	cpx glass	cpx glass	cpx glass	cpx glass	cpx glass	cpx glass	cpx glass	cpx glass	cpx glass
Na	2560 (838) 23215 (275)	2950 (307) 22163 (225)	3709 (351) 25074 (213)	3709 (265) 23591 (203)	3041 (*302*) 21365 (211)	4525 (*452*) 23665 (198)	6083 (*433*) 23294 (231)	3561 (*363*) 22107 (220)	bdl -	5638 (*502*) 28339 (223)	4154 (341) 27226 (207)
K	279 (102) 14562 (291)	103 (52) 14693 (204)	581 (103) 15772 (206)	498 (98) 14942 (232)	581 (*92*) 13033 (243)	1909 (*232*) 17599 (221)	1826 (*312*) 20754 (209)	415 (*105*) 16270 (214)	bdl -	1079 (*343*) 21916 (225)	913 (123) 15275 (213)
Ca	150086 (5800) 73870 (1250)	150086 (6100) 74268 (1130)	129450 (5980) 71242 (3850)	147514 (4800) 80403 (2100)	137400 (*6400*) 86335 (4120)	145155 (*5100*) 76620 (3560)	146086 (*4350*) 58748 (3400)	152874 (*5210*) 77187 (2980)	bdl -	146585 (*4600*) 56533 (3230)	153017 (3980) 67039 (4550)
Fe	38643 (4451) 61647 (1208)	22399 (2350) 30246 (903)	32569 (2310) 48193 (950)	34357 (1890) 48193 (860)	35134 (*1930*) 44696 (810)	34823 (*2100*) 42519 (950)	34357 (*1850*) 42674 (890)	31248 (*2210*) 34901 (730)	bdl -	42130 (*1900*) 47183 (1010)	45317 (2530) 46950 (980)
Mg	84353 (6092) 43253 (507)	96961 (6310) 45112 (466)	90573 (11665) 46575 (1800)	95300 (7600) 46456 (1540)	81600 (*4300*) 44060 (1480)	108000 (*16000*) 45660 (1840)	87000 (*8200*) 47100 (3125)	110000 (*13000*) 32183 (1225)	5900 (110) 28075 (2869)	83000 (*7900*) 33100 (1925)	86933 (4600) 33280 (1580)
Al	25520 (6890) 83792 (2340)	28709 (7650) 83050 (3050)	59765 (15843) 94219 (3525)	41540 (5760) 92220 (3100)	22900 (*2200*) 73560 (3080)	28700 (*160*) 128750 (11675)	41070 (*3000*) 105150 (4800)	36500 (*1700*) 96220 (6920)	5750 (95) 102650 (3830)	36300 (*3300*) 103575 (5925)	37783 (1700) 99238 (3920)
Mn	880 (130) 1151 (10)	915 (82) 1127 (13)	900 (110) 1211 (12)	1100 (199) 1296 (30)	1080 (*320*) 1136 (21)	1140 (*170*) 1299 (35)	1143 (*95*) 1310 (172)	1210 (120) 1359 (43)	bdl 1185 (107)	1054 (*92*) 1307 (42)	1271 (97) 1254 (28)
Ti	4370 (259) 7296 (92)	4257 (1041) 7395 (113)	2684 (29) 7070 (40)	3275 (1136) 7180 (90)	3570 (*910*) 6432 (100)	3510 (*570*) 8253 (388)	4440 (*650*) 6405 (61)	6410 (*670*) 7906 (205)	bdl 7575 (367)	8050 (*870*) 8625 (128)	5270 (139) 7526 (150)
Zr	34 (11) 103 (2)	31 (2) 105 (2)	18 (3) 111 (*5*)	33 (10) 111 (2)	bdl 99 (2)	26 (*9*) 129 (7)	33 (*7*) 198 (9)	60 (*12*) 120 (1)	bdl 133 (*5*)	82 (*12*) 143 (2)	40 (2) 128 (2)
Nb	0.11 (0.07) 13.1 (0.3)	0.20 (0.04) 13.1 (0.3)	bdl 13.7 (0.5)	1.1 (0.6) 12.7 (0.6)	bdl 10.2 (0.6)	2.4 (0.3) 15 (1)	bdl 26.2 (0.1)	bdl 14 (1)	bdl 17 (2)	bdl 18 (1)	0.7 (0.1) 14.1 (0.4)
Hf	1.6 (0.4) 2.5 (0.2)	1.6 (0.2) 2.6 (0.1)	bdl 2.8 (0.1)	bdl 2.85 (0.03)	bdl 2.2 (0.1)	bdl 2.8 (0.3)	1.2 (0.2) 3.8 (0.2)	2 (1) 2.7 (0.3)	bdl 2.9 (0.3)	3.9 (1.4) 3.3 (0.4)	1.8 (0.2) 3.3 (0.4)
Ta	0.05 (0.01) 0.68 (0.04)	0.04 (0.01) 0. 67 (0.04)	bdl 0.7 (0.2)	bdl 0.7 (0.1)	bdl 0.5 (0.1)	bdl 0.85 (0.05)	bdl 1.5 (0.2)	bdl 0.8 (0.1)	bdl 0.99 (0.13)	bdl 1.04 (0.16)	bdl 0.9 (0.1)
Th	0.06 (0.01) 2.9 (0.1)	0.06 (0.02) 2.9 (0.1)	bdl 3.4 (0.2)	bdl 3.3 (0.2)	bdl 2.5 (0.1)	bdl 3.6 (0.4)	bdl 6.3 (0.8)	bdl 3.2 (0.3)	bdl 4.1 (0.4)	bdl 4.9 (0.3)	0.20 (0.06) 3.7 (0.3)
U	0.01 0.93 (0.05)	0.03 (0.01) 0.94 (0.04)	bdl 1.0 (0.1)	bdl 1.2 (0.1)	bdl 0.8 (0.1)	bdl 1.1 (0.1)	bdl 2.24 (0.04)	bdl 1.1 (0.2)	bdl 1.4 (0.1)	bdl 1.5 (0.2)	bdl 1.2 (0.2)
Rb	bdl 57 (1)	bdl 56 (1)	bdl 64 (2)	11 (*3*) 66 (1)	bdl 53.1 (0.1)	bdl 71 (2)	8 (*4*) 120 (4)	bdl 69 (4)	bdl 78 (6)	bdl 95 (1)	2.2 (0.3) 70 (3)
Sr	54 (8) 503 (6)	52 (2) 499 (5)	59 (1) 531 (2)	83 (*8*) 540 (6)	55 (*16*) 442 (4)	71 (*18*) 631 (13)	87 (*16*) 698 (15)	84 (*13*) 594 (8)	bdl 652 (21)	60 (*8*) 693 (26)	78 (6) 605 (3)
Cs	bdl 2.4 (0.1)	bdl 2.4 (0.1)	bdl 2.7 (0.2)	bdl 3.0 (0.2)	bdl 2.2 (0.3)	bdl 3.3 (0.3)	bdl 4.8 (0.1)	bdl 2.9 (0.1)	bdl 3.3 (0.5)	bdl 3.9 (0.2)	bdl 3.0 (0.3)
Ba	0.41 (0.01) 534 (9)	0.76 (0.37) 532 (7)	12 (7) 536 (7)	30 (13) 553 (17)	16 (9) 450 (2)	bdl 670 (39)	43 (22) 1013 (43)	15 (7) 589 (4)	bdl 773 (4)	bdl 749 (29)	20.8 (0.6) 606 (1)

Table 3 Continued

Pb	0.12 (0.15)	0.14 (0.05)	bdl	bdl	bdl	bdl	bdl	bdl	bdl	bdl	bdl
	1.1 (0.5)	11.7 (0.4)	bdl	bdl	0.9 (0.1)	bdl	bdl	bdl	bdl	bdl	bdl
Sc	119 (21)	113 (5)	80 (10)	87 (8)	87 (*27*)	110 (*13*)	88 (5)	112 (19)	bdl	155 (14)	93 (3)
	28 (1)	30 (1)	40 (1)	40 (2)	40 (1)	27 (3)	23 (1)	43 (2)	19 (1)	22 (1)	26 (1)
V	248 (23)	764 (86)	120 (16)	174 (49)	133 (*17*)	237 (*43*)	263 (*41*)	385 (*36*)	bdl	505 (*50*)	199 (8)
	190 (2)	162 (4)	201 (5)	194 (4)	184 (2)	182 (4)	180 (6)	217 (4)	157 (2)	198 (1)	224 (3)
Cr	3229 (708)	4460 (605)	4445 (345)	2390 (1259)	2210 (*44*)	1740 (*600*)	1100 (*120*)	1200 (*190*)	bdl	1400 (*230*)	1617 (92)
	80 (12)	96 (9)	77 (23)	57 (1)	318 (2)	35 (*17*)	31 (*11*)	163 (3)	bdl	28 (*12*)	26 (*13*)
Co	28 (2)	15 (3)	22 (5)	33 (2)	26 (*11*)	13 (*7*)	19 (*4*)	21 (*9*)	bdl	43 (*3*)	36 (1)
	34 (2)	12 (1)	24 (1)	25 (1)	27 (1)	19 (1)	17 (1)	17 (1)	10 (1)	15 (1)	21 (10)
Ni	139 (12)	44 (18)	37 (*17*)	60 (*6*)	bdl	51 (*18*)	bdl	bdl	bdl	137 (*18*)	177 (10)
	43 (9)	7 (1)	15 (2)	26 (2)	33 (1)	12 (1)	8 (2)	9 (1)	bdl	9 (1)	12 (1)
Y	15 (2)	17 (1)	17 (2)	bdl	bdl	bdl	bdl	bdl	bdl	bdl	bdl
	19.9 (0.3)	20.2 (0.3)	19 (1)	bdl	bdl	bdl	bdl	bdl	bdl	bdl	bdl
La	1.9 (0.4)	1.8 (0.2)	bdl	1.5 (*0.5*)	bdl	2.6 (*1.1*)	bdl	3.9 (*1.7*)	bdl	4.7 (*1.2*)	3 (0.2)
	15.6 (0.3)	16.01 (0.24)	17.1 (0.5)	17.9 (0.3)	14.7 (0.2)	20.9 (0.9)	33 (2)	19 (1)	22 (1)	25 (2)	20 (1)
Ce	7.3 (1.7)	6.7 (0.7)	6.7 (0.3)	5.8 (3.4)	bdl	7.8 (*2.3*)	bdl	11.2 (*3.5*)	bdl	13 (*2*)	10.1 (0.5)
	34.5 (0.5)	35.1 (0.6)	36 (1)	37 (1)	30 (1)	42 (1)	67 (4)	37 (1)	45.2 (0.5)	49 (2)	41 (1)
Pr	1.4 (0.3)	1.3 (0.1)	1.8 (0.3)	1.1 (*0.4*)	bdl	1.6 (*0.7*)	1.4 (*0.2*)	2.1 (*0.3*)	bdl	2.6 (*0.5*)	1.9 (0.1)
	4.4 (0.1)	4.5 (0.1)	4.5 (0.2)	5.2 (0.1)	3.9 (0.3)	5 (0.5)	7.8 (1.2)	4.9 (0.2)	5.1 (0.2)	5.9 (0.3)	5.2 (0.3)
Nd	8.5 (1.5)	7.9 (0.7)	11 (1)	7.2 (2.1)	bdl	8.3 (*4.2*)	7.2 (*0.9*)	14 (*5*)	bdl	16 (*3*)	11.7 (0.4)
	19 (1)	19.4 (0.5)	20 (1)	23 (2)	17 (1)	24 (2)	35 (4)	21 (2)	22 (1)	25 (2)	24 (1)
Sm	3.02 (0.61)	3.03 (0.4)	3.4 (0.6)	3.8 (*0.2*)	bdl	bdl	bdl	bdl	bdl	5.5 (*2.2*)	4.4 (1.1)
	4.5 (0.3)	4.7 (0.3)	4.89 (0.03)	5.9 (0.6)	4.4 (0.6)	5.4 (1)	7.7 (0.8)	5.3 (0.6)	5.4 (0.4)	6.1 (1.5)	5.8 (0.4)
Eu	0.9 (0.1)	0.8 (0.1)	0.9 (0.2)	bdl	bdl	bdl	0.8 (0.1)	bdl	bdl	1.1 (*0.4*)	1.5 (0.2)
	1.5 (0.1)	1.5 (0.1)	1.6 (0.2)	1.9 (0.6)	1.5 (0.2)	1.8 (0.2)	2.5 (0.2)	1.9 (0.3)	1.6 (0.5)	1.9 (0.2)	1.7 (0.1)
Gd	3.7 (0.4)	3.5 (0.3)	3.1 (*0.2*)	2.7 (*0.2*)	bdl	bdl	bdl	5.1 (1.6)	bdl	5.8 (*2.1*)	4.9 (0.9)
	4.5 (0.2)	4.4 (0.3)	4.6 (0.4)	5.5 (0.6)	4.1 (0.4)	4.8 (0.7)	6.3 (0.3)	5.3 (0.3)	4.4 (0.5)	5.8 (1.2)	5.1 (0.8)
Tb	0.53 (0.07)	0.57 (0.05)	bdl	0.44 (*0.1*)	bdl	bdl	0.38 (*0.05*)	bdl	bdl	1.1 (*0.3*)	0.68 (0.05)
	0.63 (0.04)	0.66 (0.05)	0.66 (0.01)	0.74 (0.16)	0.59 (0.08)	0.86 (0.09)	1.02 (0.23)	0.76 (0.13)	0.72 (0.11)	0.88 (0.17)	0.73 (0.11)
Dy	3.3 (0.4)	3.52 (0.05)	3.9 (1.2)	2.6 (*0.8*)	bdl	bdl	bdl	5.8 (*0.4*)	bdl	4.7 (*1.7*)	4.4 (0.5)
	3.8 (0.2)	3.9 (0.2)	3.8 (0.1)	4.5 (0.4)	3.6 (0.3)	4.9 (0.4)	5.6 (0.2)	4.1 (0.4)	4.2 (0.6)	4.2 (0.2)	4.2 (0.3)
Ho	0.64 (0.07)	0.66 (0.05)	0.76 (0.21)	bdl	bdl	0.59 (0.33)	bdl	bdl	bdl	0.89 (*0.39*)	0.84 (0.12)
	0.75 (0.05)	0.77 (0.04)	0.81 (0.1)	0.92 (0.18)	0.65 (0.08)	0.93 (0.16)	1.13 (0.22)	0.81 (0.14)	0.80 (0.14)	0.90 (0.12)	0.90 (0.12)
Er	1.59 (0.27)	1.75 (0.18)	1.53 (0.34)	1.12 (*0.11*)	bdl	bdl	bdl	bdl	bdl	2.62 (*0.95*)	2.14 (0.12)
	2.12 (0.13)	2.04 (0.15)	2.04 (0.19)	2.31 (0.29)	1.94 (0.18)	2.22 (0.19)	3.07 (0.6)	2.14 (0.2)	2.09 (0.35)	2.15 (0.3)	2.11 (0.34)
Tm	0.20 (0.03)	0.22 (0.03)	0.19 (0.08)	bdl	bdl	bdl	bdl	bdl	bdl	bdl	0.32 (0.04)
	0.27 (0.02)	0.29 (0.04)	0.28 (0.02)	0.36 (0.05)	0.25 (0.03)	0.32 (0.03)	0.37 (0.04)	0.31 (0.04)	bdl	0.30 (0.05)	0.28 (0.09)
Yb	1.24 (0.22)	1.43 (0.16)	bdl	bdl	bdl	bdl	bdl	bdl	bdl	bdl	1.73 (0.29)
	1.78 (0.15)	1.87 (0.21)	1.91 (0.38)	2.34 (0.17)	1.87 (0.32)	2.07 (0.44)	2.65 (0.07)	2.01 (0.27)	2.01 (0.57)	2.26 (0.3)	1.78 (0.68)
Lu	0.17 (0.02)	0.21 (0.01)	bdl	bdl	bdl	bdl	bdl	bdl	bdl	bdl	0.26 (0.03)
	0.27 (0.03)	0.27 (0.02)	0.29 (0.06)	0.36 (0.06)	0.28 (0.08)	0.33 (0.03)	0.49 (0.12)	0.33 (0.04)	0.31 (0.03)	0.4 (0.09)	0.31 (0.05)

Notes: cpx = clinopyroxene; standard deviation is reported in brackets.

For single analysis Int2SE (i.e., analytical error) is reported also in brackets but in italic; bdl = below detection limit.

Table 4 Major and trace elements partition coefficients between clinopyroxene and glass for experimental samples

Run#	APR16-1C	APR16-35	APR16-C1Ac	APR16-C1Ad	APR16-C2Aa	APR16-C2Ab	APR16-C2Ac	APR16-C2Ad	APR16-C2Bd	APR16-C3Ac
Na	0.110 (0.011)	0.133 (0.023)	0.148 (0.012)	0.157 (0.021)	0.142 (0.018)	0.191 (0.023)	0.261 (0.034)	0.161 (0.013)	0.199 (0.026)	0.147 (0.011)
K	0.019 (0.001)	0.007 (0.001)	0.037 (0.008)	0.033 (0.009)	0.044 (0.008)	0.11 (0.01)	0.088 (0.005)	0.026 (0.005)	0.049 (0.006)	0.042 (0.002)
Ca	2.03 (0.14)	2.02 (0.03)	1.82 (0.15)	1.83 (0.15)	1.59 (0.12)	1.89 (0.12)	2.47 (0.25)	1.98 (0.15)	2.59 (0.25)	2.28 (0.13)
Fe	0.59 (0.07)	0.61 (0.08)	0.66 (0.08)	0.69 (0.08)	0.77 (0.08)	0.77 (0.08)	0.78 (0.08)	0.88 (0.08)	0.87 (0.08)	0.97 (0.09)
Fe_{M1}	0.293	0.367	0.329	0.421		0.410	0.411	0.45	0.535	0.672
Fe_{M2}	0.297	0.247	0.329	0.268		0.358	0.372	0.43	0.338	0.293
Mg	1.94 (0.04)	1.92 (0.07)	2.23 (0.24)	2.12 (0.72)	1.85 (0.12)	2.41 (0.37)	2.55 (0.38)	2.03 (0.14)	2.5 (0.3)	2.68 (0.27)
Mg_{M1}	1.809	1.811	2.074	1.991		2.232	2.382	1.809	2.353	2.552
Mg_{M2}	0.135	0.106	0.158	0.129		0.18	0.167	0.219	0.143	0.129
Al	0.304 (0.123)	0.346 (0.121)	0.634 (0.169)	0.45 (0.064)	0.311 (0.033)	0.223 (0.045)	0.389 (0.019)	0.39 (0.018)	0.35 (0.038)	0.381 (0.023)
Mn	0.721 (0.357)	0.631 (0.211)	0.751 (0.412)	0.623 (0.269)		0.737 (0.205)	0.912 (0.247)	0.909 (0.367)	0.855 (0.278)	0.739 (0.297)
Ti	0.599 (0.155)	0.576 (0.088)	0.380 (0.092)	0.456 (0.116)	0.555 (0.144)	0.425 (0.075)	0.693 (0.072)	0.811 (0.108)	0.932 (0.125)	0.700 (0.059)
Zr	0.329 (0.106)	0.300 (0.024)	0.163 (0.027)	0.301 (0.090)		0.199 (0.011)	0.165 (0.008)	0.500 (0.004)	0.573 (0.009)	0.310 (0.016)
Nb	0.008 (0.005)	0.015 (0.003)		0.087 (0.004)			0.094 (0.001)			0.048 (0.009)
Hf	0.671 (0.169)	0.622 (0.085)					0.314 (0.015)	0.727 (0.082)	1.194 (0.135)	0.562 (0.089)
Ta	0.070 (0.007)	0.062 (0.008)								
Th	0.020 (0.005)	0.019 (0.006)								0.055 (0.001)
U	0.011 (0.001)	0.032 (0.009)								
Rb				0.166 (0.003)			0.068 (0.003)			0.031 (0.003)
Sr	0.108 (0.017)	0.104 (0.004)	0.111 (0.002)	0.153 (0.002)	0.122 (0.001)	0.106 (0.002)	0.125 (0.003)	0.141 (0.002)	0.086 (0.003)	0.129 (0.010)
Ba	0.001 (0.001)	0.001 (0.001)	0.0232 (0.0003)	0.054 (0.002)	0.0349 (0.0002)		0.042 (0.002)	0.0248 (0.0002)		0.034 (0.001)
Pb	0.112 (0.051)	0.012 (0.004)								
Sc	4.24 (0.74)	3.74 (0.19)	2.01 (0.26)	2.18 (0.23)	2.20 (0.08)	4.09 (0.40)	3.84 (0.17)	2.58 (0.12)	7.06 (0.24)	3.60 (0.18)
V	1.30 (0.12)	4.71 (0.54)	0.597 (0.083)	0.892 (0.252)	0.722 (0.008)	1.31 (0.03)	1.46 (0.04)	1.77 (0.03)	2.55 (0.01)	0.886 (0.037)
Cr	41 (11)	47 (8)	57 (18)	42 (22)	6.9 (0.1)	50	35	7.3 (1.2)	50	63 (4)

Table 4 Continued

Co	0.83 (0.07)	1.25 (0.23)	0.92 (0.21)	1.32 (0.08)	0.95 (0.40)	0.68 (0.38)	1.12 (0.24)	1.21 (0.52)	2.87 (0.35)	1.71 (0.78)
Co_{M1}	0.64	1.11	0.71	1.15		0.46	0.9	0.93	2.67	1.54
Co_{M2}	0.18	0.14	0.2	0.17		0.22	0.22	0.28	0.19	0.17
Ni	3.21 (0.71)	6.29 (2.81)	2.38 (1.17)	2.33 (0.28)		4.31 (0.43)			15.6 (2.3)	15 (2)
Y	0.770 (0.105)	0.848 (0.031)	0.886 (0.122)							
La	0.119 (0.026)	0.110 (0.012)		0.082 (0.001)		0.124 (0.005)		0.20 (0.01)	0.19 (0.01)	0.150 (0.098)
Ce	0.213 (0.051)	0.191 (0.021)	0.187 (0.009)	0.158 (0.091)	0.187 (0.006)			0.282 (0.009)	0.254 (0.011)	0.248 (0.015)
Pr	0.326 (0.074)	0.295 (0.032)	0.397 (0.066)	0.213 (0.005)		0.312 (0.031)	0.181 (0.027)	0.424 (0.015)	0.441 (0.022)	0.360 (0.029)
Nd	0.451 (0.082)	0.406 (0.035)	0.535 (0.069)	0.309 (0.096)		0.349 (0.023)	0.208 (0.025)	0.638 (0.048)	0.658 (0.045)	0.489 (0.028)
Sm	0.670 (0.143)	0.649 (0.095)	0.688 (0.129)	0.641 (0.061)					0.902 (0.027)	0.768 (0.175)
Eu	0.637 (0.099)	0.540 (0.059)	0.587 (0.128)				0.313 (0.025)		0.575 (0.056)	0.839 (0.135)
Eu^{2+}	0.137	0.132	0.140	0.193				0.179	0.111	0.169
Eu^{3+}	0.756	0.729	0.772	0.718				1.071	1.032	0.877
Gd	0.819 (0.134)	0.777 (0.088)	0.668 (0.056)	0.495 (0.055)				0.955 (0.055)	1.008 (0.203)	0.968 (0.233)
Tb	0.831 (0.122)	0.872 (0.106)		0.595 (0.127)			0.376 (0.085)		1.29 (0.25)	0.926 (0.155)
Dy	0.865 (0.111)	0.896 (0.054)	1.021 (0.319)	0.588 (0.047)				1.398 (0.135)	1.12 (0.05)	1.04 (0.14)
Ho	0.849 (0.104)	0.859 (0.078)	0.941 (0.285)			0.636 (0.110)			0.989 (0.132)	0.933 (0.182)
Er	0.749 (0.134)	0.859 (0.078)	0.752 (0.181)	0.487 (0.061)					1.22 (0.17)	1.01 (0.17)
Tm	0.752 (0.124)	0.774 (0.149)	0.676 (0.289)							1.14 (0.39)
Yb	0.699 (0.135)	0.764 (0.120)								0.972 (0.405)
Lu	0.625 (0.110)	0.753 (0.070)								0.831 (0.164)

Notes: standard deviation is reported in brackets. D_{M1} and D_{M2}, and Eu^{2+} and Eu^{3+} partition coefficients were recalculated following the procedure described in section 4.1.

Table 5 Best fits for E, r_0 and D_0 obtained by regression of clinopyroxene/liquid partition coefficients of divalent, trivalent and tetravalent cations in M1 and M2 sites

Run#	APR16-1C	APR16-35	APR16-C1Ac	APR16-C1Ad	APR16-C2Aa	APR16-C2Ab	APR16-C2Ac	APR16-C2Ad	APR16-C2Bd	APR16-C3Ac
M2^{2+}										
D_0	2.38±0.29	2.38±0.49	2.25±0.33	2.02±0.71	2.31±0.07	2.27±0.40	3.07±0.47	2.46±0.38	3.19±0.49	2.68±0.32
r_0	1.081±0.005	1.083±0.002	1.079±0.005	1.088±0.003	1.059±0.001	1.077±0.006	1.081±0.006	1.078±0.005	1.080±0.003	1.084±0.004
r_0 (WB97)	*1.081*	*1.082*	*1.082*	*1.083*		*1.079*	*1.076*	*1.084*	*1.078*	*1.084*
E	271±22	287±20	260±24	246±31	200±20	252±29	274±27	236±22	286±19	249±18
E (WB97)	*180*	*180*	*179*	*179*		*180*	*180*	*180*	*181*	*183*
M1^{2+}										
D_0	5.34±1.35	7.07±3.11	4.64±1.84	3.74±1.01		6.55±1.27	6.50±2.65	3.47±0.78	9.95±0.07	7.37±1.92
r_0	0.616±0.014	0.610±0.011	0.621±0.013	0.639±0.013		0.614±0.013	0.617±0.012	0.646±0.009	0.634±0.004	0.634±0.009
E	504±133	461±60	484±72	523±148		473±82	468±54	530±74	596±5	455±77
M2^{3+}										
D_0	0.860±0.006	0.857±0.002	0.879±0.001	0.614±0.001		0.653±0.005	0.373±0.008	1.165±0.013	1.128±0.002	1.139±0.008
r_0	1.0297±0.0002	1.0257±0.0005	1.0300±0.0002	1.022±0.001		1.033±0.001	1.033±0.001	1.0301±0.0003	1.0323±0.0003	1.0292±0.0005
r_0 (WB97)	*1.0208*	*1.0221*	*1.0220*	*1.023*		*1.019*	*1.016*	*1.0239*	*1.0177*	*1.0245*
E	325±6	326±3	322±1	307±4		305±3	304±3	304±1	310±4	300±2
E (WB97)	*270*	*270*	*269*	*269*		*270*	*270*	*270*	*272*	*275*
M1^{3+}										
D_0	40.05±0.07	40.07±0.10	40.12±0.28	40.05±0.11	11.01±0.55	40.07±0.11	40.03±0.06	20.04±0.05	42.21±1.99	40.11±0.51
r_0	0.664±0.008	0.665±0.006	0.654±0.004	0.655±0.017	0.664±0.002	0.661±0.002	0.660±0.01	0.666±0.001	0.672±0.001	0.663±0.001
E	1499±2	1499±1	1499±1	1499±5	1202±48	1499±1	1499±1	1499±1	1499±4	1499±1
M1^{4+}										
D_0	3.60±1.29	3.50±1.31					1.98±0.83	2.52±0.99	6.21±1.82	2.31±0.94
r_0	0.659±0.001	0.659±0.001					0.650±0.005	0.658±0.002	0.660±0.001	0.656±0.002
r_0 (H11)	*0.649±0.007*	*0.649±0.007*	*0.649±0.007*	*0.649±0.007*	*0.649±0.007*	*0.649±0.007*	*0.649±0.007*	*0.649±0.007*	*0.649±0.007*	*0.649±0.007*
E	3077±559	3115±634					2404±703	1967±623	3014±518	2024±578
E (H11)	*2936±722*	*2936±722*	*2936±722*	*2936±722*	*2936±722*	*2936±722*	*2936±722*	*2936±722*	*2936±722*	*2936±722*

Note: D_0: strain-compensated partition coefficient. E: Young Modulus of the lattice site (GPa). r_0: optimum site radius (Å). D_0, r_0 and E were calculated using the SIMPLE and DOUBLE FIT program (Dalou et al., 2018). Values in italic are the lattice strain parameters $r_0^{2+,+3}$ and $E^{2+,+3}$ for the M2 site calculated by the relations of Wood and Blundy (1997), and the average r_0^{4+} and E^{4+} values obtained for the M1 site of clinopyroxene by Hill et al. (2011).

Supplementary Material 1

Phase relations, texture and chemical composition of natural samples

Natural SCE and SOG rocks contain ~10-20 vol.% of medium-grained olivine and clinopyroxene phenocrysts, dispersed in a microcrystalline groundmass made of olivine + clinopyroxene + plagioclase + titanomagnetite ± glass.

Natural clinopyroxene (Cpx) phenocrysts of SCE and SOG samples show sub-rounded edges, sometimes with olivine overgrowth, glass-bearing spongy cellular textures, and patchy zoning (Fig. 1a-c). The composition is diopsidic (Wo_{49-51} En_{40-45} Fs_{6-9}; Table S2 in Supplementary Material 2). The Mg# value (Mg# = MgO/(MgO + FeO_{tot}) assuming all Fe^{2+} and Fe^{3+} as FeO_{tot}) of large crystals (from 350 μm up to 3 mm in size) ranges between 0.85-0.88, the TiO_2 contents are between 0.61-1.02 wt.% while those of Al_2O_3 vary in a wide range in the zoned crystals (3.89-5.31 wt.%). Cr_2O_3 content in this population of clinopyroxenes is from 0.62 to 0.94 wt.%.

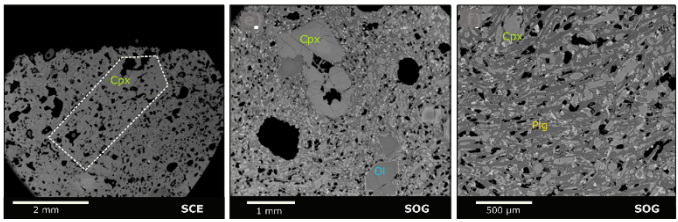

Figure 1 *Backscattered (BSE) images of experimental and natural samples. a) Natural Cpx in SCE sample characterized by glass-bearing spongy cellular texture. White dotted line marks the edges of the crystal; b) Cpx with sub-rounded edges and olivine overgrowth in a microcrystalline groundmass made of Ol + Cpx + Plg + Ox ± glass; c) imagination of the groundmass in which it is possible to recognize oriented Plg, Cpx and Ox. Abbreviation: Cpx: clinopyroxene; Ol: olivine; Plg: plagioclase.*

Clinopyroxene trace elements content

Average compositions of trace elements concentrations analysed by LA-ICP-MS technique in natural clinopyroxene are reported in Table 1.

C1-normalized trace elements for natural Cpx from SOG and SCE samples show trends for LILEs, REEs + Y, HFSEs and TEs similar to those of synthetic Cpx of the experimental runs (Fig. 3 in the main text). Evident differences between these Cpx are observed in the fractionation of LILEs and HFSEs. Indeed, natural SOG and SCE Cpx are more enriched in LILEs and pentavalent HFSEs than synthetic ones. In particular, C1-normalized patterns for SOG and SCE are L/HREE-enriched (i.e., La_N/Yb_N = 1.43-2.04 and 1.42-3.73, respectively) with a maximum at Nd (up to ~46 and 27, respectively). Furthermore, in both samples no Eu anomalies are evident (Eu/Eu* = 0.85-0.94 and 0.90-0.96, respectively). Normalized patterns of both SOG and SCE Cpx are characterized by evident troughs at Pb, Nb, Co and Ni, in agreement with what observed for synthetic Cpx.

Table 1 Trace elements for natural clinopyroxene crystals

Clinopyroxene												
Natural Cpx												
	SOG-4	σ	SOG-7	σ	SOG-9	σ	SOG-10	σ	SCE-5	σ	SCE-6	σ
LILE												
Rb	2.35	1.72	1.75	2.05	5.75	3.03	4.42	4.01	0.24	0.29	4.16	4.27
Sr	79	8	118	39	92	21	98	20	71	4	99	39
Cs	0.09	0.08	0.07	0.08	0.15	0.05	0.17	0.16	0.03	0.02	0.21	0.21
Ba	14	8	14	12	31	16	21	19	2.25	2.03	38.41	41.08
Pb	0.89	0.51	0.73	0.48	2.10	3.06	3.05	4.62	0.39	0.13	1.43	0.92
HFSE												
Zr	57	7	66	26	45	7	35	9	30	12	40	5
Nb	0.91	0.35	0.81	0.63	1.59	0.64	0.84	0.65	0.23	0.08	1.31	1.21
Hf	2.17	0.27	2.50	1.00	1.52	0.22	1.30	0.19	1.33	0.62	1.69	0.15
Ta	0.08	0.02	0.08	0.05	0.10	0.03	0.06	0.03	0.04	0.01	0.10	0.07
Th	0.21	0.09	0.19	0.11	0.36	0.18	0.25	0.18	0.07	0.02	0.30	0.26
U	0.05	0.03	0.05	0.04	0.12	0.06	0.07	0.06	0.03	0.03	0.10	0.07
REE + Y												
Y	22	5	26	9	14	1	14	2	11	4	15	2
La	4.22	1.45	5.18	1.72	3.16	0.74	2.32	0.80	1.94	0.35	3.41	1.32
Ce	15	6	19	6	9	1	7.99	2.54	7.53	1.36	11.11	3.29
Pr	2.84	0.99	3.57	1.18	1.69	0.22	1.37	0.26	1.46	0.25	2.00	0.52
Nd	16	5	21	7	10	1	8.51	1.72	8.68	1.85	11	2
Sm	4.90	1.39	6.27	2.08	3.08	0.24	2.81	0.66	2.90	0.76	3.56	0.62
Eu	1.58	0.47	1.91	0.63	0.95	0.05	0.94	0.36	0.96	0.22	1.17	0.16
Gd	5.54	1.59	6.62	2.60	3.71	0.36	3.26	0.32	3.20	0.85	3.97	0.74
Tb	0.79	0.19	0.95	0.36	0.54	0.04	0.47	0.02	0.53	0.14	0.64	0.10
Dy	4.22	1.08	5.05	1.94	2.83	0.16	2.62	0.12	2.53	0.80	3.31	0.45
Ho	0.80	0.19	0.92	0.31	0.51	0.03	0.49	0.05	0.45	0.15	0.59	0.09
Er	1.98	0.49	2.24	0.78	1.42	0.05	1.29	0.16	1.18	0.41	1.50	0.17
Tm	0.26	0.07	0.29	0.10	0.17	0.02	0.16	0.02	0.15	0.06	0.20	0.03
Yb	1.65	0.48	1.94	0.71	1.07	0.07	1.12	0.32	0.94	0.36	1.28	0.14
Lu	0.22	0.06	0.24	0.09	0.15	0.01	0.14	0.01	0.13	0.04	0.16	0.01
TE												
Sc	101	15	118	39	107	3	113	9	96	1	108	13
V	235	35	287	104	231	14	232	12	235	63	239	12
Cr	1231	852	663	381	1701	544	6812	927	4495	1440	5330	2974
Co	30	1	37	10	31	2	31	2	29	2	30	1
Ni	143	25	162	54	173	14	221	8	185	20	177	18

Notes: σ standard deviation.

Supplementary Material 2

Table S1 Detection limits for all trace elements and analyses of USGS BCR-2G glass

Instrument ICP MS: iCAP Q (Thermo, Germany) + UV laser probe UP213 (NEWwave Research, USA) installed at Charles University, Faculty of Science, Prague 2

		45Sc ablace	51V ablace	52Cr ablace	59Co ablace	60Ni ablace	85Rb ablace	88Sr ablace	89Y ablace	90Zr ablace	93Nb ablace	133Cs ablace	137Ba ablace	139La ablace	140Ce ablace	141Pr ablace	146Nd ablace	147Sm ablace
DL	ppm	1.000	0.080	0.300	0.095	0.450	0.150	0.095	0.045	0.150	0.025	0.010	0.075	0.005	0.020	0.005	0.015	0.020
Reference material																		
BCR-2G (n=5)	ppm	31.85	440.95	16.50	37.69	13.41	46.99	354.60	35.03	192.13	13.62	1.14	676.44	24.87	53.47	6.77	29.70	6.91
	SD	1.78	27.67	1.11	2.47	1.77	1.44	21.94	2.21	16.83	0.89	0.06	23.53	1.44	3.23	0.48	1.82	0.66

151Eu ablace	157Gd ablace	159Tb ablace	163Dy ablace	165Ho ablace	166Er ablace	169Tm ablace	172Yb ablace	175Lu ablace	178Hf ablace	181Ta ablace	208Pb ablace	232Th ablace	238U ablace
0.004	0.010	0.003	0.020	0.003	0.015	0.003	0.025	0.005	0.010	0.010	0.105	0.010	0.005
2.01	6.95	1.07	6.41	1.32	3.57	0.53	3.51	0.54	4.96	0.82	10.54	6.28	1.71
0.11	0.47	0.08	0.50	0.11	0.25	0.04	0.23	0.04	0.39	0.03	0.35	0.11	0.09

Table S2 Electron-microprobe analyses of synthetic and natural clinopyroxenes. All Fe as FeO

Clinopyroxene	*Synthetic Cpx*																		*Natural Cpx*			
	APR16-1C	σ	**APR16-35**	σ	**APR16-C1Ac**	σ	**APR16-C1Ad**	σ	**APR16-C2Aa**	σ	**APR16-C2Ab**	σ	**APR16-C2Ac**	σ	**APR16-C2Ad**	σ	**APR16-C2Bd**	σ	**APR16-C3Ac**	σ	**SCE**	σ	**SOG**	σ
T (C°)	1225		1225		1250		1250		1220		1220		1220		1220		1170		1080					
Time (h)	3		6		6		9		0.25		3		6		9		9		6					
H_2O_T	0.96		1.7		2.03		1.95		1.92		1.56		2.47		1.3		2.02		6.5					
N	6		6		6		6		3		3		4		4		4		6		4		4	
SiO_2	50.67	0.66	51.84	0.33	51.36	0.99	51.54	0.73	51.96	1.14	51.42	1.42	50.05	0.48	51.04	0.35	49.10	0.44	50.21	0.76	51.83	0.35	50.04	0.45
TiO_2	0.66	0.04	0.82	0.26	0.69	0.19	0.58	0.12	0.76	0.26	0.91	0.25	0.99	0.22	0.78	0.08	1.18	0.13	0.95	0.08	0.61	0.10	1.02	0.14
Al_2O_3	6.83	1.45	6.44	0.89	6.06	1.33	5.00	0.81	5.63	1.76	6.85	3.05	9.42	3.17	6.17	0.47	9.49	2.70	7.13	0.32	3.89	0.38	5.31	0.41
FeO	4.64	0.32	2.53	0.40	4.19	0.56	4.42	0.48	4.52	0.54	4.28	0.91	4.42	0.87	4.02	0.54	5.42	1.40	5.83	0.56	3.74	0.41	4.62	0.38
MnO	0.11	0.05	0.11	0.03	0.10	0.05	0.09	0.03	0.08	0.02	0.12	0.03	0.15	0.03	0.12	0.04	0.14	0.03	0.12	0.04	0.07	0.02	0.08	0.01
MgO	16.22	0.21	16.68	0.54	16.65	0.97	16.63	0.49	16.26	0.84	15.50	2.27	14.20	1.98	16.49	0.18	13.88	1.41	14.21	0.42	15.58	0.42	14.53	0.33
CaO	20.56	1.10	21.37	0.69	20.79	0.31	20.64	0.41	21.28	0.48	20.31	1.48	20.44	0.85	21.39	0.78	20.51	0.67	21.41	0.31	23.84	0.35	24.14	0.42
Na_2O	0.47	0.08	0.41	0.05	0.50	0.07	0.50	0.07	0.41	0.09	0.61	0.28	0.82	0.31	0.48	0.06	0.76	0.30	0.56	0.07	0.26	0.11	0.24	0.10
K_2O	0.02	0.00	0.02	0.00	0.07	0.03	0.06	0.02	0.07	0.05	0.23	0.32	0.22	0.18	0.05	0.02	0.13	0.09	0.11	0.04				
Cr_2O_3																					0.94	0.12	0.62	0.13
Total	100.21		100.23		100.52		99.66		101.14		100.39		100.81		100.66		100.65		100.53		100.75		100.61	
Mg#	0.86		0.92		0.88		0.87		0.86		0.86		0.85		0.88		0.82		0.81		0.88		0.85	
$^{Cpx-liq}KD_{Fe-Mg}$	0.33	0.02	0.32	0.02	0.30	0.05	0.33	0.04	0.43	0.06	0.33	0.08	0.31	0.06	0.37	0.05	0.35	0.07	0.36	0.01				
Si	1.84		1.87		1.86		1.88		1.87		1.86		1.81		1.84		1.78		1.83		1.88		1.83	
Ti	0.02		0.02		0.02		0.02		0.02		0.02		0.03		0.02		0.03		0.03		0.02		0.03	
Al	0.29		0.27		0.26		0.22		0.24		0.29		0.40		0.26		0.41		0.31		0.17		0.23	
Cr	0.00		0.00		0.00		0.00		0.00		0.00		0.00		0.00	0	0.00		0.00		0.03		0.02	
Fe^{3+}	0.03		0.00		0.03		0.02		0.00		0.00		0.00		0.04	0	0.01		0.02		0.02		0.06	
Fe^{2+}	0.11		0.08		0.10		0.11		0.14		0.13		0.13		0.08		0.15		0.16		0.09		0.08	
Mn	0.00		0.00		0.00		0.00		0.00		0.00		0.00		0.00		0.00		0.00		0.00		0.00	
Mg	0.88		0.90		0.90		0.91		0.87		0.84		0.76		0.89		0.75		0.77		0.84		0.79	
Ca	0.80		0.82		0.80		0.81		0.82		0.79		0.79		0.83		0.80		0.84		0.93		0.95	
K	0.00		0.00		0.00		0.00		0.00		0.01		0.01		0.00		0.01		0.01		0.00		0.00	
Na	0.033		0.029		0.036		0.035		0.029		0.043		0.057		0.034		0.054		0.040		0.018		0.017	
Al^{IV}	0.163		0.134		0.145		0.118		0.126		0.137		0.192		0.158		0.215		0.167		0.116		0.172	
Al^{VI}	0.129		0.139		0.114		0.097		0.114		0.156		0.209		0.105		0.191		0.140		0.050		0.057	
Wo	44		46		44		44		45		45		47		45		46		47		49		50	
En	48		48		49		49		48		48		45		48		45		43		45		42	
Fe	8		4		7		7		7		7		8		7		10		10		6		8	

Notes: Mg# = [MgO/(MgO+FeO$_{tot}$)] molar, assuming all Fe^{3+} and Fe^{2+} as FeO$_{tot}$.
σ standard deviation; H_2O_T = water content in the melt determined by the by-difference calculation method (respect to the total of EMP analyses); N = number of analyses.
$^{Cpx-liq}KD_{Fe-Mg} = Fe_{cpx}*Mg_{liq}/Mg_{cpx}*Fe_{liq}$ (calculated assuming all Fe as Fe^{2+} in both phases).

Table S3 Electron-microprobe analyses of experimental glasses. All Fe as FeO

Table S3 Electron-microprobe analyses of experimental glasses. All Fe as FeO

Glass

	APR16-1C	σ	APR16-35	σ	APR16-C1Ac	σ	APR16-C1Ad	σ	APR16-C2Aa	σ	APR16-C2Ab	σ	APR16-C2Ac	σ	APR16-C2Ad	σ	APR16-C2Bc	σ	APR16-C2Bd	σ	APR16-C3Ac	σ
T (C°)	1225		1225		1250		1250		1220		1220		1220		1220		1170		1170		1080	
Time (h)	3		6		6		9		0.25		3		6		9		6		9		6	
H_2O_f	0.96		1.7		2.03		1.95		1.92		1.56		2.47		1.3		3.77		2.02		6.5	
N	6		6		6		7		4		4		5		5		4		4		5	
SiO_2	49.52	0.19	51.79	0.19	50.26	0.22	49.94	0.38	50.71	0.46	51.49	0.42	51.84	0.51	51.64	0.49	53.03	0.25	51.91	0.68	52.46	0.48
TiO_2	1.33	0.17	1.41	0.17	1.46	0.04	1.42	0.04	1.28	0.05	1.52	0.10	1.69	0.21	1.38	0.08	1.74	0.18	1.60	0.06	1.41	0.03
Al_2O_3	16.42	0.07	17.03	0.07	18.15	0.73	17.10	0.25	15.82	0.16	19.24	0.61	20.29	0.42	17.80	0.60	20.13	0.20	19.37	0.55	19.29	0.23
FeO	7.86	0.12	4.12	0.12	6.35	0.25	6.41	0.19	5.87	0.56	5.57	0.87	5.64	0.67	4.56	0.15	6.07	0.67	6.21	0.81	6.04	0.37
MnO	0.15	0.03	0.17	0.03	0.13	0.03	0.14	0.04	0.12	0.03	0.16	0.02	0.16	0.03	0.13	0.03	0.15	0.03	0.16	0.04	0.16	0.04
MgO	8.34	0.16	8.70	0.16	7.46	0.69	7.84	0.13	8.97	0.09	6.44	0.30	5.57	0.32	8.13	0.57	4.99	0.01	5.56	0.16	5.30	0.51
CaO	11.16	0.10	11.56	0.10	10.36	0.68	11.61	0.16	12.33	0.11	9.71	0.38	8.45	0.47	10.96	0.57	7.38	0.40	8.09	0.78	9.38	0.08
Na_2O	3.11	0.05	3.07	0.05	3.46	0.22	3.28	0.06	2.94	0.03	3.25	0.16	3.23	0.16	3.02	0.32	2.96	0.28	3.91	0.55	3.67	0.35
K_2O	1.76	0.05	1.78	0.05	1.94	0.18	1.86	0.04	1.60	0.03	2.16	0.14	2.57	0.28	1.99	0.18	2.91	0.18	2.70	0.34	1.84	0.19
P_2O_5	0.36	0.04	0.38	0.04	0.42	0.03	0.39	0.04	0.35	0.02	0.47	0.02	0.57	0.11	0.39	0.02	0.65	0.18	0.49	0.03	0.45	0.04
*Total:	98.19		98.02		97.97		98.05		98.08		98.44		97.53		98.70		96.23		97.98		93.49	
Mg#	0.65		0.79		0.68		0.69		0.52		0.67		0.64		0.76		0.60		0.62		0.61	

Note: Mg# = [MgO/(MgO+FeO)]molar ratio, assuming FeO= FeO_{tot}

σ standard deviation; H_2O_f = water content in the melt determined by the by-difference calculation method (respect to the total of EMP analyses); N = number of analyses.

* analyses are normalized to 100but the original total is reported.

Table S4 Ionic radius of the elements reported in the Onuma diagrams taken from Shannon (1976)

Site	Fold coordination	Valence	Cations	Ionic radius (Å)
M1	VI	Divalent	Ni	0.69
			Mg	0.72
			Co	0.74
			Fe	0.78
			V	0.79
			Mn	0.83
		Trivalent	Al	0.53
			Cr	0.61
			Sc	0.74
		Tetravalent	Ti	0.6
			Hf	0.71
			Zr	0.72
M2	VIII	Monovalent	Na	1.18
			K	1.51
			Rb	1.61
		Divalent	Ni	0.83
			Mg	0.89
			Co	0.90
			Fe	0.92
			Mn	0.96
			Ca	1.12
			Eu	1.25
			Sr	1.26
			Pb	1.29
			Ba	1.42
		Trivalent	La	1.16
			Ce	1.14
			Pr	1.13
			Nd	1.11
			Sm	1.08
			Eu	1.06
			Gd	1.05
			Tb	1.04
			Dy	1.03
			Y	1.02
			Ho	1.01
			Er	1
			Tm	0.99
			Yb	0.98
			Lu	0.97
		Tetravalent	U	1
			Th	1.05

Supplementary Material 3

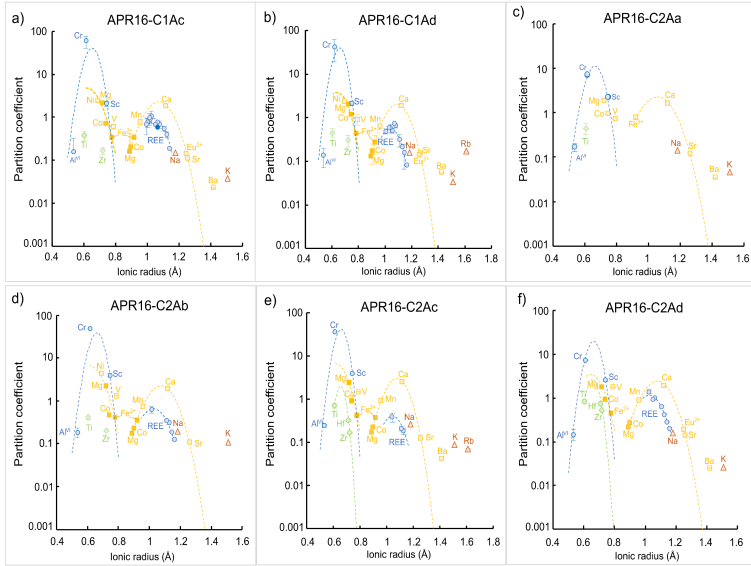

Fig. S1. *Onuma diagrams for clinopyroxene-liquid partition coefficients for mono-, di-, tri-, and tetravalent cations versus ionic radii (in Å; Shannon, 1976) for VI- and VIII-fold coordinated sites along with the results of the lattice strain fits in M1 and M2 sites for samples (a) APR16-C1Ac (1250 °C, 6 hours), (b) APR16-C1Ad (1250 °C, 9 hours), (c) APR16-C2Aa (1220 °C, 0.25 hours), (d) APR16-C2Ab (1220 °C, 3 hours), (e) APR16-C2Ac (1220 °C, 6 hours), (f) APR16-C2Ad (1220 °C, 9 hours). Symbols are as in Figure 6.*

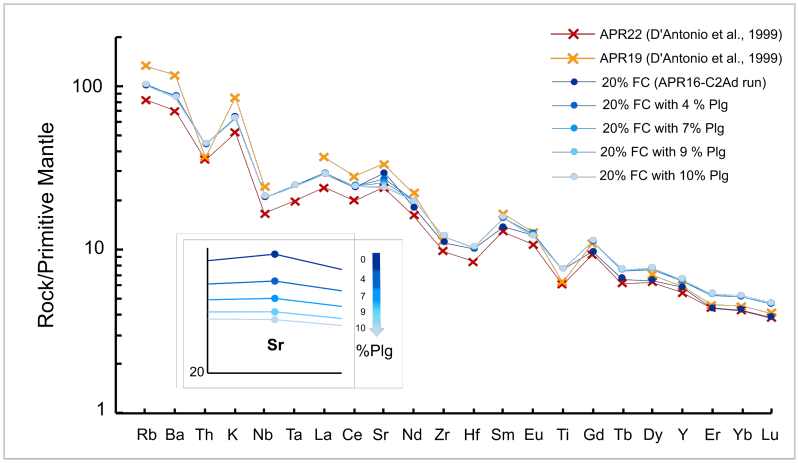

Fig. S2. *Primitive Mantle normalized (McDonough and Sun, 1995) trace elements patterns for the predicted composition of differentiated melts obtained after 20% of fractional crystallization from the K-basaltic parental magma (APR22). The differentiated melts are obtained using the crystallized phase assemblage determined for runs APR16-C2Ad (Cpx(17)+Ol(3)) plus the addition of plagioclase (from 5 to 20%) with the crystallizing mass (20%) constant. The inset shows Sr pattern decreasing with increasing the amount of plagioclase. The modelled compositions were calculated by using the Excel© spreadsheet program of Ersoy and Helvaci (2010).*


BB